

Dynamic magnetic particle actuation for integrated lab-on-chip biosensing

Citation for published version (APA):

Reenen, van, A. (2014). *Dynamic magnetic particle actuation for integrated lab-on-chip biosensing*. [Phd Thesis 1 (Research TU/e / Graduation TU/e), Applied Physics and Science Education]. Technische Universiteit Eindhoven. <https://doi.org/10.6100/IR773244>

DOI:

[10.6100/IR773244](https://doi.org/10.6100/IR773244)

Document status and date:

Published: 01/01/2014

Document Version:

Publisher's PDF, also known as Version of Record (includes final page, issue and volume numbers)

Please check the document version of this publication:

- A submitted manuscript is the version of the article upon submission and before peer-review. There can be important differences between the submitted version and the official published version of record. People interested in the research are advised to contact the author for the final version of the publication, or visit the DOI to the publisher's website.
- The final author version and the galley proof are versions of the publication after peer review.
- The final published version features the final layout of the paper including the volume, issue and page numbers.

[Link to publication](#)

General rights

Copyright and moral rights for the publications made accessible in the public portal are retained by the authors and/or other copyright owners and it is a condition of accessing publications that users recognise and abide by the legal requirements associated with these rights.

- Users may download and print one copy of any publication from the public portal for the purpose of private study or research.
- You may not further distribute the material or use it for any profit-making activity or commercial gain
- You may freely distribute the URL identifying the publication in the public portal.

If the publication is distributed under the terms of Article 25fa of the Dutch Copyright Act, indicated by the "Taverne" license above, please follow below link for the End User Agreement:

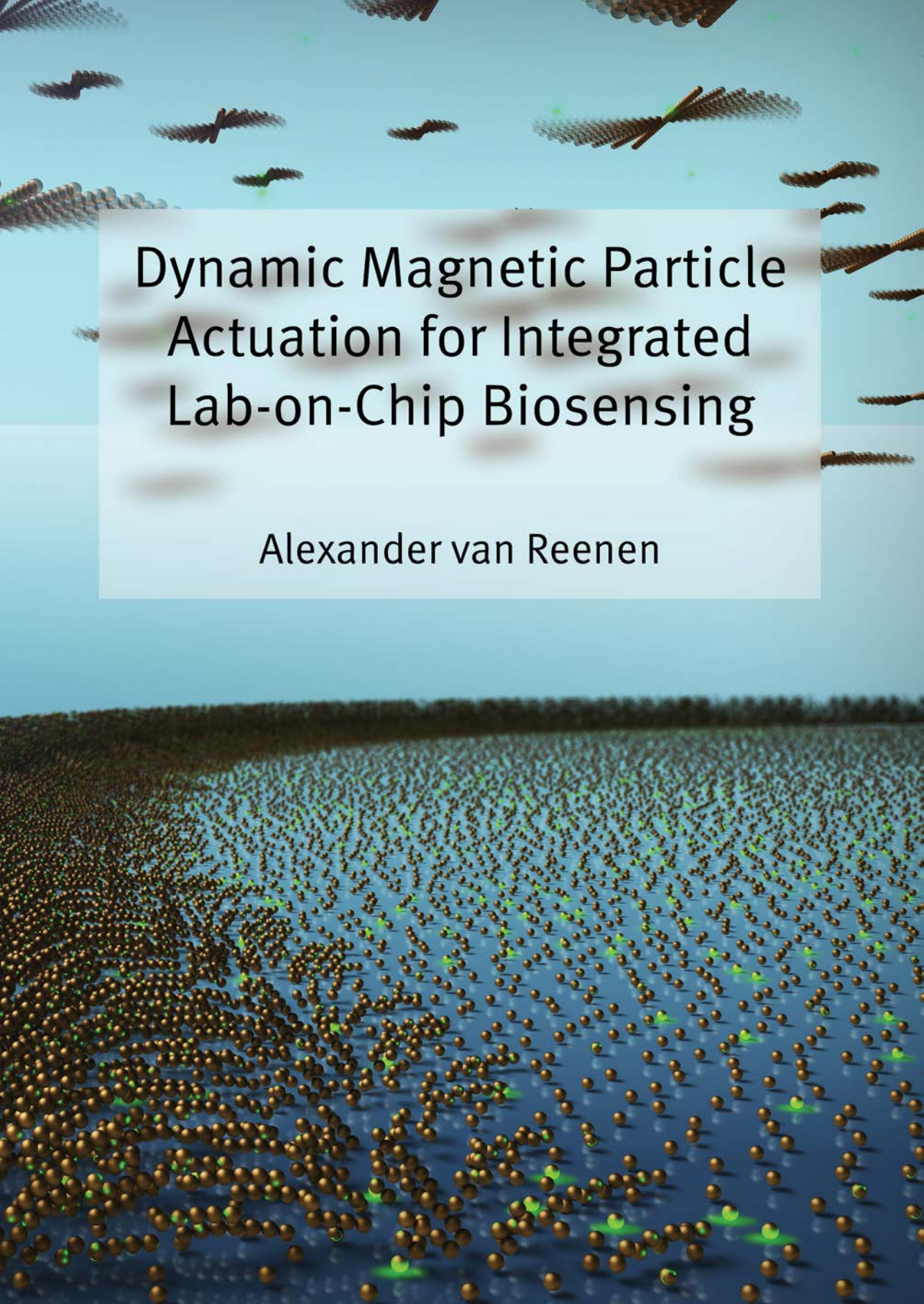
www.tue.nl/taverne

Take down policy

If you believe that this document breaches copyright please contact us at:

openaccess@tue.nl

providing details and we will investigate your claim.



Dynamic Magnetic Particle Actuation for Integrated Lab-on-Chip Biosensing

Alexander van Reenen

Dynamic magnetic particle actuation for integrated lab-on-chip biosensing

Dynamic magnetic particle actuation for integrated lab-on-chip biosensing / by Alexander van Reenen.

Technische Universiteit Eindhoven, 2014.

A catalogue record is available from the Eindhoven University of Technology Library.
ISBN: 978-90-386-3622-1

This thesis was prepared using Word 2007.

Cover design: ICMS Animation Studio, TU/e

Printed by: Proefschriftmaken.nl || Uitgeverij BOXPress

This research is supported by the Dutch Technology Foundation STW, which is part of the Netherlands Organisation for Scientific Research (NWO) and partly funded by the Ministry of Economic Affairs (project number 10458).



Dynamic magnetic particle actuation for integrated lab-on-chip biosensing

PROEFSCHRIFT

ter verkrijging van de graad van doctor aan de
Technische Universiteit Eindhoven, op gezag van de
rector magnificus, prof.dr.ir. C.J. van Duijn, voor een
commissie aangewezen door het College voor
Promoties in het openbaar te verdedigen
op maandag 2 juni 2014 om 16.00 uur

door

Alexander van Reenen

geboren te Eindhoven

Dit proefschrift is goedgekeurd door de promotoren en de samenstelling van de promotiecommissie is als volgt:

voorzitter:	prof.dr. H.J.H. Clercx
1 ^e promotor:	prof.dr.ir. M.W.J. Prins
2 ^e promotor:	prof.dr.ir. J.M.J. den Toonder
copromotor:	dr.ir. A.M. de Jong
leden:	Prof.Dr. R. Zengerle (Universität Freiburg)
	prof.dr.ir. A. van den Berg (UT)
	prof.dr. G.J.L. Wuite (VU)
	prof.dr.ir. H.J.M. Swagten

Summary

The aging population and increases in chronic diseases put high pressure on the healthcare system, which drives a need for easy to use and cost-effective medical technologies. *In vitro* diagnostics (IVD) plays a large role in delivering healthcare and within the IVD market, decentralized diagnostic testing, i.e. point-of-care testing (POCT), is a growing segment. POCT devices should be compact and fully integrated for maximum ease of use. A new class of POCT technologies is appearing based on the use of actuated magnetic particles. The use of magnetic particles has important advantages: they have a large surface-to-volume ratio, are conveniently bio-functionalized, provide a large optical contrast, and they can be manipulated by magnetic fields for full control of the integrated biosensing assay. Based on these properties, magnetic particles have been applied to perform key processing steps in integrated microfluidic assays, such as mixing, analyte capture, washing, buffer exchange and labeling for the final detection step.

In this thesis, we have improved the understanding of magnetic particle-based biosensing assays by combining experimental studies with theoretical model descriptions of individual magnetic actuation processes. We have characterized the different binding processes in the assay, identified the limitations therein and developed novel actuation tools to optimize these steps and their integration. Specifically, we have studied and developed methods (i) to rapidly and efficiently capture molecular analytes from sample fluid using magnetic particles, (ii) to control and redisperse particle distributions and (iii) to accelerate molecular sandwich formation of analytes captured by magnetic particles to a sensor surface. Lastly, we considered the integration of the different processes within a single microfluidic biosensing assay.

Magnetic particles are well-suited for the capture of analyte from biological samples due to their high surface-to-volume ratio and the availability of many bio-functionalization options. We have unraveled the fundamental process of particle-based affinity capture of target analytes using experiments and numerical simulations on several experimental model systems. The capture process first consists of volume transport to generate encounters between particles and analytes. Subsequently, near-surface transport occurs to reach alignment between the binding sites. Lastly, a chemical reaction takes place to bind the reactants. For the particle-based capture of proteins, it is found that association is limited by both transport processes. In

particular, we have shown that depletion zones are formed in the protein concentrations near the reactive particle surfaces, especially for high magnetic particle concentrations. By magnetically actuating magnetic particles, these depletion zones can be reduced. The application of magnetic field gradients and rotating magnetic fields allows to respectively translate and rotate chains of magnetic particles through the fluid volume. Using a model system comprising target proteins labeled with fluorescent dye molecules, we determined and studied association rate constants as a function of the type of actuation, different actuation parameters and the magnetic particle concentration. We have shown that capture rates can be improved by one up to two orders of magnitude, indicating that magnetic particle actuation allows one to reduce incubation times or improve capture efficiencies in a diagnostic microfluidic assay.

When exposed to magnetic fields, magnetic particles tend to aggregate and drift toward magnet poles. This effect reduces the effectiveness of magnetic particles when magnetic actuation is applied. The opposite process, disaggregation and particle movement away from external magnets is not straightforward to achieve with magnetic fields. We have developed novel magnetic actuation protocols to disaggregate and redistribute collections of magnetic particles. In one approach, we take advantage of repulsive magnetic dipole-dipole interactions between particles confined at a physical boundary, using out-of-plane fields and field gradients. We developed a numerical Brownian dynamics simulation model in order to analyze the experimental data on the field-induced particle dynamics. Furthermore, the developed disaggregation protocol was found to be useful to accurately characterize distributions of magnetic dipole moments of magnetic particles, by a method called intra-pair magnetophoresis. To translate and redistribute particles over a surface, we developed a method called rotaphoresis, in which an applied rotational motion of chains of particles near a solid surface is effectively converted into translational motion along the surface. By tuning the time-dependent properties of the magnetic field, large clusters of particles can be made to move over a surface at velocities of several mm/s, while disaggregating within a few seconds. Based on this study, we conclude that interesting and functional particle behavior can be obtained by applying time-dependent magnetic fields in three dimensions.

Lastly, we investigated whether magnetic actuation could be used to accelerate the binding of targets captured by magnetic particles to a sensor surface. To analyze bond formation in detail, a model system was employed in which the captured targets were 200 nm fluorescent nanoparticles. This enabled us to directly distinguish specific bonds from non-specific bonds in experiments. Using numerical Brownian dynamics simulations of the binding reaction, a magnetic actuation protocol was developed to keep particles in touch with the surface and to speed up the exposure of the particle surface to the sensor surface. It was found that magnetic actuation can reduce incubation times by roughly a factor 3. Importantly, experimental data showed that non-specific interactions can hamper the exposure of the full particle surface to the sensor surface. We expect that the incorporation of magnetic stringency steps in the incubation protocol can further accelerate specific bond formation by at least one order of magnitude.

Together, the methods described in this thesis are supportive for the development of integrated microfluidic diagnostic assays in which all the processing steps are rapidly and efficiently performed using magnetic fields. Actuation protocols to speed up binding processes can be combined with the actuation methods to control and reset the particle distributions. Our findings show that magnetic actuation can reduce operation times of several key steps in an assay by one to two orders of magnitude, and may thereby significantly improve lab-on-chip device operation.

We expect that integrated magnetic actuation-based biosensing systems will have a large impact on society in the future. Such systems will allow quantitative decentralized in-vitro diagnostic testing in a rapid manner with a user-friendly “sample-in result-out” type of performance, in hand-held and desktop-sized instruments. By virtue of these properties, the systems can help to improve patient diagnostics, patient monitoring and disease management, with impact on the quality, accessibility and cost-effectiveness of future healthcare.

Contents

Summary	v
1. Introduction – Integrated lab-on-chip biosensors based on magnetic particle actuation.....	1
1.1 Introduction	2
1.2 Microfluidic mixing of fluids	4
1.2.1 Mixing a flowing fluid using magnetic particles.....	4
1.2.2 Mixing a static fluid using magnetic particles.....	6
1.3 Capture of analytes from sample fluids	8
1.3.1 The analyte capture process	8
1.3.2 Analyte capture using magnetic particles in a flowing fluid	10
1.3.3 Analyte capture using magnetic particles in a static fluid	12
1.4 Analyte detection.....	13
1.4.1 Magnetic particles as carriers.....	13
1.4.2 Agglutination assays with magnetic particles	17
1.4.3 Surface binding assays using magnetic particles.....	20
1.4.4 Magnetic stringency	23
1.5 Integration of magnetic actuation processes	24
1.6 Aim and outline of the thesis.....	28
2. Accelerated particle-based target capture – the roles of volume transport and near-surface alignment.....	31
2.1 Introduction	32
2.2 Theoretical considerations.....	32
2.3 Experimental section	35
Particles and Chemicals	35
Passive transport experiment	36
Fluid agitation by vortex mixing.....	36
Magnetic rotation.....	37
2.4 Capturing particles by passive diffusive transport.....	37
2.4.1 Influence of the planar substrate	39
2.4.2 Influence of electrostatic interactions.....	39
2.4.3 Influence of the size of the targets	41
2.4.4 Influence of the biochemical binders	43
2.5 Fluid agitation by vortex mixing	44
2.6 Actuation by stationary magnetic rotation.....	45
2.7 Conclusions	47

2.8 Appendix	49
2.A Loss in target concentration or saturation of the reactive surface	49
2.B The response of magnetic particles in a rotating magnetic field	50
2.C Radial transport near a rotating sphere.....	50
2.D Lifetime of an encounter complex	51
2.E Brownian rotation of a capture particle in an external magnetic field.....	52
3. Dynamic actuation of magnetic particle chains for accelerated target capture	55
3.1 Introduction.....	56
3.2 Experimental section.....	57
3.2.1 Model system for particle-based target capture	57
3.2.2 Preparation and filling of the incubation chamber	58
3.2.3 Magnetic field generation	59
3.2.4 Magnetic redistribution of particles after actuation	59
3.2.5 Quantification of target capture	59
3.2.6 Verification of the specificity of antibody capture	60
3.2.7 Determination of rate constants for association and dissociation	61
3.3 Results and discussion	62
3.3.1 Mixing induced by rotating magnetic particle chains	62
3.3.2 Effect of magnetic particle actuation on the capture process	65
3.3.3 Comparing experimental data to Brownian dynamics simulations.....	68
3.3.4 Influence of field rotation parameters.....	70
3.3.5 Influence of the magnetic particle concentration	72
3.5 Conclusions.....	75
3.6 Appendix	78
3.A Field calibration of the 5-pole electromagnet	78
3.B Rotaphoresis to redistribute particles	78
3.C The mixing index	80
3.D Comparison of particle-based capture with planar surface assays	81
3.E Brownian dynamics simulation of the capture process	82
3.F SEM image of M270 magnetic particles	84
4. Dynamics of Magnetic Particles near a Surface: Model and Experiments on Field-Induced Disaggregation	85
4.1 Introduction.....	86
4.2 Theoretical considerations	87
4.3 Experimental section.....	89
4.3.1 Experimental setup	89
4.3.2 Characterization of the setup	90
4.4 Results	92
4.4.1 Initialization of particle distribution	92
4.4.2 Overcoming non-specific interparticle adhesion	93
4.4.3 Simulation of the separation dynamics of two-particle clusters	95
4.4.4 Parameters influencing the separation probability	95
4.4.5 Disaggregation of chain- and sheet-like particle clusters	98
4.4.6 Repeated disaggregation of large particle clusters.....	101
4.5 Conclusions.....	104
4.6 Appendix	105
4.A Error analysis of the excluded volume force between particles	105
4.B Numerical scheme: error analysis	106
4.C Breaking two-particle clusters in the absence of a field gradient.....	107

5. Quantification of magnetic particle properties by intra-pair magnetophoresis	109
5.1 Introduction	110
5.2 Methods.....	111
5.3 Results	112
5.4 Discussion and Conclusions	116
5.5 Appendix	117
5.A Intra-pair separation due to repulsive dipole-dipole interaction between the two particles.....	117
5.B Hydrodynamic interactions between particles.....	119
5.C Electrostatic interactions between particles.....	120
5.D Translating a pair distribution into a single moment distribution.....	122
5.E Gaussian distributions: change in width by pair-averaging	124
5.F Influence of the magnetic field due to particle magnetization	125
5.G Estimation of the smallest particle size for intra-pair magnetophoresis	126
6. Magnetic field-induced rotaphoresis for controlled redistribution of magnetic particles over a surface	129
6.1 Introduction	130
6.2 Experimental section	131
6.3 Numerical methods.....	132
6.4 Results and discussion	133
6.4.1 Rotaphoresis to redistribute particle clusters over a surface.....	133
6.4.2 Particle velocities induced by rotaphoresis	137
6.4.3 Disaggregation of particle clusters by rotaphoresis.....	138
6.4.4 Influence of particle size and surface functionalization	142
6.5 Conclusions	143
7. Magnetic field accelerated molecular bond formation in surface-binding assays based on magnetic particles	145
7.1 Introduction	146
7.2 Methods.....	147
7.2.1 Materials	147
7.2.2 Attaching fluorescent nanoparticles to magnetic microparticles	149
7.2.3 Characterization of the remanent magnetic moment	149
7.2.4 Sandwich formation experiments.....	149
7.2.5 Brownian dynamics simulation of the surface binding reaction.....	150
7.3 The remanent moment of superparamagnetic particles	151
7.3.1 Response of magnetic particles in a rotating magnetic field	152
7.3.2 Numerical model of the remagnetization dynamics	155
7.3.3 Determining the magnitude of the remanent moment	158
7.4 Binding of particles with a target to a reactive surface	160
7.4.1 Numerical Brownian dynamics simulations.....	160
7.4.2 Experimental results.....	164
7.5 Discussion and Conclusions	167
7.7 Appendix	169
7.A Calibration of the magnetic setup.....	169
7.B Comparing magneto-crystalline anisotropy with shape anisotropy	169
7.C Validation of numerical Brownian rotation	172
7.D Statistics of fluorescent target capture by magnetic particles.....	172

8. Conclusions and Outlook.....	175
8.1 Introduction.....	176
8.2 Fundamental biophysical tools.....	176
8.2.1 Characterization of magnetic particles	176
8.2.2 Experimental model systems to study magnetic particle-based binding processes	177
8.2.3 Simulation models to study microfluidic process steps based on magnetic particles	179
8.3 Function-oriented research.....	180
8.3.1 Specific capture of analytes using magnetic particles.....	180
8.3.2 Redistribution of magnetic particles	181
8.3.3 Sandwich formation in surface-binding assays with magnetic particles.....	182
8.4 Integration: towards particle-based assays controlled and optimized by magnetic fields.....	183
Bibliography	187
Samenvatting	199
Publications	203
Curriculum vitae.....	207
Dankwoord	209

1

Introduction – Integrated lab-on-chip biosensors based on magnetic particle actuation

*The demand for easy to use and cost effective medical technologies inspires scientists to develop innovative lab-on-chip technologies for in vitro diagnostic testing. To fulfill the medical needs, the tests should be rapid, sensitive, quantitative, miniaturizable, and need to integrate all steps from sample-in to result-out. In this chapter, we sketch the context for this thesis by reviewing the use of magnetic particles that are magnetically actuated to perform the different process steps required for integrated lab-on-chip diagnostic assays. We discuss the use of magnetic particles to mix fluids, to capture specific analytes, to concentrate analytes, to transfer analytes from one solution to another, to label analytes, to perform stringency and washing steps, and to probe biophysical properties of the analytes, distinguishing methodologies with fluid flow and without fluid flow (stationary microfluidics). Our review focuses on efforts to combine and integrate different magnetically actuated assay steps, with the vision that it will become possible in the future to realize integrated lab-on-chip biosensing assays in which all assay process steps are controlled and optimized by magnetic forces. Finally, we formulate the central aim of this thesis and introduce the subsequent chapters.**

*Parts of this chapter have been published as a review: A. van Reenen, A.M. de Jong, J.M.J den Toonder and M.W.J. Prins, Integrated Lab-on-Chip Biosensors based on Magnetic Particle Actuation – a Comprehensive Review, *Lab on a Chip*, DOI: 10.1039/C3LC51454D , 2014.

1.1 Introduction

The aging population and increases in chronic diseases put high pressure on the healthcare system, which drives a need for easy-to-use and cost-effective medical technologies.¹ *In vitro* diagnostics (IVD) plays a large role in delivering healthcare: it makes up a few percent of a hospital's budget but leverages the majority of all critical decision-making such as admittance, discharge, and medication.²⁻³ Decentralizing diagnostic testing, i.e. point-of-care testing (POCT), is a growing segment in the IVD market. POCT reduces the turn-around times to the physician, resulting in faster treatment decisions, giving improved workflows and improving the quality of care.⁴ Furthermore POCT devices create new opportunities to perform testing in less expensive settings such as the doctor's office and the home. This enables the possibility to deliver cost-effective care, e.g. remotely monitoring the progress of patients, personalization of treatment, and reducing the number of visits needed to the hospital.

Applications for which POCT is very relevant are for example the detection of proteomic markers to diagnose cardiac diseases and the detection of nucleic acid markers in case of infectious diseases. The detection of these biomarkers requires that POCT devices contain not only a sensing technology, but can also perform all the sample pretreatment steps that are required in the assay, thus becoming so-called lab-on-a-chip or micro-total-analysis systems,⁵ in which microfluidics plays an important role.⁶ As biomarkers are typically present at very low concentrations within complex samples that contain high concentrations of background material, the methodologies should be highly selective and accurate. In case of protein biomarker detection, molecular selectivity can be obtained by making use of antibodies in immunoassays⁷, and a high sensing accuracy can be achieved by introducing labels in the assay. In nucleic-acid assays purification and biochemical amplification steps are typically applied.⁸

Concerning protein biomarker detection, several immunoassay sensing technologies have been developed, such as nanoparticle labeling⁹⁻¹¹, label-free electrical detection¹², fluorescence detection¹³⁻¹⁴ and oligonucleotide labeling combined with biochemical amplification¹⁵. While the detection sensitivities of these technologies can be high, the integration of these platforms in cost-effective lab-on-chip devices is complicated because several active fluidic steps are required to enable sample-pretreatment⁹⁻¹⁵, (bio)chemical development^{9, 15} or washing using buffer fluids⁹⁻¹⁵. Therefore, it is important to face the challenge of total integration¹⁶ and design solutions that facilitate all assay steps, from sample preparation to final detection.

For several decades magnetic particles have been applied in pipette-based assays, ranging from manual assays for basic research to assays in high-throughput instruments for centralized laboratories.¹⁷ The main advantages of using magnetic particles* are that they have a large surface-to-volume ratio, are conveniently bio-

* In the scientific literature, the terms 'magnetic particle' and 'magnetic bead' are often interchangeably used. We use 'magnetic particle' because it is more general, as 'magnetic bead' mostly relates to spherical particles made of composite material.

functionalized, and that they can be manipulated by magnetic fields, thereby simplifying extraction and buffer replacement steps. Particles are commercially available with different sizes, magnetic properties and surface coatings. Most particles are synthesized by coprecipitation or thermal decomposition.¹⁸ The magnetic core can be composed of e.g. iron oxides (like magnetite Fe_3O_4 or maghemite $\gamma\text{-Fe}_2\text{O}_3$) or pure metals (like Fe and Co) or alloys (like FePt). The magnetic material is protected by a coating that can be polymeric or inorganic and also serves as a starting point for bio-functionalization. When many separate magnetic grains are embedded inside a non-magnetic matrix,¹⁹ the particle as a whole can exhibit superparamagnetic behavior²⁰, i.e. the particles are paramagnetic with a very high magnetic susceptibility.

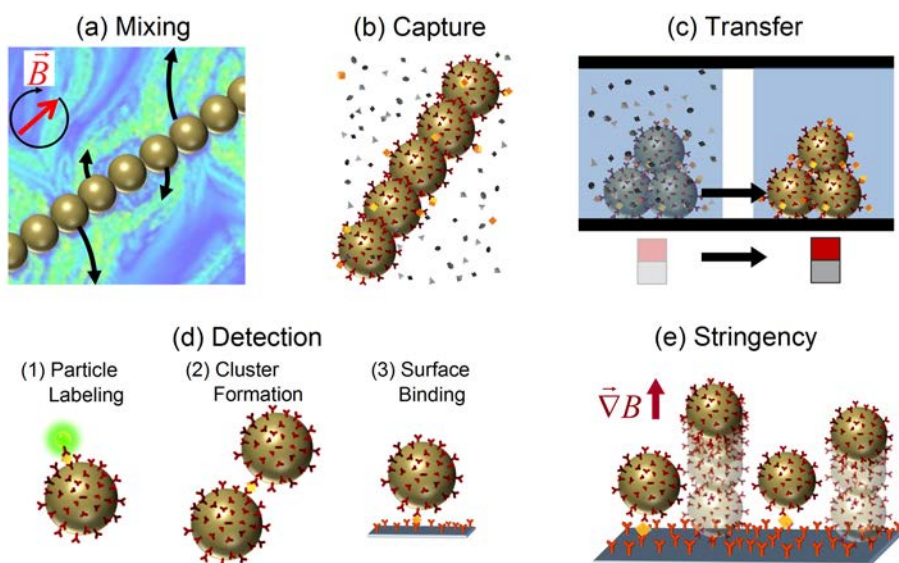


Figure 1.1 Application of magnetic particles in several process steps of a lab-on-chip diagnostic assay. Actuated by applied magnetic fields, magnetic particles have been used (a) to mix fluids, (b) to selectively capture specific analytes, (c) to transfer analytes to another fluid, (d1) to label particles for detection, (d2) to form clusters for detection, (d3) to induce surface binding for detection, and (e) to apply stringency forces in order to improve the signal-to-noise ratio. (a) Adapted with permission from ref²¹. Copyright 2007 The American Physical Society.

The availability of magnetic particles and corresponding assay reagents has formed a solid starting point for explorations toward miniaturization, i.e. efforts to realize integrated and miniaturized technologies based on magnetic particles and small fluid volumes.^{18, 22} It is difficult in principle to manipulate fluids at small scales, due to high flow resistances, dominance of capillary forces, and difficulties to achieve mixing at low Reynolds numbers. Yet, the manipulation of magnetic particles by magnetic fields scales favorably with system miniaturization, because close to the field generators the magnetic fields are strong, because magnetic field gradients are large close to structures with high curvature, and in addition only short distances need to be traveled in miniaturized devices. This has led e.g. to the concept of

stationary microfluidics²³⁻²⁵, in which overall fluid manipulation is minimized and the control of assay steps is mainly effectuated by magnetic particles and magnetic forces.

Magnetic particles are highly versatile and have been studied for many process steps that are required for lab-on-chip diagnostic assays. Magnetic particles have been applied (see Figure 1.1) to mix fluids, to selectively capture specific analytes (i.e. the biomarkers that need to be detected), to concentrate analytes, to transfer analytes from one solution to another, to label analytes, to perform stringency and washing steps, and to probe biophysical properties of the analytes. In this chapter, an overview will be given of the accomplishments of magnetic particles in all these functions, to provide the context for this thesis. The review presented in this chapter is centered around the concept that the integration of point-of-care assays can be facilitated by using actuated magnetic particles. We describe key assay steps in which magnetic particle actuation can play a role: mixing (Section 1.2), analyte capture (Section 1.3), and analyte detection (Section 1.4). These three process steps are essential in every assay based on molecular binding affinity. We focus on the application of magnetic actuation in immunoassays and somewhat less on nucleic-acid detection assays. Thereafter we summarize the status of the *integration* of the different magnetically actuated assay steps with the vision that in the future it will become possible to realize integrated lab-on-chip biosensing assays in which all assay processes are controlled and optimized by magnetic forces. Lastly, based on this review, the aim of this thesis is formulated and the outline of this thesis will be described.

1.2 Microfluidic mixing of fluids

The mixing of fluids has been a topic of long-standing interest in the microfluidic community. Due to the small dimensions in microfluidic devices, viscous forces generally dominate the fluid behavior, resulting in slow and inefficient mixing. In most POCT devices, rapid mixing of two or more fluids or solutes is an essential step. Methods based on magnetic particles and magnetic fields have been investigated with the aim to improve microfluidic mixing. The methods can be separated in two classes: (i) mixing of fluid layers in a laminar fluid flow and (ii) mixing of fluid in a static fluid compartment, as is discussed in the following sections.

1.2.1 Mixing a flowing fluid using magnetic particles

In the presence of a magnetic field, magnetic particles tend to form chains and supra-particle structures due to the magnetic dipole-dipole interaction between the particles. Such magnetic structures can be used to stir fluids at the microscale. Hayes et al.²⁶ found that applying a magnetic field to a suspension of superparamagnetic particles in a microfluidic channel causes the formation of dynamic and reversible self-assembled regularly-spaced supra-particle structures (see Figure 1.2a). The formed structures or “plugs” could be rotated through all axes, without losing structural form. In addition, these plugs resist deformation during pressure flow conditions and as such are able to influence fluid flow within a microchannel.

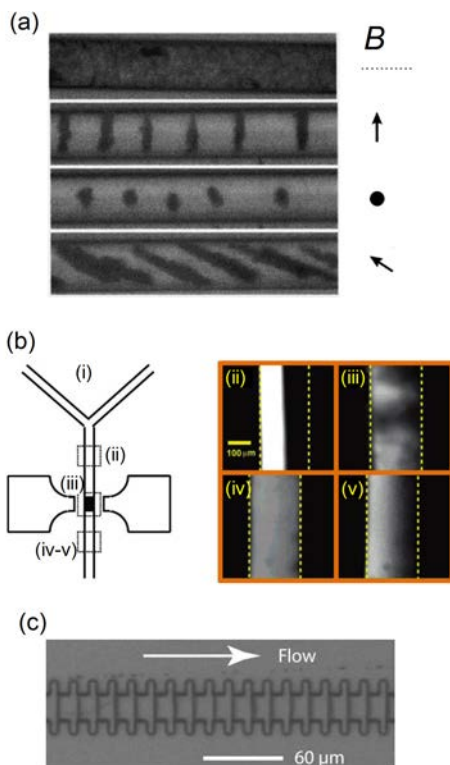


Figure 1.2 Examples of various assembled magnetic particle structures to increase particle-fluid interactions with a microfluidic flow. (a) Formation of supra-particle structures of superparamagnetic particles ($\text{\O}1\text{-}2\ \mu\text{m}$) within a microchannel ($\text{\O}20\ \mu\text{m}$) for different field orientations, as indicated by the arrows to the right of the images. (b) Fluid mixing of parallel fluorescent and non-fluorescent streams within a channel by magnetically retaining and actuating supraparticle structures. The fluorescence images (ii-v) on the right are taken at different locations as indicated in panel (i): (ii) before mixing; (iii) during mixing; (iv) after mixing using a 20 Hz sinusoidal external field; and (v) after mixing using a 5 Hz square-shaped external field. (c) Optical image of a microchannel engineered to assemble and retain magnetic particles into plugs across the channel. In the image, 20 plugs are shown and fluid flows from the left to the right. (a) Reprinted with permission from ref.²⁶. Copyright 2001 American Chemical Society. (b) Reprinted with permission from ref.²⁷. Copyright 2004 American Chemical Society. (c) Reprinted with permission from ref.²⁸. Copyright 2004 American Chemical Society.

Rida and Gijs²⁹ showed that supra-particle structures can be retained at a well-defined position within a microchannel by focusing the magnetic field and by using ferromagnetic particles. Using a local alternating magnetic field, they found that the rotational motion of the particles enhances the fluid perfusion through the magnetic structure.²⁷ The strong particle-fluid interaction could be controlled by the field frequency and amplitude, as well as the fluid flow rate, and the effectiveness was analyzed by studying the mixing of two parallel flow streams within the microchannel (see Figure 1.2b). Starting from a laminar flow pattern, a 95% mixing efficiency was obtained using a mixing length of only 400 μm and flow rates in the order of 0.5 cm/s. The efficient fluid mixing was attributed to the chaotic splitting of fluid streams through the dynamic and randomly porous structure of the particle aggregate, combined with the relative motion of the fluid with respect to the magnetic particles. This type of magnetic micromixer was also studied using a numerical model in order to find optimal magnetic actuation conditions for different microchannel dimensions.³⁰ In another study³¹, microchannels were connected to a microfluidic mixing chamber in which ferromagnetic particles were actuated using rotating fields to efficiently mix fluids flowing up to 5 mm/s. Suzuki et al.³² combined a two-dimensional serpentine channel with pulsed lateral magnetic particle translation to create the typical stretching and folding behavior of the fluid that is characteristic for chaotic mixing.

Another interesting development has been the use of multiple small particle plugs instead of one large particle plug. Multiple plugs can be stably formed and retained in a channel by integrating soft-magnetic elements in the channel walls³³, or by using a channel with a periodically varying cross-section and a magnetic field orthogonal to the channel (see Figure 1.2c).²⁸ The advantage of using distributed particle plugs in a fluid flow is that the biochemical reactions on the particles are more easily controlled and monitored.

Magnetic particles are effective for achieving fluid mixing in microchannel flows, but strong forces are needed to retain the particles in the channel. Generally ferromagnetic particles with high magnetic content need to be used because the magnetic forces achievable with superparamagnetic particles are too weak.³⁴ However, Moser et al.³⁵ showed that superparamagnetic particles can be used if the fields are generated by a combination of ferromagnets and electromagnets. An advantage of using superparamagnetic particles instead of ferromagnetic particles is that superparamagnetic particles lose their magnetization when the field is turned off, facilitating the redispersion of particles in solution. This is very important in case the particles are needed for further assay steps such as target capture or detection.

1.2.2 Mixing a static fluid using magnetic particles

In microfluidic systems, fluid mixing is not necessarily performed in a fluid flow. Fluid mixing is also relevant in static fluid compartments, e.g. to mix a sample with reagents after loading the sample into a microfluidic reaction chamber, or to homogenize reagents and avoid near-surface reactant depletion during a biochemical reaction at a surface. For such applications, superparamagnetic particles have been shown to be very useful, as we describe in this section.

Vuppu et al.³⁶⁻³⁷ were one of the first to discover that superparamagnetic particles form rotating chains in a rotating magnetic field. The rotors could be assembled dynamically and the length and speed was found to be varying in time (see Figure 1.3a), and as such the method was reported to be suitable for micromixing applications in biosensing.

To understand the dynamic behavior of the chains in more detail, models have been developed in which particle chains were treated as three-dimensional circular cylinders³⁸, as chains of circles in two dimensions^{21, 39} and as chains of spheres in three dimensions⁴⁰⁻⁴³. To characterize the chain behavior, most studies^{21, 39-40, 44} used the dimensionless Mason number, which is the ratio between the rotational shear forces (i.e. hydrodynamic drag) and the magnetic interaction forces:

$$\text{Ma} = \frac{\eta\omega}{\mu_0\chi_p H^2}, \quad (1.1)$$

with η the dynamic viscosity of the fluid, ω the field rotation frequency, μ_0 the permeability of free space, χ_p the magnetic susceptibility of the particle and H the magnetic field strength. It has been found^{21, 39} that for high Mason numbers (i.e. low magnetic torques), particle chains split up in small chains that only mix well in the vicinity of the particle chain. Conversely, for low Mason numbers (i.e. high magnet-

ic torques) particle chains are rigid, and demonstrate little mixing near the center of the particle chain and better mixing towards the ends of the chains (see Figure 1.3b). The best mixing conditions were obtained at intermediate Mason numbers where chains break and reform repeatedly, creating a fluid flow that is characteristic for chaotic mixing⁴⁵. To characterize the induced chaotic mixing, Kang et al.²¹ computed the Lyapunov exponents⁴⁵ at different Mason numbers (see Figure 1.3c), which are a measure for the spatial divergence of two artificial fluid tracers that are initially separated by a very small distance. As shown in Figure 3c, for intermediate Mason numbers, the highest Lyapunov exponents are found, indicating the optimal regime for chaotic mixing.

As the reported optimal values for the Mason number vary in literature, a modified Mason number was introduced by Gao et al.⁴¹ which more exactly describes the torques and includes the number of particles, N , within a chain. The number R_T equals the ratio of torques (rather than forces) and was defined as:

$$R_T = 16 \frac{\eta \omega}{\mu_0 \chi_p^2 H^2} \frac{N^3}{(N-1) \left(\ln \left(\frac{N}{2} \right) + \frac{2.4}{N} \right)}. \quad (1.2)$$

Using R_T , the rotational behavior of a particle chain can be described independent of the number of particles. In case $R_T > 1$ the chain exhibits breaking behavior, whereas for $R_T < 1$, the particle chain remains rigid; this was shown in numerical simulations as well as in experiments.

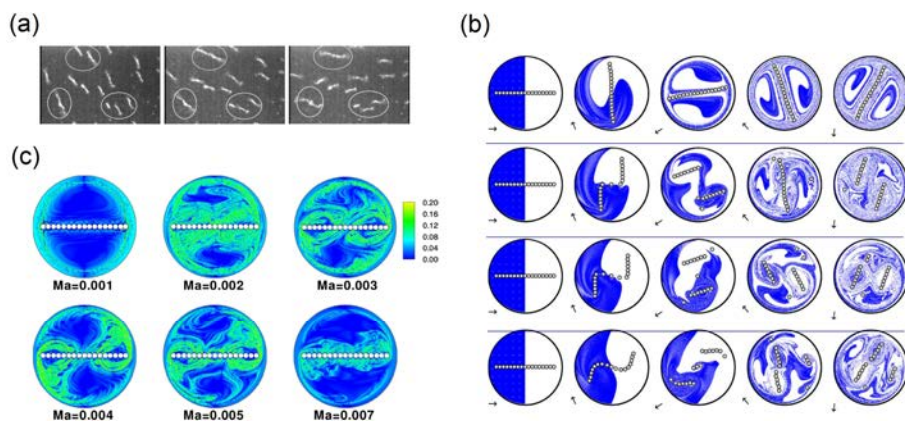


Figure 1.3 Examples of magnetic particle-based mixing within a static fluid. (a) In a rotating field (3.2 Hz), magnetic particles form chains that grow and fragment dynamically. (b) Result of 2-D numerical simulations of a particle chain in a rotating field, showing the progress of mixing at different time points (to the right), for four different Mason numbers: (from top to bottom resp.) $Ma = 0.001$, 0.002 , 0.003 and 0.005 . Initially, the fluid interface is perpendicular to the chain. (c) Results of 2-D numerical simulation, showing the spatial distributions of the maximum Lyapunov exponent at several Mason numbers. (a) Reprinted with permission from ref³⁶. Copyright 2003 American Chemical Society. (b,c) Reprinted with permission from ref²¹. Copyright 2007 The American Physical Society.

Experimental mixing studies were performed in microliter reaction chambers^{42, 46-48} and in droplets⁴³. In general, the experiments confirm theoretical data⁴⁷, but simulations fail to describe systems in which the particle density is high. Over time, particle chains grow in length⁴⁸ and interact with other chains^{43, 46-47}, which is not covered in simulations of isolated chains.

In conclusion, the mixing capabilities of chains of superparamagnetic particles in a rotating magnetic field have been well studied. Optimal chaotic mixing is obtained for long chains that exhibit breaking and reformation behavior. This type of mixing is particularly interesting to accelerate (bio)chemical reactions in static microfluidic compartments, as it allows to homogenize fluids and overcome diffusion limitations.

1.3 Capture of analytes from sample fluids

The high surface-to-volume ratio and the availability of many bio-functionalization options make magnetic particles well-suited for the capture of analyte from biological samples. The analyte capture can be of specific as well as non-specific nature. Non-specific capture has been mainly developed for the isolation and purification of nucleic acids from lysed samples. In particular magnetic silica particles have been found to be very useful for nucleic acid preparation and detection.⁴⁹⁻⁵² Capture relies on the physisorption of the nucleic acids to the particles and is followed by fluid exchange steps to achieve isolation and purification. Specific capture requires particle functionalization with specific capture molecules, such as antibodies, with a high affinity to the analyte that is to be detected. In either case, the analyte capture rate scales with the total surface area of the suspended particles and therefore with the particle concentration. However, the use of a very high concentration of particles has disadvantages for downstream processes in an integrated multi-step lab-on-chip assay. High particle concentrations generally increase non-specific particle-particle and particle-surface interactions, enhance field-induced particle aggregation, cause steric hindrance in particle concentration steps, obstruct chemical reactions on the particles and sterically hinder reactions between the particles and a biosensing surface. Therefore, it is desirable to decrease particle concentrations while still maintaining high capture rates. To this end, magnetic actuation-based mixing techniques can be applied as discussed in the previous section. In the following paragraphs, we will discuss the effects of applying magnetic actuation for analyte capture, with a focus on the process of *specific* analyte capture. We describe the basic mechanisms underlying particle-based affinity capture of target analytes and review the literature on specific analyte capture by magnetic particles in flowing and static fluids.

1.3.1 The analyte capture process

The specific capture of analytes from a fluid onto magnetic particles is driven by (i) encounters between target analytes and bio-functional molecules on the surfaces of the particles, and (ii) the subsequent biochemical reactions between analytes and the surface-coupled capture molecules. This creates two avenues to accelerate the capture rate, firstly by increasing encounters and secondly by increasing the biochemi-

cal reaction rate. In contrast, the specificity of the capture is exclusively generated by the biochemical reaction. For example, in immunoassays antibodies are coupled to the particles for specific capture of analytes from the fluid. The analytes are typically present in very low concentrations within a complex sample containing a high concentration of background material, such as blood or saliva. In such complex matrices, non-specific adhesion of non-targeted molecules to the magnetic particles can seriously hamper the effectiveness of the assay. Therefore, it is essential to have control over the surface properties and to have a detailed understanding of the specific and non-specific surface reactions.

The process of particle-based capture of target analytes is similar to a bimolecular binding process⁵³⁻⁵⁴, i.e. it consists of an encounter step between the two components, which leads to a transient complex that can subsequently react chemically and become a bound complex. The total process is characterized by the overall rate constant of association, k_a (unit $M^{-1}s^{-1}$). For typical protein-protein interactions, the association rate constant ranges between 10^3 and $10^9 M^{-1}s^{-1}$. The association rate constant of specific protein-protein interactions is to a large extent determined by the fact that the two macromolecules can only bind if their outer surfaces are aligned and oriented in a very specific manner.⁵³ A relative translation by a few Angstroms or a relative rotation of a few degrees is enough to break the specific interactions. In general, the association rate of a protein complex is limited by diffusion, by geometric constraints of the binding sites, and may be further reduced by the final chemical reaction. In practice, usually either diffusion or the chemical reaction dominantly limit the reaction rate, although there is no simple test available to determine which process is the most important. Nevertheless, there are two indications for a diffusion limitation.⁵³ First, diffusion-controlled rate constants are usually high ($>10^5 M^{-1}s^{-1}$). Second, diffusion-controlled association involves only local conformational changes between unbound proteins and the bound complex, while reaction-controlled association typically involves gross changes such as loop reorganization or domain movement.⁵³ Typical antibody-antigen association rate constants are in the range of 10^5 - $10^7 M^{-1}s^{-1}$, which indicates that such reactions are generally diffusion-controlled.^{53, 55-56}

While most literature has focused on understanding the bimolecular reaction between two proteins that are free in solution, here we are interested in the case that one of the proteins is immobilized on the surface of a particle. So the bimolecular reaction involves the binding between a reactive particle and a protein, where the biochemical specificity to the targeted protein is determined by the capture proteins coupled to the particle. We have performed an experimental study⁵⁷ to identify to what extent different stages of the binding process are limiting. This study is presented in detail in Chapter 2. In particular, the diffusive encounter step was split up into the process of diffusion transport through the fluid volume and the process of near-surface alignment. Where volume transport generates the first encounters between particles and target proteins, the subsequent near-surface alignment process deals with the alignment rate of the binding sites of the reactants. The volume transport is essentially a translational process, while the alignment is determined by both the translational and the rotational mobility of the reactants. In experiments, the

different processes were studied under different types of particle actuation, for different target sizes, for different types and concentrations of proteins on the particle surface, and for different ionic strengths of the medium. It was found that both volume transport and the alignment of binding sites determine the association rate constants for particle-based target capture.

When free proteins react in solution, the alignment process (i.e. rotational diffusion) is an important restriction due to the highly specific alignment constraints^{55, 58}, but volume transport (i.e. translational diffusion) is not a limitation. In case one of the two proteins is attached to a surface, however, volume transport can become a limitation⁵⁹. Depending on the number of binding sites at the surface and the intrinsic chemical reaction rate, reactants can become depleted close to the surface, and depletion can be reduced by actively transporting the fluid over the surface.⁶⁰ Therefore, depletion can also play a role in particle-based target capture, which means that reaction rates may be positively influenced by actively applying volume transport processes. Indeed, increased reaction rates have been observed when actively moving particles through the fluid using magnetic fields⁶¹, and when applying flows to induce fluid perfusion through clusters of magnetic particles⁶². Limitations due to the specific alignment constraints can be further overcome by maximizing the number of binding sites on the particle surface and by improving the orientation of the immobilized proteins. Equally important, the surface properties of the particles should be optimized to reduce non-specific interactions and to make particle-based assays suitable for operation in complex fluids. In practice, the surface optimization process is more easily performed for particles than for planar surfaces, due to the fact that surface engineering can be applied with a higher throughput to particles in solution than to surfaces in microdevices.

1.3.2 Analyte capture using magnetic particles in a flowing fluid

Improving the capture efficiency of target analytes from a fluid means that the interaction between the analyte and the capture agents (e.g. antibodies) should be maximized. For example, in surface plasmon resonance biosensing, a surface with immobilized antibodies is used to capture analytes from a fluid that is flowing past the surface.⁶³ Without a flow, the analyte concentration at the surface can become limited by diffusion, which reduces the binding rate. The application of a fluid flow overcomes the diffusion limitation, maintains a maximum analyte concentration at the surface and therefore keeps the binding rate at a maximum value. The total binding rate scales linearly with the number of binding sites and therefore also with the available surface.

Immobilizing antibodies on micro- or nanoparticles increases the reactive surface-to-volume ratio during incubation. In a moving fluid, the particles in principle follow the fluid flow such that the particle-fluid interaction is not improved unless other forces are exerted on the particles. Here the magnetic properties of magnetic particles can be exploited, as external fields can be used to retain the particles within a fluid stream.⁶⁴⁻⁶⁵ Hayes et al.⁶⁴ showed that a so-called bed of superparamagnetic microparticles can be formed within a micro-capillary (see Figure 1.4a), which can be used to perform flow-based immunoassays. The static configuration was however

far from optimal, as fluid perfusion through the bed was minor and most fluid flowed past the bed, requiring the bed to be 1-3 mm in length. In addition, the applied flow rates were limited (~ 0.1 cm/s) in order to allow analytes to diffuse into the particle bed and to prevent superparamagnetic particles from being dragged along with the flow.

To improve flow-based assays, other groups replaced superparamagnetic particles by ferromagnetic particles, and formed dynamic particle structures over the whole cross-section of a channel.^{27, 66} By blocking the whole cross-section of the channel, all fluid passed through the small pores between the particles. It was shown²⁷ that alternating the local magnetic field enhanced the perfusion of fluid through the randomly varying porous structure of the particles. To reduce the cluster size and to improve confinement of small particle clusters in plugs, microchannel structures have been modified using microfabrication techniques^{28, 67}.

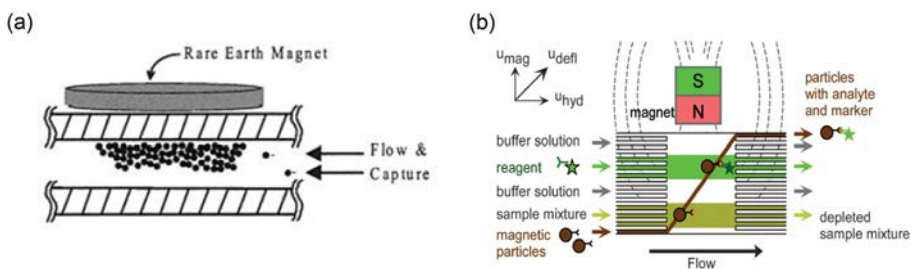


Figure 1.4 Examples of magnetic particles applied to capture analytes from fluid flows. (a) Using a rare earth magnet near a capillary, a packed bed of superparamagnetic particles can be formed at the channel wall. Reagent solutions can be flowed past the bed to effectively reduce diffusion lengths. (b) Design of a particle-based continuous flow reactor: magnetic particles are moved through multi-laminar reagent streams using an external magnet to perform a sandwich assay on the particle surface. (a) Reprinted with permission from ref⁶⁴. Copyright 2001 American Chemical Society. (b) Reproduced from ref⁶⁸ with permission from The Royal Society of Chemistry.

The use of ferromagnetic particles seriously complicates downstream detection steps, because the magnetically induced clustering of the particles is practically irreversible in a microchip. Superparamagnetic particles do not suffer from irreversible magnetic clustering, but in a flow the particles are not easily retained as they typically have smaller magnetic moments. Very strong field gradients are required^{35, 62, 69} which complicates microfluidic integration. Nonetheless, superparamagnetic particles with high magnetic content have been shown to be useful for target capture in a microfluidic flow, for example by moving particles laterally through flow streams containing different reagents within a single microchannel, and by subsequently collecting the particles in a separate outlet (see Figure 1.4b).^{68, 70-72} Ganguly et al.⁷² found that this method of magnetophoretic mixing strongly depends on the particle concentrations, the flow fraction of the analyte stream, and on the flow rate. In magnetophoretic mixing, particle-fluid interactions can be high, and the superparamagnetic nature of the particles in principle enable the addition of subsequent detection steps.

Overall, several studies have reported the use of actuated magnetic particles in microfluidic flows to perform analyte capture from the fluid. In most studies, analyte capture was evaluated by determining a limit of detection (LoD). However, it is difficult to attribute significance to reported LoD's due to the lack of standardized conditions (biomarker, biomaterials, sample matrix, incubation times, detection method, data analysis, etc.) as we will discuss in Section 1.4. It would be useful if future studies expressed the data in terms of association rate constants and included the dependence on process parameters such as flow speed, number of particles, etc. This may help to gain insights into the role of the underlying processes (such as translational and rotational transport limitations) and will help to reveal scaling relationships for microfluidic system design.

1.3.3 Analyte capture using magnetic particles in a static fluid

An alternative approach to perform analyte capture from fluid, is to actuate magnetic particles in an overall static fluid volume, within the so-called stationary microfluidics concept. An advantage of performing analyte capture in a non-flowing fluid is that the sample fluid is very efficiently used, because no sample is discarded in order to develop a flow. Furthermore, fluid pumping techniques are not required, which simplifies the total microfluidic system, i.e. the cartridge, the analyzer, and the cartridge-analyzer interface.

Analyte capture using magnetic particles in a static microfluidic chamber was shown by Bruls et al.²⁵ A sample fluid was inserted in a cartridge and filled the reaction chamber by capillary forces. Thereafter, a dry reagent containing magnetic particles automatically dissolved into the fluid, allowing the magnetic particles to capture analyte from the solution. The capture process itself was not actively steered by magnetic forces. Tanaka et al.⁷³ showed that rotating magnetic fields (at 30-90 Hz) can be used to agitate clusters of magnetic particles in a reaction chamber to bind target proteins on the antibody-coated surface of the particles. Quantitative data on the enhancement of the binding rate was not shown. In another study⁷⁴, magnetic particles were suspended in a capillary tube that was positioned between two ferromagnets. Due to the magnetic fields, the particles were arranged into chains and rotation of the capillary was applied to enhance the fluid-particle interaction. Target capture was quantified using an ELISA and compared for different Mason numbers by altering the rotation speed of the capillary tube. It was found that an acceleration of at least one order of magnitude could be obtained by rotating magnetic particle chains compared to a zero rotation speed of the capillary tube. It was found that small Mason numbers (corresponding to long chains that break and reform) generate the largest enhancement for analyte capture. In chapter 6, we present a study on the inverse arrangement, which is the application of rotating magnetic fields to magnetic particles suspended in a reaction chamber. From experimental data, association rate constants were determined and compared to numerical simulations of the capture process. It was found that capture rates can be improved by one to two orders of magnitude by using (i) magnetic field gradients to move particles through the fluid and (ii) rotating magnetic fields to enhance the particle fluid interaction over shorter length-scales

These studies show that magnetic particle-based target capture can be accelerated by applying time-dependent magnetic fields to particles in a static fluid volume. As mentioned in the previous section, it would be useful if future studies reported data in terms of the association rates and included the influence of actuation parameters, such as field strength, field frequency and field direction. This would allow for a comparison between the different devices and actuation methods.

1.4 Analyte detection

After the capture of target analytes, further processing is needed for accurate and specific detection. When the magnetic particles are used as carriers only, then the captured analytes are exposed to further (bio)chemical processes and are typically detected by luminescent labels such as enzymes or fluorescent molecules. Magnetic particles can also serve as a label, to signal molecular binding at a sensing surface, or to signal molecular binding between particles in an agglutination assay. Here we review different methods to perform the detection step and focus on the potential for total lab-on-chip integration of the assay.

An evaluation of the analytical performance of a detection methodology is often done by measuring dose-response curves. In many publications, attention is primarily given to the limit of detection (LoD) derived from a dose-response curve⁷⁵. However, papers of exploratory research generally report very limited statistics. The LoD's are mostly based on a low number of data points and LoD confidence intervals are hardly ever given. Furthermore, the chosen assay (biomarker, biomaterials, sample matrix, incubation times, etc.) has a strong influence on the LoD, so LoD's of papers with different assays cannot be compared. Finally, for medical applications it is not the LoD but the limit of quantification (LoQ) that is of prime relevance, i.e. the lowest biomarker concentration that can be quantified with a given required precision (typically <30%).⁷⁶⁻⁷⁷ The LoQ is close to the LoD if a dose-response curve has a good sensitivity, i.e. if the signal changes strongly as a function of the target concentration. However, if a dose-response curve has a very weak dependence on concentration (e.g. if the signal scales with the logarithm of the concentration), it might even be impossible to precisely quantify the target concentration. In view of the above, when discussing the literature we will mention the measured target and sample matrix, the character of the reported dose-response curves, and an order of magnitude for the LoD or LoQ. When estimating the LoQ for linear dose-response curves, we will use the definition that the LoQ equals ten times the standard deviation of the blank divided by the slope of the dose-response curve.⁷⁷

1.4.1 Magnetic particles as carriers

When magnetic particles are used as a carrier or substrate for the detection of target analytes, the particles are first used to capture target analytes, subsequently the captured analytes are labeled and finally the label is detected.⁷ For accurate detection, it is important that only bound analytes are labeled, and that only bound labels are detected. This requires several washing or separation steps to be performed, i.e. the

particles need to be exposed to different fluids. After the labeling step, detection can be performed close to a surface or in the bulk of the fluid.

As detection labels, fluorescent dyes or chemiluminescent molecules are most frequently used. Fluorescent labels have for example been used in microfluidic flow-based assays with supra-particle structures^{64, 72}, magnetic particle plugs^{28, 69} and isolated particles⁶⁸. In these assays, the single fluorescent dye molecules could not be resolved and instead the overall fluorescence from the particles was detected, e.g. using a CCD camera. The reported detection limits are typically on the order of several tens of picomolar and assays have mostly been performed in buffer.¹⁸ The dose-response curves tend to be sublinear and as a consequence the limits of quantification are expected to be higher than the reported limits of detection. The detection limits are quite high due to the relatively weak signal per label, while the background fluorescence from magnetic particles is significant. To reduce background, evanescent fields have been applied to only excite fluorescent dyes close to a substrate⁷⁸, but this has not resulted in a clear improvement of the detection limit.

To allow detection with single-molecule resolution, Todd et al.¹³ used magnetic particles to capture the analytes and labelled them with fluorescent detection antibodies. After a buffer exchange, the detection antibodies were eluted, separated from the magnetic particles and counted with single molecule resolution while flowing through a capillary. From the data, we estimate a LoQ of a few femtomolar for the detection of interleukin-17 in plasma or serum. The dose-response curve shows a dynamic range of almost 5 orders of magnitude. For other analytes – among which was cardiac troponin (cTnI) and tumor necrosis factor (TNF- α) – similar or slightly higher LoQ's were obtained. The method gives a very high sensitivity, but requires numerous fluid handling steps (e.g. washing, buffer exchange, elution, flows) and would be difficult to miniaturize for hand-held device operation.

Enzymes have also been used as labels in so-called enzyme-linked immunosorbent assays (ELISA). Enzymes are available that convert substrates suited for luminescence^{74, 79-84} or electrochemical⁸⁵⁻⁸⁶ detection. Generally luminescence-based ELISA's involve a washing step after enzyme labeling, followed by exposure of the particles to a fluid containing the reactants, after which bulk luminescence is detected.^{74, 79-81} A main advantage of using enzymatic labels is that the signal is amplified by the enzymatic conversion process. To reach single-target sensitivity, Rissin et al.⁸² loaded single magnetic particles in separate microwells, which were subsequently used as isolated ELISA reaction chambers (see Figure 1.5). When the number of particles is higher than the number of targets, digital counting is possible, which allows the detection of single analytes according to Poisson statistics. In buffer, streptavidin- β -galactosidase could be detected with an estimated LoQ of a few attomolar and a dynamic range of 4 orders of magnitude. In serum, prostate specific antigen (PSA) and TNF- α could be detected with estimated LoQ's close to a femtomolar (based on the quasi-linear dose-response curve at low concentrations). Concerning the integration of the technology, several aspects have been investigated such as rapid array loading⁸⁷, low-cost fabrication of array wells⁸³ and multiplexed assays⁸⁸, but complete miniaturization and integration are still a challenge.

Another assay employing magnetic particles is the so-called nanoparticle-based bio-bar code assay described by Nam et al.⁹. Analyte targets were captured by magnetic microparticles and subsequently labeled with gold nanoparticle probes that contained both specific antibodies and DNA fragments. Magnetic separation and buffer exchange were performed, and thereafter the DNA was amplified and stained for optical detection. For detection of PSA in buffer, we estimate a LoQ of a few attomolar from the reported dose-response curve. The method gives a very high sensitivity, but the numerous fluid handling steps strongly complicate the integration into a point-of-care system.

Hahn et al.⁸⁹ demonstrated an assay in which large magnetic particles with a diameter of 6 μm were labelled with magnetic nanoparticles. The labelled particles were detected by isomagnetophoresis, which discriminates small differences in magnetic susceptibility by measuring particle deflection in a streaming paramagnetic salt solution. The measurement principle is based on a delicate balance between magnetic and fluidic forces, and would be difficult to integrate into a point-of-care system.

The above-mentioned assays involve the application of microfluidic fluid flows and/or pipetting steps. An alternative to manipulating fluids is to keep the fluids stationary, and to transport magnetic particles from one stationary fluid into another stationary fluid by using magnetic forces.^{23-24, 50, 90-93} The two fluids, e.g. fluid A and

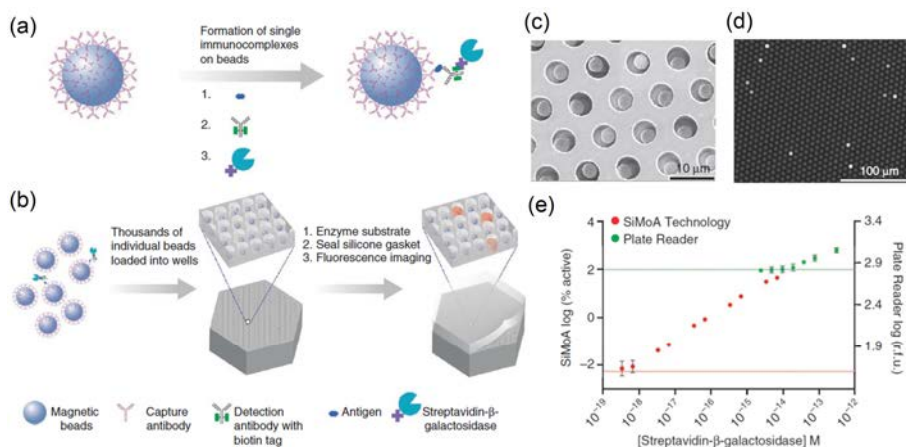


Figure 1.5 Digital ELISA based on arrays of femtoliter-sized wells. (a,b) Single protein molecules are captured and labeled on particles using standard ELISA reagents (a), and particles with or without a labeled immunoconjugate are loaded into femtoliter-volume well arrays for isolation and detection of single molecules by fluorescence imaging (b). (c) Scanning electron micrograph of a small section of a femtoliter-volume well array after particle (\varnothing 2.8 μm) loading. (d) Fluorescence image of a small section of the femtoliter-volume well array after signals from single enzymes are generated. The concentration of protein in bulk solution is correlated to the percentage of particles that carry a protein molecule. (e) Log-log plot of signal output (% active particles for single-molecule array (SiMoA) or relative fluorescence units (r.f.u.) for plate reader) as a function of the concentration of streptavidin- β -galactosidase (S β G) captured on biotinylated particles. Reprinted with permission from ref.⁸². Copyright 2010 Nature Publishing Group.

fluid B, are separated by a medium that does not mix with the aqueous fluids, for example a non-polar fluid or a gas. When a sufficiently high force is applied to the magnetic particles, the particles are pulled out of fluid A through the interface between fluid A and the medium; thereafter they are pulled through the interface between the medium and fluid B, into fluid B. Alternatively, the fluid interfaces can be moved over the particles, e.g. by using electrowetting^{80, 94}. The process of transferring magnetic particles between the fluids is controlled by a balance between the magnetic forces on the particles and the forces caused by interfacial tension, so-called capillary forces. Therefore, we propose to very generally refer to these transfer mechanisms as Magneto-Capillary Particle Transfer (MCPT).

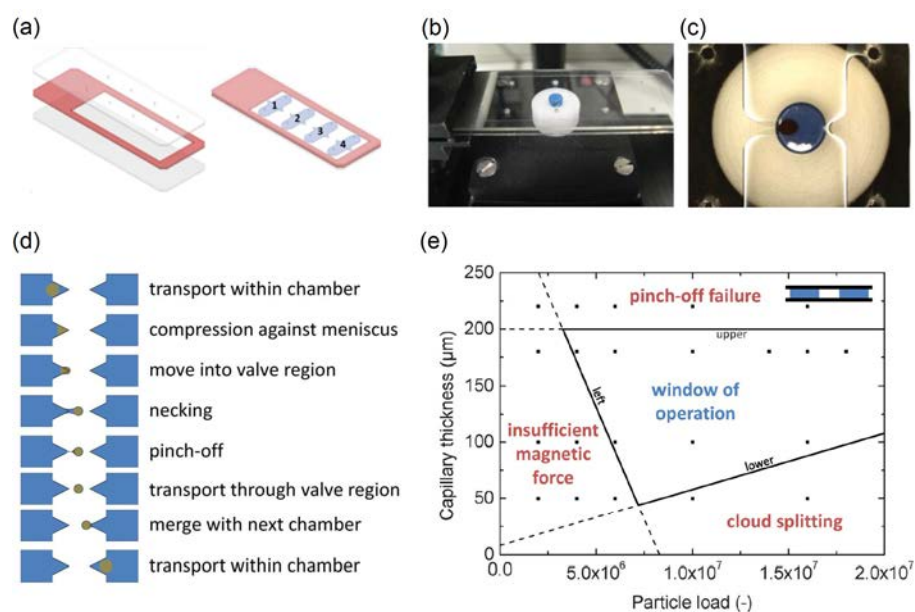


Figure 1.6 Example of Magneto Capillary Particle Transfer (MCPT). (a) Schematic drawing of a patterned air valve cartridge in exploded view (top) and assembled view (bottom) as developed by Den Dulk et al.⁵⁰. Double-sided tape joins the transparent planar top and bottom parts. Aqueous liquids (blue) with a typical volume of 15 μL are confined in four chambers by a pattern of hydrophilic and hydrophobic regions. (b) The MCPT cartridge in the experimental setup, showing the permanent magnet (dark, 4 mm \varnothing) embedded in a white background, gently touching the bottom of the cartridge. (c) Top view microscope image, showing two translucent aqueous chambers and the magnet in the valve region between the chambers. The magnet draws a cloud of magnetic particles (the even darker spot in front of the magnet) from the left chamber to the right chamber. (d) The different phases of the transfer of magnetic particles (white spot) from one liquid (dark) to another through an air-valve. (e) Parameter space of capillary thickness (distance between the planar top and bottom parts) and particle load. The squares indicate the experiments that were performed for a given cartridge design. The areas in the diagram describe the behavior of the magneto-capillary valve. In the central region successful MCV crossing was observed. In the three outer regions non-ideal operation was observed. Reproduced from ref⁵⁰ with permission from The Royal Society of Chemistry.

MCPT has been studied in many different device geometries, like tubes⁹⁵⁻⁹⁶, single-plane devices^{23-24, 51, 80, 92, 94}, vertical slits^{91, 97}, arrays of wells⁹⁰ and bi-plane capillary devices^{50, 93, 98-100}. MCPT has been applied for the purification and enrichment of nucleic acids^{23-24, 50, 90-91, 93, 101, 96, 99} and proteins^{50, 95, 98}. For example, Den Dulk et al.⁵⁰ used a bi-plane capillary device with liquid-gas interfaces (see Figure 1.6) and reported enrichment factors for nucleic acids and proteins between one and two orders of magnitude. Furthermore, it was shown that high washing efficiencies could be obtained due to very low amounts of co-transported fluid. Using MCPT, complete lab-on-chip assay integration has been demonstrated including the detection step. Nucleic acids^{51, 100} and proteins⁹⁹ have been detected, using oil-filled^{51, 100} or air-filled⁹⁹ capillary valves. The latter paper reports assay dose-response curves. Magnetic particles were moved over a cartridge through different chambers and incubation in each chamber was performed under actuation by a rotating magnetic field. In the assay, target interleukin-8 in buffer with 10% human serum was captured and fluorescently labeled after a washing step. The corresponding dose-response curves had a segment with a linear relationship between signal and concentration, with an LoD/LoQ in the picomolar range.

In the carrier-only assays, the particles are exposed to multiple fluids, as is also done in high-throughput robotic pipetting-based assays. An advantage of carrier-only assays is that one can make use of reagents that are very similar to the ones used in commercial pipetting-based assays. Another advantage is that the detection can occur in the bulk fluid, so the control of cartridge surfaces is not very critical. The most important disadvantage is that the integration of multiple fluids complicates the device technology. Furthermore, carrier-only assays require relatively strong magnetic fields, which can cause non-specific binding between the particles. For reliable detection, particle aggregation needs to be overcome and we will further discuss this in Section 1.5.

1.4.2 Agglutination assays with magnetic particles

Agglutination assays exploit the fact that aggregates of particles are formed when specific analytes are present in the sample fluid*. The particles are provided with target-binding molecules and the analytes should have at least two epitopes that can react with the particles. The degree of aggregation is a measure for the concentration of analytes within the fluid. In magnetic agglutination assays, the formation of particle clusters is accelerated by bringing particles together under the influence of a magnetic field. Two types of magnetic agglutination assays can be distinguished: (i) assays in which the magnetically actuated particles form clusters while being exposed to a fluid stream, and (ii) assays in which the fluid is static.

An assay with a streaming fluid was reported by Degre et al.¹⁰² They flowed magnetic particles through a microfluidic channel past two external magnets. The combination of the attractive magnetic dipole-dipole interactions between particles and the shear flow results in the formation of chain-like particle aggregates. Beyond

* In the scientific literature, the terms 'particle agglutination', 'particle aggregation' and 'particle clustering' are interchangeably used.

the magnets, clusters disaggregate or remain clustered depending on the number of captured analytes. In the original publication¹⁰², no dose-response curves, high-statistics data, or measurements of noise or non-specific background were reported.

Moser et al.⁶² applied localized magnetic fields to retain and dynamically actuate superparamagnetic particles in a microchannel flow, thereby enhancing the perfusion of the magnetic particles (see Figure 1.7a1). After switching off the magnetic

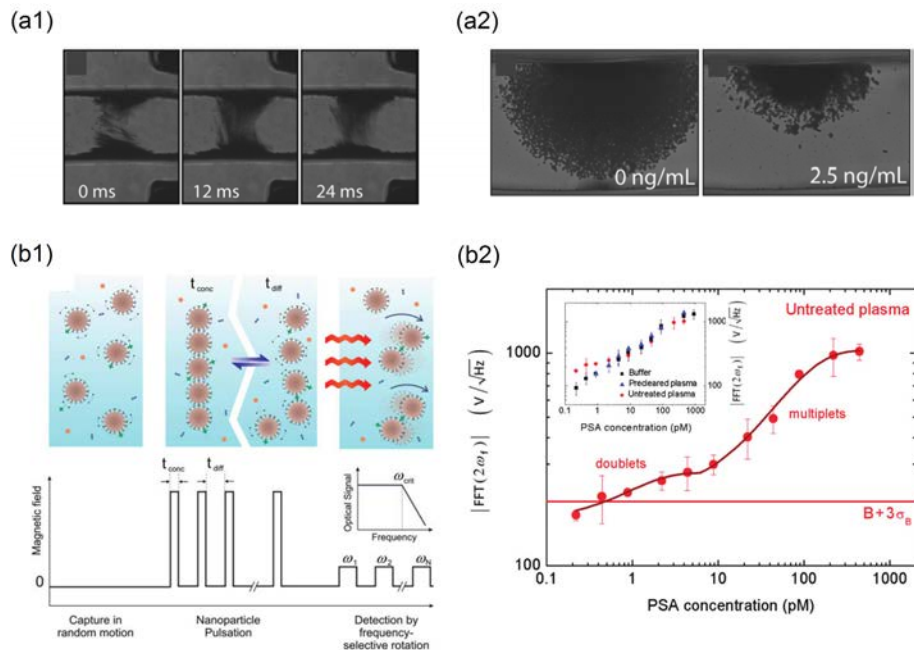


Figure 1.7 Agglutination sandwich assays based on magnetic particles. (a1) Dynamic particle plug in a microchannel with a flowing fluid. The particles were actuated by an external magnet at 70 Hz to induce continuous motion of particles in the center of the channel and thereby allow efficient perfusion of the analyte solution. (a2) After stopping the fluid flow and releasing the magnetic field, the area occupied by the particles is analyzed for different target target biotin-BSA concentrations. (b1) One-step homogeneous assay technology based on magnetic nanoparticles in a static fluid. First the biological sample was spiked with nanoparticles. Targets were captured by diffusive motion. Subsequently cluster formation was accelerated by applying pulses of the magnetic field to bring particles together (t_{conc}) and to allow diffusion to enhance bond formation (t_{diff}). The formed clusters were detected by applying rotating fields with increasing rotation frequencies and measuring the optical scattering signal. The result was a curve of the optical scattering signal as a function of the frequency (see inset); the plateau reveals the number of clusters in solution, while the critical frequency reveals the cluster size and the viscosity of the sample. In (b2) the resulting dose-response curve for PSA in untreated blood plasma is shown. The inset shows the dose-response curves in buffer, precleared plasma, and untreated plasma. The fitted line is based on a model description which takes account of the cluster size. The horizontal line shows the level of the blank plus three times the standard deviation of the blank. (a) Reproduced from ref⁶² with permission from The Royal Society of Chemistry. (b) Reprinted with permission from ref¹⁰³. Copyright 2012 American Chemical Society.

field, the thermal diffusivity of the particle cloud was measured, revealing the degree of particle aggregation. The area of the released plug was measured to quantify analyte capture. A dose-response curve was reported for the detection of biotinylated bovine serum albumin (BSA) in buffer, showing a logarithmic characteristic. The LoD is in the picomolar range, but the LoQ will be much higher due to the logarithmic dose-response characteristic.

Baudry et al.¹⁰⁴ showed that particle aggregates can be formed effectively in a static fluid. After target capture, field-induced chains of particles were formed in order to accelerate the formation of target-induced clusters. The particle clustering was detected using turbidimetry, as the scattering properties of particle clusters differ from unclustered particles. A slightly sub-linear dose-response curve was shown for the detection of ovalbumin in buffer, with a LoD in the low picomolar range.

Park et al.¹⁰⁵⁻¹⁰⁷ monitored the growth of particle chains in a rotating magnetic field by measuring light transmittance through the sample volume. As particles form aggregates, longer chains are obtained for increased target concentrations, causing larger fluctuations in the transmitted light. For avidin in buffer, sub-linear dose-response curves were obtained with a LoD just below the nanomolar.

Magnetic particle aggregation can also be quantified by using NMR sensing, as demonstrated in many publications from the Weissleder group¹⁰⁸⁻¹⁰⁹. The aggregation assays have nearly all been done using small nanoparticles (with a diameter of a few tens of nm) and in one publication also using microparticles¹⁰⁹. In the latter case, magnetic fields were applied to enhance particle aggregation. In buffer, antibodies to influenza were detected. The dose-response data were recorded on a logarithmic scale, which makes it difficult to quantify a LoD or LoQ, but picomolar target concentrations were resolvable.

When the analyte concentration is much smaller than the magnetic particle concentration, only few particle aggregates are formed, governed by Poisson statistics. Many particles will not form any clusters, some particles will form two-particle clusters, and larger clusters will be rare. Ranzoni et al.¹⁰³ showed that specific doublet formation in the low-concentration regime can be enhanced by applying a pulsed magnetic field during incubation, i.e. to alternately bring particles in close contact and let them freely diffuse to form specific bonds (see Figure 1.7b1). Furthermore, the optical detection sensitivity of doublets was improved by measuring the optical scattering in a rotating magnetic field.¹¹⁰ A dose-response curve was shown for the detection of PSA directly in undiluted blood plasma. The curves had an undulating character (see Figure 1.7b2), revealing regimes of clusters of different sizes, with an LoD around a picomolar.

The two main challenges of particle-based cluster assays are (i) to ensure good contact between the particles in order to increase assay kinetics, and (ii) to minimize non-specific particle clustering in complex biological samples. Magnetic fields help to bring the particles together and thereby enhance the inter-particle binding kinetics. However, magnetic fields may also increase the non-specific binding between the particles. Assays in a fluid stream require high magnetic forces to avoid that the particles are pulled along with the flow. High magnetic forces increase the risk of non-specific binding between the particles. In contrast, the agglutination assays in a

non-flowing fluid can be carried out in weak magnetic fields and thereby avoid strong interactions between the particles.¹⁰³ When further technological improvements are made, we expect that static-fluid magnetic agglutination assays may become a very interesting format for point-of-care applications.

1.4.3 Surface binding assays using magnetic particles

In a surface binding assay, magnetic particles are used as labels that bind in a biologically specific manner to a surface and thereby report the presence of a specific molecular species. Most commonly a sandwich format is used, with specific binders being immobilized on the particles and on the surface, which capture the target on two different epitopes. Preferably, all analytes in the fluid become sandwiched between a particle and the surface, which is possible when the concentration of particles exceeds the analyte concentration. To ensure efficient capturing and labeling, the magnetic particles need to efficiently (i) capture targets from solution (cf. Section 3), (ii) be brought to the surface, and (iii) interact with the surface on molecular length scales. The transportation toward the surface can be achieved relatively easily by applying magnetic field gradients towards the sensor surface¹¹¹⁻¹¹². It is more difficult to control the particle-surface interaction, because particles concentrated at a surface mutually exhibit magnetic particle-particle and steric particle-particle interactions. In addition, rotational exposure of the particles to the surface is important and non-specific interactions between the particles and the surface should be minimized¹¹³⁻¹¹⁴.

Several methods have been developed to optimize the particle-surface interactions. Bruls et al.²⁵ developed an actuation protocol in which in-plane fields, out-of-plane fields, and field-free phases are alternated. In-plane fields bring particles to the surface, out-of-plane fields generate chains, while the field-free phase allows free Brownian motion of the particles in order to optimize their rotational and translation exposure to the surface. In this way, effective specific sandwich formation was shown. The protocol keeps the particles in constant motion relative to the sensor surface, which may also minimize non-specific binding with the surface. Dose-response curves were determined for the detection of cardiac troponin (cTnI) in buffer and in undiluted blood plasma. The dose-response curves were practically linear with LoD's around a picomolar.

Gao and Van Reenen et al.¹¹⁵ developed an actuation protocol to induce repulsive magnetic dipole-dipole interactions between particles at a surface. This method is presented in detail in Chapter 3. The method consists of aligning particle aggregates with a surface by using field gradients and in-plane oriented magnetic fields, followed by the application of an out-of-plane magnetic field while a field gradient maintains the particles at the surface. In this way, clusters of microparticles were shown to disaggregate. By repeatedly applying these two steps, clusters consisting of tens of particles could be almost completely redispersed over the surface in a short time. Evaluation of this method in a surface-based assay has however not yet been performed.

Some papers report studies in which fluid flow is an essential component. Morozov et al.¹¹⁶⁻¹¹⁷ combined flows past a sensor surface with electrophoresis to bind

bacterial toxins to a surface and thereafter with magnetophoresis to attract magnetic particles to the surface to form the sandwich. To wash away particles bound to the surface by weaker non-specific bonds, shear flows were applied.¹¹⁸ Assays were performed on five different bacterial toxins in different media (i.e. buffer, water, milk and meat extract). Reported dose-response curves all had a logarithmic character. LoD's were reported of several tens of femtomolars, however, in view of the large error bars and the logarithmic dose-response curve, the LoQ's will be much higher.

Tekin et al.¹¹⁹ flowed magnetic particles ($\varnothing 2.8 \mu\text{m}$) past a sensor surface that was provided with regularly spaced smaller magnetic particles ($\varnothing 1.0 \mu\text{m}$) coated with antibodies. In this way, the larger magnetic particles containing captured analytes were transported to the sensor surface and could interact with the smaller magnetic particles, assisted by attractive magnetic dipole-dipole interactions. Applying this method to a sandwich assay for biotinylated anti-streptavidin and TNF- α in fetal bovine serum, dose-response curves were obtained with a logarithmic character: a 100 million-fold increase in analyte concentration gave a 5-10 fold increase of signal. LoD's were reported of several tens of attomolar, however, due to the logarithmic dose-response curve one cannot define a LoQ, because across the whole measurement range it is not possible to quantify the analyte concentration with an accuracy of 30%.

As described above, the method to assist the binding of particles at the sensor surface is very important for the character of the dose-response curve and the resulting detection sensitivity. Now we will discuss the next step, namely the detection of bound particle labels at a sensing surface. A method to detect particle labels should be sensitive, but in addition, one should consider the influence of the different methods on lab-on-chip integration, the cost effectiveness of the resulting disposable cartridge, and the miniaturization potential of the reader instrument. In particular, one should consider the compatibility of the detection methods with the presence of magnets around the microfluidic reaction chamber and near the sensing surface, in order to allow magnetic control of the particle-based assays.

In early reports, magnetic nanoparticle labels were detected by magnetic coils¹²⁰, SQUID¹²¹, magnetoresistive sensors^{11, 111, 122-124} and Hall sensors¹²⁵. Although it is possible to combine magnetic sensing with the application of magnetic fields^{111, 123}, it is complicated because magnetic fields tend to perturb the measurements. Furthermore, the use of lithographically made sensing chips adds costs to the disposable cartridge and demands cartridge assembly technologies suited for high numbers of electrical interconnects.

Optical detection methods are not perturbed by the presence of magnetic fields and are compatible with cost-effective mass-manufactured cartridges. Magnetic particles can be optically detected on a transparent surface in several ways, e.g. by using bright-field illumination^{114, 126} or dark-field illumination¹¹⁶. A particular challenge is to design the system in such a way that magnet poles can be positioned very close to the sensing surface. Bruls et al.²⁵ described a detection system based on the principle of frustrated total internal reflection (f-TIR) as depicted in Figure 1.8. A

light-emitting diode was used to create an evanescent wave at the sensor surface via total internal reflection. The presence of magnetic particles at the surface frustrates the evanescent wave, causing a reduction of reflected light. The amount of particles at the sensing surface was recorded as a function of time by monitoring the reflected light intensity. The advantage of using f-TIR is that it is highly surface-sensitive and suited for close integration of electromagnets.

Magnetic nanoparticle labels have also been detected by grating-coupled surface plasmon resonance (GC-SPR)¹²⁷, which is an evanescent-field technique based on a thin gold film at the sensing surface. Different assay formats were compared for the detection of β human chorionic gonadotropin (β hCG) in buffer. A clear influence of magnetic actuation on the dose-response curve was observed, leading to detection in the picomolar range.

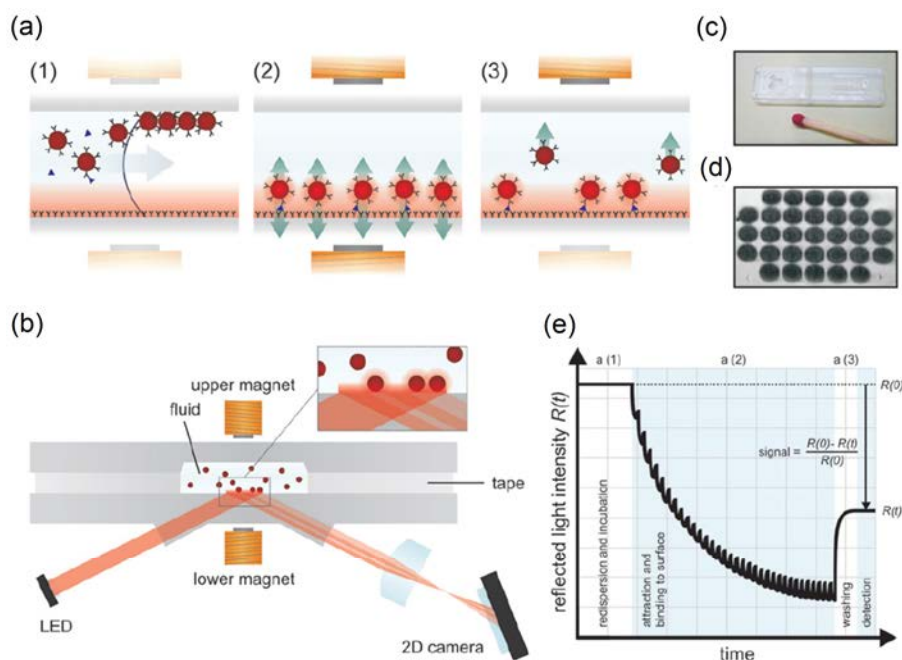


Figure 1.8 Optomagnetic immuno-biosensor based on actuated magnetic particles (\varnothing 500 nm). (a) Schematic representation of the reaction microchamber and the successive assay processes: (1) filling of the microchamber, particle redispersion, and analyte capture; (2) particle actuation during the surface-binding phase; and (3) magnetic removal of free and weakly bound particles from the sensing surface. (b) The fluid microchamber is placed in the optomagnetic system with electromagnets and detection optics. Light reflects from the sensor surface with an intensity that depends on the concentration of nanoparticles at the sensor surface, by the mechanism of frustrated total internal reflection (f-TIR). (c) An assembled disposable cartridge consisting of two structured plastic parts connected by double-sided adhesive tape. The cartridge contains a sample inlet, a channel, a reaction chamber (1 μ L), and a vent. (d) f-TIR image of magnetic particles bound to the sensor surface via an immunoassay on 31 capture spots of 125 μ m diameter each. (e) Schematic real-time curve of the measured optical signal for a single capture spot. The assay phases a1–a3 are indicated. The signal modulation in phase a2 is caused by switched actuation of the magnetic particles. Reproduced from ref²⁵ with permission from The Royal Society of Chemistry.

1.4.4 Magnetic stringency

A stringency process aims to improve the specificity of detection, by separating unbound and weakly bound from strongly bound species. In the detection methods discussed above, signals are generated by bonds formed between magnetic particles (agglutination assay) or between particles and a surface (surface binding assay). The bonds should be biologically specific. However, bonds can also have a non-specific nature, i.e. the bond is not mediated by an analyte molecule, which results in a false positive signal. Non-specific bonds can originate from several types of interactions, e.g. van der Waals interactions, electrostatic interactions, hydrophobic interactions, etc.¹²⁸ In diagnostic tests, non-specific interactions cause background levels as well as statistical variations of the results, and thus affect the limit of quantification and the precision.

The development of a diagnostic test always involves a series of optimizations in the biochemical and chemical domain in order to improve the specificity of detection, e.g. by optimizing the affinity molecules and coupling chemistries, by blocking the surfaces, and by dissolving reagents into the sample, such as pH buffers, salts, surfactants, and blockers for specific macromolecular interferences. The aim of the optimization is to reduce the formation of non-specific bonds and to preserve or improve the specificity of the targeted bonds. In an assay involving magnetic particles, there is an additional degree of freedom, namely the forces that can be applied to the particles. Magnetic forces can be used to separate bound from unbound particles. Furthermore, when the particle labels are bound to a surface, magnetic field gradients can be applied in order to apply stringency to the bonds and thereby dissociate weak non-specific bonds. Also, the response of molecular bonds to applied stresses can be recorded, giving even more detailed information about the bonds.

An early report on the application of magnetic stringency to non-covalent bonds was published by Danilowicz et al.¹²⁹ A permanent magnet was used to apply a constant force to ensembles of bound particles and the dissociation of bonds was recorded as a function of time. Jacob et al.¹³⁰ used an electromagnet which allowed a larger force range to be studied, thereby yielding reliable dissociation rate constants for the biomolecular bonds. Furthermore, they demonstrated that populations of specific and non-specific bonds could be distinguished within the shape of the force-induced dissociation curves. These studies were performed using large magnetic particles as labels (4.5 μm in ref.¹²⁹, and 2.8 μm in ref.¹³⁰). It is convenient to use large particles for biophysical studies because large forces can be applied to single particles. However, large particles are less suited for integrated biosensing because they diffuse slowly, sediment easily, and they limit the dynamic range of detection due to steric hindrance.

Using particles with diameters of a few hundred nanometers, Bruls et al.^{25, 111, 123} have demonstrated the use of magnetic stringency in integrated surface-binding assays, see Figure 1.8a,e. Here, magnetic stringency removes unbound and weakly bound particles from the surface. In fact, it replaces the fluidic wash step in traditional affinity assays. The magnetic stringency obviates the need for fluid manipulation, which simplifies the assay and makes it highly suited for integration in a completely stationary assay concept.

In the future, magnetic stringency may go beyond the application of bound-free separation and the measurement of dissociation properties of molecular bonds. For example, by applying rotating magnetic fields, it has been shown that it is possible to probe the properties of DNA¹³¹⁻¹³² and protein complexes¹³³ that are sandwiched between particles and a surface. Although still very remote from integrated biosensing, the principle of characterizing molecular bonds in a detailed biophysical manner may in the future help to further increase the specificity of biosensing.

1.5 Integration of magnetic actuation processes

Integration is the act of making something into a whole by bringing all parts together. For an engineer, it is the process of (i) defining an overall technological function that needs to be realized, (ii) designing a system architecture and its underlying components, and (iii) quantifying all interactions within the system and feeding this back on the technical function definition. For a given functional aim, one can select different system architectures that each have their own inherent advantages and challenges. As reviewed in the previous paragraphs, the manipulation of magnetic particles by magnetic fields allows one to control in a microfluidic format a list of important assay steps for diagnostic testing. Now we will review how the integration of different assay process steps is proceeding, moving toward integrated assays that perform a series of sophisticated steps, controlled by magnetic forces.



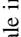
In Table 1.1, we summarize the state-of-the-art in the use of magnetic particle actuation for integrated detection assays. The top row lists the key assay process steps. The left-most column lists the assay concepts, i.e. carrier-only assays, agglutination assays, and surface-binding assays. We make a distinction between flow-assisted devices in which active channel flows are used, and stationary-fluidic devices in which continuous fluid motion is absent. Within the Table matrix, we have classified the type of magnetic actuation used at the intersection between assay-concept and process-step. The gray-scales indicate the type of actuation used: without magnetic fields (light-grey), with static fields (mid-grey), with dynamic fields (dark grey), or not applicable (slanted line). The references of process-step and assay-concept serve as examples. The assay-concept references are focused on total assay integration; they report dose-response curves acquired by detection on the microfluidic chip.

The first set of rows describes assays in which magnetic particles act as carriers only. In such assays the labeling step involves the addition of for example enzymatic or fluorescent labels. Therefore, a fluidic washing step or a fluid exchange step is essential prior to and after the labeling, in order to effectuate a separation between bound and free analytes, and between bound and free labels. One way to achieve a particle-fluid exchange step is by applying a continuous fluid flow while external magnets retain the magnetic particles within a liquid.^{28, 64, 68} Also, one can manipulate fluids by merging and splitting droplets in so-called digital microfluidics^{80-81, 94}. Alternatively, rather than moving fluids, one can switch the magnetic particles from one stationary fluid to another, by so-called Magneto-Capillary Particle Transfer (MCPT)^{23-24, 50-51, 80-81, 90-91, 93, 95, 99-100}. Intrinsic to magnetic carrier assays is the need






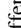





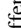





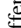
for relatively strong magnetic fields to retain particles in a flow or to traverse capillary interfaces, with the disadvantage that particles become highly concentrated and non-specific interactions are promoted. In the mentioned papers, redistribution of particles has been effectuated by removing the magnet from the sample chamber, allowing particles to spread by diffusion. The images (see e.g. refs.^{51, 99}) show that particle redispersion is incomplete; large clusters break up into small clusters, but not separate particles. We expect that improved disaggregation of particles, e.g. by magnetic field actuation¹¹⁵ and/or by further reducing non-specific interactions, will improve the assays. Magnetic stringency is not applicable in carrier-only assays because the particles are not used as labels. The carrier-only methods allow miniaturization and integration; however, a series of fluids is always needed, including active control of fluid flow and/or methods for MCPT. Generally, stationary microfluidic approaches reduce the total system complexity compared to methods that require continuous flow generation.

The second set of rows describes assays based on analyte-mediated agglutination of magnetic particles. In agglutination assays, the analyte capturing and labeling steps are performed in one and the same solution. Magnetic agglutination assays have been studied in flowing fluids^{62, 102} and stationary fluids^{103-104, 110}. Assays in fluid flow require higher magnetic forces, which promote non-specific binding between the particles. The highest assay sensitivities have been demonstrated with stationary-fluid agglutination assays^{103-104, 110}, using lower particle concentrations and lower magnetic fields than the flow-based assays. The application of pulsed magnetic fields has been shown to increase the effectiveness of molecular sandwich formation between the particles. The increase has been attributed to a combination of two effects, namely on the one hand keeping the particles in close contact with each other, while on the other hand allowing free Brownian rotation to expose all sides of the particles. Stationary-fluid magnetic agglutination assays are highly suited for miniaturization and integration, because in principle the assays can be performed in one chamber. Thus far, magnetically actuated mixing and target capture have not been applied in stationary-fluid agglutination assays, but several actuation methods^{47, 61} seem to be suited. Furthermore, when sample pretreatment steps are desired such as analyte purification or enrichment, MCPT⁵⁰ may in principle be combined with the agglutination assay.

The last set of rows in Table 1.1 describes the surface-binding assays, wherein magnetic particles interact with a sensor surface and form analyte-mediated bonds. The Table lists assays in which a magnetic field gradient is used to attract magnetic particles to the surface, thereby enhancing the local particle concentration and promoting particle-surface binding. Magnetic gradients have been combined with fluidic shear flows, in order to move particles past the surface and/or apply stringency to bound particles.¹¹⁶⁻¹¹⁹ In these papers, the surface binding steps were performed in static magnetic fields. It is important to realize that superparamagnetic particles are known to contain small ferromagnetic moments¹³⁴. Therefore, in a static magnetic field the rotation of the magnetic particles may be constrained, which may limit the surface binding effectiveness. Surface-binding assays have also been demonstrated without a fluid flow. In such stationary-fluid assays, magnetic fields have been ap-

Table 1.1 Overview of progress in the integration of magnetic actuation for different assay process steps in lab-on-chip biosensing. *Top row*: Key assay process steps. *Left-most column*: Assay concepts using magnetic particles. *Matrix*: Classification of the type of magnetic actuation used for the process steps in the different assay concepts. Greyscale indication:  performed without magnetic fields;  performed by applying static magnetic fields;  performed by applying dynamic magnetic fields; / not applied in the concept. The mentioned references serve as examples to illustrate the progress in the field; the reference list is not exhaustive. Assay-concept references have integrated the detection step and report dose-response curves.

Assay process steps

Assay concepts		References	Overall concept description	Magnetic particles are used for mixing	Magnetic capture particles are used generically ^{49,52} or specifically ^{57, 61}	Particle-Fluid exchange: continuous ⁶⁴ or by capillary transfer ^{50, 103}	Magnetic particles are redistributed	Molecular sand-bound-free which is formed with magnetic particles as label	Detection method and/or stringency
Flow-assisted	Lacharme et al. ²⁸ (2008)	Hayes et al. ⁶⁴ (2001)	Plugs ²⁸ or beds ⁶⁴ of magnetic particles are formed in a micro-channel using magnetic fields. Targets and fluorescent labels are captured from a flow.						
	Hayes et al. ⁶⁴ (2001)								
Carrier-only assay	Peyman et al. ⁶⁸ (2009)	Sista et al. ^{94,80} (2008)	Particles are moved by magnetophoresis through different fluid flows containing reagents. Magnets are used to manipulate particles, and electro-wetting is used to manipulate droplets, surrounded by oil ^{94,80} or by air ⁸¹ . Particles passively capture targets and enzyme labels.						
	Sista et al. ^{94,80} (2008)								
Stationary fluid	Ng et al. ⁸¹ (2012)	Gotheil et al. ⁷⁹ (2013)	Magnets translate magnetic particles through different fluid chambers, separated by air valves. Magnet rotation is applied in each fluid.						
	Gotheil et al. ⁷⁹ (2013)								
				Vuppu et al. ³⁶ Gao et al. ⁴⁷	Smith et al. ⁴⁹ Chapter 2 and 3 of this thesis	Hayes et al. ^{64, 103} Den Dulk et al. ^{50, 116}	Chapters 4 to 6 of this thesis	Ebersole ¹³⁷ ; Chapter 7 of this thesis	Lee et al. ¹³⁰ Wild'Boas et al. ¹³⁵

Agglutination assay	Flow-assisted	Degre et al. ¹⁰² (2005)	Agglutination assay partially in a microfluidic chip. Clustering is detected by monitoring particle diffusion.	Off-chip mixing	Off-chip incubation under mixing	Redispersion by diffusion after removing the magnets	Particle clustering in a static magnetic field	Dark field imaging of large aggregates
		Moser et al. ⁶² (2009)	Agglutination assay completely in a microfluidic chip, using alternating magnetic fields	Particles are actuated by an alternating magnetic field	idem	Redispersion by diffusion after switching the magnets off	Particle clustering in an alternating magnetic field	Bright field imaging of large aggregates
	Stationary fluid	Baudry et al. ¹⁰⁴ (2006)	Agglutination assay in a static field in absence of flow	Mixing in a tube	Incubation in a tube by diffusion	Diffusion by switching field off	Particles form chains in a static magnetic field	Optical scattering
		Ranzoni et al. ^{110,103} (2011)- (2012)	Agglutination assay in a pulsed rotating magnetic field	Mixing in a tube	Incubation in a tube by diffusion	Redispersion by diffusion in field-off phase	Particles form chains in a pulsed rotating magnetic field	Optical scattering in a rotating magnetic field
Surface-binding assay	Flow-assisted	Schlyapnikov et al. ¹¹⁷ (2012)	Targets are captured on a sensor surface and are thereafter labeled by magnetic particles under influence of a magnetic field gradient		Fluid is exchanged by altering fluid flow past the sensor surface		Labeling by particles is performed with flow and magnetic field gradient	Particle counting by dark field imaging
		Tekin et al. ¹¹⁹ (2013)	Targets are captured by magnetic particles in solution and thereafter attracted toward a magnetic array on a surface.	Non-magnetic microfluidic mixing	idem		Sandwich is formed on the magnetic array, in an applied magnetic field and with fluid flow	Particle counting by bright-field imaging
	Stationary fluid	Dittmer et al. ¹¹¹ (2008); Koets et al. ⁷³ (2009)	Targets are captured passively by magnetic particles and thereafter attracted to a sensor surface by magnetic fields	Off-chip mixing	Incubation by diffusion	Redispersion by diffusion in field-off phase	Particles are attracted to a surface by an applied magnetic field	Magnetic field sensing (Giant Magnetoresistance)
		Bruls et al. ²⁵ (2009)	Targets are captured passively by magnetic particles and thereafter a sandwich is formed under pulsed magnetic fields	Dried-in particles disperse into the sample fluid; no active mixing.	Incubation by diffusion	Redispersion by diffusion in pulsed magnetic field protocol	Particles are attracted to the surface and are randomized in a pulsed magnetic field	Optical scattering (frustrated total internal reflection)

plied to bring and keep particles near the surface^{25, 111, 123} and to randomize particle distributions²⁵. With current-controlled electromagnets, the particle-surface interaction has been optimized by combining pulsed magnetic fields with field-free phases for Brownian rotation.²⁵ Furthermore, stringency^{25, 111, 123} has been applied by reversing the field gradient. Surface-binding magnetic particle assays are highly suited for miniaturization and integration, as fluid manipulation is not necessary and the assay can be completely controlled by magnetic fields. A disadvantage of surface-binding assays is that the sensor surface needs to be biofunctionalized, which adds complexity to the assay. Important advantages are that magnetic stringency can be applied in the assay, and that multiplexing can be realized by preparing binding spots with different biochemical compositions. We foresee several avenues to further control and optimize surface-binding assays by magnetic actuation. For example, actuated mixing and capture^{47, 61} may help to further increase the speed and effectiveness of the capturing process, and magnetic fields may be used to redistribute particles in the assay chamber¹¹⁵.

1.6 Aim and outline of the thesis

In the previous Sections, we have reviewed the use of magnetic particles and magnetic fields to perform key processing steps in integrated microfluidic assays for lab-on-a-chip diagnostic applications. Magnetic particles have been applied to achieve mixing, washing and buffer exchange, both in fluid flow and in stationary microfluidic device architectures. Due to the high surface-to-volume ratio and their adaptable surface (bio-)functionalizations, magnetic particles are effective at achieving rapid and specific capture and labeling of targets. In addition, magnetic particles can be actuated for magnetic stringency steps, and can be accurately detected in complex fluids, most commonly by optical methods.

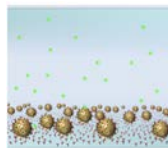
In the field of integrated magnetically actuated assays, individual process steps are being studied as well the integration of different process steps. The use of magnetic actuation processes for integration purposes is proceeding steadily, as shown in Table 1.1. There are still several white spaces where actuation principles can be applied to further enhance system integration and overall analytical performance. Scientifically speaking, several magnetic actuation processes have been qualitatively demonstrated but are not yet well characterized and modeled.

In this thesis we aim to obtain a fundamental understanding of different magnetic actuation processes in particle-based diagnostic assays. We develop model descriptions for the particle behavior and the different binding processes involved in the assay. The models are compared to experimental data, and in a next step used to optimize or develop novel actuation technologies. Lastly, we analyze and discuss the integration of process steps to realize a lab-on-a-chip biosensor in which all assay process steps are effectuated using magnetic fields.

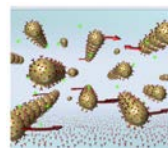
We focus on the three following processes. First, methods are investigated to improve capture of target analytes from solution by magnetic particles. Subsequently,

we study how magnetic fields can be used to control the distribution and behavior of particles near a surface. Lastly, we consider the effects of magnetic particle actuation on molecular bond formation in surface-binding assays.

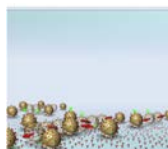
In Chapter 2, an experimental study is presented to obtain insight in the fundamental capture process of targets from a fluid by magnetic particles. Using different sorts of fluid actuation, the influence of physical transport processes, i.e. translational and rotational motion, is distinguished from the chemical reaction. In this chapter the potential impact of magnetic actuation on the capture rate is evaluated.



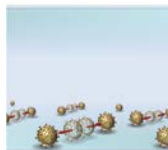
In Chapter 3, we study the effect of magnetic actuation on the capture of proteins from solution. Magnetic particles are moved in chains through the fluid by applying rotating magnetic fields and field gradients. We quantify association rate constants for different sorts of actuation and as a function of field strength, rotation frequency and particle concentration. To interpret the experimental data, we compare the results to numerical Brownian dynamics simulations of the capture process.



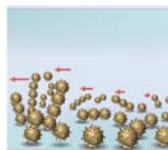
Chapter 4 introduces a numerical method to study the behavior of ensembles of magnetic particles near a physical boundary. The method is applied to study a novel method by which multi-particle clusters can be disaggregated, based on inducing repulsive magnetic dipole-dipole interactions between the particles. The underlying dynamics of the disaggregation process are clarified as a function of particle properties, field properties, and cluster geometry.



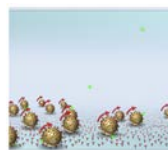
Based on the field-induced disaggregation principle, in Chapter 5 we introduce intra-pair magnetophoresis as a method to characterize in detail the properties of magnetic particles. By measuring the separation rate of disaggregating two-particle clusters, magnetization curves and magnetization distributions are accurately quantified.



In Chapter 6 we show that so-called rotaphoresis can be used to redistribute magnetic particles over a surface. Rotaphoresis, which refers to translational motion induced by rotation, is obtained by magnetically rotating chains of particles orthogonal to a surface. We find that interesting collective particle behavior can be obtained by the application of magnetic fields at relatively high frequencies with orientations in three dimensions.



In Chapter 7 we investigate how magnetic particles – after target capture – can be most effectively actuated to form a target-induced sandwich bond on a reactive surface. The rotational response of single magnetic particles to a rotating field is measured and modeled. Using a model sandwich system in experiments and numerical simulations, the effect of magnetic actuation is bench-



marked against no magnetic actuation to quantify the improvement due to actuation.

To conclude, in Chapter 8, we consider the integration of the different actuation methods. Finally, we discuss further work towards integrated lab-on-a-chip bio-sensing assays in which all assay process steps are controlled and optimized by magnetic forces.

2

Accelerated particle-based target capture – the roles of volume transport and near-surface alignment

*The upcoming generations of high-sensitive and miniaturized biosensing systems need target capture methods that are as efficient and as rapid as possible, with targets ranging from molecules to cells. Capture of the targets can be achieved using particles coated with affinity molecules, but there are still fundamental questions as to the processes that limit the association rates. In this chapter we quantify and compare the reaction rates of particle-based target capture with different types of actuation, namely (i) passive thermal transport, (ii) fluid agitation by vortex mixing, and (iii) actively rotating particles. In the experiments, we use fluorescent nanoparticles as targets which are biochemically captured by magnetic microparticles, and the capture efficiency is quantified using fluorescence microscopy with single target resolution. The data unravel the contributions of volume transport, near-surface alignment, and the chemical reaction to the overall rate constant of association. Vortex mixing versus passive transport gives an increase of the reaction rate constant by more than an order of magnitude, implying that the encounter frequency and the near-surface alignment probability are increased. The importance of near-surface alignment is underscored by the data of active particle rotation; the binding probability per encounter is 4-fold enhanced on rotating capture particles. We discuss the implications of our results for different biological systems and for the development of novel actuation methods in particle-based target capture.**

*This chapter has been published in: A. van Reenen, A.M. de Jong, and M.W.J. Prins, Accelerated Particle-based Target Capture – the Roles of Volume Transport and Near-Surface Alignment, *The Journal of Physical Chemistry B* **117**, 1210-1218 (2013).

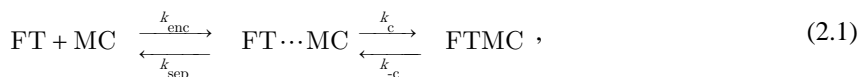
2.1 Introduction

Affinity molecules are widely used for the capture and extraction of specific targets from a biological sample, e.g., cells, proteins, or nucleic acids. The affinity molecules are generally immobilized on a solid carrier, and the targets are captured from the fluid onto the carrier by specific binding to the affinity molecules. In many assay systems, magnetic micro- or nanoparticles are used as carriers for the affinity molecules, because magnetic particles have a high surface-to-volume ratio, are mobile in the fluid, and can be manipulated by magnetic fields. Applications range from cell extraction¹³⁸⁻¹³⁹, immunoassays^{9, 25, 140}, nucleic-acid extraction¹⁴¹⁻¹⁴², to the latest ultrahigh-sensitivity affinity assays which count target molecules with single-molecule resolution^{13, 82}. Ultrahigh-sensitivity affinity assays are particularly challenging when the biological targets are to be captured from a small sample volume. In small samples only very few targets are available in the assay and the assay precision becomes limited by counting statistics, so every target needs to be captured from solution and the capturing effectiveness needs to be close to unity.

In this chapter, we investigate the processes that limit the association rate in particle-based target capture, to lay the foundation for novel particle-based target capture methods for small sample volumes. We describe a theoretical framework and experiments that separate the processes of volume transport, near-surface alignment, and the chemical binding reaction (see Figure 2.1a). In the experiments the capture of fluorescent target particles (FT) by magnetic capture particles (MC) is recorded with single-target resolution as a function of time, which gives the overall target capture rate. In order to unravel the contributions of volume and near-surface transport, we report and analyze experiments with fluid agitation and experiments with magnetic particle rotation, using passive target capture as the reference (see Figure 2.1b). In the conclusion section, we will discuss the implications of our results for the capturing of different biological targets (from molecular biomarkers to biological cells) and for the development of novel actuation methods in microfluidic particle-based affinity capture.

2.2 Theoretical considerations

We model the capture of fluorescent target particles (FT) by magnetic capture particles (MC) in analogy to a bimolecular binding process^{53, 55, 143}. Such a process is usually considered to consist of a (diffusional) encounter step and a subsequent intramolecular chemical reaction to obtain the bound complex (FTMC):



with k_{enc} the encounter rate constant, k_{sep} the separation rate constant, k_{c} the rate constant for complex formation, and $k_{\text{-c}}$ the rate of decomplexation. The intermediate state, FT \cdots MC, formed after encountering, is often named the encounter (or transient) complex. On the basis of this reaction scheme, the overall rate constant of association k_{a} is given by:

$$k_a = k_{\text{enc}} \cdot \frac{k_c}{k_{\text{sep}} + k_c} \quad (2.2)$$

Note that k_a equals the product of the encounter rate constant, k_{enc} , and the probability that the subsequent chemical reaction will occur, $[k_c / (k_{\text{sep}} + k_c)]$. If the chemical reaction is fast relative to the separation of the encounter complex ($k_c \gg k_{\text{sep}}$), the association rate constant is limited by the encounter rate constant, so $k_a \approx k_{\text{enc}}$. If the separation is much faster than the chemical reaction ($k_{\text{sep}} \gg k_c$), then the

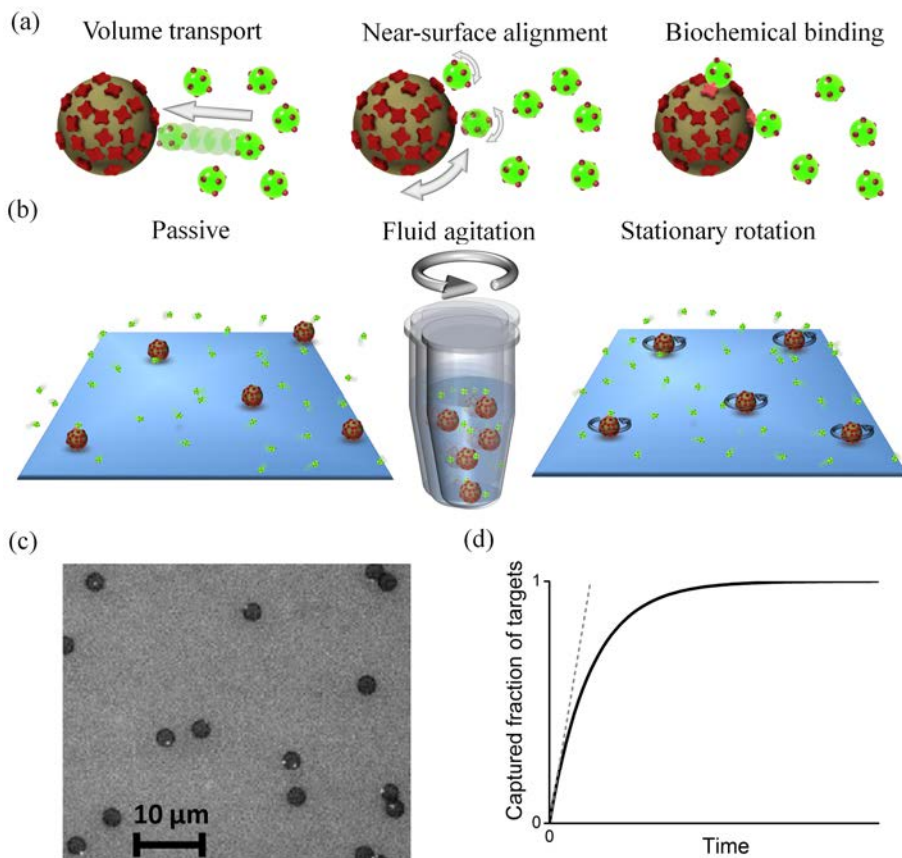


Figure 2.1 Principle of particle-based target capture and experimental approach. (a) Schematic representation of the different stages in the capture process of targets (green) by capture particles (grey). Targets and capture particles are sketched with multiple binding sites (in red). The stages are: (i) volume transport creates target-particle encounters, (ii) near-surface transport creates alignment of binding sites, and (iii) the chemical reaction forms the bonds. (b) Schematic representation of the applied actuation methods: (i) passive transport only by diffusion, (ii) fluid agitation by vortex mixing, and (iii) magnetic rotation of the capture particles. (c) Microscope image of biotinylated fluorescent nanoparticles (200 nm) captured by streptavidin-coated microparticles (2.8 μm) on a glass surface. Single bound targets are identified and counted as the reaction proceeds. (d) Sketch of the captured fraction of targets as a function of time. The reaction rate constant is deduced from the initial slope (dashed line) or from the exponential time constant.

chemical reaction becomes rate limiting and $k_a \approx k_c K_{\text{enc}}$, with $K_{\text{enc}} = k_{\text{enc}} / k_{\text{sep}}$ the equilibrium constant for forming the encounter complex.

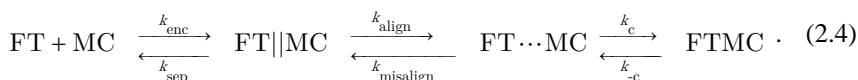
As Schreiber et al.⁵³ noted for protein association kinetics, there is no simple test to determine whether the encounter or the chemical reaction step is rate limiting. But it is known that encounter (i.e., diffusion) limited rate constants are typically high, i.e., above $10^5 \text{ M}^{-1}\text{s}^{-1}$, as is for instance the case for the streptavidin–biotin complex¹⁴⁴ and for typical antibody–antigen complexes⁵⁵, and that within these reactions only local conformational changes occur. In contrast, reaction-limited protein associations generally involve gross molecular changes like loop reorganization and domain movement.

Several theoretical studies have been performed to determine the association rate constants for diffusion limited reactions. In the case of two uniformly reactive spheres with immediate binding (i.e., hit-and-stick behavior) Smoluchowski¹⁴⁵ found by solving the diffusion equation:

$$k_{\text{enc}}^{\text{dif}} = k_{\text{dif}} = 4\pi DR \quad (2.3)$$

Here, D and R represent, respectively, the relative translational diffusivity and the center-to-center distance of the spheres when in contact ($R = R_1 + R_2$, with R_1 and R_2 the radii of the two respective spheres). The units of k_{dif} are m^3s^{-1} . For two protein-sized spheres, Eq. 2.3 predicts rate constants in the order of $10^9 \text{ M}^{-1}\text{s}^{-1}$, which is much larger than what is typically observed for protein molecules (10^5 - $10^7 \text{ M}^{-1}\text{s}^{-1}$)⁵³. It has been shown theoretically^{53, 58} that the reduction can be attributed to the required alignment of the position and relative orientation of the reactive binding sites on the proteins.

In analogy to the binding reaction between two proteins, the binding of two particles with distributed binding sites (as in Figure 2.1a) should be viewed as a multistep process, namely first translational volume transport to create encounters of the reacting particles (FT||MC), and thereafter particle movements to achieve near-surface alignment of the reactive binding sites on the particles (FT...MC):



In this equation all rate constants have units s^{-1} , except for k_{enc} which has units $\text{M}^{-1}\text{s}^{-1}$. Here we have introduced the near-surface alignment rate constant, k_{align} , and in the backward direction the near-surface misalignment rate constant, k_{misalign} . In case the chemical reaction is much faster than alignment process ($k_c \gg k_{\text{align}}$), the overall rate constant of association is given by:

$$k_a = k_{\text{enc}} \cdot \frac{k_{\text{align}}}{k_{\text{sep}} + k_{\text{align}}} = k_{\text{enc}} \cdot p_{\text{align}} = k_{\text{enc}} \frac{K_{\text{enc}} k_{\text{align}}}{k_{\text{enc}} + K_{\text{enc}} k_{\text{align}}} \quad (2.5)$$

We have defined p_{align} as the probability to reach alignment during an encounter. The right-hand side of Eq. 2.5 can also be obtained by solving the diffusion equation of two uniformly reacting spheres with a partially adsorbing surface and an intrinsic

rate constant $\kappa \equiv K_{\text{enc}}k_{\text{align}}$ (see also Collins and Kimball¹⁴⁶, who derived a similar equation for the reaction scheme in Eq. 2.1).

The rate J at which targets are captured is proportional to the overall association rate constant:

$$J = \frac{d[\text{FTMC}]}{dt} = k_a[\text{FT}][\text{MC}], \quad (2.6)$$

For short times, the reaction product increases linearly in time:

$$[\text{FTMC}] = k_a[\text{FT}]_{t=0}[\text{MC}]_{t=0} \cdot t. \quad (2.7)$$

For longer times, the concentration of one or both species may become depleted, causing a decrease in the reaction rate. More specifically, in case the number of capture particles is much larger than the number of target particles, then the concentration of unbound targets [FT] decreases over time and the amount of captured targets evolves as follows:

$$[\text{FTMC}] = [\text{FT}]_{t=0} \left(1 - e^{-t/\tau} \right), \quad \text{with } \tau = \left(k_a[\text{MC}]_{t=0} \right)^{-1}. \quad (2.8)$$

In our experiments, we could optically distinguish the first three states described in Eq. 2.4. In the free state (left) the particles are optically clearly separated. When the particles form an encounter complex, a gap between the particles cannot be optically resolved but the particles are still mobile with respect to each other. In the latter two states the particles are in contact and not anymore mobile with respect to each other. We note that biochemical dissociation does not play a role in our experiments, due to the strong binding that occurs between the particles.

2.3 Experimental section

Particles and Chemicals

Superparamagnetic particles (M270, either carboxylated or streptavidin coated, 2.8 μm diameter) were purchased from Dynal Biotech. Fluorescent particles (Fluospheres, carboxylated, yellow/green, 0.2 μm) were purchased from Invitrogen. EZ-link biotin-PEO₃-amine was obtained from Pierce. Antibiotin antibodies and streptavidin were obtained from Thermo scientific. Fluorescent particles were coated with biotin using standard EDC coupling chemistry. Centrifugation at 14,000 rpm in a centrifuge was carried out to separate the fluorescent particles from unbound biotin. The ζ -potential of the biotinylated fluorescent particles and M270 streptavidin magnetic particles was measured using a Malvern Zetasizer nano ZS. The ζ -potential was ~ -22 mV and ~ -15 mV respectively.

Carboxylated magnetic particles were coated with either streptavidin or antibiotin antibodies using standard EDC-NHS coupling. To control the loading of streptavidin on the particles, BSA was coated competitively at different concentrations, i.e., 0.0005, 0.005, 0.05, or 0 mg BSA/mL in combination with 0.5 mg/mL streptav-

idin. The relative streptavidin loading was verified by means of enzyme-linked immunosorbent assay (ELISA) using biotin-HRP. The luminescence signal was measured using a Fluoroskan Ascent FL and the data is shown in Figure 2.2.

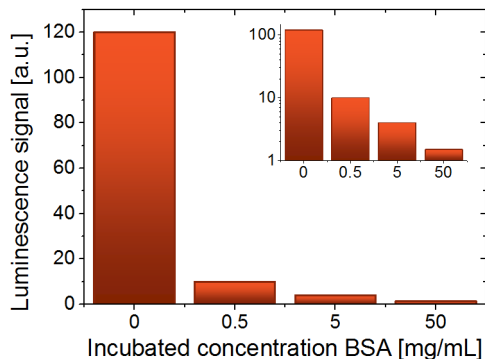


Figure 2.2 Characterization of relative loading of streptavidin on magnetic particles using ELISA for different concentrations of BSA incubated in competition with streptavidin. In order to evaluate the loading, an excess of biotinylated HRP (Horse-radish peroxidase) was incubated after functionalization. After washing unbound biotin-HRP away, luminol was added which exhibits chemiluminescence in the presence of HRP. The luminescence signal therefore is a measure for the amount of streptavidin on the particles. The inset shows the luminescence signal for the different cases on a logarithmic scale.

Passive transport experiment

Stock solutions of magnetic capture particles (6.7×10^8 particles/mL) and fluorescent target particles (4.55×10^{12} particles per mL) were diluted respectively 200 and 30 times in PBS containing 0.1% BSA. A glass substrate with a spacer (height 100 μm) was prepared and 0.5 μL magnetic particle solution was pipetted on the substrate. Subsequently, a 9 μL droplet containing fluorescent particles solution was pipetted in the cell. The fluid cell was closed with a glass coverslip and placed under the microscope (Leica DM6000) with a 63 \times immersion objective lens for analysis. The magnetic particles sediment to the surface within a minute. The surface was scanned for magnetic particles and of each particle a picture was taken using an EM-CCD camera (Andor Solis) and the corresponding time was recorded. Images were processed to count both the number of capture particles and captured target particles.

Fluid agitation by vortex mixing

Solutions of fluorescent as well as magnetic particles were mixed together in an Eppendorf tube to a final fluorescent particle concentration of ~ 600 particles/ μL . The final volume was 200 μL . These tubes were placed on a shaker (Eppendorf Thermomixer Comfort) at 1400 rpm. At several times, a fraction of 8 μL was extracted from the tubes in order to evaluate the capture efficiency. These small volumes were pipetted into a fluid cell and analyzed under the microscope. To increase the number of magnetic particles within one field-of-view ($142 \times 107 \mu\text{m}^2$), a ferromagnet was

used to concentrate sedimented particles on the bottom center of the fluid cell. Typically, five images were recorded with 700–1300 particles inside the field-of-view.

Magnetic rotation

Magnetic particles were rotated using a quadrupole electromagnet¹⁴⁷. The four electromagnets were powered with sinusoidal currents at different phase lags such that a horizontal continuously rotating magnetic field was created at the center where the sample was placed. The magnet generates only a very small vertical field gradient, giving a force on the particles on the order of the gravitational force. The horizontal gradient was insignificant since the particles were not observed to translate horizontally in the magnetic field. In a typical experiment, the sample was prepared and placed under the microscope, and after approximately 60 s the rotating magnetic field was started and measurements were performed.

2.4 Capturing particles by passive diffusive transport

The reference method for target capturing is an experiment without any actuation, so that the transport is driven only by diffusion. We have measured the corresponding reaction kinetics by recording the capture of fluorescent targets by magnetic particles sedimented on a glass substrate, as sketched in the left panel of Figure 2.1b. Only the top hemisphere of the magnetic capture particles was monitored, i.e., the side that is exposed to the bulk fluid, as shown in Figure 2.1c; we therefore included a factor of 2 in calculating the reaction rate constants per capture particle. The capture process was monitored for about 25 min (see Figure 2.3a) and the overall association rate constant was determined using a linear fit corresponding to Eq. 2.7. We verified that the capture process did not significantly alter the concentration of fluorescent target particles in solution (the amount of captured target particles was always much smaller than the total amount of target particles in solution) and neither the reaction surface of capture particles (the target particles never saturated the binding area of the capture particles); see the Appendix 2.A.

We have studied the association rate as a function of the density of magnetic particles on the surface expressed as the surface coverage, see Figure 2.3b,c. For low surface coverage ($<1.4 \pm 0.6\%$) the association rate constant (Figure 2.3c) is found to be independent of the surface coverage and the capture curves (see inset) are linear over the measured time-span. This is the regime wherein target transport to the capture particles is dominated by radial diffusion. For higher surface coverage, the amount of captured targets increases over time in a sublinear fashion, namely as $t^{1/2}$ (Figure 2.3a). This behavior corresponds to a system with an absorbing plane and a diffusion-limited supply of targets. The data in the regime of high surface coverage ($>1.4\%$ capture particles on the glass substrate; Figure 2.3c) corresponds to the average reaction rate over the measured time-span. The average reaction rate constant is found to decrease with an increasing density of capture particles on the surface, which is caused by overlap of target depletion zones that are formed around capture particles¹⁴⁸. An overlap of depletion zones of neighboring particles results in a shift from radial to linear symmetry of the transport process, causing a decrease of the

supply of targets per capture particle and therefore a decrease of the encounter rate. The decrease of the reaction rate per capture particle should occur when the diffusion length is comparable to the distance between the particles. For these measurements, we estimate that $L_{\text{avg}} \sim 0.5(Dt)^{1/2} \sim 28 \mu\text{m}$, corresponding to a surface coverage of $\sim 0.9\%$, which is in agreement with our measurements. In the regime of high surface coverage ($>1.4\%$) the average rate constant scales as the inverse of the surface coverage, see the Supporting Information. In this regime the total amount of captured targets is independent of the number of capture particles, which is in agree-

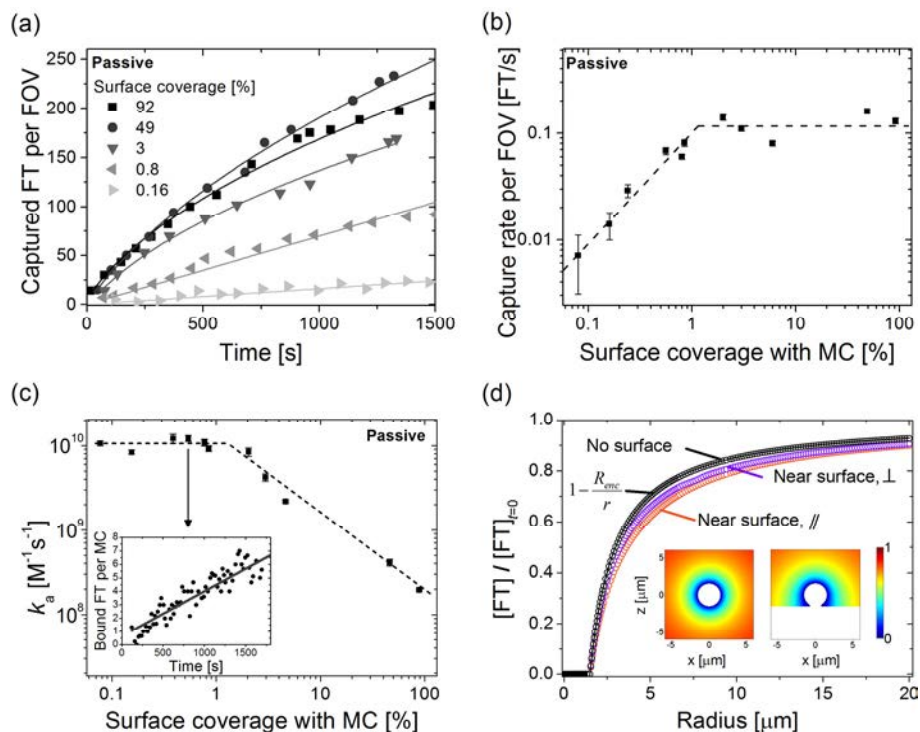


Figure 2.3 Quantification of passive target capture by particles sedimented on a planar non-reactive surface. (a) Measured and fitted capture of fluorescent targets, as observed within a single field of view. For surface coverages $> 1\%$ the applied fit function is of the shape $y(t) = y_0 + \sqrt{A(t-t_0)}$, with y_0 , t_0 and A as fit parameters. For surface coverages $< 1\%$, a linear fit is applied. (b) Average capture rates per field of view as obtained from linear fitting of the data in panel a. (c) Overall reaction rate constant for different densities of magnetic capture particles (MC) on the surface. The dashed line is a guide to the eye. Each data point is collected from a time-dependent measurement of target binding, as depicted in the inset. A linear fit (solid line in the inset) is used to determine the overall reaction rate constant, using Eq. 2.7 and including a factor two to correct for measuring one side of the particle. Since for high surface coverages ($>1.4\%$) the capture rate is time-dependent (see panel (a)), k_a corresponds to an average over the measured time-span. (d) Steady-state concentration profiles of an absorbing sphere for different system geometries: dispersed in an infinite medium in the presence or absence of a non-absorbing surface. The profiles are plotted with respect to the center of the particle. The solid line represents the analytical steady-state solution of the diffusion equation.

ment with the interpretation that the system acts as an effective absorbing plane for target particles and that the number of capture particles is irrelevant.

In the regime of radial transport, the overall rate constant of association is found to be $k_a = 1.0 \pm 0.2 \times 10^{10} \text{ M}^{-1} \text{ s}^{-1}$ (see Figure 2.3c). Interestingly, the measured rate constant is significantly smaller than the calculated association rate constant for a diffusion limited reaction [see Eq. 2.3]: $k_{\text{dif}} = 2.4 \times 10^{10} \text{ M}^{-1} \text{ s}^{-1}$. This means that an additional process is limiting the reaction. In order to unravel the origin of the limiting process, we will now analyze (i) the influence of the planar glass substrate on the measured association rate, (ii) the influence of electrostatic repulsion between the particles, (iii) the influence of the size of the targets, and (iv) the influence of the biological molecules on the particles.

2.4.1 Influence of the planar substrate

Targets do not adsorb to the planar glass substrate, but the presence of the substrate may still limit the supply of targets to the capture particles. Finite-element simulations were carried out using Comsol Multiphysics 3.5a to compute the steady-state concentration profiles for a sphere in an infinite medium and a sphere near a non-absorbing surface, see Figure 2.3d. We have also calculated the steady-state concentration profile by analytically solving the diffusion equation for an absorbing sphere with an encounter radius $R_{\text{enc}} = R_{\text{MC}} + R_{\text{FT}} = 1.5 \text{ }\mu\text{m}$ in an infinite medium (see the solid line). The numerical solution in case of an absent surface shows excellent agreement with the analytical solution. The computations show that the presence of a non-absorbing surface slightly decreases the target concentration compared to the situation when no surface is present. From the computations, we can derive the diffusive flux of targets at the encounter radius of the top hemisphere. We find that the nearby non-absorbing surface causes a decrease of the encounter rate by 13% ($\varepsilon = 0.133 \pm 0.001$). Therefore, we conclude that the nearby non-absorbing surface has only a minor effect on the overall rate constant of association.

2.4.2 Influence of electrostatic interactions

The target as well as the capture particles have a negative surface charge (see Experimental section) so electrostatic repulsion may play a role in limiting the overall association rate. The electrostatic repulsion between the particles was studied by varying the ionic strength of the buffer solution, namely by diluting the PBS buffer from physiological concentration ($\sim 0.18 \text{ M}$) down to $\sim 0.01 \text{ M}$, see Figure 2.4a. The reaction rate increases as a function of the ionic strength and saturates near the physiological concentration. Therefore we conclude that the electrostatic repulsion is nearly completely screened at physiological salt levels.

We can compare these findings to calculations by DLVO theory. The interactions between charged surfaces within a liquid medium are described by the so-called DLVO theory developed by Derjaguin, Landau, Verwey and Overbeek. An overview of this theory for the field of biophysics has been given by Leckband and Israelachvili¹²⁸.

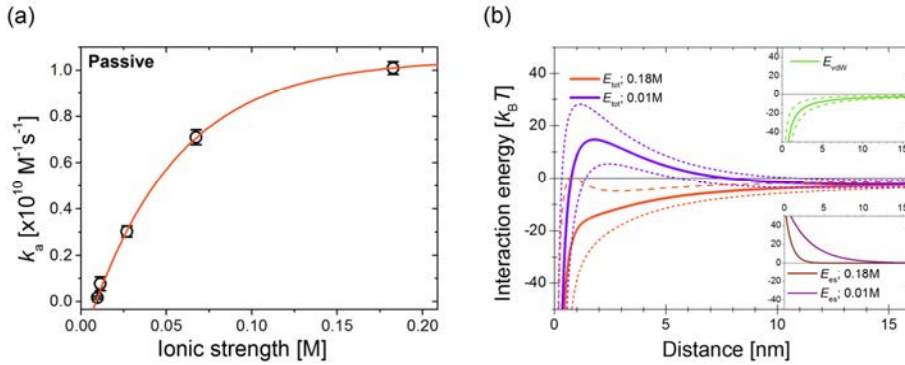


Figure 2.4 (a) Experimentally determined association rate constant for different ionic strengths of the PBS solution. As a guide to the eye, the data is fitted using a curve of the form $y(x)=y_0[1-\exp(A \cdot (x-x_0))]$. (b) Computed DLVO interaction energies for the interaction between two spherical particles (R_1 and R_2) in a liquid medium at $T = 293 \text{ K}$. Dashed lines indicate error margins. The insets show separately the computed van der Waals and electrostatic interaction. Curves have been calculated for 0.01 M PBS and 0.18 M PBS. The energies are given in units of $k_B T$.

Here, we estimate the energies of the electrostatic interaction as well as the Van der Waals interaction, for the case of two interacting spheres, with radius R_1 and R_2 , corresponding respectively to the capture particle and the target particle.

First, the electrostatic (double-layer) interaction energy between two spheres, at a separation x , is given by

$$E_{es} = \frac{R_1 R_2}{R_1 + R_2} Z \exp(-\kappa x), \quad (2.9)$$

in which κ is the inverse Debye length, which depends on the ionic strength of the liquid medium, and Z is the interaction potential¹²⁸, which depends on the surface potential ψ_0 of both surfaces and on the dielectric constant of the medium ϵ , i.e.

$$Z = 64\pi\epsilon\epsilon_0 \left(\frac{k_B T}{e} \right)^2 \tanh\left(\frac{ze\psi_{0,1}}{4k_B T} \right) \tanh\left(\frac{ze\psi_{0,2}}{4k_B T} \right), \quad (2.10)$$

with z the valency of the electrolyte. To approximate the surface potential, we use the measured Zeta potential of the particles (see Experimental section 2.3). As the Zeta potentials of both target and capture particles are negative, the electrostatic interaction is repulsive, and will – if large enough – prevent the particles from coming into contact. We find that for a 0.18 M PBS solution, the electrostatic energy equals the thermal energy ($k_B T$) at an inter-particle distance of only $\sim 3 \text{ nm}$, whereas for a 0.01 M (diluted) PBS solution, the thermal energy level is reached at $\sim 13 \text{ nm}$.

In addition we consider the Van der Waals interaction, which is given by

$$E_{vdw} = -\frac{A}{6x} \frac{R_1 R_2}{R_1 + R_2}, \quad (2.11)$$

with A the Hamaker constant, which, for interactions in a liquid medium such as water, is reported to be typically in the range of $0.5\text{-}1.5 \times 10^{-20}$ J.¹²⁸ In Figure 2.4b, the total interaction energy (Van der Waals and electrostatic) is plotted for the cases of a 0.01 M and a 0.18 M PBS solution. For 0.18 M PBS no energy barrier is found that could prevent physical contact between the spheres, whereas for the 0.01 M PBS an energy barrier with a height of $\sim 10 k_B T$ is found. Such an energy barrier would significantly reduce the amount of targets that can physically encounter the magnetic particles.

Since the results in Figure 2.3 were obtained using an undiluted 0.18 M PBS solution, we conclude that electrostatic interactions do not limit the association rate.

2.4.3 Influence of the size of the targets

The overall rate constant of association was measured for three different sizes of the target particles, as shown in Figure 2.5. The graph also shows the calculated diffusion-limited rate constant in case of immediate binding between the particles, i.e. a hit-and-stick behavior, as expressed by Eq. 2.3. For all sizes, the measured association rate (k_a) is lower than the diffusion-limited hit-and-stick rate (k_{dif}). This indicates that an additional process reduces the binding probability after an encounter between particles. As discussed earlier, the limiting process might be the chemical reaction, or the process of near-surface alignment of the binding sites to enable the chemical reaction. Since the binding affinity of streptavidin to biotin is high, and as the particles contain many streptavidin/biotin molecules on their surfaces, it is not the chemical reaction that limits the target capture rate (data will be shown in the next paragraph).

Figure 2.5 shows that the ratio between k_{dif} and k_a depends not strongly on the size of the targets: the ratio is about a factor 2.5 for the 100 nm targets and about 1.5

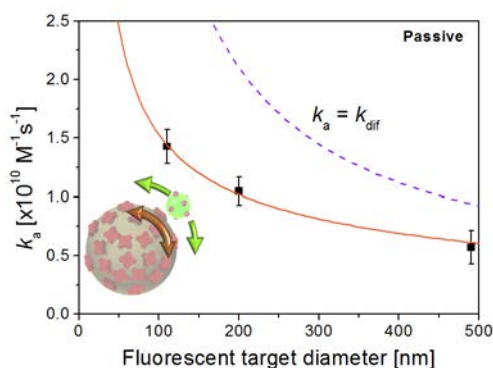


Figure 2.5 Reaction rate constant for different sizes of the fluorescent targets. Each data point represents three measurements. The dashed line represents the theoretical rate constant in case the intrinsic rate constant κ is much larger than the encounter rate constant k_{enc} . The solid line corresponds to the model described with Eq. 2.5 (right side), using Eq. 2.12: $K_{enc}k_{align} = C_1 \cdot R_{MC}^{-3} + C_2 \cdot R_{FT}^{-1}$, in which C_1 and C_2 are fit parameters.

for the 500 nm targets. So let us now develop a description of the target size dependence of the overall association rate, starting from Eq. 2.5. The encounter rate k_{enc} is given in Eq. 2.3 and is proportional to the diffusivity (Stokes–Einstein relationship, proportional to $1/R$) and the radii of the particles (R). In our system the two particle types have strongly unequal radii: $R_{\text{MC}} \gg R_{\text{FT}}$. Therefore, the encounter rate k_{enc} is proportional to $R_{\text{MC}}/R_{\text{FT}}$. As separation is diffusive, the separation rate k_{sep} is proportional to $1/R_{\text{FT}}$.

To reach near-surface alignment of the binding sites, it is required that a binding site on the target particle comes in the vicinity of a binding site on the capture particle. In other words, binding sites of both particles must be present in the interaction area, in between the particles. The process of near-surface alignment involves the mutual surface scanning and probing of the two particles, which can have contributions from translational as well as rotational processes (as illustrated by the inset of Figure 2.5). The processes can be thermally excited (Brownian motion) or can be driven by an applied excitation (magnetic or fluidic actuation). A full theoretical analysis of these coupled processes is outside the scope of this study; instead we follow a heuristic approach in order to come to scaling relationships with the radii of the particles.

Concerning the contribution of translational transport to the near-surface alignment process, we expect that the alignment rate is determined by the fastest particles, so by the target particles, with a displacement scaling as $1/R_{\text{FT}}$. Concerning rotation, the time required for rotational randomization scales with the third power of the radius ($\sim 1/R^3$) and equals the time needed for Brownian diffusion over a distance of the diameter of the particle.¹⁴⁹ In water, the time required for total rotational randomization is 3×10^{-6} s for biomolecules with a size of 10 nm, 3 ms for a 100 nm sized particle, 3 s for particles or cells with a size of 1 μm , and 3000 s for cells with a size of 10 μm . In view of the observed weak dependence of $k_{\text{dif}}/k_{\text{a}}$ on target size (see Figure 2.5) we conclude that the rotation of the target particles (scaling as $1/R_{\text{FT}}^3$) is not a dominant limiting factor in the experiment.

Interestingly, the Brownian rotation of the capture particles generates surface displacements that are of similar magnitude as the translational diffusion of the target particles (see the inset of Figure 2.5). For example, during a time-span of 0.1 s, the root-mean-square displacement by translational diffusion of a free 200 nm target particle in water is ~ 0.6 μm ; and the root-mean-square displacement of the outer surface of the capture particle due to rotational diffusion is ~ 0.2 μm . These values show that the diffusive translation of the target particle and the rotational diffusion of the capture particle are expected to contribute roughly equally to the process of near-surface alignment. Therefore, we propose a dependence of the near-surface alignment rate on the particle radii of the form:

$$k_{\text{align}} = C_1 R_{\text{MC}}^{-3} + C_2 R_{\text{FT}}^{-1} \quad (2.12)$$

Applying this equation in the right-hand side of Eq. 2.5, and using $k_{\text{enc}} = k_{\text{dif,surf}} = (1 - \varepsilon) \cdot k_{\text{dif}}$, to the data in Figure 2.5, we find a good fit with $K_{\text{enc}} C_1 = (2.9 \pm 0.7) \times 10^{-8} \text{ M}$

$^1 \cdot \text{m}^3 \cdot \text{s}^{-1}$ and $K_{\text{enc}} C_2 = (10 \pm 3) \times 10^2 \text{ M}^{-1} \cdot \text{m} \cdot \text{s}^{-1}$. Interestingly, both contributions to the alignment rate are found to be on the same order of magnitude.

From the experimental data and the model, we conclude that near-surface alignment is indeed a limiting factor in the process of target capture. The capture process starts with volume transport driven by translational diffusion, and subsequently near-surface alignment is required to enable a chemical reaction between the molecules on the surfaces of the particles. Near-surface alignment is distinctly different from volume transport in that rotational diffusion plays an important role.

It would be interesting to directly measure the rotational processes in the experiment. The fluorescent target particles studied in this chapter have a rotational randomization time on the order of a few tens of milliseconds. This time is much smaller than the inter-frame time in the experiment (~ 10 frames per second give an inter-frame time of ~ 100 ms). So we conclude that we are not able to record in detail the particle dynamics during a single encounter due to the limited frame rate in the present experimental setup. For further studies either a more light sensitive high speed camera is needed or a different technique may be used such as fluorescence correlation spectrometry.

2.4.4 Influence of the biochemical binders

We have studied the influence on the association rate of the biochemical binding molecules that are coupled to the surfaces of the particles. Passive transport experiments were performed with streptavidin or with antibiotin antibodies as the molecules on the capture particles, see Figure 2.6. Both molecules are good binders, but streptavidin has a 10-100 times higher reported association rate to biotin than antibiotin: about $10^8 \text{ M}^{-1} \text{ s}^{-1}$ for streptavidin^{144, 150} versus 10^6 to $10^7 \text{ M}^{-1} \text{ s}^{-1}$ for antibiotin⁵⁵. Interestingly, in our particle-based experiments we find only a very small difference (factor 1.4 ± 0.3) in the association rate constant for streptavidin versus antibiotin coated capture particles, see top part of Figure 2.6a.

We have also studied the overall reaction rate constant for different amounts of streptavidin on the capture particles. The streptavidin density on the particles was reduced by competitive coating of carboxyl particles with streptavidin and BSA (see Experimental section 2.3). The reduced streptavidin loading of the particles was qualitatively confirmed by ELISA measurements, as shown in Figure 2.2. For different streptavidin densities, we monitored the capture reaction in a passive target capture experiment (see bottom part of Figure 2.6a). We observe a strong dependence of the reaction rate constant on the streptavidin loading, as is shown in Figure 2.6b. We attribute the decrease of the association rate with decreasing streptavidin density to the fact that the association rate is limited by near-surface alignment. The data show that the overall rate constant of association hardly depends on the bond type but does depend on the density of available binding sites on the capture particles. Therefore, we conclude that mainly near-surface alignment reduces the binding probability upon encounter, and not the chemical reaction.

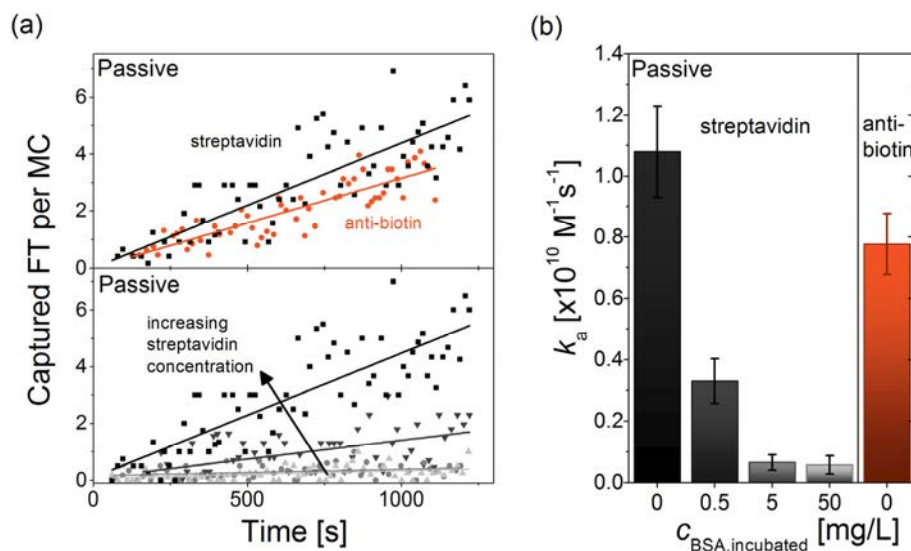


Figure 2.6 Influence of the surface functionalization of the capture particles on the reaction rate. (a) (top) Capture of biotinylated targets by microparticles coated with streptavidin (•) or with anti-biotin (◦). The lines represent linear fits of the data. (bottom) Capture of biotinylated targets by microparticles with different streptavidin surface densities. (b) The overall rate constant of association k_a is shown for streptavidin and anti-biotin capture proteins and different loading of streptavidin. As a measure for the streptavidin loading, the concentration of BSA, $C_{\text{BSA,incubated}}$ is shown which was incubated simultaneously during the coating with capture proteins (also see Experimental section and Figure 2.2).

2.5 Fluid agitation by vortex mixing

The effect of fluid agitation on the overall rate constant of association was studied by applying vortex mixing. The amount of formed FTMC complexes was determined as a function of time by extracting a small amount of fluid from the reaction mixture at different times and by counting the number of capture particles and captured targets. We employed target concentrations of ~ 1 fM, which is substantially lower than the concentrations used in the experiments without fluid agitation (0.8 pM). The reason for using a very low concentration is to prevent multi-particle clustering during the experiment.

Target capture was measured for different concentrations of magnetic particles (see Figure 2.7a). Because of the low target concentration, a depletion of targets from the whole sample volume was observed over time, in agreement with Eq. 2.8. The corresponding fits give values for k_a as shown in Figure 2.7b. The average overall rate constant of association when applying fluid agitation was found to be $k_a = 17.5 \pm 1.5 \times 10^{10} \text{ M}^{-1} \text{ s}^{-1}$. This is more than an order of magnitude higher than the association rate constant that we found in the case of passive transport, i.e. $1.0 \pm 0.2 \times 10^{10} \text{ M}^{-1} \text{ s}^{-1}$. The association rate constant also exceeds the intrinsic rate constant that was determined in passive experiments with the same capture particles, i.e. $\kappa = K_{\text{enc}} k_{\text{align}} = 2.1 \pm 0.2 \times 10^{10} \text{ M}^{-1} \text{ s}^{-1}$. Consequently, fluid agitation enhances not only the frequen-

cy at which target particles and capture particles encounter, but also the probability that particles bind during an encounter, by at least 9 ± 2 times.

These results also support the hypothesis that the chemical reaction rate constant is not a limiting factor, as the chemical reaction cannot be enhanced by physical transport processes. We hypothesize that by applying fluid agitation, the mobility of a target during an encounter is increased, such that a larger surface area is probed for possible binding sites as compared to diffusive transport. As a result, the binding probability for each encounter is increased. To test this hypothesis in a more controlled manner, we have also used magnetic fields to rotate the magnetic capture particles during the reaction.

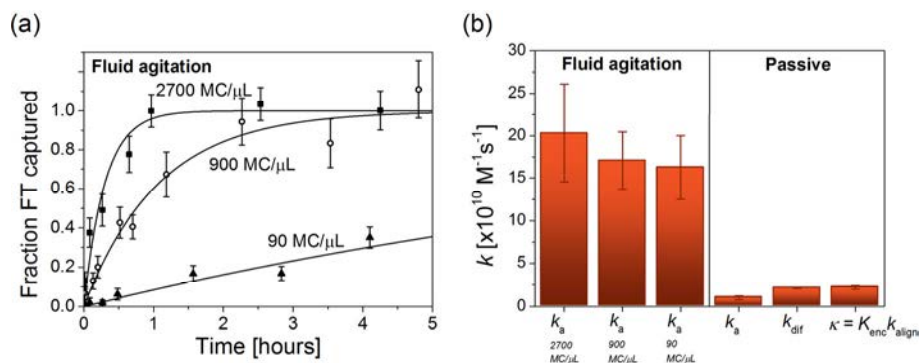


Figure 2.7 Quantification of target capture by fluid agitation. (a) Target capture during actuation by means of vortex mixing. Different concentrations of magnetic particles (MC) were studied. A fit based on Eq. 2.8 was used to determine the overall rate constant of association. (b) The overall rate constant of association, in case of fluid agitation with different concentrations of MC (left) and for passive target capture (right).

2.6 Actuation by stationary magnetic rotation

We have studied the effect of rotation of the capture particles on the association rate constant. The experiments were performed in the same way as passive transport experiments, but now a rotating magnetic field was applied in the same plane as the surface on which the magnetic particles were sedimented. A rotating field causes the superparamagnetic particles to rotate, due to a small ferromagnetic moment in the particles¹³⁴. For a more detailed characterization and description, see Appendix B, or the reference¹³³ or section 7.3. Because of the very small Reynolds number for this system, i.e. $Re < 10^{-4}$ for a 1 Hz rotation, viscous forces dominate the fluid flow, and therefore no radial transport of targets is induced by the particle rotation. As verification, we have numerically compared radial transport by diffusion with radial transport induced by particle rotation (see Appendix 2.C)¹⁵¹. From this estimation, we find that diffusive transport has a contribution to the radial target transport that is at least a factor 500 times larger as compared to induced fluid flow. Consequently, the target transport toward the capture particles is governed by diffusion and the particle rotation only affects the particle-to-target near-surface alignment process.

In Figure 2.8b, the overall rate constant of association, k_a , is shown as a function of the rotation frequency of the magnetic field. At low frequencies k_a equals the value for passive transport. For increasing frequencies an increase of the association rate constant is observed, and above 1 Hz the association rate constant saturates. We can understand this saturation behavior from the rotation characteristics of the particles (e.g. see the Appendix 2.B). The particles synchronously follow the rotating field up to a frequency where the hydrodynamic drag becomes higher than the magnetic torque, i.e. at about 1.5 Hz. Above this critical frequency the particles do not completely follow the rotating magnetic field anymore and assume a wiggling motion with a lowered net rotation frequency. Our data show that the wiggling motion is still effective for enhancing the capture process, generating a k_a with a value of about $1.5 \pm 0.2 \times 10^{10} \text{ M}^{-1} \text{ s}^{-1}$. For much higher frequencies the particle association rate should return to the passive transport value, but this is not visible in the graph because 20 Hz was the maximum frequency that could be applied with the magnet.

As no additional radial transport of targets is realized, the increase in reaction rate constant must be due to an enhanced near-surface alignment probability. Using Eq. 5 and assuming that the chemical reaction is not limiting, we have determined the intrinsic rate constant for different rotation frequencies, as shown in Figure 5b. The applied rotation clearly causes more targets to associate to the capture particles.

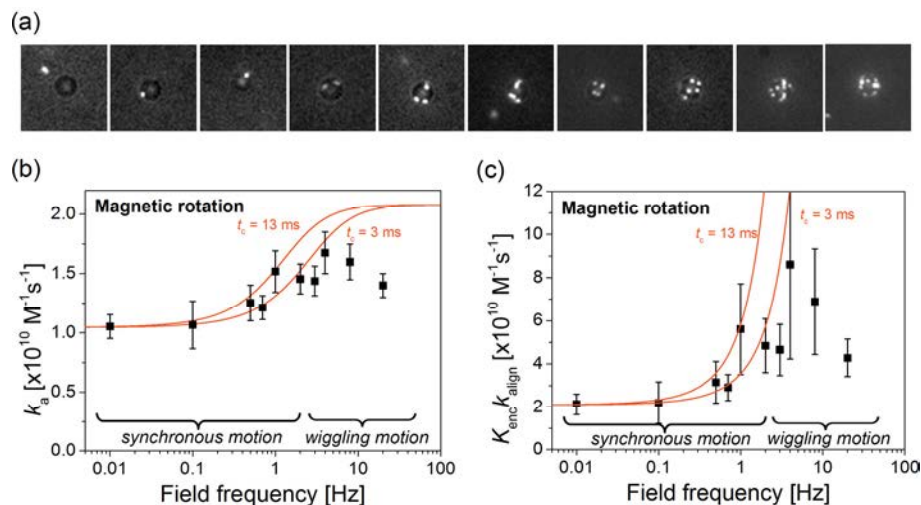


Figure 2.8 Influence of stationary rotation of a magnetic particle on the capture rate. (a) Snapshots of magnetic particles and bound fluorescent particles at different times during the incubation at a field rotation frequency of 1 Hz, over a time period of 20 minutes. (b) The overall rate constant of association k_a for capture particles that rotate on a glass surface, measured as a function of the rotation frequency of the applied field (5 mT). Up to ~ 1.5 Hz the particles exhibit synchronous rotations, and above ~ 1.5 Hz wiggling motion is observed. The lines correspond to the combination of Eqs. 2.5 and 2.13, with t_c the average lifetime of the encounter complex. (c) The corresponding intrinsic rate constant $\kappa = K_{\text{enc}} k_{\text{align}}$ has been determined using Eq. 2.5 and assuming no rate limitations due to the chemical reaction. The lines correspond to the model of Eq. 2.13.

It is interesting to see whether we can apply the scaling relationship for the particle size dependence of the association rate, as proposed in Eq. 2.12. In case of applied magnetic rotation, the first term of Eq. 2.12 ($C_1 \cdot R_{\text{MC}}^{-3}$) should be altered because that term relates to the rotational motion of the capture particle. The R_{MC}^{-3} -character stems from the rotational viscous drag term in the rotational diffusion constant of the capture particle, $D_{\text{rot,MC}}$. Due to the magnetically driven rotation with angular velocity ω , the root-mean-square rotation is effectively enhanced: $\theta_{\text{rms}} \rightarrow \theta_{\text{rms}}^* = \theta_{\text{rms}} + \omega t_c$. Here t_c is the average lifetime of the encounter complex in case the chemical reaction does not proceed. From the separation rate constant, we estimate that the average lifetime of the encounter complex is in the range of 3 ms to 13 ms (see Appendix 2.D). Consequently, we include additional rotation in Eq. 2.12 as:

$$k_{\text{align}} \cong C_1 \cdot R_{\text{MC}}^{-3} \cdot \frac{D_{\text{rot,MC}} + \sqrt{t_c \cdot D_{\text{rot,MC}} \cdot \omega + 4^{-1} t_c \omega^2}}{D_{\text{rot,MC}}} + C_2 \cdot R_{\text{FT}}^{-1}, \quad (2.13)$$

which for $\omega \rightarrow 0$ reduces to Eq. 2.12. We have neglected the influence of the applied magnetic field on the rotational diffusion itself, because the external magnetic field has only a minor influence on the rotational Brownian diffusion during an encounter (see the Appendix 2.E). Using the estimated lifetime of the encounter complex and the earlier found values for the constants C_1 and C_2 (see Figure 2.5), we can calculate the dependence of the association rate constant on the particle angular velocity, which is plotted in Figure 2.8.

We find that the values are indeed in agreement with the experimental data for frequencies up to a few hertz, whereafter the synchronous rotational motion stops and is replaced by a decreasing wiggling motion of the particles.

The results in Figure 2.8 show that the process of near-surface alignment limits the capture rate and not the biochemical association, which is consistent with the data reported in Figure 2.3, Figure 2.5 and Figure 2.6. Furthermore, by applying a heuristic model description of the near-surface alignment process (Eqs. 2.12 and 2.13), we find that the translation of the target particles and the rotation of the capture particles are important factors contributing to the near-surface alignment.

2.7 Conclusions

We have presented a detailed study on target capture using biochemically coated microparticles. Three different types of actuation were employed and the corresponding reaction rate constants were determined by quantifying the reaction kinetics with single target resolution. With respect to passive target capture, fluid agitation affects the overall rate constant of association in two ways. Fluid agitation increases the encounter rate of target and capture particles (volume transport), and interestingly, it also increases the probability of binding during an encounter (near-surface alignment). Continuous rotational actuation of capture particles also provides an increase in the overall rate constant, but not in the encounter rate, so rotation generates an increase of the binding probability or the near-surface alignment rate when particles encounter. The increase in binding probability is attributed to a

combination of enhanced displacement and reorientation near the reactive surface, which increases the probability that binding sites align. We have shown that for our model system with 200 nm sized targets, the overall rate constant of association can be increased by a factor of at least 18 ± 5 by applying fluid agitation, representing a significant acceleration of target capture by both volume transport and near-surface alignment processes.

We have obtained the above insights from model experiments with nanoparticle targets, with binding via biotin/streptavidin and biotin/antibiotin, and with buffer solutions. Yet the field of particle-based target capture is much broader, with the targets ranging from small molecules to large cells, with molecular capture moieties ranging from strong binders to weak binders, and with the fluids ranging from simple buffers to complex matrices such as blood and saliva. Now let us discuss the follow-up questions that are raised by the results of this chapter.

Cells are large and diffuse slowly, so both volume and near-surface transport will be limiting the reaction rate constant. Molecular targets are small and diffuse relatively fast. Yet diffusive motion is random and therefore translation over large distances is relatively inefficient. Locally, the diffusive translation and rotation of molecules is very efficient. Therefore, for molecular targets the near-surface translation and rotation after an encounter will be less limiting to the overall reaction in comparison to the volume transport that is required to generate the encounters.

Concerning the fluid matrix, in this study we have employed solutions with a viscosity close to water. In real-life situations the biological targets may be captured from complex matrices such as blood or saliva, which have higher viscosities. A higher viscosity will slow down the transport in the fluid as the viscous drag is increased, and as a consequence both volume transport and near-surface alignment will become even more limiting with respect to the chemical reaction.

Our results shed light on the underlying processes determining the overall association rate in biochemical particle-based target capture. The insights are particularly important for the development of target capture methods for small microliter-sized sample volumes. In small sample volumes, global mixing by mechanical vortexing cannot be applied, because global mixing requires relatively large fluid volumes, i.e., at least on the order of 100 μL . For small volumes novel actuation methods need to be developed, e.g., based on active particle rotations and displacements. For such purposes magnetic particles are particularly advantageous as they can be manipulated with relative ease using externally applied magnetic fields.

In summary, we have presented a comprehensive methodology to quantify contributions of volume transport, near-surface alignment and biochemical association to the rate constants of particle-based target capture. Our results consistently highlight the importance of volume transport and near-surface alignment and pave the way for a range of further studies on the acceleration of particle-based target capture and for the development of ultrahigh-sensitive technologies for the analysis of small sample volumes.

2.8 Appendix

2.A Loss in target concentration or saturation of the reactive surface

As discussed in the Theoretical considerations section 2.2, Eq. 2.7 may only be applied to determine the reaction rate constant in case no significant depletion in reactants occurs. Here, the potential loss of reactants during the reaction is estimated.

The magnetic capture particles are completely covered with streptavidin, as specified by the manufacturer. Consequently, more than one target particle may bind to a capture particle, up to a maximum of ~ 800 target particles, in which case steric hindrance prohibits the binding of more target particles. In our experiments, due to the limited capture time which is considered, no more than 10 target particles are observed per capture particle. Taking into account only the top hemisphere of the target particles, this would correspond to a reduction of less than 3% in reactive surface of a capture particle, which is a negligible loss.

We can estimate the loss in target particle concentration, both for high and for low concentrations of capture particles. $\sim 5 \times 10^6$ target particles are initially present in the sample fluid. For relatively low concentrations of capture particles (i.e. less than 4×10^3 MC in sample chamber), the maximum amount of bound targets per capture particle was ten FT for a time-span of 25 minutes. This corresponds to a loss in target concentration $< 1\%$, which has a negligible effect on the capture rate. For relatively high concentrations of capture particles, less than 300 bound targets are observed in a single field of view (containing at maximum $\sim 2 \times 10^3$ capture particles). In total, at maximum $\sim 3 \times 10^5$ capture particles are dispersed in the fluid chamber ($0.5 \mu\text{L}$ of 7×10^8 MC/mL). From these numbers, it follows that $\sim 1\%$ of the target particles are captured after 25 minutes, which is negligible as well.

Based on these estimations, it is concluded that no significant losses in reactants occur in the considered time-span.

2.B The response of magnetic particles in a rotating magnetic field

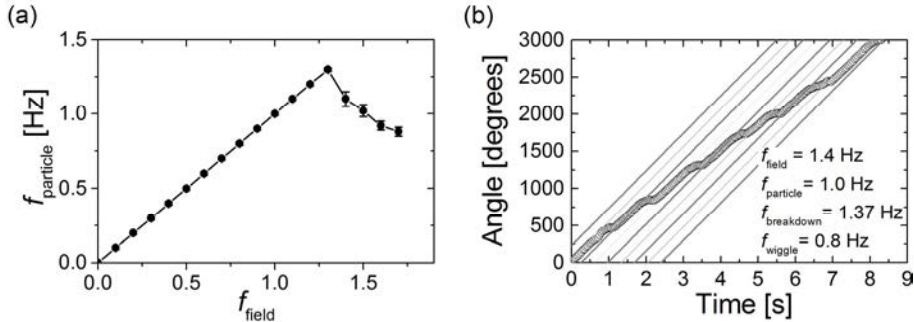


Figure B.1 Rotational response of an unbound magnetic particle on a glass surface in a rotating magnetic field (5 mT). This behavior is reported and described in more detail by van Reenen et al.¹³³. (a) For low rotation frequencies of the magnetic field, the particle synchronously follows the field. Above a certain threshold frequency, called the breakdown frequency, the particle cannot follow the magnetic field anymore and assumes a wiggling motion. (b) Above the breakdown frequency, the particle exhibits a wiggling motion, i.e. it sometimes does and sometimes does not follow the field.

2.C Radial transport near a rotating sphere

The flow around a steadily rotating sphere in an infinite reservoir containing a non-compressible and homogeneous fluid has been studied extensively, both analytically and experimentally (see Fosdick et al. (1980)¹⁵¹ for an overview). We consider in spherical coordinates (r, θ, φ) a sphere with radius $r = R$ that is rotating in the φ -direction with an angular velocity Ω . For this system, an analytical solution describing the steady flow field has been derived assuming no-slip conditions at the sphere boundaries. In our case, we are interested in the radial transport of fluid towards the rotating sphere, i.e.

$$u_{r,rot}(r, \theta) = -\frac{1}{2}\Omega^2 \left(\frac{R^5}{4\nu r^2} \right) \left(1 - \frac{R}{r} \right)^2 (3 \cos^2 \theta - 1), \quad (\text{C.1})$$

with ν the kinematic viscosity (i.e. $\sim 10^{-6}$ m²/s for water at $T = 293$ K; ν equals the dynamic viscosity divided by the mass density of the fluid). Eq. 4S shows that there is an inward flow of fluid at the poles of the sphere ($\theta = 0^\circ$) and an outward flow of fluid at the equator ($\theta = 90^\circ$) due to centrifugal forces. The inward flow is maximal at $\theta = 0^\circ$ and it is found to be maximal at a radial distance of $r = 2R$, e.g. taking $\Omega = 2\pi \cdot 10$ as an upper limit in our experiment: $u_{r,rot}(2R, 0) = -1.7 \times 10^{-10}$ m/s. Note that the minus-sign indicates that the fluid is moving towards the sphere. We can use $u_r(r, 0)$ as an upper limit for the velocity at which target particles are transported towards the capture particle surface.

Now let us compare the rotation-induced with the concentration gradient-induced inward flow velocity of target particles. Using the analytical steady-state solution of the concentration profile, C^{ss} [see Figure 2.3d and Smoluchowski

(1914)¹⁴⁵] and Fick's first law, we can determine the radial velocity of target particles:

$$u_{r,dif}(r) = \frac{J|_{r'=r}}{[FT]_{t=0}} = -D \frac{dC^{ess}}{dr'} \Big|_{r'=r} = -D \frac{d\left(1 - \frac{R}{r'}\right)}{dr'} \Big|_{r'=r} = -D \frac{R}{r^2}. \quad (\text{C.2})$$

Here J is the diffusion flux of targets. We find that the concentration gradient-induced flow velocity also depends on the radial coordinate; due to assumed symmetry it does not depend on θ or φ . Using Eq. B.1 and B.2, we can determine the contribution of diffusive transport with respect to rotation-induced transport, as shown in Figure C.1. We find that for $r \rightarrow \infty$, diffusive transport is ~ 525 times larger than rotation induced transport (at 10 Hz rotation), whereas for short distances, this factor increases up to $\sim 10^6$.

As a consequence, radial transport induced by a 10 Hz rotation of a $r = 1.4 \mu\text{m}$ sphere is negligible as compared to diffusive transport due to the concentration gradient. In our experiments, the nearby surface decreases diffusive transport, but only by a very small amount ($\sim 10\%$). The surface also slightly lowers the rotation-induced transport. So we conclude that in our experiments no measurable radial transport of targets is induced by the rotation of the magnetic particles.

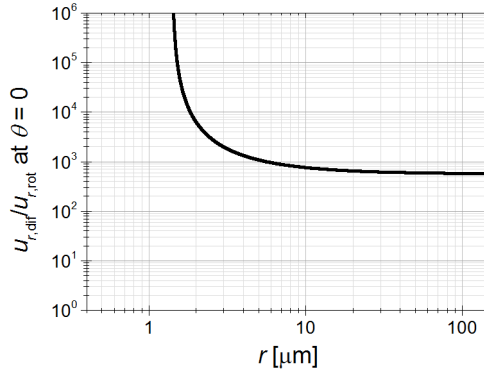


Figure C.1 Comparison between rotation-induced radial transport and diffusion-induced radial transport of targets. The curve corresponds to a rotation frequency of 10 Hz.

2.D Lifetime of an encounter complex

A good estimate of the lifetime of an encounter complex is the reciprocal of the rate constant which governs the separation of the encountered particles, i.e. $t_c \cong k_{sep}^{-1}$. In return, the separation rate constant may be obtained by estimating the equilibrium constant for complex formation $K_{enc} (= k_{enc} / k_{sep})$ and using the Smoluchowski equation, Eq. 2.3. An analytical equation for this equilibrium constant was found by Shoup et al.¹⁵². Based on classical statistical mechanics, they found analytically that the equilibrium constant for a spherically symmetric system without any additional

interaction forces between the particles is simply equal to the reaction volume, i.e. the volume in which the binding reaction can occur. The system which we study here is indeed to a large extent spherically symmetric. Also, no significant interaction forces (typically electrostatic) are present at large distances due to the high ionic strength of the buffer solution (see section 2.4.2). Consequently, a good approximation of the encounter complex equilibrium constant may be obtained by calculating the reaction volume, which we estimate to be the whole volume of 5 up to 20 nm away from the capture particle: $0.12 \mu\text{m}^3$ up to $0.5 \mu\text{m}^3$ respectively. In other words, it is assumed that the particles have formed an encounter complex when distanced by 5 up to 20 nm. Using this estimation for the equilibrium constant K_{enc} and using $k_{\text{enc}} = k_{\text{dif}}$, we find that t_c ranges between 3 ms and 13 ms.

2.E Brownian rotation of a capture particle in an external magnetic field

In Eq. 2.13, it is assumed that the effect of the external magnetic field on the Brownian rotation of the capture particle is negligible. Here, we support this assumption by estimating the energy involved to rotate the ferromagnetic moment of the capture particle in a static magnetic field. It was reported by Janssen et al.¹⁵³ that the locked magnetic moment of the M270 magnetic particles equals $(1.3 \pm 0.4) \times 10^{-16} \text{ Am}^2$. In the presence of an external magnetic field ($B = 5 \text{ mT}$), the magnetostatic energy is $U = \vec{m} \cdot \vec{B}$. Thus we find that an angular misalignment between the magnetic moment and the field of $\sim 6^\circ$ comes at a cost of about one times $k_B T$. Now let us compare this angle to the root-mean-square rotation angle of the capture particle after 0.01 seconds, which is the typical encounter complex lifetime as estimated in Appendix 2.D. Using $\theta_{\text{rms}} = (2D_{\text{rot,MC}} t)^{0.5}$, we find a root-mean-square rotation of $\theta_{\text{rms}} \cong 2^\circ$. This angle is small and involves a magnetostatic energy of only $0.1 k_B T$. So we conclude that the presence of an external field of 5 mT negligibly affects the Brownian rotation of the magnetic capture particle.

Moreover, we have numerically computed the angular excursion of a magnetic particle for the following three cases: (i) no external magnetic field, (ii) a static magnetic field of 5 mT and (iii) a magnetic field of 5 mT that rotates at 1 Hz. Brownian rotation was included following the numerical scheme as described and verified by Grassia et al.¹⁵⁴, which defines an effective Brownian motion torque, τ_{random} . The angular excursion was computed using a forward Euler method with timesteps of $\Delta t = 0.1 \text{ ms}$:

$$\theta_{i+1} = \theta_i + \Delta t \cdot \left[\frac{mB \sin(\omega t - \theta_i) + \tau_{\text{random}}}{8\pi\eta C R_{MC}^3} \right]. \quad (\text{E.1})$$

Here $C \cong 1.2$ is a correction factor to account for the additional viscous drag¹⁵³ on the particle due to the nearby physical surface.

In Figure E.1a the angular excursions are plotted for the three different cases. From the computed data, the angular difference in excursion over 0.01 s (roughly equal to the encounter lifetime) was determined, as shown in Figure E.1b and Figure E.1c. Comparing cases (i) and (ii), i.e. the absence and presence of a static field, no

significant differences are found. A static magnetic field of 5 mT causes a reduction of the root-mean-square angular rotation of $\sim 3\%$. Also compared to a rotating magnetic field (1 Hz and 5 mT), no significant deviation is found in the root-mean-square rotation, other than the mean excursion which is clearly non-zero due to the forced particle rotation.

Based on these results, we conclude that an external magnetic field of 5 mT has a negligible effect on the Brownian rotation of the capture particle.

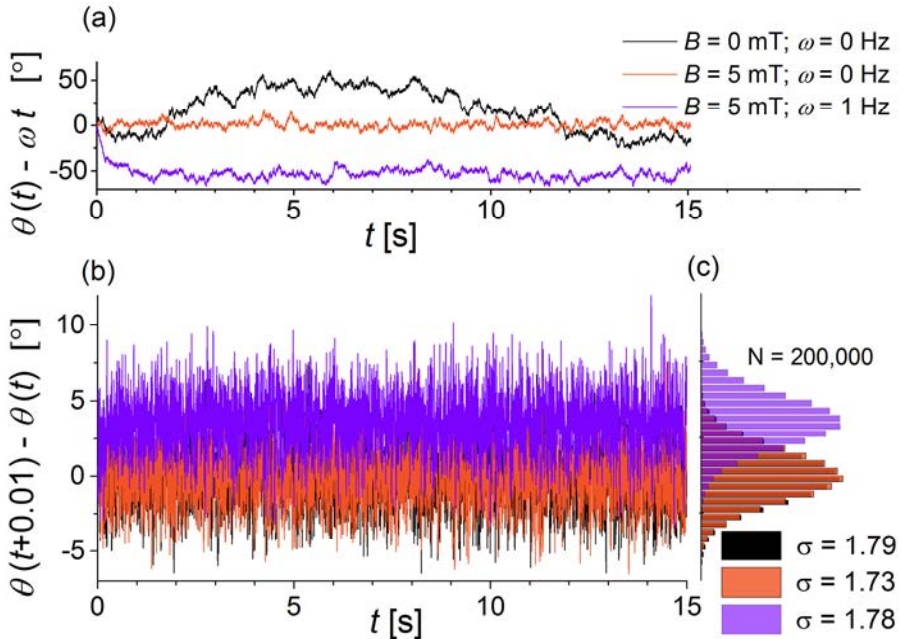


Figure E.1 Simulation of angular excursion of a capture particle in the absence or presence of a static or rotating external magnetic field. (a) Computed excursion with respect to the magnetic field direction for the different cases. (b) Processed data from the angular excursion: the angular difference in excursion over 0.01 s, i.e. the estimated lifetime of the encounter complex. (c) Histograms corresponding to the data in (b). The determined standard deviation is shown in the figure. Note that the data corresponding to an absent external magnetic field (black curves in (b) or bars in (c)) falls for a large part behind the data corresponding to a static magnetic field (red curves and bars).

3

Dynamic actuation of magnetic particle chains for accelerated target capture

*Upcoming generations of highly sensitive and miniaturized biosensing systems need target capture methods that are as efficient and as rapid as possible. Particles are very effective for target capture from solution due to their high surface-to-volume ratio and adaptable surface functionalization. Here, we study the effectiveness of protein capture by magnetic particles and quantify association rate constants in experiments and numerical simulations. The data reveal that depletion of target analyte occurs near the surface of the particles caused by the high density of capture molecules on the particle surface. To overcome depletion effects and enhance protein capture rates, we increase the interaction between the particles and the fluid by applying rotating magnetic fields and magnetic field gradients. We quantify the dependence of the association rate constant on actuation parameters and the particle concentration, showing that association rate constants can be improved by one or two orders of magnitude. We envisage that the reported methods will be very useful in future microfluidic sensing applications of magnetic particles.**

*Parts of this chapter have been published: Y. Gao, A. van Reenen, M.A. Hulsen, A.M. de Jong, M.W.J. Prins, and J.M.J. den Toonder, Chaotic Fluid Mixing by Alternating Microparticle Topologies to Enhance Biochemical Reactions, *Microfluid Nanofluid*, **16**, 265-274, 2014. Other parts of this chapter are in preparation for publication: A. van Reenen, A.M. de Jong, and M.W.J. Prins, Dynamic Actuation of Magnetic Particle Chains for Accelerated Capture of Analytes from Liquid.

3.1 Introduction

Since ancient times¹⁵⁵⁻¹⁵⁹, small particles and granular materials have been used to extract precious or harmful targets from complex fluid mixtures. For example, charcoal was used by the ancient Phoenicians to purify drinking water^{157, 159}, and by the ancient Greeks against food poisoning due to the adsorption of bacterial toxins¹⁵⁹. In Roman times, mercury was used to refine gold and silver from low-grade ore mixtures¹⁵⁵⁻¹⁵⁶. In more recent history, packed beds¹⁵⁸, fluidized beds¹⁶⁰, activated carbon¹⁵⁹ or filter columns¹⁶¹ have been used for all sorts of purification, filtration or extraction purposes. In all these applications, reaction rates are optimized by using dense particle suspensions to maximize the surface contact area of the solid phase with the fluid. For several decades, these principles have been studied for clinical use to extract substances from a biological matrix, based on generic physicochemical capture principles^{142, 162} or on biologically specific capture e.g., using immunoassays⁷. Due to its applicability in complex fluids, specific capture using colloidal particles forms the basis of many analytical technologies in bio-analysis and *in vitro* diagnostics.

In medical diagnostic applications, colloidal particles with magnetic properties are particularly useful as they can be easily extracted from the fluid by magnetic forces. Moreover, their magnetic properties can be exploited to effectuate series of processing steps in a diagnostic assay, such as buffer exchange⁵⁰, washing²⁵, concentration^{25, 50} and labeling^{25, 103}. By integrating the various steps, complete assays can be automated in a lab-on-chip testing device. Several methods based on magnetic particles have demonstrated detection of biological analytes with single-molecule resolution.^{9, 13, 82}

However, while the use of high concentrations of particles speeds up the affinity capture in integrated lab-on-chip assays^{9, 13, 25, 103, 114}, it has significant disadvantages for downstream processes. High particle densities (i) increase non-specific particle-particle and particle-surface interactions, (ii) enhance field-induced particle aggregation, and (iii) cause steric hindrance of subsequent biochemical reactions.

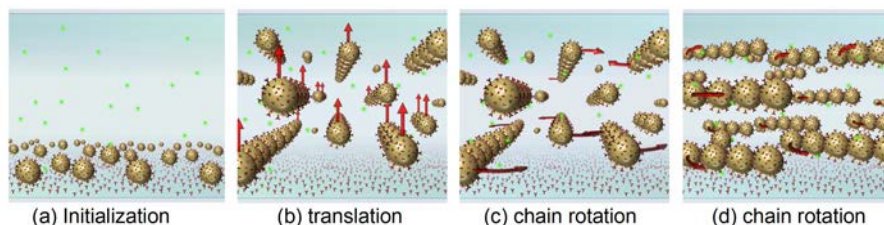


Figure 3.1 Concept sketch of dynamic magnetic particle actuation to accelerate capture of target analytes from a sample fluid. (a) First the sample fluid containing the targets (small green spheres) enters the microfluidic reaction chamber containing the magnetic particles (brown spheres). (b) Using field gradients, particles can be translated through the liquid, while particles form into chains that are aligned in the direction of the external field. (c,d) Rotating the magnetic field causes chains to rotate within the sample fluid. Rotating particle chains can dynamically break and reform depending on the ratio between the magnetic forces and the viscous forces acting on the particles.

The problem of using dilute particle suspensions is that an enhancement of the particle-fluid interactions is needed to avoid a decrease of the effective capture rate. However, with sample volumes typically being minute, turbulent fluid mixing^{13, 82} cannot be applied and flow-based microfluidics^{28, 62, 83} complicate device integration to generate the fluid flows. Therefore, new methodologies are needed in order to be able to use dilute particle concentrations in small sample volumes while maintaining a high capture rate.⁵⁷

To this end, we study here the particle-based capture efficiency as a function of the particle density, and how this relation can be understood based on the fundamental kinetic and diffusive processes. For optimal target capture, particles should contain as many binding sites as possible. We show that particles with high reactivities cause diffusive target depletion zones near the particles, which lead to reduced capture rates. To overcome local depletion and recover high capture rates, magnetic actuation can be used to enhance particle-fluid interactions (see Figure 3.1). The local fluid can be mixed using rotating magnetic fields and field gradients can be used to move particles through the fluid to maximize the scavenging efficiency of the particles. To quantify target capture in a direct way, we employ an experimental model system, with fluorescently labeled antibodies as targets. To interpret the data, we apply theoretical frameworks for particle chain behavior^{21, 41, 47} and target capture^{53, 57}. Finally, we discuss the applicability of the studied techniques in the development of future diagnostic testing technologies.

3.2 Experimental section

3.2.1 Model system for particle-based target capture

To study target capture processes, an experimental model system was used consisting of protein G-coated magnetic particles and fluorescently labeled antibodies (Figure 3.2d). Magnetic particles ($\varnothing 2.8 \mu\text{m}$, carboxylated M270, Dynal Biotech) were coated covalently with recombinant protein G (Thermo Scientific) using standard EDC-NHS coupling chemistry. As targets, we used goat anti-mouse IgG antibodies labeled with Alexa Fluor® 488 dye (Invitrogen). Both the particles and target antibodies were diluted in assay buffer, i.e. phosphate buffered saline containing 0.1% bovine serum albumin, BSA, (Merck) and 0.02% Tween-20 (Thermo Scientific).

To quantify the maximum binding capacity of the magnetic particles, we performed a supernatant assay in which magnetic particles ($\sim 9 \times 10^6$ particles/ μL) were incubated with ~ 60 nM antibodies for 3 hours. After a magnetic washing step, we measured the fluorescence of the supernatant using a Fluoroskan Ascent FL. Compared to a control in which no magnetic particles were incubated, a 4.4 ± 0.3 % decrease was found in the fluorescence signal, from which we calculate that a single magnetic particle can bind $(1.8 \pm 0.2) \times 10^5$ antibodies.

To visualize fluid mixing as induced by the magnetic particles, $\varnothing 500$ nm fluorescent spheres (FluoSpheres COOH, Invitrogen) were used as tracer particles. The tracer particles were suspended together with magnetic particles in water containing

50% glycerol, to increase the viscosity of the fluid to ~ 6 mPa. This reduced the diffusive mass transport of the fluorescent tracer particles and enabled us to more clearly discriminate advective transport from diffusive transport.

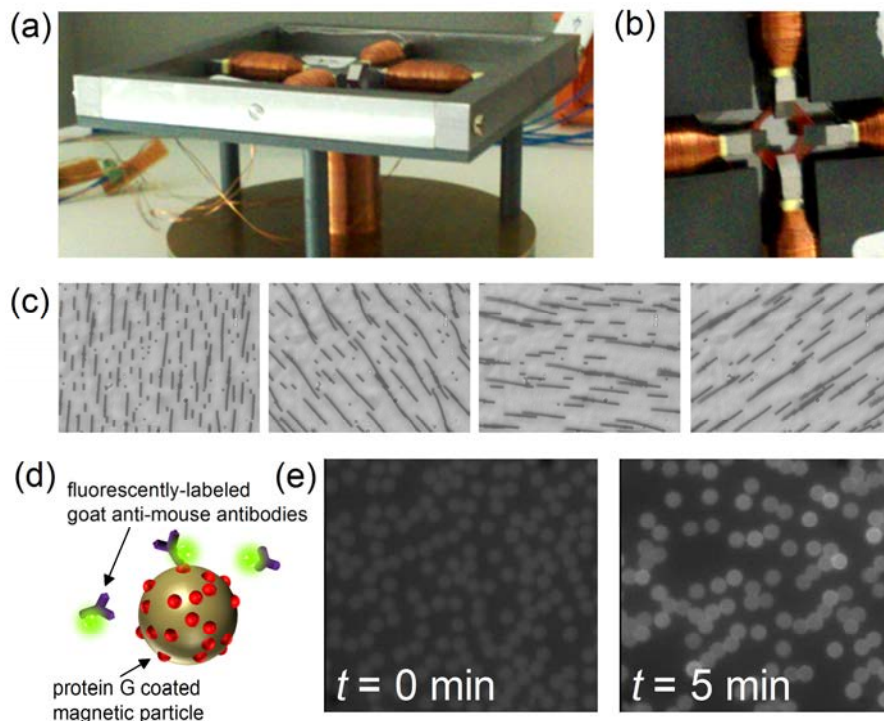


Figure 3.2 Studying particle-based target capture under dynamic magnetic particle actuation. (a) External magnetic fields were generated by a 5-pole electromagnet containing soft iron parts to concentrate field lines at (b) its center where the incubation chamber is located. (c) Microscope images of rotating chains of magnetic particles. (d) The experimental model system to study the capture process. (e) Fluorescence microscopy images of particles before and after magnetic actuation. The average fluorescence of the particles is compared to the background to quantify the capture of targets. Due to the auto-fluorescence, particles are also visible in case no targets are added. The observed variation in fluorescence per particle is attributed to the variations in particle capture rates depending for example on the position of the particle within an aggregate.

3.2.2 Preparation and filling of the incubation chamber

Microfluidic incubation chambers were used that were shaped as a flat cylinder (Figure 3.2b). Chambers were made by assembling adhesive Secure-Seal™ Hybridization chambers (\varnothing 9 mm, height = 0.6 mm; Electron Microscopy Sciences) to a glass cover slip (VWR) that was cleaned beforehand using isopropanol. On the non-adhesive side, the Hybridization chambers had a 0.25 mm thick polycarbonate sheet containing two inlets to fill the 38 μ L chamber. This sheet was transparent to allow imaging from this side using a microscope (Leica DM6000). Prior to an experiment,

the incubation chamber was filled with assay buffer (containing no particles or targets) to block the chamber with BSA which minimizes non-specific adhesion.

In experiments, a 4 μL magnetic particle suspension (2×10^5 particles/ μL ; unless stated otherwise) was inserted in the incubation chamber by means of a pipette. After one minute – to let the particles sediment to the bottom surface – the incubation chamber was filled with the target solution ($\sim 34 \mu\text{L}$ and diluted to 110 pM; unless stated otherwise). To prevent evaporation losses, the chamber was sealed using adhesive port seals as supplied together with the Hybridization chambers.

3.2.3 Magnetic field generation

To generate time-dependent magnetic fields in the incubation chamber, an electromagnet setup was designed and built consisting of five electromagnets (see Figure 3.2a,b). The setup consists of a quadrupole electromagnet (800 windings with $\varnothing 0.25$ mm copper wires) to generate magnetic fields, oriented in-plane with respect to the bottom surface of the incubation chamber (see Figure 3.2b). A separate electromagnet (1600 windings with $\varnothing 0.25$ mm copper wires) is positioned below the center of the quadrupole electromagnet to allow for the generation of fields oriented out-of-plane. Using the quadrupole electromagnet, magnetic fields can be generated that rotate in-plane with respect to the incubation chamber (see Figure 3.2c), whereas by combining the bottom electromagnet with two opposite electromagnets of the quadrupole, magnetic fields can be generated that rotate out-of-plane. To guide field lines to the incubation chamber, soft iron parts were implemented in the setup.

The electromagnets were powered using a controller that was steered using LabView software to allow for the application of actuation protocols to each coil separately that can vary in time in terms of the amplitude, frequency and waveform (i.e. sinusoidal) of the current. The calibration of the magnetic field was performed using a Gauss meter (5100 series F.W. Bell); the data can be found in Appendix 3.A.

3.2.4 Magnetic redistribution of particles after actuation

After the application of each actuation sequence to incubate the particles, particles were actively disaggregated and redistributed over the bottom surface by means of a method called rotaphoresis (see Chapter 6 and Appendix 3.B). The redistribution of particles by means of rotaphoresis allowed us to microscopically evaluate all particles distributed over the surface.

3.2.5 Quantification of target capture

To quantify target capture for different types of actuation, we monitored the fluorescence intensity of the particles. Before actuation and after the application of a single actuation protocol, the incubation chamber was placed under a microscope (Leica DM6000). Using a water immersion objective lens ($63\times$) the bottom surface with particles was imaged at a final magnification of $630\times$. The redistributed particles stayed on the bottom surface by gravitational forces. Excitation light ($\lambda = 480 \pm 20$ nm) was generated by an external light source (Leica EL6000) combined with a L5 (Leica) filter cube. Fluorescence (within the range of $\lambda = 527 \pm 15$ nm) was recorded

using an EMCCD camera (Andor Luca S). For each measurement, images were taken from three random locations (with a field of view of $142 \times 107 \mu\text{m}^2$). After a measurement, the incubation chamber was placed back into the electromagnet setup to start the next actuation sequence.

Images (see Figure 3.2e) were processed using ImageJ software (<http://rsb-web.nih.gov/ij/>) and Matlab (Mathworks) to determine the average fluorescence intensity of the particles with respect to the background intensity. The used method is shown in Figure 3.3. First, the area occupied by the magnetic particles was determined by making a binary image using ImageJ (see Figure 3.3b,c). Subsequently Matlab software was used to determine the average intensity of the pixels corresponding to the particles or the background. In Figure 3.3d the average intensity of the particles with respect to the background is shown for different thresholds to obtain the binary image. Based on this, a relative error of 10% is estimated for a single measurement. As the intensity is averaged over the number of pixels, a single measurement is independent of the number of particles within a single field of view.

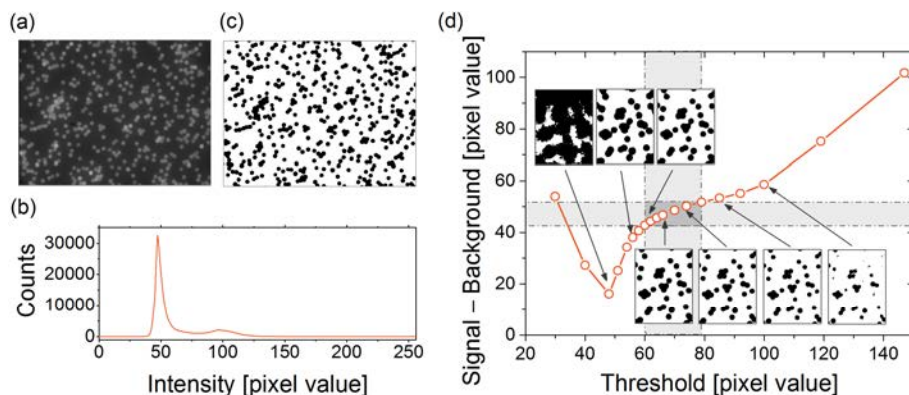


Figure 3.3 Image processing to determine the fluorescence of the magnetic particles with respect to the background. (a) Original fluorescence image (b) Histogram of pixel intensities for the original image. By setting a threshold in between the two peaks, i.e., at a pixel value of 70, (c) a binary image is obtained. The binary image is used as a mask to determine the fluorescence signal from the particles and the surrounding background. In (d) the average pixel intensity of the particles with respect to the background is shown for different values of the threshold for the binary image. Corresponding binary images are shown for several data-points. The gray bars indicate the region in which the threshold results in binary images containing particles with sizes that are approximately equal compared to the fluorescence images.

3.2.6 Verification of the specificity of antibody capture

We compared target capture with our experimental model system to several control experiments, to investigate whether capture was specific. In each measurement equal concentrations of reagents were incubated in a micro-centrifuge tube on a vortex mixer (mixing at 1400 rpm for 30 minutes). After incubation, the magnetic particles were washed magnetically, re-suspended in assay buffer and pipetted in an incubation chamber. After sedimentation, fluorescence images of the particles were recorded and fluorescence signals were determined.

First, we tested different surface functionalizations of the particles: see the white bars in Figure 3.4. A clear increase in signal was found for protein G-coated particles compared to the other surface functionalizations. The relatively high signal for the controls can be mainly attributed to the autofluorescence of the magnetic particles; compare the black bar in Figure 3.4. Lastly, we also included a measurement of the protein G-coated particles for the case of 30 minutes of magnetic actuation: the 6th (orange) bar. Interestingly, magnetic actuation shows a larger increase in target capture compared to vortex mixing. This is already a first indication of the effectiveness of magnetic actuation in target capture.

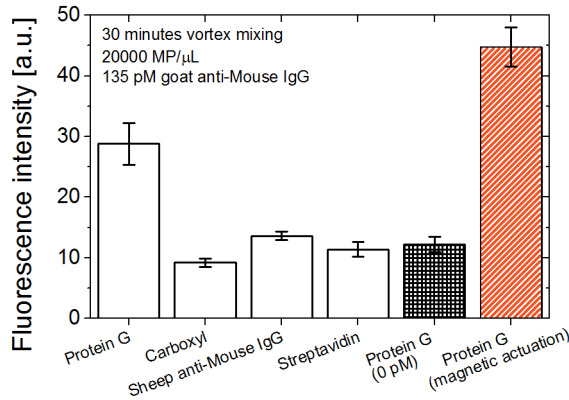


Figure 3.4 Control experiments for the specificity of the experimental model system: goat anti-mouse IgG and protein G-coated magnetic particles. The average particle fluorescence was measured after 30 minutes of incubation of the reagents on a vortex mixer, except for the orange bar. Different surface functionalizations were tested: protein G; carboxyl (hydrophilic); sheep anti-mouse IgG and streptavidin. To determine the contribution to the fluorescence intensity due to the auto-fluorescence of the magnetic particles, a measurement was performed with a zero target concentration (i.e. the black bar). The error bars correspond to the standard deviation in the determined fluorescence intensity.

3.2.7 Determination of rate constants for association and dissociation

From the experimental data, rate constants were determined by analyzing the time-dependence of the fluorescence intensity of the particles. The kinetic analysis is based on the overall association reaction between a magnetic particle (MP) and an antibody (Ab), described as



in which k_a and k_d respectively are the association rate constant and the dissociation rate constant. Based on this equation, the rate at which antibodies are captured and bound to magnetic particles is:

$$\frac{d[\text{boundAb}]}{dt} = k_a[\text{Ab}][\text{MP}]\theta - k_d[\text{boundAb}] \quad (3.2)$$

Here, the brackets indicate concentrations of the different species, which depend on time. In Eq. 3.2, [boundAb] is used instead of [MPAb] to better express that multiple antibodies can bind to the same magnetic particle. To account for saturation of the particle surface, the term θ is included in Eq. 3.2, which represents the ratio between the number of free and accessible binding sites compared to the total number of binding sites (i.e. free, occupied or inaccessible). Initially, θ is equal to 1, but its value will drop to zero as the particle surface becomes saturated and covered by bound antibodies. In experiments we used a [MP]:[Ab] ratio of 1:5000, and compared to the binding capacity of $(1.8 \pm 0.2) \times 10^5$ antibodies per magnetic particle (see Section 3.2.1), we estimate that only 3% or less of the available binding sites will react. Based on these considerations, we assume that $\theta = 1$ in our experiments, and the corresponding solution of Eq. 3.2 then is:

$$[\text{boundAb}] = \frac{k_a[\text{MP}][\text{Ab}]}{k_a[\text{MP}] + k_d} \left(1 - \exp\left(-\left(k_a[\text{MP}] + k_d\right)t\right) \right). \quad (3.3)$$

Assuming that [boundAb] scales linearly with the particle fluorescence, Eq. 3.3 can be applied to experimental data to extract both the association and the dissociation rate constants. However, this is only possible when the exponential behavior is observed, as the initial rate of the kinetic regime (i.e. the limit of small t) does not depend on the dissociation rate constant, but only on the association rate constant.

3.3 Results and discussion

To study the effect of magnetic particle actuation on the capture of analytes, we first characterized the mixing characteristics of rotating particle chains, and subsequently quantified rate constants from actuation experiments on a model system. Besides experimental data, we also show simulation results of the capture process for simplified actuation protocols. Lastly, we present experimental data on scaling relations between the capture rate and different actuation parameters.

3.3.1 Mixing induced by rotating magnetic particle chains

Fluid mixing induced by rotating chains of particles was studied in experiments using fluorescent tracer particles with a diameter of 500 nm. Tracer particles were used in two ways: (i) in a dilute suspension to determine particle trajectories; and (ii) in a dense suspension with a dye-water interface to quantify interfacial mixing. In the experiments, we focused on two types of chain rotation, i.e. rigid chains and chains that exhibited breaking-and-reformation behavior.

In Figure 3.5, trajectories are shown of tracer particles in the vicinity of rotating chains of particles. For rigid rotating chains (Figure 3.5a,b), the trajectories are steady, slightly modulated circles around the center of the rotating particle chain, similar as was observed by Franke et al.¹⁶³. The oscillations of the tracer particles correspond to the rotational frequency of the chains and depend on the relative distance to the chain. Specifically, when a tracer particle is located outside the rotational range of the chain (i.e., $x^2 + y^2 > 1$ in Figure 3.5b), the amplitude and the wavelength of the oscillation decreases.

In the regime of periodic chain breaking and chain reformation (Figure 3.5a,c), the trajectories of the tracer particles become chaotic, i.e., significant radial transport of the tracer particles is observed. This is in contrast to chains that remain rigid during rotation (Figure 3.5b). For rigid chains, the tracer particles are confined within well-defined regions, indicating that mass transport is linear. When the chains periodically break-up and reform, the tracer particles are distributed spatially along the radial range of the chain, indicating that enhanced chaotic mass transport is induced. These findings agree with results reported by Kang et al.²¹ from 2D numerical simulations of rotating particle chains (compare Figure 1.3b,c).

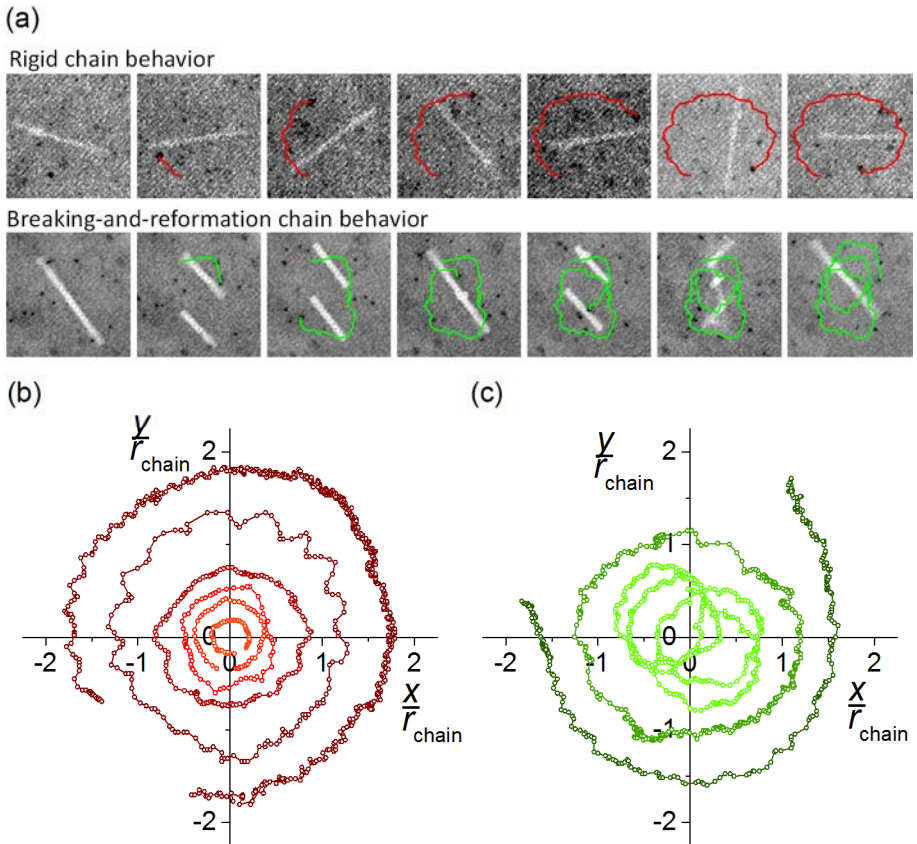


Figure 3.5 Fluid mixing induced for varying rotational behavior of particle chains by tracing suspended fluorescent particles with a diameter of 500 nm. (a) Snapshots of the induced motion of tracer particles for a chain that exhibits rigid chain behavior (top) or breaking-and-reformation behavior (bottom). The colored lines connect the same tracer particle. In between the snapshots, the magnetic field undergoes multiple rotations. (b) Tracked trajectories of tracer particles starting at different positions for chains which remain rigid during rotation. The axes are made dimensionless by dividing the distance of the particle with respect to the center of the particle chain with the radius of the particle chain. (c) Tracked trajectories for chains which exhibit breaking-and-reformation behavior.

In Figure 3.6, data is shown of fluid mixing by an isolating rotating particle chain at a dye-water interface. The interface was obtained by pipetting a dense suspension of tracer particles in a fluid chamber containing the same fluid.⁴⁷ Before the chains were rotated, the fluid near the chain was unmixed and a clear interface could be seen between the dye and the uncolored water (see the leftmost snapshot in Figure 3.6a). After 15 rotational cycles of the magnetic field, it was found that the two fluids within the range of the particle chain were mixed.

Mixing was quantified by determining the mixing index from the images (see Appendix 3.C or ⁴⁷ for the method). The mixing index is defined as the ratio of the variance and the average fluorescence intensity. As the chain rotates, the variance decreases, whereas the average fluorescence intensity remains more or less constant. In Figure 3.6b, the average mixing indices are shown as obtained from six rotating magnetic particle chains in the two different mixing regimes. The shaded areas correspond to the calculated standard deviations. Clearly, alternating topological changes of the chains yield a better homogenization of fluid with the mixing index approaching a value around 0.1. Rigid chains, on the other hand, result in a value of the mixing index of only around 0.5, indicating a lesser degree of homogenization.

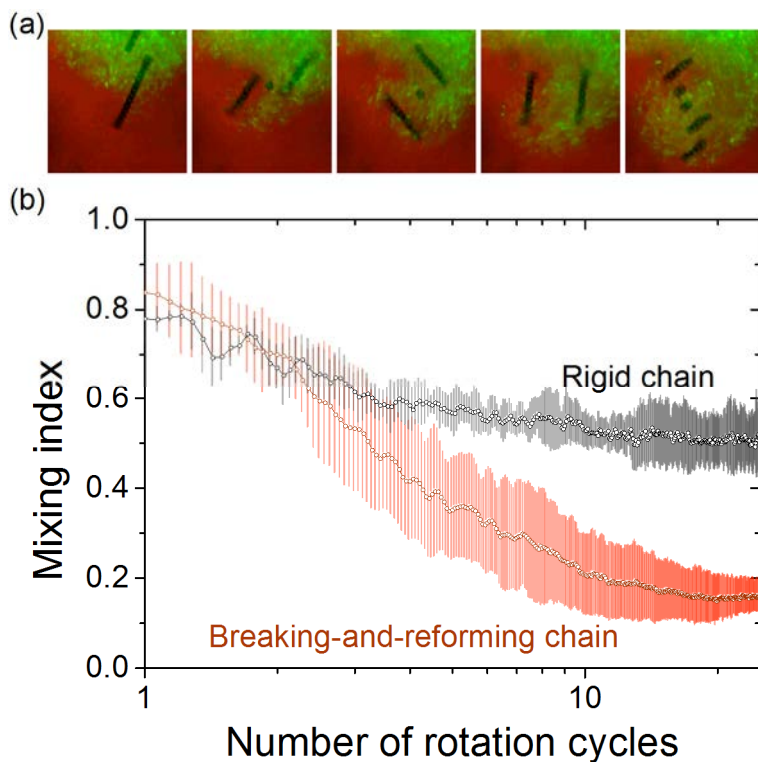


Figure 3.6 Quantification of fluid mixing by rotating magnetic particle chains at a fluorescent dye interface within a water medium. (a) Microscope image of a particle chains exhibiting breaking-and-reformation behavior at the interface. (b) Mixing index for different rotational behaviors of the particle chains. For each case, three measurements were averaged.

Based on these results, we conclude that the rotation of magnetic particle chains is effective for inducing fluid mixing within the range of the particle chain. Furthermore, chains that exhibit breaking-and-reformation behavior mix better compared to chains that remain rigid during rotation. Since the induced fluid mixing is effective only in the vicinity of the particle chain, for mixing of a fluid on a large scale, it is important that chains are long. In addition, as particle chains only mix within the plane of rotation, we expect that mixing can be further enhanced by altering the plane of rotation or by applying field gradients to translate particles through the fluid while they are rotating.

3.3.2 Effect of magnetic particle actuation on the capture process

We studied the capture of proteins from a fluid using magnetic particles for different magnetic actuation protocols (see Figure 3.7). As a reference, we applied no magnetic actuation. Without magnetic actuation, particles sediment in a random distribution at the bottom of the incubation chamber. In case of magnetic actuation, firstly, field gradients were applied to translate particles repeatedly up and down through the incubation chamber ($B_{\text{grad},z}$), as sketched in Figure 3.7a. During this process, particles form into chain-like structures oriented in the direction of the applied field; the orientation of the magnetic field was fixed in-plane with the bottom surface of the incubation chamber. To study the rotation of chains of magnetic particles, magnetic fields were applied that rotated in-plane ($B_{\text{rot},h}$) or out-of-plane ($B_{\text{rot},v}$) with respect to the bottom surface.

As shown in Figure 3.7b, the actuation of magnetic particles has a strong effect on the capture rate. In case of actuation, the measured curves show an initial kinetic regime and a saturation of the particle fluorescence after several tens of minutes. By fitting Eq. 3.3 to the data, we determined the association and dissociation rate constants for the different cases (see Figure 3.7c). For the dissociation rate constant, similar values are found with an average value of $k_d = 1.5 \pm 0.7 \times 10^{-4} \text{ s}^{-1}$. This value is consistent with the dissociation rate constant of goat-IgG and protein G of $k_d \approx 1 \times 10^{-4} \text{ s}^{-1}$ as reported in the literature based on localized surface plasmon resonance (LSPR).¹⁶⁴ The association rate constants on the other hand show a significant variation for the different types of actuation. Compared to no actuation, a field gradient of $\sim 4 \text{ T/m}$ – which corresponds to a single particle moving at $12 \mu\text{m/s}$ – results in an increase in k_a by a factor of 8 ± 4 . Combined with a rotating magnetic field, the increase becomes even larger. We find that out-of-plane rotating fields, with an increase in k_a of 36 ± 7 times, are more effective than in-plane rotating fields. Thus, moving particles through the sample volume yields a substantial increase in the rate at which target antibodies are captured.

We attribute the observed increase in association rate constant to the fact that local depletion zones in the target concentration are formed near the particles. Such concentration gradients near the particles point to a (translational) diffusion limitation in the capture process and hence can explain why enhanced particle-fluid interaction

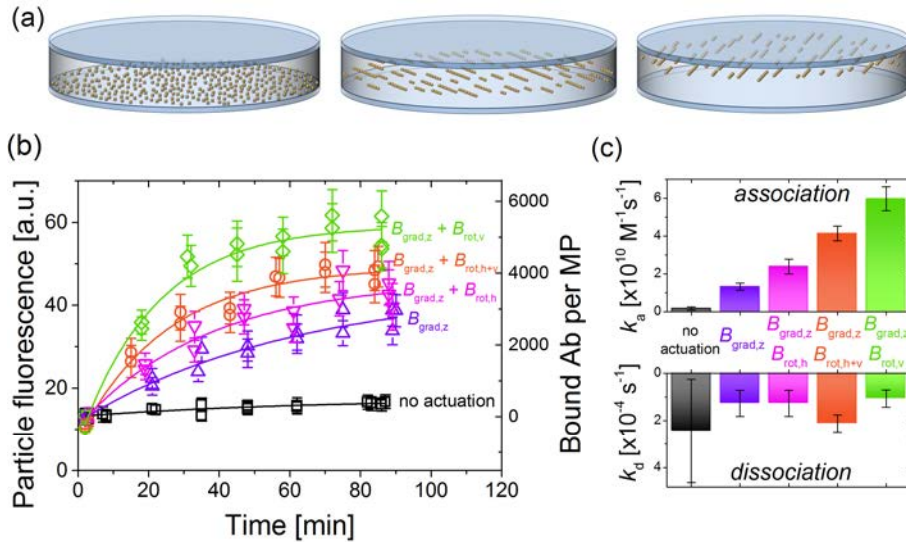


Figure 3.7 Magnetic actuation of ensembles of particles. Target capture measured for different types of magnetic actuation: no actuation; only translation ($B_{grad,z}$); and translation combined with rotation in-plane ($B_{rot,h}$), out-of-plane ($B_{rot,v}$), or alternating in both directions ($B_{rot,h+v}$). For magnetic actuation we used $B = 20$ mT and a rotating frequency of $\omega = 0.2$ Hz. (a) Sketch of the typical effect of actuation. Initially, particles are distributed over the bottom surface of the incubation chamber. By magnetic actuation, the particles are moved in a layer-like fashion upwards and downwards through the fluid, and form (rotating) chains. After actuation, the particles are redistributed over the surface and the fluorescence due to captured targets on the particle surface is measured. (b) Time-dependence of the fluorescence signal. The lines correspond to fits based on Eq. 3.3 to determine k_a and k_d . From the fit parameters, the particle fluorescence is correlated to the number of bound antibodies per magnetic particle, as shown on the right axis. (c) Fitted association and dissociation rate constants for the cases corresponding to panel b. Used particle concentrations were 2×10^5 particles/ μL in a fluid volume of approximately $36 \mu\text{L}$.

increases the capture rate. In the following paragraphs, we will discuss the underlying processes in more detail to prove this hypothesis.

In the literature on the bimolecular association of proteins (e.g. see ref ⁵³), it is found that the association of proteins to antibodies is generally limited by diffusive transport and not by the chemical reaction which finally binds the proteins. This diffusive limitation in antibody-protein association is, however, not so much caused by the relative translational diffusion, but by the angular constraints – or: the relative binding site orientation – that need to be met before the antibody can bind the protein. For example, it has been shown by Schmitz and Schurr⁵⁸ that moderate angular constraints decrease diffusion-controlled association rate constants by several orders of magnitude⁵³. Rate constants for antibody-protein association are typically in the order of $k_a = 10^4$ - $10^6 M^{-1}s^{-1}$ ^{53, 164}. This is low compared to the diffusive encounter rate as expected based on relative translational diffusion alone, which is in the order of 10^9 - $10^{10} M^{-1}s^{-1}$ as follows from the Smoluchowski equation¹⁴⁵:

$$k_{dif} = 4\pi DR, \quad (3.4)$$

with D and R being respectively the combined diffusivity and the encounter radius of the reacting proteins. Therefore for values of k_a as typically found for antibody-protein association, no depletion zones would be expected.

For the particle-based association of proteins, we find values of k_a (Figure 3.7c) that are much closer to the diffusive encounter rate which we estimate at $k_{\text{dif}} = 4\pi(D_{\text{MP}} + D_{\text{IgG}})(R_{\text{MP}} + R_{\text{IgG}}) = 4.1 \times 10^{11} \text{ M}^{-1}\text{s}^{-1}$, where a hydrodynamic radius of $\sim 5.5 \text{ nm}$ was used for goat IgG¹⁶⁵. This constant is only a factor 6.9 ± 0.7 larger than the maximum association rate constant that we find in experiments, namely $k_a = 6.0 \pm 0.6 \times 10^{10} \text{ M}^{-1}\text{s}^{-1}$. As a consequence, a limitation by translational diffusion cannot be neglected for the association of protein targets to particles (see Appendix 3.D for a discussion about particle-based capture versus planar capture).

In a previous study where the process of particle-based capture of proteins was investigated using a model system with 200 nm particles as targets⁵⁷ (see Chapter 2), we found that the capture process is limited both by the translational and rotational diffusion of the reacting species. The results in Figure 3.7 suggest that this is also the case for the capture of proteins. Furthermore, the large difference between the k_a for particle-based protein association and antibody-protein association can be attributed to (i) the larger encounter radius because of the relatively large magnetic particle, and (ii) the high number of binding sites on the magnetic particle compared to a single antibody. When the surface of the magnetic particle is completely filled with binding sites, the magnetic particle can bind a target protein in almost any orientation, and during a collision with a target protein, the target protein can interact with multiple binding sites. In this way, the probability to bind is much higher for a protein encountering a magnetic particle, than for a protein encountering an antibody free in solution. Thus, in particle-based association of proteins, orientational constraints for binding are reduced to such an extent that also the number of encounters becomes a limitation for the association rate.

Therefore, we conclude that depletion layers form due to the slow diffusion of targets in case the magnetic particles are immobile at the bottom of the incubation chamber (see Figure 3.7). By moving particles through the fluid, these depletion layers around the particles can be reduced. As depletion zones grow over time, enhanced interaction of the particles with the fluid, for example by applying rotating fields, diminishes the depletion zones even further. As concentration gradients are mainly developed orthogonal to the layer of particles (compare Figure 3.7a), out-of-plane rotation of magnetic particles is the most effective to reduce the concentration gradients (compare section 3.3.1)⁴⁷.

Based on these findings and discussion, we further explored the particle-based capture process, in the following directions. First, we developed a numerical model based on Brownian dynamics to quantitatively validate the expressed hypotheses. Secondly, we quantified the capture rate as a function of various field actuation parameters. Thirdly, we studied the acceleration of target capture for different magnetic particle concentrations.

3.3.3 Comparing experimental data to Brownian dynamics simulations

The experiments of Figure 3.7 involve the following interactions: (i) the hydrodynamic interactions between the particles and the targets; (ii) the magnetic interactions between the magnetic particles; and (iii) the binding process of the targets to the particles. The hydrodynamic interactions between (spherical) particles have been modeled in the literature¹⁶⁶, but the dynamic particle behavior induced by the magnetic interactions complicates the hydrodynamic interactions. For example, the chain rotation induces chaotic fluid mixing, which is difficult to model in two dimensions²¹, let alone in three dimensions. Since we are mainly interested in the binding process and not in the magnetic particle interactions, simulating the experimental system of Figure 3.7 is unnecessarily difficult.

Therefore, we designed an experiment which excluded the magnetic and hydrodynamic interactions between the magnetic particles. Specifically, we characterized the capture rate of magnetic particles at very dilute particle concentrations (100 particles/ μL). Furthermore, we compared capture of targets on the one hand for particles lying on a surface and on the other hand for particles showing linear translation through a fluid due to gravitational forces, by repeatedly turning the fluid cell upside down. In Figure 3.8a the measured fluorescence intensity is shown for both cases. The induced particle velocity of $v_{\text{MP}} = 5.1 \mu\text{m/s}$ is estimated by balancing the Stokes drag with the gravitational force on a single particle: $6\pi\eta R_{\text{MP}}v_{\text{MP}} = 4\pi R_{\text{MP}}^3 (\rho_{\text{MP}} - \rho_{\text{medium}})g$. Comparing both cases, it is found that the capture rate is higher by a factor of 1.9 ± 0.1 when particles translate through the fluid.

With these results as a reference, we numerically modeled the capture process in a similar system based on Brownian dynamics. For the specific details of the method, see Appendix 3.E. Most importantly, as sketched in Figure 3.8b, we simulate a magnetic particle at different translation velocities within a rectangular fluid cell with a height equal to the incubation chamber. The width of the fluid cell was set at $100 \mu\text{m}$ and periodic boundary conditions were used to the sides. For target antibodies, spherical particles were assumed with corresponding hydrodynamic radii¹⁶⁵. Initially, target particles are randomly distributed and we compute their random displacement and rotation due to Brownian motion as well as hydrodynamic interactions due to the movement of the magnetic particle through the fluid. We neglect interactions between the target particles because the target concentrations are dilute. The capture process is modeled by treating the boundary of the magnetic particle as being partially absorbing. Specifically, binding is assumed only for angular differences smaller than a pre-defined angle $\alpha \in [0, \pi]$ between (i) the orientation vector of the target and (ii) the relative position vector between the particle and the target. In other words, the target needs to orient itself towards the magnetic particle in order to bind. In case $\alpha = \pi$, targets “bind” to the particle independent of their orientation. In case of $0 < \alpha < \pi$, targets only bind for a limited range of orientations, and otherwise reflect from the surface. In this way, constraints to the relative binding orientation can be imposed. Lastly, a numerical timestep of $3 \mu\text{s}$ was chosen, which is small enough to keep propagation errors negligible (see Appendix 3.E), which is important for a reliable outcome of a forward Euler method.

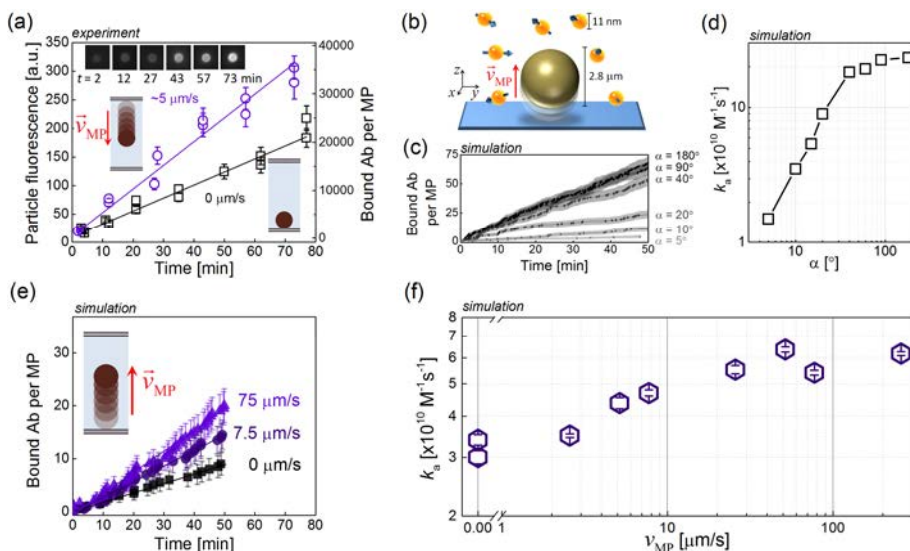


Figure 3.8 Linear translation of single particles. Comparison of target capture in experiments and numerical simulations. (a) Capture of fluorescently labeled antibodies (110 pM). Particles were moved through the incubation chamber by gravitational forces (see inset illustration) by reversing the chamber every 2 minutes, leading to an estimated particle velocity of 5.1 $\mu\text{m/s}$. The inset images show fluorescence microscope images of particles at different incubation times. The indicated number of bound antibodies per magnetic particle on the right axis follows from the fits in Figure 3.7b. The solid lines correspond to least-squares linear fits to the data. (b) Schematic overview of the system simulated by Brownian dynamics, showing the magnetic capture particle (brown) and the target particles (orange). (c) Simulated capture of antibodies for varying binding range α of the targets (see values to the right of the right axis). The target concentration was 0.1 pM. From linear fits to the data, (d) corresponding association rate constants were determined. (e) Simulated capture for different particle velocities and for $\alpha = 10^\circ$. The inset figure shows that particles start at the bottom and move up and down through the fluid. From linear fits to the data, (f) the association rate constants are determined as a function of the particle velocity.

First, we simulated target capture by non-actuated (i.e., sedimented) magnetic particles for different values for the binding range α . As shown in Figure 3.8c,d, the binding rate strongly depends on α , especially at low values. For a binding range of $\alpha \cong 10^\circ$, we find similar association rate constants as in experiments (Figure 3.8a). Note that the different target concentrations vary by a factor of 1.1×10^3 ; this means that in experiments at 0.1 pM approximately 12 targets would be bound after 50 minutes. Compared to completely absorbing spheres, i.e., $\alpha = \pi$, the association rate constant for $\alpha \cong 10^\circ$ is less by a factor of 7 ± 1 . In the literature, it has been reported⁵³ that binding ranges of $\alpha \cong 5^\circ$ lead to association rate constants similar as found for free antibody-antigen association. The larger binding range that we find is likely caused by the presence of multiple binding sites within close proximity on the surface of the magnetic particles. During an encounter with a particle, a target protein can interact with multiple binding sites, which is much less probable for a protein free in solution. The interaction with multiple binding sites effectively increases the allowed binding range for which the target can react.

Next, assuming $\alpha = 10^\circ$, we simulated the effect of active particle translation through the sample volume. As shown in Figure 3.8e,f, we find that increased translation velocities enhance the capture rate. For a velocity similar to gravitation, the obtained increase is a factor of 1.4 ± 0.2 , which is smaller than the increase of 1.9 ± 0.3 that was found in experiments (Figure 3.8a). Compared to the simulations, the experimental system however exhibits (i) non-spherical targets, namely antibodies which have a flexible structure allowing a dynamic configuration; (ii) magnetic particles with surface irregularities ranging from $10^1 - 10^2$ nm in size (see Appendix 3.F); (iii) specific interactions that may act on a longer range than a hard-sphere collision. All these factors can possibly influence the near-surface alignment process during the encounter. In spite of neglecting these factors, the simulated improvement comes close to the experimental values and thereby shows that the enhancement in the capture rate can be understood from the physical transport processes of the particles and the targets in the fluid. By actively moving particles through the fluid, the capture rate increases. From this it follows that more encounters occur between targets and magnetic particles and thus that the target concentration becomes depleted near the particle surface.

Having shown that local target depletion plays an important role in the capture of proteins using magnetic particles; in the following Sections we study the influence of different actuation parameters and the particle concentration on the achievable target capture rate.

3.3.4 Influence of field rotation parameters

We investigated the influence of chain rotation on the capture rate. In a rotating magnetic field, magnetic particles form into chains and experience a magnetic torque to align the chains with the (rotating) field. The magnetic torque is countered by hydrodynamic drag, and depending on the ratio of these interactions the chains either follow the rotating field or not. This particular behavior is typically characterized by the dimensionless Mason number²¹:

$$\text{Ma} = \frac{\eta\omega}{\mu_0 MH} \equiv \frac{4\pi R_{MP}^3 \eta\omega}{3mB} . \quad (3.5)$$

For high Mason numbers, chains show breaking-and-reformation behavior, inducing chaotic fluid mixing.^{21, 47} Optimal mixing effects have been reported^{21, 74} to occur when chains show breaking-and-reformation behavior with relatively long chain fragments. In case rotating chains remain rigid, no chaotic mixing is induced (see section 3.3.1); and when the fragmented chains are short, mixing is only efficient close to the original chain.

We have quantified association rate constants for different Mason numbers by varying the magnetic field strength and by varying the rotation frequency of the rotating field. For increasing field strength, see Figure 3.9a,b, longer chains are formed and the association rate constant is the highest for the maximum field strength that can be generated. While the chain length influences the volume that is mixed, it is not represented within the Mason number.⁴¹ Furthermore, the Mason number is de-

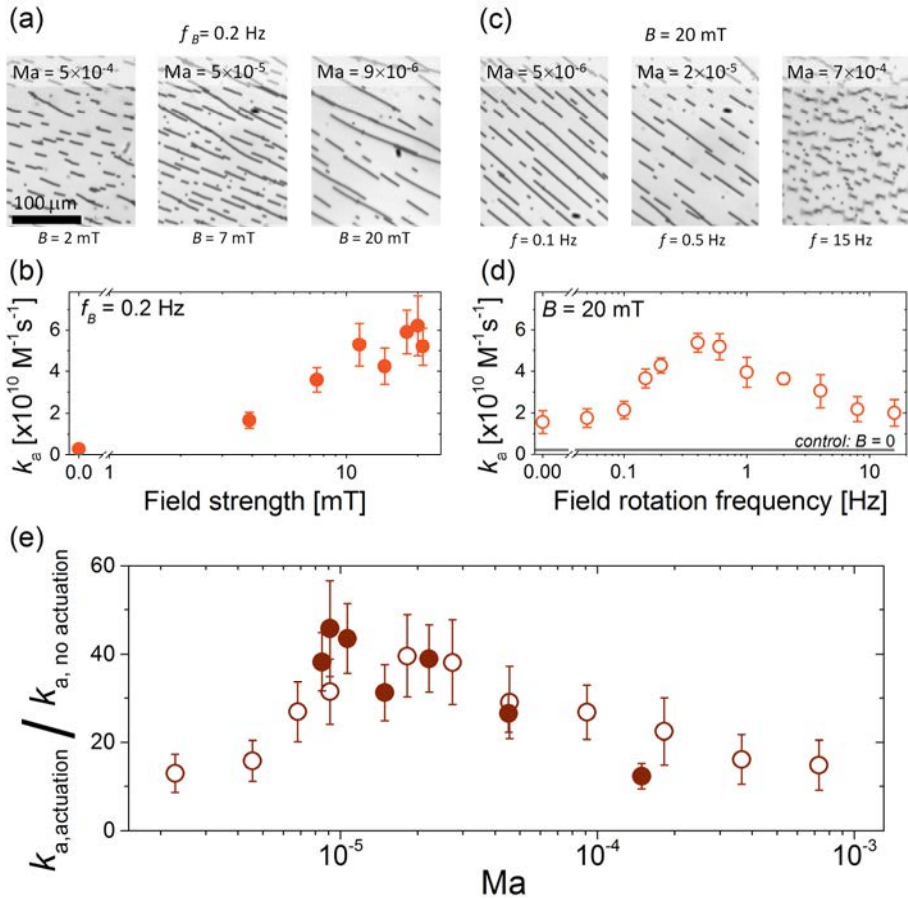


Figure 3.9 Target capture by magnetically actuated ensembles of magnetic particles for different field rotation frequencies ω and magnetic field strengths B . (a) Microscope images of particle chains for varying B and $\omega = 0.2$ Hz. (b) The corresponding association rate constants. (c) Microscope images of particle chains for varying ω and $B = 20$ mT. (d) The corresponding association rate constants. (e) Relative increase in k_a compared to no actuation for different Mason numbers, as corresponding to data in panel b and d, respectively represented by the closed circles (●) and the open circles (○). The applied field rotation was alternated in-plane and out-of-plane.

finned for an isolated chain of particles, whereas in our experiments the chains interact with other chains and become longer if the field strength is increased. As longer chains mix over a larger volume, it is reasonable why k_a is the highest for the highest field strength.

For varying rotation frequencies of the magnetic field (see Figure 3.9c,d), we do observe that an intermediate field rotation frequency is the most optimal for rapid target capture. For larger frequencies, particle chains remain relatively short (see Figure 3.9c; similar to low field strengths) and show less mixing²¹. For lower frequencies, the formation of longer chains is observed (see Figure 3.9c; similar to high field strengths). In this case however, k_a decreases. This is reasonable considering

that in the limit of $\omega = 0$ no mixing is induced. Rotation of the particle chain will only be effective when the particle displacement is large compared to the diffusion of the targets. Also this aspect is not reflected in the Mason number, but it is in the Péclet number, being the ratio between advective transport and diffusive transport. For a chain with a length of 15 ± 5 particles, random diffusion over a similar length is achieved in a time period corresponding to a field rotation frequency of 0.06 ± 0.04 Hz. Below this frequency, chain rotation is not effective anymore to enhance the capture rate. Consequently, the optimal field frequency is governed by a balance between on the one hand the rate of mixing and on the other hand the mixed volume. This implies that the frequency should not be too low or too high, but intermediate.

In Figure 3.9e, the relative increase in k_a with respect to no actuation is plotted for the combined data-sets of varying B and ω , but now expressed in terms of the corresponding Mason numbers (Eq. 3.5). The different datasets are found to show considerable overlap, indicating that the Mason number is still useful to roughly assess the capture behavior of rotating particle chains in spite of neglecting the influence of the chain length and diffusion. Figure 3.9e shows an apparent optimal capture regime at a Mason number of $(1.8 \pm 1.0) \times 10^{-5}$, with an increase in capture rate by a factor 40 ± 10 . Using 2D-simulations on isolated chains consisting of 17 particles, Kang et al.²¹ found optimal mixing at a higher $Ma = 0.002$. First of all, the inserted parameters were different, as for example the particle susceptibility was assumed to be constant, while at a field strength of 10 mT, the particle magnetization shows saturation behavior¹⁶⁷. From this it follows that the susceptibility (represented in M in Eq. 6.5) decreases with increasing field strength. More noteworthy is the fact that the optimal Ma in the simulations corresponded to the lowest value for which breaking-and-reformation behavior of the particle chain was observed. As was also mentioned in the paper, larger particle chain would still exhibit breaking-and-reformation behavior below $Ma = 0.002$, resulting in a lower optimal Ma . In our experiments, particle chains are not isolated, and interact with other chains. As a result particle chains show breaking-and-reformation behavior below $Ma = 0.002$, which may explain why optimal capture is observed at lower Mason numbers.

3.3.5 Influence of the magnetic particle concentration

In Figure 3.10 we show how the association rate constant depends on the concentration of magnetic particles in the fluid. As shown in Figure 3.10a, we only applied particle concentrations below a full coverage of the surface of the incubation chamber. As shown in Figure 3.10b, without magnetic actuation, the k_a is roughly the same at low particle concentrations. Above a certain threshold, the k_a becomes smaller with increasing particle concentration. This behavior is similar as previously observed⁵⁷ for a different experimental model system comprising \varnothing 200 nm fluorescent particles as targets (see Chapter 2). For low particle concentrations, it was found that the reaction reached a steady-state in which the concentration gradient or depletion zone around each particle is constant in time. As long as particles are sufficiently separated – i.e., at low particle concentrations – these concentration gradients or depletion zones do not overlap and the k_a remains unaffected by the particle concentration. As soon as these depletions zones start to overlap – i.e. at higher par-

particle concentrations – the depletion zones will expand further, thereby reducing k_a , either until a new steady-state is obtained, or when the volume is depleted of targets. From Figure 3.10b, we find that the k_a drops starting at a concentration of $\sim 2 \times 10^3$

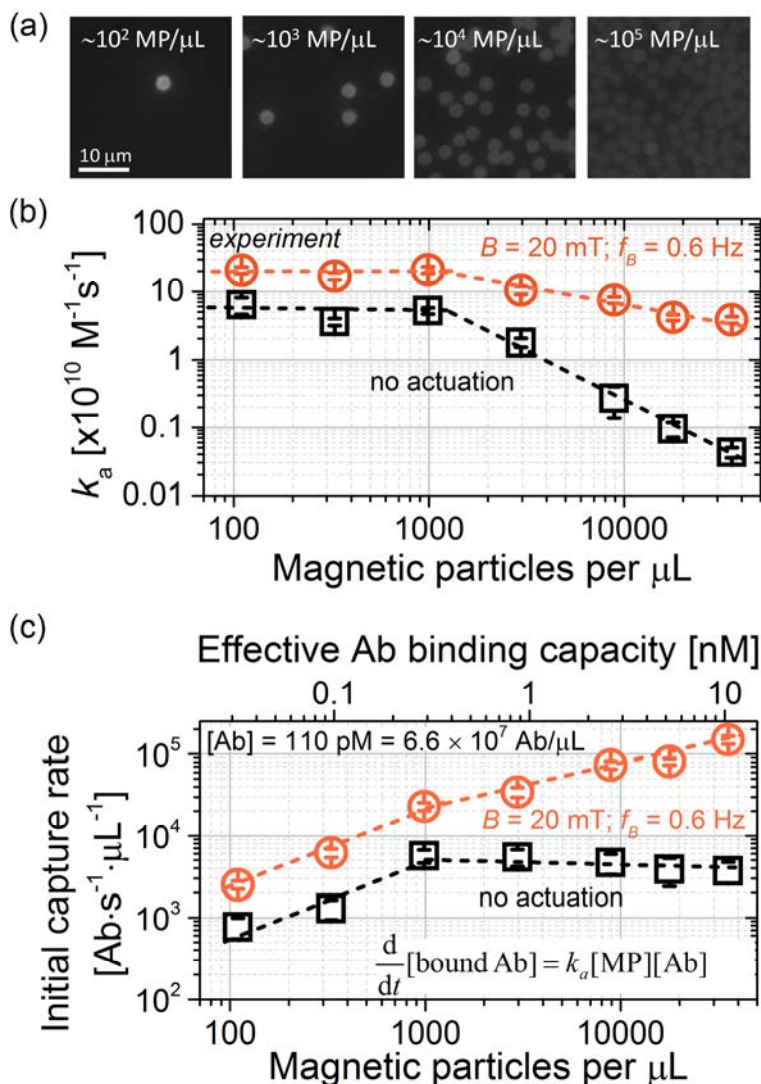


Figure 3.10 Target capture by magnetically actuated ensembles of magnetic particles for varying magnetic particle concentration. (a) Fluorescence microscopy images of magnetic particles after 30 min of incubation without actuation. (b) Experimentally determined association rate constant with and without actuation ($B = 20 \text{ mT}$; $\omega = 0.6 \text{ Hz}$; alternated in-plane and out-of-plane rotation). Using this data, we compute (c) the antibody capture rate per μL at short times for an antibody concentration of 110 pM. On the top x-axis the corresponding binding capacity is plotted (see Section 3.2.1). The dashed lines are drawn to guide the eye.

particles/ μL . For a sample volume of $36 \mu\text{L}$, sedimented particles will on average be separated by about $20 \mu\text{m}$. As follows from the steady-state solution of the diffusion equation for an absorbing particle (see Figure 2.3d)⁵⁷, at half this distance the target concentration is $\sim 86\%$. Particles that are separated by less than $20 \mu\text{m}$ will therefore show partial overlap of their depletion zones and have a reduced association rate constant.

This effect is also observed in case particles are magnetically actuated (see Figure 3.10b). Compared to no actuation, an elevated k_a is found for all particle concentrations. Furthermore, the threshold in particle concentration above which the k_a starts to decrease, is found to be the same for both cases, but the decrease is less strong in case of magnetic actuation. The effect of magnetic actuation becomes clearer when considering the antibody capture rate at short incubation times (see Figure 3.10c). For low particle concentrations, the capture rate is found to increase with increasing particle concentration. As soon as the depletion zones start to overlap, no actuation leads to constant capture rates, whereas magnetic actuation enhances the capture rate with increasing particle concentration. Interestingly, the results in Figure 3.10c demonstrate that magnetic particle actuation achieves similar or even higher capture rates with fewer particles.

From the values of k_a in Figure 3.10, we quantified the increase in the target capture rate, as shown in Figure 3.11a. Magnetic actuation has the highest impact at high particle concentrations, when depletion is the strongest. In this regime, the capture rate can be improved by 1 to 2 orders of magnitude. For low particle concentrations, we find an increase in the capture rate of 3 ± 1 by actuating the particles, showing also for isolated particles that movement through the fluid enhances the encounter rate. For a part, this increase can be attributed to the presence of a nearby surface in case of no actuation (compare Section 2.4.1). Yet the steady-state solution of the diffusion equation¹⁴⁵ clearly shows that individual particles form a depletion zone near their surface. In case that the binding probability of an encounter is equal to unity, the target concentration $c(r)$ depends on the radial distance $r \in [R, \infty)$ from the particle center as $c(r) = c(\infty) \cdot (1 - R/r)$ with R the encounter radius of the target and the particle. For the system studied here, the binding probability is less than unity, since $k_a < k_{\text{dif}}$ (see Eq. 3.4). Consequently, depletion zones are expected to be smaller in amplitude, but enhanced particle-fluid interactions will still have a reducing effect on the depletion zones and thereby improve the capture rate.

To analyze experimental data quantitatively, target capture was simulated for different particle concentrations by varying the width of the simulated fluid cell (see Appendix 3.E). Due to the applied periodic boundary conditions, particles are distributed in a square lattice. Actuation of the particles consisted only of linear translation of particles upwards and downwards through the fluid volume, corresponding to the application of a field gradient, but without magnetic dipole-dipole interactions between the particles. As shown in Figure 3.11b, a similar threshold behavior is obtained in simulations as was found in the experimental data shown in panel a. The simulated improvements in the capture rate are less, as was expected for actuation consisting only of particle translation. Comparing the k_a determined for (i) translation and (ii) combined translation and rotation in Figure 3.7c, it is found that the k_a

of the latter is higher than the k_a of the former by a factor of 4 ± 2 . A similar difference is obtained when comparing the data in panels a and b of Figure 3.11. We therefore conclude that numerical simulations confirm the increase in the capture rate that is possible by magnetic actuation.

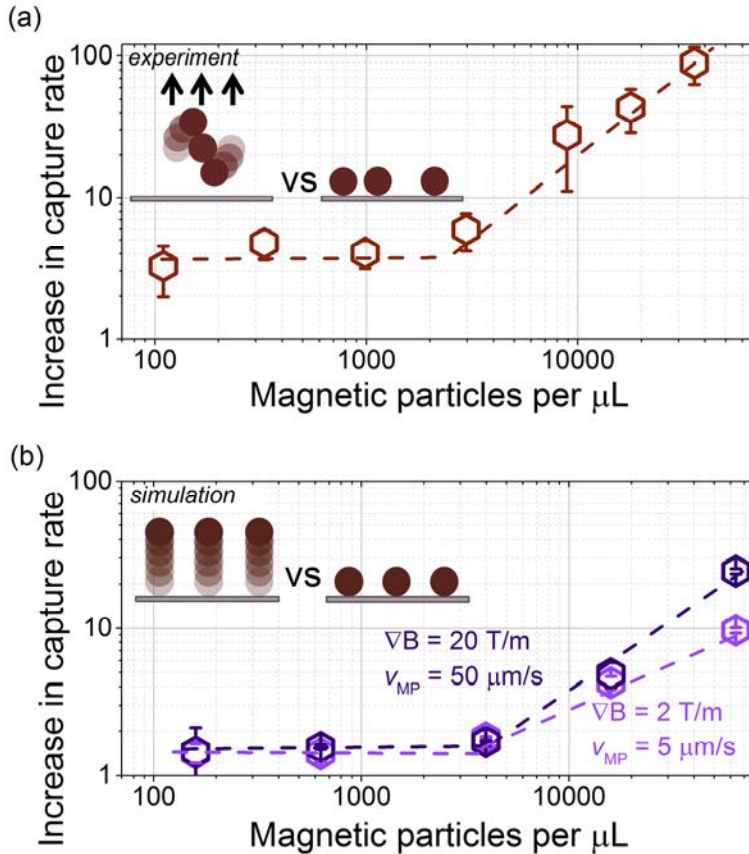


Figure 3.11 Relative increase in capture rate as found (a) in experiments on the magnetic actuation of ensembles of particles as shown in Figure 3.10; and (b) in simulations on the linear translation of single particles through the sample volume (for two different field gradients). The dashed lines are drawn to guide the eye.

3.5 Conclusions

In summary, we investigated the use of magnetic particles for affinity capture of biological targets from a fluid. Target capture becomes very efficient when magnetic particles are functionalized with a high density of specific binding sites on their surface. We have shown that, as a result, depletion zones form near the particles, especially at elevated particle concentrations. To maintain high capture rates, depletion can be reduced by magnetically actuating the magnetic particles to enhance the particle-fluid interaction. We have shown that magnetic actuation is most effective

when magnetic field gradients and rotating fields are combined to translate and rotate magnetic particle chains in the fluid. Using experiments, we quantified that magnetic actuation can increase association rate constants by one or two orders of magnitude. Using numerical Brownian dynamics simulations, we confirmed experimental observations and showed that detailed information can be obtained on the binding process, such as the relative orientation that is required to bind. We have also shown that optimal target capture is achieved for low Mason numbers as long as the Péclet number is sufficiently high ($Pe > 1$). Lastly, for higher particle concentrations, magnetic actuation becomes increasingly more effective, as local depletion of targets plays a larger role.

The improvement in the protein capture rate was quantified in a model system comprising 2.8 μm sized magnetic particles. These particles show significant sedimentation when not actuated. Smaller particles also show sedimentation. By calculating the barometric height for particles with a radius $R_{\text{MP}} \geq 100$ nm and a volumetric mass density equal to the particles used in this study (i.e., 1.4×10^3 kg/m^3 according to the manufacturer's specifications), we estimate that most particles will be present in a layer near the surface with a height $h \leq 100$ μm . For magnetic particles with such sizes, we therefore expect that actuated movement of the particles through the solution can enhance the capture rate, because magnetic actuation can be used to bring the layer of particles to regions where almost no particles are present. As most magnetic particle-based assays that have been reported^{9, 13, 25, 82, 103, 114} employ particles with diameters ranging from 500 nm to several micrometers, magnetic actuation for target capture is very relevant to accelerate microfluidic assays.

Both experiments and numerical calculations show that magnetic actuation most effectively enhances target capture at high particle concentrations. However, in a complete detection assay, high concentrations of particles hinder further processing steps, like bond-formation at a sensor surface, or detection. Therefore, by balancing high capture kinetics with minimal hindrance of further processing steps, we assume that particle concentrations are optimal when not far below a full coverage of the detection surface. For such concentrations, we have shown that magnetic actuation can improve the capture kinetics by almost two orders of magnitude. In many reported assays based on magnetic particles^{9, 13, 25, 103, 114}, particle concentrations are larger by at least two orders of magnitude compared to the highest concentration we studied here (i.e., $\sim 4 \times 10^4$ particles/ μL). The application of magnetic actuation for target capture should make it possible to lower the particle concentration and reduce their negative effects, while maintaining or even increasing the capture efficiency. As a result, assay performances can potentially be significantly improved.

In this study, the capture kinetics was quantified by determining association rate constants. To enable close comparison with other techniques, we believe that quantifying rate constants is the most reliable method as it allows a deep insight in the capture process. In addition, different actuation methodologies would be directly comparable if a standard assay would be used. The model system used in this study is suitable for that, as the protein G-IgG complex is well-studied and commonly

used.^{164, 168-169} If the target molecule is already labeled, target capture can be measured in a direct way and further fluid handling steps are avoided.

The particle-protein system used in this Chapter can be useful to further bridge the gap between experimental and theoretical research on biological association kinetics. As shown, theoretical modeling is facilitated by the relatively well-defined geometry of one of the reacting species, but also by the fact that a microparticle can bind many targets. Combined with experiments, we expect that insights can be obtained on various binding properties of proteins, such as: association and dissociation rate constants (for different types of immobilizations); the number of binding sites; binding orientations; the influence of long-range interactions (such as electrostatics), etc.

Dynamic magnetic particle actuation for target capture is of particular interest for improving lab-on-a-chip applications. The methods can be applied not only for the capture of proteins, but also for small molecules, nucleic acids, or cells. Compared to other microfluidic capture methods that require the generation of fluid flow^{28, 62, 83}, mechanical movement of magnets^{50, 81} or of fluid containers⁷⁴ to enhance particle-fluid interaction, the magnetic actuation proposed in this Chapter requires only stationary electromagnets and a current controller. In this way, an instrument-cartridge system is possible in which the instrument contains the actuation technology, while the disposable cartridge can be relatively simple. Therefore, we expect that magnetic actuation will enable fast-operating, fully integrated and cost-effective biosensing systems with high sensitivity.

Throughout history, dense concentrations of colloidal or granular particles have been applied for the rapid and efficient extraction of target material from complex fluid mixtures. In medical applications, such particles can be used to effectively capture analytical targets from complex biological fluids. However, the use of high particle concentrations in these applications complicates downstream processing of the captured targets. By making the particles magnetically responsive and manipulating them with magnetic fields, we have shown that it is possible to achieve similar or even higher extraction rates with dilute particle suspensions. So, magnetic particle actuation leads to fast capture kinetics and facilitates carrying out the further processing steps in a diagnostic assay. With the fundamental suitability to extract target analytes from a fluid, and the practical suitability for integrated lab-on-chip diagnostic testing, we believe that magnetic particles will have a significant impact on future medical technologies.

3.6 Appendix

3.A Field calibration of the 5-pole electromagnet

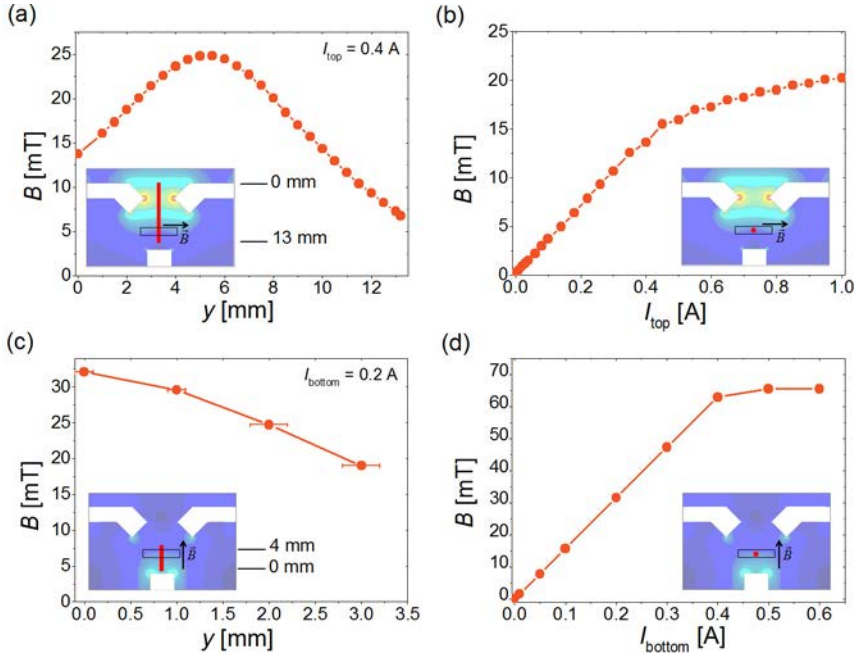


Figure A.1 Field calibration data of the 5-pole electromagnet measured using a Gauss meter (F.W. Bell). In each calibration figure the inset shows a cross-section of the electromagnets (showing two top magnets and the bottom magnet). The cross-sectional views show the position (red rectangles) and the component (black arrows) of the measured field. The location of the incubation chamber is indicated by the black open rectangle. In the background of the cross-sectional views, the (relative) field strength is plotted (following a heat color map) as obtained from simulations using Comsol Multiphysics. The following field calibrations are shown in the different panels: (a) In-plane field dependence of the distance from the top magnets for the case two opposite top magnets are powered in series at $I_{top} = 0.4$ A. (b) The in-plane field dependence to the current I_{top} at the position of the incubation chamber, for the case two opposite top magnets are powered in series. (c) Dependence of the out-of-plane field to the distance from the bottom magnet for the case that only the bottom magnet is powered at $I_{bottom} = 0.2$ A. (d) Dependence of the out-of-plane field to the current I_{bottom} at the position of the incubation chamber, for the case that only the bottom magnet is powered.

3.B Rotaphoresis to redistribute particles

To overcome the effects of particle drift and particle aggregation during actuation, we applied the method of magnetic rotaphoresis as is described in detail in chapter 6. Here, we will shortly summarize the applied fields and the effects.

Basically, the rotaphoretic protocol that was applied consisted of the following elements: (i) a field gradient of ~ 4 T/m oriented towards the surface, in order to bring and keep particles close to the surface (x,y -plane); (ii) a magnetic field rotating

out-of-plane (e.g. x,z -plane) with respect to the surface at 20 Hz, with an out-of-plane (z) component of 15 mT and an in-plane (x) component of 6 mT; (iii) an alternating magnetic field orthogonal to the applied rotating field, e.g. in the y -direction in case the field rotates in the x,z -plane. The effect of such a protocol on magnetic

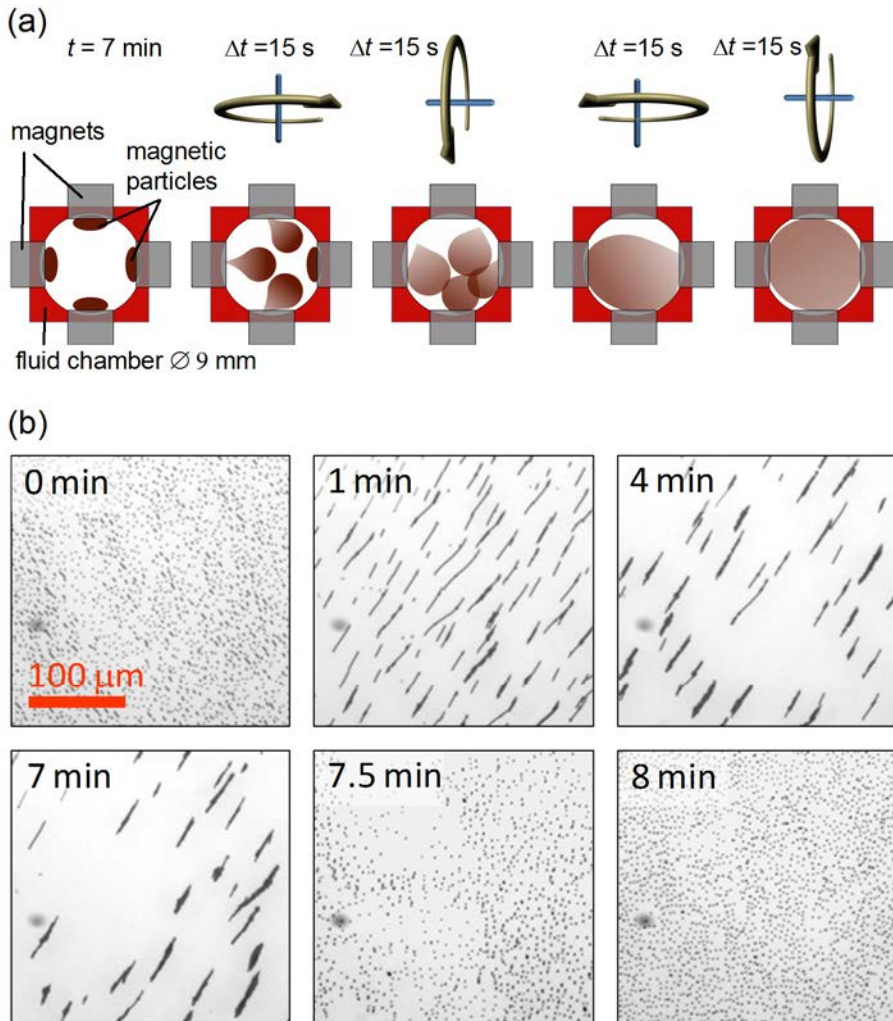


Figure B.1 Overview of the applied rotaphoresis to redistribute particles over the bottom surface of the incubation chamber after magnetic actuation for target capture. (a) Schematic representation of the applied actuation protocol and the effect on the particle distribution (from left to right), in case initially all particles (brown) are collected at the magnets (gray) on all four sides. As indicated by the arrows, rotaphoresis was applied towards each magnet for 15 seconds to move all particles away from the side of the incubation chamber. (b) Microscope images of magnetic chain actuation followed after 7 minutes by particle redistribution by rotaphoresis. The used microscope objective magnification was 10 times and images of the bottom-center of the incubation chamber were taken by a Redlake MotionPro X3 high speed camera. At $t = 0$ min, magnetic field of 10 mT was applied, rotating in-plane with respect to the surface at a frequency of 0.1 Hz. At $t = 7$ min, rotaphoresis was applied for 1 minute: 15 seconds in each direction in-plane.

particles is the following. Chains of particles traverse or “walk” over the surface in the direction depending on the rotation of the magnetic field. The velocity of the particle chains depends on their size: larger chains move faster than smaller chains, and separate particles are nearly immobile. Furthermore, due to the hydrodynamic drag and the normal forces from the surface, particle chains break up in smaller chains, and eventually most particles split up in separate particles. Finally, as the out-of-plane (z) component of the magnetic field with respect to the surface is larger than the in-plane components, separate particles will repel each other more strongly than that they will attract each other when the field is oriented in-plane. This effect prevents redistributed particles to reform into chains while the rotaphoresis protocol is applied.

Lastly, in order to redisperse particles from all magnet poles back into the incubation chamber and over the whole bottom surface, the rotaphoretic protocol was applied in all directions (in-plane; see Figure B.1a). More specifically, rotaphoresis was applied to first move particles consecutively in the $+x$ -direction, the $-y$ -direction, the $-x$ -direction and the $+y$ -direction. Rotaphoresis was applied for 15 seconds in each direction, resulting in a total time of 1 minute to redistribute particles over the surface.

In Figure B.1b, snapshots are shown of a magnetic actuation protocol that first consists of magnetic chain actuation for target capture (i.e. for the first 7 minutes), followed by one minute of rotaphoresis. As shown, magnetic chain actuation first causes particles to form chain-like aggregates that drift away from the center of the incubation chamber. Application of the above-described rotaphoresis protocol causes a complete redistribution of the particles over the surface.

3.C The mixing index

To quantify the mixing induced by rotating particle chains at a dye-water interface (see Figure C.1), we used a mixing index⁴³, Mi . The mixing index is scaled between 0 and 1, i.e., in a perfectly mixed system $Mi = 0$, while in an unmixed system $Mi = 1$. The mixing index is defined as the ratio of the variance and the average of the fluid fluorescent intensities:

$$Mi = \frac{\frac{1}{N} \sum_N \left(I_k - \frac{\sum_N I_k}{N} \right)^2}{\left(\frac{\sum_N I_k}{N} \right)^2} = \frac{\text{var}(I)}{\bar{I}^2}, \quad (\text{C.1})$$

The term I_k is the fluorescent intensity at a pixel k , and I is the average over N pixels corresponding to the fluid confined within the rotational range of the chain. The volumetric boundary in which the mixing of a dye-water interface was investigated is restricted to the rotational plane of the magnetic particle chain, i.e., the focal plane of the microscope. However, the extracted fluorescence intensities, I , used to characterize the corresponding mixing, Mi , do have fluorescence interferences from above and below the focal plane of the microscope. Nevertheless, these interferences occur for both the rigid and break and reform regimes which still allow us to use this approach to characterize the differences in mixing between these two regimes. Moreo-

ver, both actuation regimes are conducted under similar experimental conditions, i.e., a single and isolated rotating magnetic particle chain with no magnetic particle chains above and below the rotational plane of the corresponding particle chain.

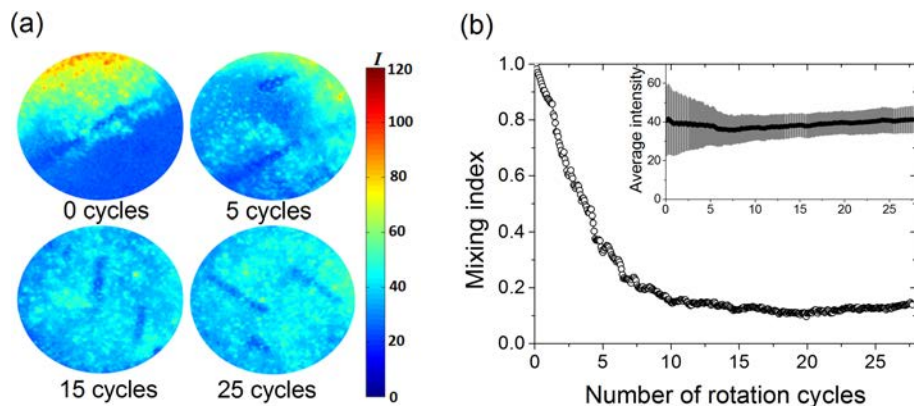


Figure C.1 Quantifying fluid mixing induced by the alternating topological changes of a rotating magnetic particle chain. (a) The mixing of a dye-water system is shown qualitatively. The color bar indicates the emitted intensity of the fluorescent dye. (b) Mixing index as a function of the field rotational cycles. In the inset, the average fluorescence intensity of the fluid is shown along with the standard deviations.

3.D Comparison of particle-based capture with planar surface assays

It is insightful to compare the kinetic analysis of particle-based target capture to a technique that is typically used to quantify rate constants of biomolecular reactions, namely surface plasmon resonance (SPR).¹⁷⁰ In SPR, targets are captured from a fluid flow by biomolecules which are immobilized on a planar sensor surface. This process has similarities to target capture by actuated magnetic particles. Conversely, no magnetic actuation corresponds to SPR without a fluid flow, which generally results in the formation of target depletion zones near the sensor surface. Concerning the assay kinetics in SPR (i.e., with a fluid flow), the concentration of targets in solution is dominant over the number of binding sites on the solid phase, in contrast to our experiments, where targets are only few compared to the number that can be bound in total by the magnetic particles. As a result, in SPR analysis an equation is used other than Eq. 3.2, because the exponential behavior in SPR depends on the target concentration instead of the concentration of magnetic particles or binding sites; i.e., [MP] should be replaced by [Ab].

SPR data allow one to determine rate constants without quantifying the number of binding sites on the bio-functionalized surface. It should be noted however, that the determined rate constants do not completely represent the rate constants of the bimolecular reaction free in solution. For example, the fact that and the way in which biomolecules are attached to the surface affect the rate constants, but also the application of a fluid flow has an effect on the encounter rate.

In the current study, we are not primarily interested in the bimolecular association rate between the targets and the proteins immobilized on the particle surface. Instead, we are primarily interested in the association rate between targets and a magnetic particle. This association process is made selective by using proteins with a particular specificity to the targets. Here, the bimolecular association rate plays a role, but other factors are equally important, such as the density of capture proteins and the way in which they are immobilized on the particle surface. For example, the capture rate will be high in case capture proteins are present at a high density with their binding sites oriented towards the fluid, compared to the case that only few capture proteins are present and have their binding sites oriented in-plane with respect to the particle surface. These aspects, including the bimolecular association rate constant, are all reflected by the (particle-based) association rate constants determined in our experiments.

3.E Brownian dynamics simulation of the capture process

The particle-based capture process was numerically simulated using Brownian dynamics.

We simulated the dynamics in a rectangular fluid cell with a variable width (e.g., 100 μm) and a height equal to the experimental incubation chamber, namely 600 μm . The fluid cell contains a single spherical magnetic particle with a radius of 1.4 μm that is moved up and down through the fluid cell at different velocities due to an applied field gradient, i.e.

$$V_{\text{MP}} = \frac{m}{6\pi\eta R_{\text{MP}}} \frac{dB}{dz}. \quad (\text{D.1})$$

Here, m is the magnetic moment of the particle,¹⁶⁷ η the dynamic viscosity of the fluid and R_{MP} is the radius of the magnetic particle. As targets, spherical particles were assumed with a hydrodynamic radius of $R_{\text{IgG}} = 5.5$ nm which is equal to the reported hydrodynamic radius of antibodies in PBS.¹⁶⁵ Initially, these particles are randomly distributed over the simulated volume and for each particle we compute the random displacement and rotation due to Brownian motion as well as hydrodynamic interactions due to the movement of the magnetic particle through the fluid. Interactions between the target particles were neglected because target concentrations are dilute.

The random displacement of target particles in all directions, $\Delta\mathbf{r}$, corresponding to Brownian motion over a discrete timestep Δt follows from the fluctuation-dissipation theorem: (e.g. see Grassia et al.¹⁵⁴)

$$\Delta\mathbf{r}_i = \mathbf{n}_{\text{rand},3} \sqrt{\frac{24k_{\text{B}}T}{6\pi\eta R_{\text{IgG}}}} \Delta t, \quad (\text{D.2})$$

in which $\mathbf{n}_{\text{rand},3}$ is a 1x3 vector with random numbers, chosen independently at each numerical time-step from a normalized Gaussian distribution with zero mean and

variance 12^{-1} . Similarly, we also compute the orientation, i.e., $\theta \in [0, \pi]$ and $\varphi [-\pi, \pi)$, of each target, which is subjected to Brownian rotation about three axes (x , y and z):

$$\Delta \mathbf{a} = \mathbf{n}_{\text{rand},3} \sqrt{\frac{24k_B T}{8\pi\eta R_{\text{lgG}}^3} \Delta t} \cdot \quad (\text{D.3})$$

Hydrodynamic interactions acting on targets due to the moving magnetic particle are accounted by computing the flow field \mathbf{u} due to a sphere moving through a fluid, i.e.¹⁶⁶

$$\mathbf{u} = \frac{1}{8\pi\eta\Delta r} \left[\left(\mathbf{F} + \frac{(\Delta \mathbf{r} \cdot \mathbf{F}) \Delta \mathbf{r}}{\Delta r^2} \right) + \frac{R_{\text{MP}}^2}{\Delta r^2} \left(\frac{1}{3} \mathbf{F} + \frac{(\Delta \mathbf{r} \cdot \mathbf{F}) \Delta \mathbf{r}}{\Delta r^2} \right) \right]. \quad (\text{D.4})$$

Here, $\Delta \mathbf{r}$ is the center-to-center distance between the target and the magnetic particle, and \mathbf{F} is the force acting on the magnetic particle, which is the magnetic gradient force. Based on the small size of the target particles we assume that the target particles are dragged along with the induced flow.

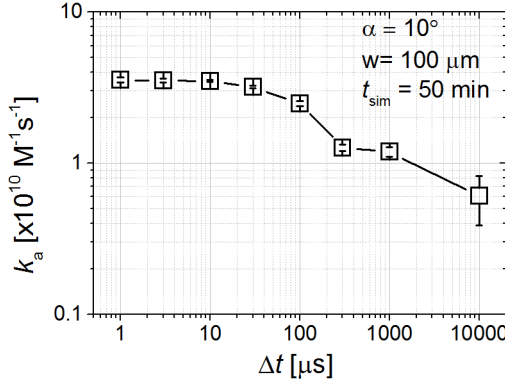


Figure E.1 Influence of the numerical time-step on the association rate constant as obtained from least-squares linear fits to simulated binding data. For time-steps below 10 μs , the found association rate constant does not depend on the time-step anymore.

In the simulations, the following boundary conditions were applied to a rectangular unit cell with a height of 600 μm , and width and length of 100 μm . To the top and the bottom of the cell, reflective boundary conditions were applied representing the boundaries of the incubation chamber. To the sides, periodic boundary conditions were applied. Considering that one magnetic particle is initially situated in the bottom center of the unit cell, the periodic boundary conditions imply a periodicity of particles over the surface. Basically, the particles are ordered in a square lattice with a unit cell with a width of 100 μm . As a result, varying the width of the unit cell alters the initial concentration of particles at the surface. Lastly, the boundary of

the magnetic particle is treated as being partially absorbing, i.e. binding only occurs for angular differences smaller than a pre-defined angle $\alpha \in [0, \pi]$ between (i) the orientation vector of the target and (ii) the relative position vector between the particle and the target. In other words, the target needs to orient itself towards the magnetic particle to bind. In case $\alpha = \pi$, targets “bind” to the particle independent of their orientation. In case of $0 < \alpha < \pi$, targets only bind for a limited range of orientations, and otherwise reflect from the surface. In this way, constraints to the relative orientation can be imposed. Lastly, the time-steps were chosen to be $3 \mu\text{s}$, which is small enough to keep propagation errors negligible (see Figure E.1) which is important for a reliable outcome of a forward Euler method. So, for time-steps of $3 \mu\text{s}$, the outcome of the numerical simulations is independent of the time-step.

3.F SEM image of M270 magnetic particles

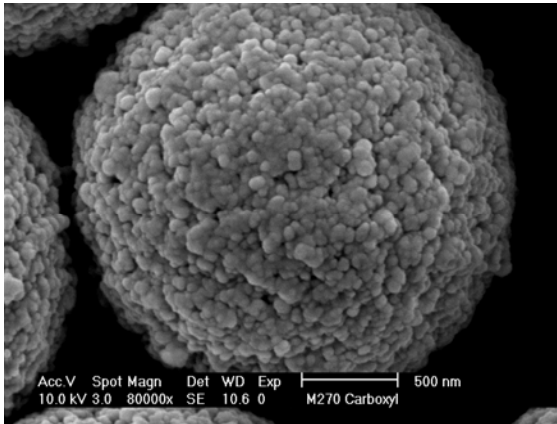


Figure F.1 Scanning electron microscope image of a Dynal M-270 superparamagnetic particle before protein G is covalently coupled to the carboxyl groups using EDC-NHS coupling chemistry. From these images we estimate that surface irregularities are sized ranging in between 10-200 nm.

4

Dynamics of Magnetic Particles near a Surface: Model and Experiments on Field-Induced Disaggregation

*Magnetic particles are widely being used in biological research and bioanalytical applications. As the corresponding tools are progressively being miniaturized and integrated, the understanding of particle dynamics and the control of particles down to the level of single particles become important. Here we describe a numerical model to simulate the dynamic behavior of ensembles of magnetic particles, taking account of magnetic inter-particle interactions, interactions with the liquid medium and solid surfaces, as well as thermal diffusive motion of the particles. The model is verified using experimental data of magnetic field-induced disaggregation of magnetic particle clusters near a physical surface, wherein the magnetic field properties, particle size, cluster size and cluster geometry were varied. The model clarifies how the cluster configuration, cluster alignment, magnitude of the field gradient, and the field repetition rate play a role in the particle disaggregation process. We demonstrate the disaggregation of large clusters of several tens of particles, within about one minute. We expect that the simulation model will be very useful for further in silico studies on magnetic particle dynamics in biotechnological tools.**

* Parts of this chapter have been published in: Y. Gao[†] and A. van Reenen[†], M.A. Hulsen, A.M. de Jong, M.W.J. Prins, and J.M.J den Toonder, Disaggregation of Microparticle Clusters by Magnetic Dipole-Dipole Repulsion near a Surface, *Lab on a Chip* **13**, 1394 (2013); and are in preparation for publication: A. van Reenen, Y. Gao, A.M. de Jong, M.A. Hulsen, J.M.J den Toonder, and M.W.J. Prins, Dynamics of Magnetic Particles near a Surface, Model and Experiments on Field-induced Disaggregation, *Phys Rev E*, accepted. [†]equal contributions

4.1 Introduction

Magnetic particles are widely applied in biosciences and *in vitro* diagnostics, mainly because such particles can be manipulated and interrogated by magnetic fields without perturbing the biological matter under study.^{9, 18, 22, 25, 103, 132, 171} To get a high total effective surface area for biological binding and processing, the assays are always performed with ensembles consisting of many individual magnetic particles. With the advent of novel experimental techniques to actuate and detect magnetic particles^{25, 47, 50, 62, 103, 115, 130}, on the level of ensembles as well as on the level of individual particles, and with the advent of corresponding miniaturized microfluidic devices^{25, 50, 81, 99, 103}, the need appears to understand and predict the behavior of magnetic particles in variable configurations. Yet it is difficult to model and predict the dynamics of particle ensembles because the behavior of the particle ensemble is not simply an extrapolation of the behavior of single particles, due to the strong magnetic interactions between the particles¹⁷², the hydrodynamic interactions between the particles¹⁷²⁻¹⁷³, and the interactions between the particles and microdevice surfaces^{25, 115, 147}. To avoid tedious experimentation and trial-and-error studies, it is important to develop modeling tools for *in silico* studies of the behavior of particles in time-varying magnetic fields and complex device geometries.

Here, we propose a model and a numerical approach to simulate magnetic particle dynamics at a fundamental level. The model integrates the known basic interactions that have already been studied separately, namely Brownian motion¹⁷⁴, magnetic gradient forces¹⁷⁵⁻¹⁷⁶, magnetic dipole-dipole interactions^{25, 119} and particle surface interactions^{25, 115, 174}.

To evaluate the proposed numerical model, we compare it to a novel method to magnetically disaggregate clusters of magnetic particles (see Figure 4.1): by first aligning particle-clusters at a physical surface (Figure 4.1a,b) and by subsequently inducing repulsive magnetic dipole-dipole interactions between the particles which separates the particles (Figure 4.1c). Using this technique, we show that clusters can be disaggregated which consist of several tens of particles.

In this study, we compare the experimental data to simulated data, and we use the numerical model to study the influence of underlying parameters such as the cluster configuration and the particle size. In this way, a fundamental understanding

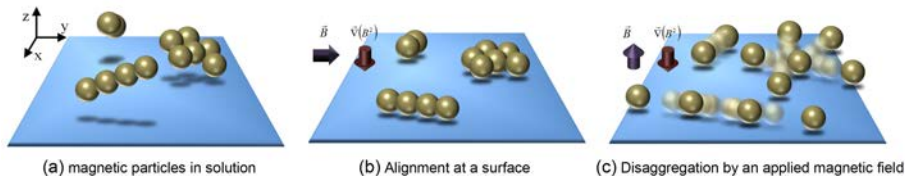


Figure 4.1 Schematic disaggregation of magnetic particle clusters. (a) Clustered groups of magnetic particles are present in solution and (b) are drawn to a physical surface by means of a field gradient. A horizontal magnetic field is applied to optimize parallel alignment of the clusters with the surface. (c) Application of a vertical magnetic field oriented orthogonal to the surface in combination with a field gradient results in breaking of the particle clusters by magnetic dipole-dipole repulsion.

of field-based disaggregation is obtained and criteria are identified for optimal functional performance. Finally, we discuss how the simulation of multi-particle dynamics can be broadly applied for the development of magnetic particle-based biotechnological tools.

4.2 Theoretical considerations

Ensembles of magnetic actuated magnetic particles were numerically simulated with Brownian dynamics using Matlab (Mathworks). The force on each Brownian particle consists of three terms: (i) a friction force which tends to decrease the energy of the particle, (ii) a random (Brownian motion) force which increases the energy of the particle and (iii) a systematic force due to the interaction potential energy between Brownian particles plus any external forces.¹⁷⁷ The Brownian dynamics simulation¹⁷⁷⁻¹⁷⁸ of an N -particle system involves integrating the following Langevin equation:

$$\frac{\partial}{\partial t} \mathbf{r} = \boldsymbol{\mu} \cdot \mathbf{F}_{\text{net}}(t) + k_B T (\nabla \cdot \boldsymbol{\mu}) + \mathbf{v}^{\text{ran}}(t), \quad (4.1)$$

where \mathbf{r} , \mathbf{F}_{net} , \mathbf{v}^{ran} are, respectively, the vectors containing the $3N$ coordinates of the particle positions, the forces acting on the particles and the random velocities of the particles due to Brownian motion. Furthermore, $\boldsymbol{\mu}$ is the $3N \times 3N$ translational mobility tensor, containing 3×3 blocks $\boldsymbol{\mu}_{ij}$ with $i, j = 1 \dots N$. The tensor $\boldsymbol{\mu}_{ij}$ is the mobility matrix approximated by the Rotne-Prager-Blake tensor¹⁷⁹. In particular, this tensor accounts for the hydrodynamic interactions of particles with other particles and the surface¹⁸⁰; for the explicit entries, see for example von Hansen *et al.*¹⁷⁹. The blocks $\boldsymbol{\mu}_{ii}$ correspond to the self-mobilities of the particles and are diagonal matrices whereas the other blocks $\boldsymbol{\mu}_{ij}$ with $i \neq j$ correspond to the hydrodynamic interactions between particles i and j . Note that the mobility tensor relates to the Diffusion tensor via $\mathbf{D} = k_B T \cdot \boldsymbol{\mu}$, with $k_B T$ being the Boltzmann factor. Lastly, the second factor on the right-hand side of Eq. 4.1 compensates for the spatial variation in the particle mobility due to the Brownian motion^{154, 179}.

Next, we describe expressions for the basic physical forces in the system, namely magnetic dipole-dipole interactions, magnetic gradient forces, excluded volume forces, and random thermal excitations (Brownian motion). The expressions are adapted to the process of magnetic field-based disaggregation of magnetic particles, as sketched in Figure 4.2.

In an external magnetic field \mathbf{H} superparamagnetic particles become magnetized and obtain a magnetic moment: $\mathbf{m} = V\chi\mathbf{H}$, which depends on the volume V and the magnetic susceptibility of the particle χ . In case multiple, N , particles are present, the magnetic dipole-dipole interaction force $\mathbf{F}_{\text{dd},i}$ acting on particle i is given by^{40, 172},

$$\mathbf{F}_{\text{dd},i} = \frac{3\mu_0}{4\pi} \sum_{j=1, j \neq i}^N \frac{m_i m_j}{r_{ij}^4} \left[\left(1 - 5(\hat{\mathbf{m}} \cdot \hat{\mathbf{r}}_{ij})^2 \right) \hat{\mathbf{r}}_{ij} + 2(\hat{\mathbf{m}} \cdot \hat{\mathbf{r}}_{ij}) \hat{\mathbf{m}} \right], \quad (4.2)$$

where m_i is the dipole moment of the i^{th} particle; $\hat{\mathbf{m}}$ is the unit vector of the magnetic moment, which is assumed to be aligned with the external field \mathbf{H} . Here we neglect the (minor) influence of other particles on the magnetic field; r_{ij} the distance between the centers of the i^{th} and j^{th} particles; and $\hat{\mathbf{r}}_{ij}$ its corresponding unit vector. Furthermore, we assume that a physical surface is present at $z = 0$. Both a magnetic field gradient that is oriented towards the physical surface and gravity result in an additional downward force on each particle:

$$\mathbf{F}_{\text{down},i} = \mathbf{F}_{\text{mg},i} + \mathbf{F}_{\text{buoyancy}} = \frac{V\mu_0\chi}{2} \frac{\partial H^2}{\partial z} \hat{\mathbf{e}}_z - V(\rho_{\text{particle}} - \rho_{\text{medium}})g \hat{\mathbf{e}}_z, \quad (4.3)$$

with ρ being the volumetric mass density and g the gravitational constant. In experiments, the gradient forces are generally much larger than buoyancy forces. Another advantage of gradient forces is that their magnitude and direction with respect to the surface can be controlled by the magnetic system.

To prevent the particles from crossing the physical boundary of the surface, reflecting boundary conditions were assumed. To model the hard core interactions between particles, excluded volume force formulations^{40, 172} are implemented. The excluded volume force is formulated such that (i) upon overlap of the particles, a repulsive force is exerted which increases exponentially for increased overlap; and (ii) if the particles are not touching each other, $r_{ij} > 2R$, the force is negligible with respect to other acting forces. Mathematically, the excluded volume force between the particles is formulated as⁴¹:

$$\mathbf{F}_{\text{ev},i} = 2 \frac{3\mu_0}{4\pi(2R)^4} \sum_{\substack{j=1 \\ j \neq i}}^N m_i m_j \exp \left[-\xi \left(\frac{r_{ij}}{2R} - 1 \right) \right] \hat{\mathbf{r}}_{ij}. \quad (4.4)$$

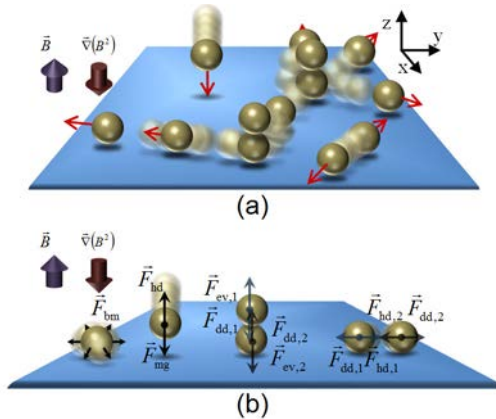


Figure 4.2 Overview of interactions of the magnetic particles. (a) Due to magnetic fields and magnetic field gradients, magnetic particles show dynamic behavior, interacting with the liquid, physical boundaries and other particles. (b) Magnetic particles undergo thermal collision forces (i.e. exhibit Brownian motion), hydrodynamic interactions, magnetic forces due to magnetic gradients and magnetic dipole-dipole interactions, which can be attractive or repulsive.

Here R is the particle radius. The parameter ξ determines at what strength this force acts at varying distances. We find that for $\xi = 3000$ the excluded volume force has a negligible effect on the computed particle movement in case particles are not in contact, as is explained in more detail in Appendix 4.A.

Lastly, the random thermal motion of the particles follows from the fluctuation-dissipation theorem^{154, 177, 179}:

$$\langle \Delta \mathbf{r}_i^{\text{ran}}(t) \Delta \mathbf{r}_j^{\text{ran}}(t) \rangle = 2k_B T \boldsymbol{\mu}_{ij} \delta t . \quad (4.5)$$

To obtain the random displacement $\Delta \mathbf{r}^{\text{ran}}$ for each particle, several mathematical approaches have been developed¹⁷⁸, of which we use the exact but time-demanding Cholesky decomposition. First, it is considered that the random displacement vector at any particular time and configuration of particles is equal to¹⁷⁸:

$$\Delta \mathbf{r}^{\text{ran}} = \sqrt{2\mathbf{B}} \cdot d\mathbf{w} , \quad (4.6)$$

with $d\mathbf{w}$ a vector with length $3N$ containing random values picked from a Gaussian distribution with zero mean and a variance equal to the (small) numerical time-step δt ; and \mathbf{B} a $3N \times 3N$ matrix which results from the factorization of the diffusion tensor $\mathbf{D} = k_B T \cdot \boldsymbol{\mu}$ as required by the fluctuation-dissipation theorem:

$$\mathbf{D} = \mathbf{B} \cdot \mathbf{B}^T . \quad (4.7)$$

Any matrix \mathbf{B} that satisfies Eq. 4.7 can be used in Eq. 4.6. So, we apply a Cholesky decomposition of \mathbf{D} to obtain an upper triangular matrix, \mathbf{C} , that satisfies Eq. 4.7:¹⁷⁸

$$\mathbf{D} = \mathbf{C} \cdot \mathbf{C}^T . \quad (4.8)$$

Based on these considerations, we integrate Eq. 4.1 with $\mathbf{F}_{\text{net}} = \mathbf{F}_{\text{dd}} + \mathbf{F}_{\text{down}} + \mathbf{F}_{\text{ev}}$ to compute the trajectories of all particles. In particular, a forward Euler method was applied using numerical timesteps of $\delta t = 10^{-6}$ s. As discussed in the Appendix 4.B, it was found that the size of δt was sufficiently small to keep computational errors well below 0.1 % relative error in position at 0.5 s of simulated time.

4.3 Experimental section

In this section the methods used to actuate and study the magnetic particles are described. First an overview will be given of the experimental setup, followed by the characterization of the magnetic actuation setup.

4.3.1 Experimental setup

A magnetic actuation setup was realized capable of manipulating suspended superparamagnetic particles tri-axially, i.e. by generating a user-specified magnetic field both in the horizontal as well as in the vertical plane⁴¹ (Figure 4.3a). The setup consists of 8 individually controlled copper coils (brown) together with 8 soft-iron (ARMCO[®]) poles (dark grey) connected by soft-iron frames (blue and red). Magnetic fields are produced by the flow of electrical currents through the coils and by following the soft-iron frames, they are guided to the sample area surrounded by the

poles. The blue soft-iron frames with 4 poles at their ends are used for the generation of the horizontal components of the magnetic field whereas the red frames are responsible for the vertical components.

A closer view of sample area is given in Figure 4.3b. Here, each copper coil is numerically assigned and the sample area is positioned at the focus point of the electromagnets. At the center of the sample area, a closed fluid cell is placed that contains a suspension of magnetic particles. The fluid cell has a diameter of 9 mm and a depth of 120 μm and is made using glass substrates and Secure-Seal spacers (Grace BIO-LABS[®]). During each experiment ($T = 293\text{ K}$), the suspended magnetic particles are actuated using the magnetic setup and the resulting dynamics are analyzed using video-microscopy.

We chose to work with polymer-based super-paramagnetic particles (2.8 μm) coated with streptavidin (Dynal[®] M-270 Streptavidin). Due to the high binding affinity of the streptavidin-biotin interaction, streptavidin-coupled M-270 particles have been utilized in numerous applications, e.g. isolation and handling of biotinylated nucleic acids, antibodies and other biotinylated ligands and targets. The undiluted stock suspension was diluted 10 times (6.5×10^7 particles/ml) using a buffer solution (PBS + 1 mg/ml BSA) before introducing into the fluid cell. The magnetic properties of the particles were characterized using VSM.

4.3.2 Characterization of the setup

The possibility of generating arbitrary magnetic fields using the setup was investigated by modeling the setup in a 3D commercial FEM package (Comsol Multiphysics[®]). The soft-iron and copper materials were modeled as linear media with relative permeabilities (μ_r) of 4750 and 1, respectively.

In the experiments we report in this chapter, we generated three particular magnetic fields: (1) a vertical field with a downward gradient by flowing currents through coils 2 and 4 simultaneously, (2) a uniform horizontal field by running currents through coils 5 and 8 and (3) a horizontally rotating field, which is created by applying currents to coils 5 to 8 that vary sinusoidally in time, and have a phase shift of 90 degrees between them. Figure 4.3c shows the computed magnetic field in the z - x (vertical) plane, generated by the flow of opposing electrical currents (0.25 A) through coils 2 and 4. As expected, the magnitude of the vertical field shows a decrease along the z -axis. In contrast, coils 5 and 8 (0.2 A) induces a more homogeneous magnetic field in the horizontal (y - x) plane (Figure 4.3d).

The setup was experimentally characterized by measuring the magnitudes of the generated magnetic fields as depicted in Figures 4.3e and f using a Gauss meter (F.W. Bell[®]). The measurements took place at the center of the setup and the electrical currents through the coils were varied from 0.1 A to 1 A. The experimentally measured values were compared with results from Comsol simulations.

The results are shown at the left y -axes of Figures 4.3e and f. It is seen that saturation of the magnetic fields occurs at electrical currents higher than 0.4 A, and below this value the experiments and computations show linear trends. The observed difference between the simulation and experiment shows that the soft-iron used in

the magnetic set-up has non-linear material properties, leading to saturation of the induced magnetic field, which is not included in the numerical simulations. In the present study, experiments were conducted at a limiting electrical current of 0.5 A as higher currents do not yield a higher magnetic field strength.

The geometry of the set-up is designed in such way that electrical currents through coils 2 and 4 (Figure 4.3c) generate in addition magnetic field gradients

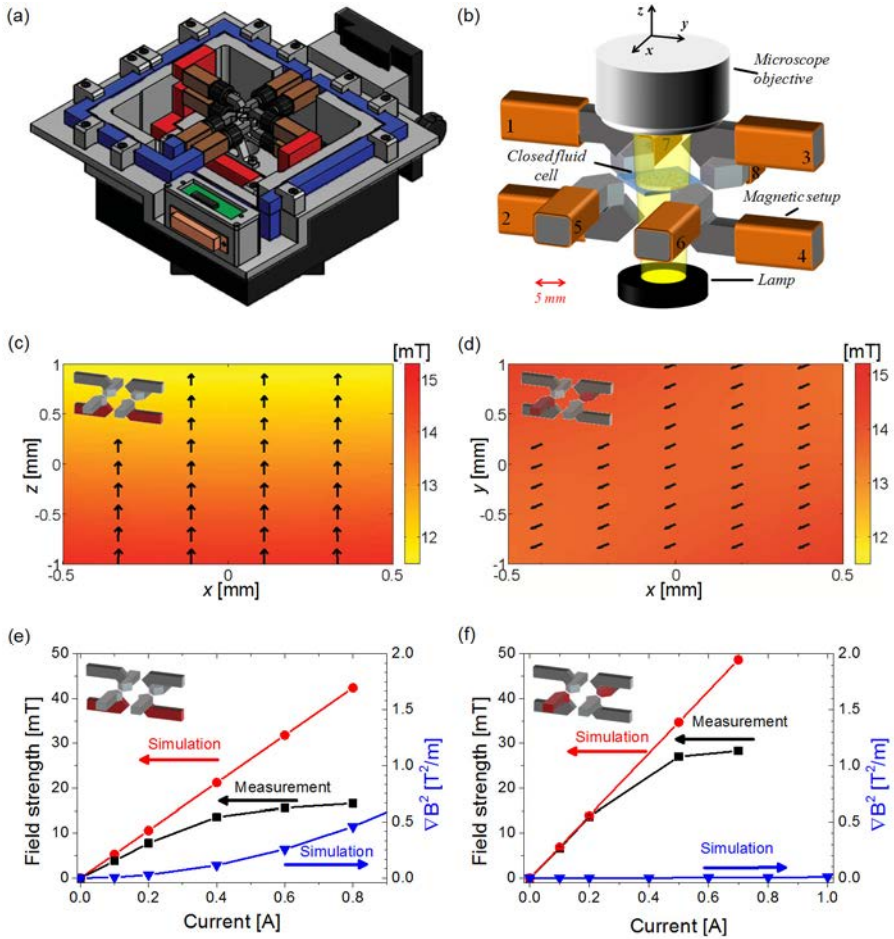


Figure 4.3 3D magnetic actuation setup. (a) AutoCAD side-view of the set-up. (b) The magnetic setup with the fluid cell at the center under a microscope. (c) Simulated vertical magnetic field induced by coils 2 and 4 at a current of 0.25 A. (d) Simulated vertical magnetic field induced by coils 5 and 8 at a current of 0.2 A. (e) (left y-axis): Experimental measurements of the magnitude of the vertical magnetic field are compared with results from Comsol simulations. (e) (right y-axis): Generated field gradient in the center of the setup as obtained from Comsol simulations. The vertical magnetic field of coils 2 and 4 induces a field gradient in the $-e_z$ direction. (f) (left y-axis): Experimental measurements of the magnitude of the horizontal magnetic field are compared with results from Comsol simulations. (f) (right y-axis): Generated field gradient in the center of the setup as obtained from Comsol simulations.

towards the corresponding poles, whereas this is not the case when coils 5 and 8 are operational (Figure 4.3d). Here, magnetic field gradients are defined as the gradients of the modulus of magnetic flux density to the square. At the right y-axes of Figures 4.3e and f, simulated field gradients are plotted for the vertical and horizontal configurations. On the one hand, coils 2 and 4 generate vertical magnetic field gradients, pulling the suspended magnetic particles to the substrate. On the other hand, coils 5 and 8 induce a homogeneous magnetic field in the horizontal plane.

4.4 Results

In the current study, we explore the possibility of manipulating a collection of sedimented superparamagnetic particles in a fluid cell, using magnetic actuation protocols. In particular, we are interested in the influence of the vertical magnetic field (Figure 4.3e). If the particles are present in the same horizontal plane, applying a vertically oriented magnetic field will cause mutual repulsion between the particles, due to the vertically oriented magnetic dipoles.

Specifically, if coils 2 and 4 are actuated with a current of 0.4 A, the corresponding magnetic field and gradient (Figure 4.3e) acting on the particles are equal to 13.6 mT and $0.1148 \text{ T}^2/\text{m}$, respectively. Referring to Eqs. 4.2 and 4.3, the generated repulsive and gradient forces on a dipole-dipole cluster are strong and are equal to $\sim 22 \text{ pN}$ and $\sim 0.3 \text{ pN}$.

This phenomenon can be exploited in a number of ways: (i) it offers the possibility to control the distribution of sedimented magnetic particles and (ii) when combined with the ability to generate horizontal magnetic fields intermittent to vertical fields, it provides a new way to disaggregate multi-particle clusters.

4.4.1 Initialization of particle distribution

Figure 4.4a shows the initial magnetic particle distribution ($t = 0 \text{ s}$) after a suspension of magnetic particles was introduced into the fluid chamber and the particles were allowed to sediment to the bottom substrate, i.e. the floor of the fluid chamber. Here, no external magnetic field was applied. The sedimented magnetic particles form a random distribution over the surface and due to the presence of a small remnant magnetic field ($\leq 1 \text{ mT}$) cluster formation of the magnetic particles is observed. This initial distribution of the magnetic particles is difficult to control and varies per experiment. However, in order to obtain experimentally repeatable and reproducible data, it is important to have a controllable and fixed initial condition of the magnetic particles.

Figure 4.4b shows the resulting configuration of the magnetic particles after applying a vertical magnetic field (14.6 mT, 12 s). The magnetic field was generated by the flow of opposing electrical currents (0.5 A) through coils 2 and 4. As shown in Figure 4.3e, also vertical magnetic field gradients were generated which pulled the magnetic particles to the chamber floor. Due to the vertical magnetic field, the sedimented magnetic particles mutually repel each. The repelling interaction causes the particles to form into a relatively uniform configuration which approximately resembles a hexagonal lattice structure.

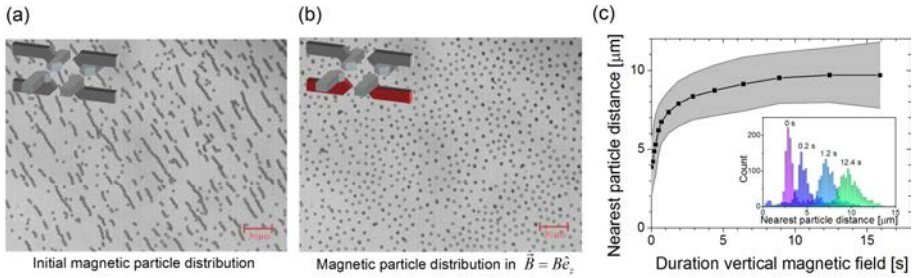


Figure 4.4 Controlling magnetic particle distribution using a vertical magnetic field (14.6 mT). (a) Initial magnetic particle distribution as the particles were introduced into the fluid chamber and allowed to sediment on the surface ($t = 0$ s). (b) After applying a vertical magnetic field, sedimented magnetic particles become vertically oriented dipoles and mutually repel each other ($t = 12$ s). (c) The average nearest neighbor distance calculated from ~ 1000 particles is plotted against the field duration. The grey area indicates the corresponding standard deviation. The inset shows distributions of the nearest neighbor distances plotted at 4 different field durations.

In Figure 4.4c, the nearest particle-neighbor distance is plotted against the actuation time. The nearest neighbor distance is calculated by averaging the nearest neighbor distances of ~ 1000 particles. The slope of the graph shows an exponential decay which we attribute to the generated repulsive force (Eq. 4.2), i.e. it is a short-range force as it is inversely dependent on the inter-particle distance to the fourth power. Eventually, the particles mutually repel each other, forming an approximately hexagonal lattice structure with an average inter-particle distance of ~ 10 μm .

From these results, it is clear that by controlling the initial concentration of the magnetic particle suspension along with the magnitude of the vertical magnetic field and its gradient, the magnetic particle distribution at the beginning of an experiment can be controlled and fixed to an almost uniform distribution.

4.4.2 Overcoming non-specific interparticle adhesion

Besides successful separation of particles (Figure 4.4), we also observed that a small fraction of particles is still present as chains aligned in the applied (vertical) field direction. We can distinguish two different ways of obtaining such vertical chains. On the one hand, thermal fluctuations of individual particles can cause the particles to move out of the horizontal plane. As a result, the lifted particles can make a transition from the weakly stable state of parallel alignment to the surface (in-plane) to the more stable state of orthogonal alignment to the surface (out-of-plane). This in-plane to out-of-plane rearrangement process is enhanced by a roughness of the physical surface and/or the particles. The in-plane stability of the particles can be enhanced by using stronger field gradients or larger particles.

On the other hand, we also observed that a few clusters realigned to the applied vertical field without any observable separation of the particles. This behavior may be attributed to non-specific interactions that keep the particles stuck to each other. Non-specific interactions may originate from Van der Waals forces or electrostatic forces for example. When magnetic fields are used to control magnetic particles, the attractive forces acting on the particles are typically on the order of 10 pN (accord-

ing to Eq. 4.2). Such forces ensure that the particles come into close contact and promote attractive non-specific interactions. This is important for particles functionalized with proteins, as in our experiments, because protein-coated particles can have a weak surface charge and contain non-polar (= hydrophobic) regions.

It is interesting to estimate whether it is possible to rupture non-specific bonds. We calculate (using Eq. 4.2) that the repulsive dipole-dipole forces which we apply to our particles are in the order of 22 pN; for a flux density in the order of 14 mT. Furthermore, we observe that two-particle clusters which do not separate realign with the magnetic field within 0.1 – 0.2 seconds. In order to dissociate such bonds, not only the force is important, but also the time during which the force is applied. A previous study on the breaking of non-specific bonds between magnetic particles and a substrate in the presence of surfactants¹⁸¹ has shown that a force of 1.2 pN needs to be applied for ~2 seconds to disrupt the weak non-specific bonds. The dissociation constant could be estimated to be 0.83 s^{-1} at a force of 1.2 pN.

At the same force, the method presented here would result in a dissociated fraction, i.e. the amount of non-specific bonds being ruptured for two particles clusters, of roughly ~0.1. However, we apply a force that is almost 20 times higher. This would definitely lead to a higher dissociated fraction as estimated here. Moreover, dissociation can still be enhanced by increasing the field gradient or by saturating the magnetic moment. Respectively, this would make the application time longer and increase the strength of the repulsive forces. Therefore, we conclude that the repelling forces exerted using the method presented in this chapter are in a force regime which can rupture non-specific bonds. In Chapter 5 we demonstrate how this experiment can be used to accurately quantify the magnetic properties of the particles.

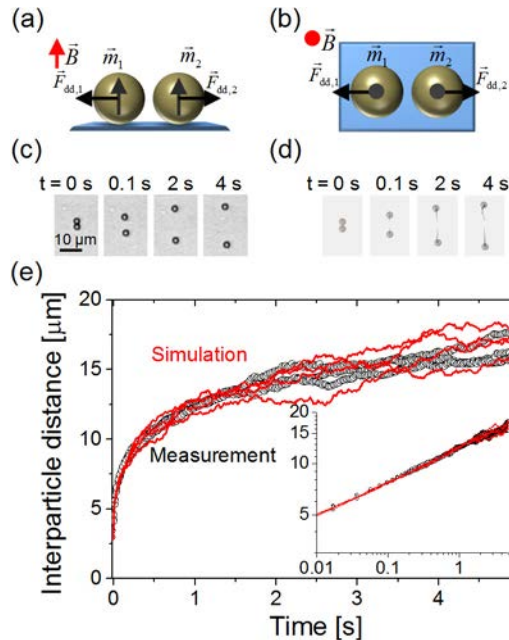


Figure 4.5 Measured and simulated disaggregation of a two-particle cluster at a physical surface in an aqueous medium. A schematic (a) side-view and (b) top-view is shown indicating the vectors corresponding to the magnetic field, magnetic moments and the magnetic dipole-dipole forces. (c) Measured top-view images at different times. ($\mathbf{B} = 15 \text{ mT } \hat{\mathbf{e}}_z$; $\nabla \mathbf{B} = -3.2 \text{ T/m } \hat{\mathbf{e}}_z$.) (d) Simulated top-view images at different times. (e) In-plane center-to-center distance between the particles as obtained from the top-view experimental (black open circles) and simulated (red lines) data. Measurements were repeated on the same particle pair. The inset shows a log-log plot of the same data.

4.4.3 Simulation of the separation dynamics of two-particle clusters

First, we experimentally recorded the response of two-particle clusters (2.8 μm diameter) on a surface after applying an out-of-plane magnetic field. From top-view images (see Figure 4.5c) the in-plane center-to-center distance was determined over time, as is shown in Figure 4.5e. Strong non-linear behavior was observed which corresponds to the reciprocal dependence of the magnetic dipole-dipole interaction force on the fourth power of the distance between the dipoles (see Eq. 4.2). At short distances, the response of the different particle pairs is similar and shows no significant fluctuations in the distance. At larger distances, fluctuations become stronger and we attribute this to the Brownian motion of the particles, which becomes more pronounced as the repulsive magnetic force has weakened.

Using the numerical approach as described, we simulated the response of two-particle clusters with similar properties; the particle properties were obtained from VSM data⁴¹ and the properties of the magnetic fields were characterized from Comsol simulations and Hall-probe measurements¹¹⁵. From the numerical data, the in-plane (top view, see Figure 4.5d) interparticle distance was determined, which is shown in Figure 4.5e for several simulations. As can be seen, the simulated interparticle distance shows exactly the same characteristics over time as was found in the experiments. Correspondence between simulation (with a similar method) and experiment was also found earlier for the breaking and reformation behavior of magnetic particle chains in a rotating magnetic field⁴¹. We therefore conclude that the used numerical method is an accurate tool to study the disaggregation behavior of magnetic particle clusters in more detail, as we show next.

4.4.4 Parameters influencing the separation probability

The separation dynamics of two-particle clusters was studied for different parameters. First, we varied the orientation of the two-particle cluster with respect to the physical surface, at the moment of application of the out-of-plane field. To this end, we define the angle of the longest axis of the two-particle cluster with the physical surface as the tilt angle, α . We refer to the tilt angle at the time of application of the out-of-plane magnetic field as the initial tilt angle, α_0 . Due to Brownian motion of the particle cluster, the initial tilt angle will not always be zero, even when an in-plane magnetic field is applied just before application of the out-of-plane magnetic field. For smaller particles, deviation from a zero initial tilt angle will be larger as compared to larger particles, due to the larger diffusivity of smaller particles. Therefore, simulations were carried out in which the initial tilt angle was varied for two different particle sizes. In particular, we considered $\varnothing 2.8 \mu\text{m}$ particles (corresponding to Dynal M-270 particles) and $\varnothing 1.0 \mu\text{m}$ particles (corresponding to Dynal My-One particles) which have a ~ 9 times smaller magnetic moment¹⁶⁷.

In Figure 4.6 both a top- and side-view are shown of typical simulated particle trajectories. It is found that for small initial tilt angles, particles irreversibly separate. For larger initial tilt angles, particles rejoin after initial separation and form vertical clusters, i.e. unsuccessful disaggregation. The driving force of this cluster reformation is the magnetic dipole-dipole interaction, which only results in complete sep-

aration of the magnetic particles in case the relative distance vector (\mathbf{r}_{ij} , see Eq. 4.2) between the magnetic moments \mathbf{m} is orthogonal to the orientation of the magnetic moments. In case the relative distance vector deviates from being orthogonal to the magnetic moment, ($\mathbf{m} \cdot \mathbf{r}_{ij} \neq 0$), the magnetic dipole-dipole interaction will lead to alignment of the moments of the two moments. Brownian motion generates variations in the direction of \mathbf{r}_{ij} and therefore additional forces are required to stabilize an orthogonal orientation of the particle clusters with respect to the external field. The presence of the surface and the field gradient can stabilize such an orientation and keep the interaction repulsive, as particles are in a local energy minimum when both are in contact with the surface. This is also observed in Figure 4.6; for a zero initial tilt angle, both particle types do not show cluster reformation.

For non-zero initial tilt angles, one of the particles is lifted initially, while also moving away from the other particle. In case the initial tilt angle is small enough the lifted particle eventually returns to the surface again due to the field gradient and then remains separated from the other particle. For higher angles the lifted particle eventually returns to the other particle and reforms the cluster.

Comparing different particle sizes, the 3 μm particles stay closer to the surface after successful separation, i.e. the average distance from the surface is much smaller than the particle radius, whereas for the smaller 1 μm particles the average distance from the physical surface is comparable to the particle radius. Comparing thermal energy to the potential energy due to the downward force ($F_{\text{down}} = 0.26 \text{ pN}$), we can estimate the distance of the particle surface from the planar surface within which a particle may be found with a probability of 0.9 (cf the barometric height). For the 2.8 μm particles, this distance is estimated to be 0.05 μm , and for the 1.0 μm particles it is 0.45 μm , and this is found to be roughly in agreement with our numerical findings.

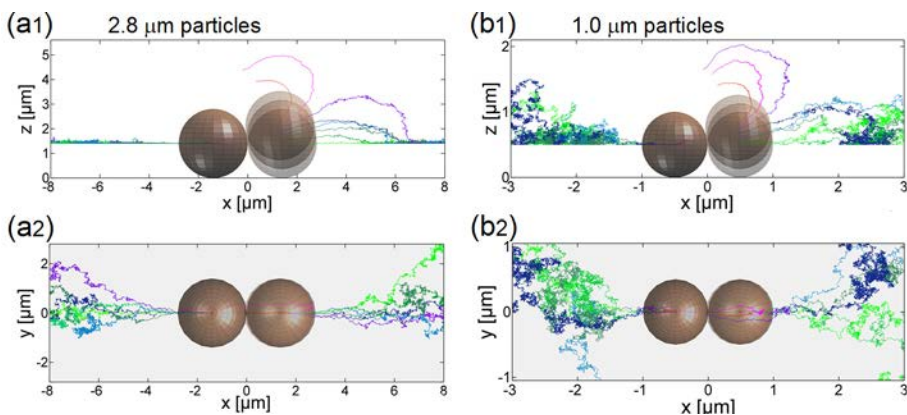


Figure 4.6 Computed particle trajectories at different initial tilt angles with respect to the surface. ($\mathbf{B} = 15 \text{ mT } \hat{\mathbf{e}}_z$; $\nabla \mathbf{B} = -3.2 \text{ T/m } \hat{\mathbf{e}}_z$) (a1) Side view and (a2) top view of simulations of 2.8 μm particles (M270). (b1) Side view and (b2) top view of simulations of 1 μm particles (MyOne). The sketched spheres represent initial positions of the particles.

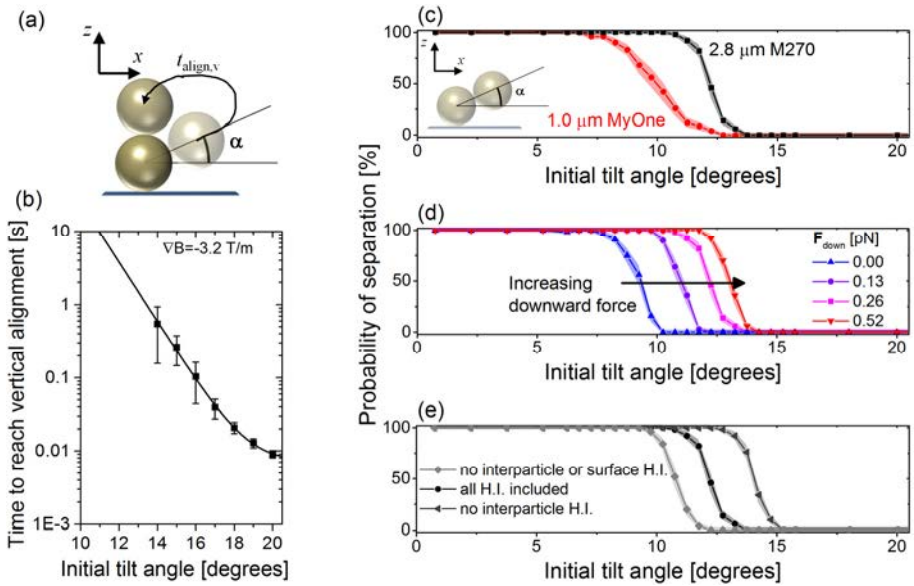


Figure 4.7 Quantification of the two-particle disaggregation dynamics in simulations. (a) Schematic showing the initial configuration of a particle cluster that is aligned with the surface at an initial tilt angle α . When a field is applied perpendicular to the surface, particles either separate, or re-align into a cluster. (b) Time required for cluster reformation as a function of tilt angle, for the cases in which clusters are reformed after application of the out-of-plane magnetic field. Datapoints represent the average over ~ 50 considered simulations. The error bars indicate the standard deviation in the found times. The solid line corresponds to a fit of the data using the fitting function: $y(x) = y(0) + A \cdot \exp(-B \cdot x)$. (b,c,e) Computed probability of successful separation as a function of the initial tilt angle with respect to the surface. (c) Data for different particles using a downward force of 0.26 pN oriented into the $-z$ - direction. (d) Data for $2.8 \mu\text{m}$ sized particles (M270) at downward forces. (e) Comparison of data for $2.8 \mu\text{m}$ sized particles (M270) in case the hydrodynamic interactions between the particles or with the surface are excluded in the simulations. Each data point corresponds to the mean of 200 simulations. Particles that did not reform into a cluster within 10 seconds contribute to successful separation. The (small) standard error of the mean is represented by the shaded area around the data.

Since Brownian motion introduces statistical variability of the numerical outcome of a simulation at a certain initial tilt angle, we carried out 200 simulations per initial tilt angle and determined the probability of successful separation for both particle types. In the simulations, a downward force of $F_{down} = 0.26$ pN was used. Each simulation was performed for 10 seconds as cluster reformation is found to occur typically in less than one second (see Figure 4.7a,b).

Figure 4.7c shows that smaller particles can reform clusters for a smaller range of initial tilt angles. Also the transition from a 100% separation probability to a 0% separation probability is broader for smaller particles, which is explained by the higher diffusivity of smaller particles. Interestingly, for both particles there is a non-zero range of initial tilt angles for which two-particle clusters can be separated with 100% success rate. This indicates the importance of initial pre-alignment of the particle pair to the physical surface.

The influence of the downward force (e.g. by a magnetic field gradient that is oriented towards the surface) during the disaggregation process was studied; see Figure 4.7d. Compared to a no downward force, we find that a downward force increases the range of initial tilt angles for which disaggregation is successful. Remarkably, in the absence of a downward force, it is found that particles may still successfully separate if the initial tilt angle of the cluster is less than $\sim 9^\circ$. Looking at this case in more detail, we find that the simulation time plays an important role. For small angles, the required time to reform a cluster is found to be (much) larger than 10 seconds (Appendix 4.C) and it increases exponentially as the initial tilt angle approaches zero. From this we conclude that a downward force is not strictly necessary, but can be used to increase the effectiveness of cluster disaggregation.

To study the role of the hydrodynamic interactions in the disaggregation process, data was generated in the absence of hydrodynamic coupling between the particles and to the surface. As shown by Figure 4.7e, hydrodynamic interactions between the particles decreases the range of initial tilt angles for which successful particle separation is achieved. This observed effect is a consequence of the two particles moving away from each other from contact, and in the viscous fluid the particles tend to drag along nearby particles behind them. The hydrodynamic interaction of the particles with the surface however is found to increase the probability of separating, and this is due to the additional drag which reduces the lifting motion from the surface that occurs when particles re-orient to reform into a cluster.

4.4.5 Disaggregation of chain- and sheet-like particle clusters

In addition to two-particle clusters, we numerically simulated the disaggregation of clusters consisting of more than two particles. For the same number of particles, different cluster configurations are possible in principle: (i) 1-dimensional clusters, i.e. chains, (ii) 2-dimensional clusters, i.e. sheets and (iii) 3-dimensional clusters. In the simulations only chain- and sheet-like clusters were considered. 3-Dimensional clusters were not considered in the simulations because of computational time costs due to the large number of particles. Experiments were performed with $2.8 \mu\text{m}$ Dynal M-270 particles (carboxylated), which are easy to optically track because they stay within the optical focus of the microscope due to the weak Brownian motion.

First, we consider the disaggregation of chain-like magnetic particle clusters. Figure 4.8a shows typical simulation results; snapshots are shown of the disaggregation of a 10-particle chain. Data for different chain lengths was processed and we determined the disaggregation effectiveness by calculating the probability that (smaller) particle chains with length N remain after application of the magnetic field: see Figure 4.8b. It is found that for chains containing more than six particles, complete disaggregation occurs less frequently and smaller chains ($N = 2,3,4$) remain. In practice, these smaller chains can be disaggregated further, by first re-aligning the chains at the surface and subsequently re-applying the out-of-plane magnetic field.

Although chains containing more than six particles occasionally are not completely disaggregated after a single application of the out-of-plane magnetic field, partial disaggregation is still achieved. This partial disaggregation may be expressed as a disaggregation efficiency, i.e. the number of obtained single particles, divided

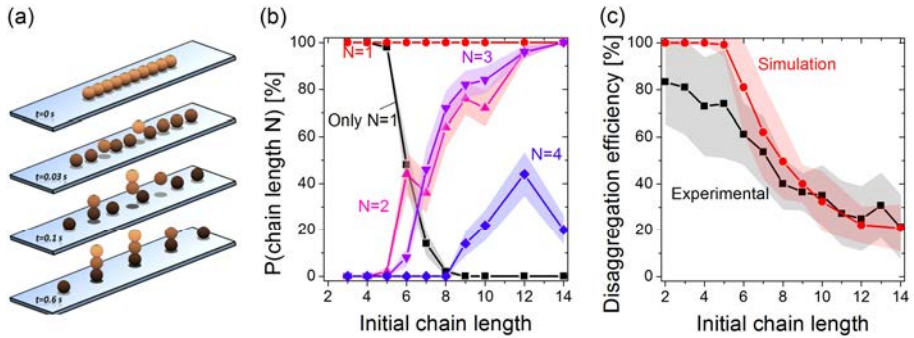


Figure 4.8 Disaggregation of magnetic particle chains at a physical surface. (a) Snapshots of the simulated disaggregation of a 10-particle chain. Besides obtaining single particles, also smaller (out-of-plane oriented) chains are observed. (b) Probability to obtain out-of-plane oriented chains with N particles after 10 s of application of the out-of-plane magnetic field. For each initial chain size 50 simulations were carried out. The standard error of the mean is represented by the shaded area. The black squares correspond to the probability to completely disaggregate a chain into separate single particles (i.e. after 10 s, all remaining clusters have a chain length of 1). The percentages do not add up to 100%, because, in a single simulation, chains of different length may be obtained, e.g. $N=1,2,3$ (see (a)). (c) Comparison of the disaggregation efficiency as found in simulation and experiment. Experimental data points correspond to at least 4 measured chains, i.e. for smaller chains more measurements (e.g. 20 two-particle clusters) were performed.

by the number of particles in the initial chain. In Figure 4.8c this disaggregation efficiency is plotted and compared to experimentally gathered data (on same particles and maintaining the same properties of the external field). It is found that for short chains, the simulations indicate complete disaggregation, while the experiments indicate disaggregation efficiencies of about 75%. For longer chain lengths, the obtained efficiency from simulations is similar to that from experimental data. Possible causes for this difference are variations in particle size or magnetic content, but also a misalignment of the chains with the surface. Variations in particle size or magnetic content might influence disaggregation less in case of longer chains. Furthermore, misalignment of the chains with the surface is likely for short chains (e.g. due to Brownian motion), but for longer chains this will be less, due to the larger size which makes Brownian motion slower.

Finally, we consider the disaggregation of two-dimensional particle clusters, i.e. sheet-like formations. Although many different types of configurations are possible for a certain number of particles within the cluster, we chose to simulate only closely-packed and highly symmetric configurations. In Figure 4.9a snapshots are shown of the simulation of a 19-particle cluster, configured in a closely-packed hexagon. In Figure 4.9b is shown the probability of obtaining a certain chain length after application of the magnetic field, for configurations, which are depicted in the graph. As can be seen, only for large particle clusters, containing more than ~ 14 particles, we find a significant probability to obtain incomplete disaggregation of the sheet-like clusters. The disaggregation efficiency (see Figure 4.9c) is also found to be high compared to chain simulations with the same number of particles.

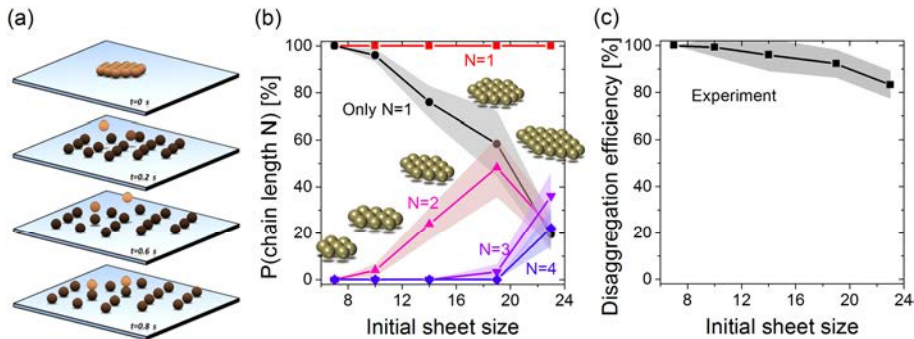


Figure 4.9 Disaggregation of sheet-like magnetic particle clusters at a physical surface. (a) Snapshots of the simulated disaggregation of a 19-particle cluster. Besides obtaining single particles, also smaller (out-of-plane oriented) chains are obtained. (b) Probability to obtain out-of-plane oriented chains with N particles after 10 s of application of the out-of-plane magnetic field. For each initial sheet size 50 simulations were carried out. The standard error of the mean is represented by the shaded area. The black squares indicate the probability to completely disaggregate a sheet-like cluster into single particles. (c) Disaggregation efficiency computed from the simulation data.

An insightful way to compare sheet-like clusters to chain-like clusters is by comparing the longest chain length present within the cluster. For example in case of a sheet-like cluster containing 14 particles, the longest chain length is four particles (see drawing in Figure 4.9b). For this particular cluster, we find a probability of about 0.25 to obtain a two-particle chain after application of the magnetic field, whereas for a chain-like cluster consisting of four particles, this probability is almost zero (see Figure 4.8b). The presence of more particles on the side of the chain apparently reduces the disaggregation efficiency. This can be understood, as for a four-particle chain within a sheet-like cluster, the additional neighboring particles contribute all to the out-of-plane component of the dipole force (see Eq. 4.2), which will result in a faster increase of the height difference between particles when a small height difference occurs, e.g. due to Brownian motion. Furthermore, for the completely surrounded particles, the in-plane component of the dipole force is for a large part canceled out, reducing the velocity with which the particles separate. In view of Eq. 4.8, the relative movement direction angle with respect to other particles increases more rapidly due to the stronger vertical and weaker horizontal component of the forces acting on the particles. A small difference in height between sheet-like clustered particles, will therefore sooner lead to vertical re-joining of the particles.

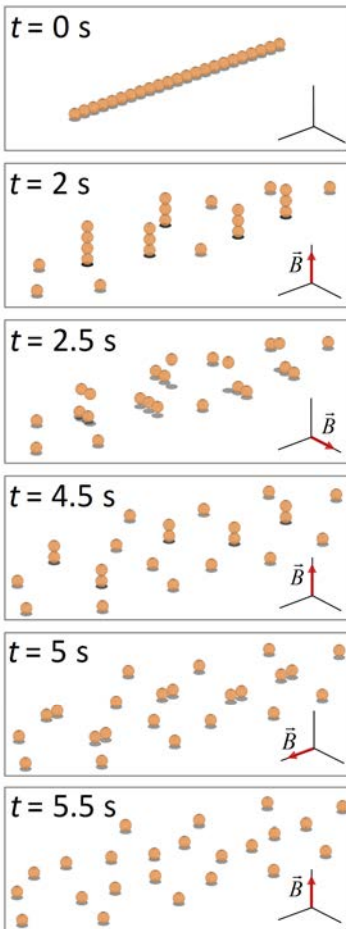
Nevertheless, comparing the different cluster configurations in terms of the total number of clustered particles, sheet-like structures lead to more separation than chain-like structures. This can be understood as follows. Consider the case of seven particles, clustered in a chain-like structure. When applying the out-of-plane magnetic field, the horizontal force acting on the centered particles is inhibited strongly. For the five centered particles, the repulsive interaction with the nearest-neighbors is cancelled out. Only more distant neighbors induce a net displacement, but the resulting force is much weaker as it depends on the 4th power of the radial distance. Consequently, the time to reach sufficient separation to prevent any re-alignment is rela-

tively long. On the other hand, in case the seven particles are structured in a hexagonal sheet-like structure, only the horizontal displacement of the centered particle is inhibited, but the other particles experience the repulsive interaction of three neighboring particles. Therefore, the time to reach sufficient separation will be much smaller for sheet-like clusters as compared to chain-like clusters.

It is interesting to note that for all cluster configurations the induced dipole-dipole interaction results in one but often more individual particles. This indicates that the repeated application of an out-of-plane oriented field should in principal result in the complete disaggregation of magnetic particle clusters. Such an actuation protocol is studied in the next section.

4.4.6 Repeated disaggregation of large particle clusters

We have studied magnetic actuation protocols aiming to achieve complete disaggregation of magnetic particle clusters. In the previous section, we have shown that the single application of an out-of-plane magnetic field to a particle cluster that is aligned to a surface results in complete disaggregation only when the particle cluster



is relatively small, i.e. consisting of less than a few tens of particles. Here, we study the repeated application of the magnetic alignment and magnetic disaggregation steps, such as to gradually break down the particle clusters to smaller fragments and finally to single particles.

Actuation protocols were studied by numerical simulations on a chain-line particle cluster consisting of 23 particles. The snapshots in Figure 4.10 show that indeed the application of a repetitive protocol can lead to complete disaggregation of the particle chain, within less than 10 seconds. Important however in this protocol is that the part in which the particles are realigned in-plane, is shorter or weaker compared to the part in which disaggregation is induced. This is because the magnetic dipole-dipole interaction force for particles with magnetic moments

Figure 4.10 Simulation of the disaggregation of a particle chain consisting of 23 particles by alternately applying an in-plane field (5 mT for 0.5 s) with an out-of-plane field (15 mT for 2 s) to respectively align the (fragmented) chains to the surface and disaggregate the chains into smaller chain fragments or separated particles. To keep the particles near the surface, a downward force of 0.26 pN was applied on each particle, corresponding to the sum of a field gradient force (2.8 T/m and 0.22 pN) and a buoyancy force (0.04 pN).

aligned in-plane can be twice as large compared to particles with magnetic moments aligned out-of-plane (see Eq. 4.2). For effective disaggregation, the in-plane alignment step should not undo the achieved particle separation, but only re-align the out-of-plane oriented chains to make further disaggregation possible.

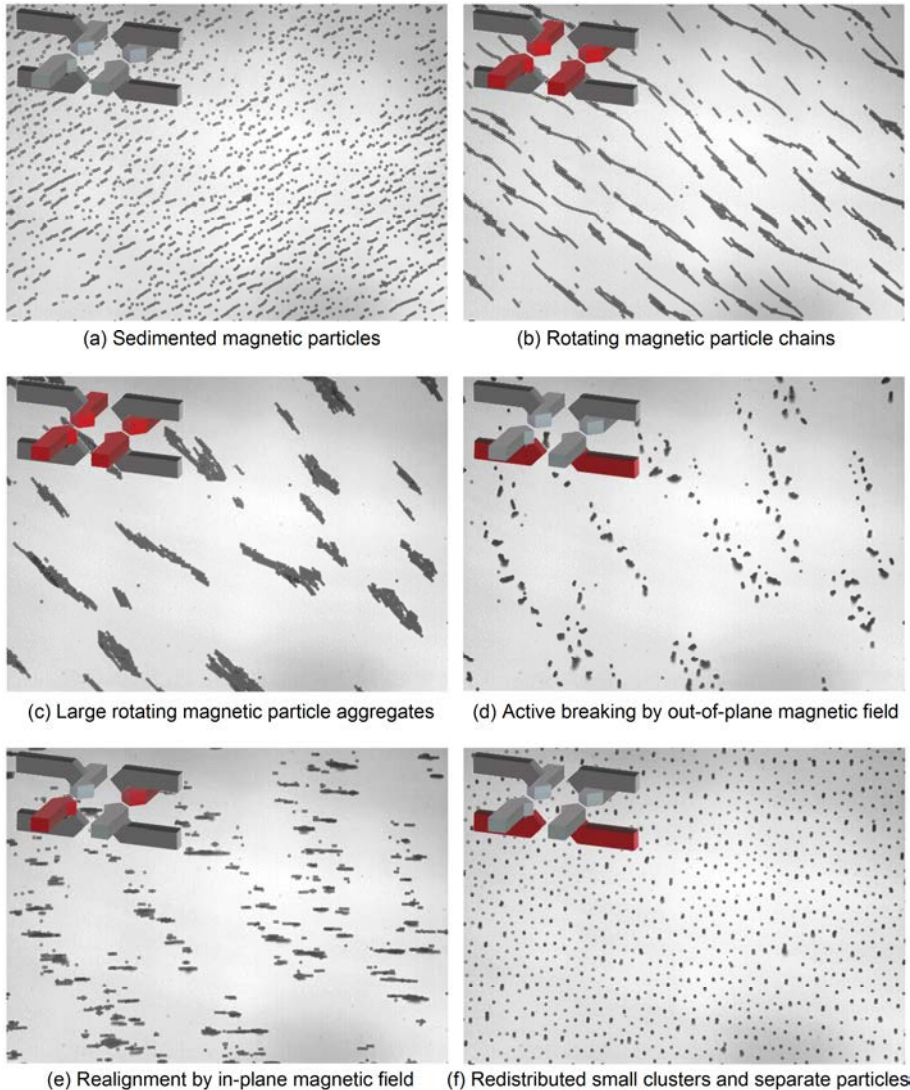


Figure 4.11 Magnetic actuation protocol to disaggregate particle clusters. (a) Initial distribution of the sedimented magnetic particles. (b) Rotating magnetic particle chains are formed with field strength equals 13.7 mT and rotational frequency equals 0.5 Hz. (c) Large rotating clusters of magnetic particles are formed. (d) Vertical magnetic field (14.6 mT) is used to break the horizontally aligned clusters. (e) Horizontal magnetic field (13.7 mT) is applied to realign the vertical clusters with the surface. (f) At the end of the protocol (50 s), the suspension is homogeneously distributed over the physical surface.

Furthermore we studied the application of a repetitive actuation protocol in experiments, to investigate whether even larger and three-dimensional multi-particle clusters can be disaggregated. Starting from a random distribution of particles (see Figure 4.11a), we formed large particle aggregates by applying an in-plane rotating magnetic field for 8 seconds (see Figure 4.11b,c). Subsequently, we repeatedly induced particle disaggregation by sequentially applying out-of-plane (Figure 4.11d) and in-plane (Figure 4.11e) magnetic fields at a frequency of 5 Hz. At the end of the disaggregation protocol (50 s), the resulting particle suspension was homogeneously redispersed over the substrate (Figure 4.11f).

Video-microscopy results from the disaggregation experiment were analyzed using computer software (ImageJ) and the results are shown in Figure 4.12. Here, both unclustered particles and particle aggregates are defined as individual entities. The total amount of the entities and the average amount of particles per entity are counted and plotted against time (Figure 4.12a). The corresponding shaded areas represent the errors related to the counting statistics.

In agreement with Figure 4.11, at the beginning of the experiment ($t = 0$ s), the average amount of particles per entity is low and the amount of entities is high. As many rotating particle chains form into few rotating clusters, the average size of the entities reaches a peak ($t \leq 8$ s). After applying the breaking protocol (starting at $t > 8$ s), both quantities return to the values similar to the beginning of the experiment.

In a similar way, Figure 4.12b shows the fraction of unclustered particles – or single particle entities – during the experiment. For $t \leq 10$ s, the single-particle fraction decreases from 0.4 to 0 due to the formation of large aggregates. When the disaggregation protocol is applied, the fraction of unclustered particles climbs up to a value around 0.3 which indicates a regeneration of $0.3 / 0.4 = 75\%$ within 50 s.

These results clearly show that the developed actuation protocols can almost completely disaggregate large multi-particle clusters. This indicates that the method has a general applicability and is not limited to only minor clustering of particles.

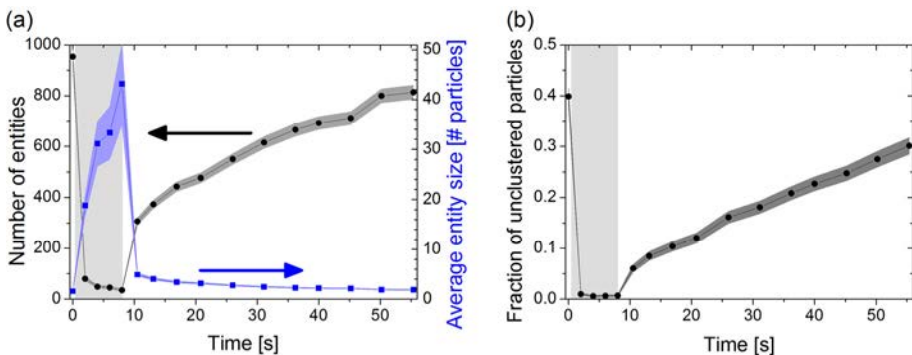


Figure 4.12 Particle analysis of the disaggregation experiment. The light grey areas indicate the period of cluster formation. The dark shaded areas indicate the error related to the Poisson distribution. (a) The total amount of entities (left y-axis) and the average amount of particles per entity (right y-axis) are plotted against time. Here, we define both unclustered particles and particle aggregates as entities. (b) The fraction of unclustered particles is plotted against time.

4.5 Conclusions

In summary, we have developed a numerical model to simulate the Brownian dynamics of ensembles of magnetic particles in a viscous fluid. To validate the model, it was applied to study the dynamics of magnetic field-based disaggregation of superparamagnetic particle clusters near a surface. Disaggregation is achieved by inducing repulsive magnetic dipole-dipole interaction forces between the particles aligned at a surface. Numerical simulation results were compared to experimental data as a function of magnetic field properties, particle size, cluster size and cluster geometry. In case of two-particle clusters, we find that the probability to disaggregate the cluster is strongly determined by the degree of alignment of the cluster with the surface, at the instant when the repulsive interaction is induced. The degree of alignment for which separation is achieved is found to depend on (i) the size of the particles, as this determines the Brownian motion, (ii) the magnetization properties of the particles, (iii) the strength of the field gradient, and (iv) the application time of the magnetic field. Typical angles with respect to the surface for which separation is achieved are on the order of 10 to 15 degrees.

The probability to reach complete cluster disaggregation scales down with cluster size and depends strongly on the cluster configuration. In particular, sheet-like clusters disaggregate more effectively than chain-like clusters containing the same number of particles. A linear configuration (1D) has two limiting effects with respect to a sheet-like configuration (2D) with the same number of particles, namely (i) a steric hindrance for particle motion toward the cluster extremities for more particles due to the reduced dimensionality, and (ii) lower repulsive dipole-dipole forces because on average the particles have fewer nearest neighbors. The insights obtained from the numerical simulations will help to improve magnetic field-based disaggregation and dispersion of magnetic particles in microfluidic applications. The disaggregation method opens new possibilities for magnetic particle based lab-on-chip applications. For example, the method may be applied to undo magnetic clustering effects that may have occurred in magnetic actuation steps such as for fluid mixing and target capturing. Also, a disaggregation step can reset the particle distribution for subsequent labeling or detection steps.

Most importantly, the method presented in this chapter to numerically simulate multi-particle dynamics has a very general applicability for particle-based biotechnological assays, because such assays are always performed using ensembles of many particles. Examples of assay processes that can be studied and optimized by the simulation methodology are surface-binding assays²⁵, agglutination assays^{62, 103}, methods to perform magnetic washing or apply stringency to particles at a biosensor surface^{25, 130, 132}, and technologies for particle-based target purification and enrichment^{50, 99}. Simulation results give detailed insights into the fundamental dynamics of magnetic particles, allow for a more in-depth interpretation of experimental data, and give new ideas on how assays can be controlled and used. We expect that the numerical simulation of multi-particle dynamics will be broadly applied and will be very useful for the further development of magnetic particle-based biotechnologies.

4.6 Appendix

4.A Error analysis of the excluded volume force between particles

To prevent simulated particles from overlapping, excluded volume forces were implemented, according to Eq. 4.4. However, following its formulation, this force may already exert a force on particles which are nearly (but not exactly) in contact. This is a non-physical effect, and the distance at which it becomes non-negligible strongly depends on the magnitude of ξ , i.e. a numerical constant which determines how fast this excluded volume force decays when the interparticle distance increases. In this respect, ξ is preferably very large. However, in case of a large value of ξ , if the situation occurs in which the particles slightly overlap, a huge repulsive force would be exerted on both particles, which may result in a huge displacement of the particles away from each other when calculating the next positions. Obviously, this effect also depends strongly on the used numerical timestep. As a consequence, the value of ξ should be chosen such that the force still exhibits a fast decay in case particles are slightly separated, while not causing any overshooting effect when the particles overlap.

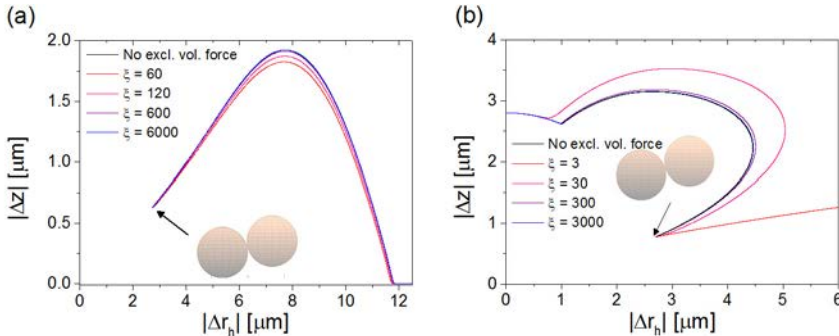


Figure A.1 The effect of the excluded volume force on the numerical outcome for (a) separating particles (2.8 μm diameter), and (b) re-colliding particles. For both situations, the relative position is shown of one of the particles with respect to the other. The initial particle configuration is shown in the figures, and the arrow indicates the corresponding starting position within the graph. Simulations were done for different values of ξ , but also for the case of no excluded volume force implemented (black lines). The simulations corresponding to the highest values of ξ are found to overlap with the simulations without excluded volume forces implemented (both are difficult to distinguish within the graphs).

To find the optimal value for ξ , simulations (timestep 10^{-6} s) were performed of two-particle clusters in different configurations and with varying values of ξ . In Figure A.1 computed trajectories are shown for two starting configurations, i.e. in case (a) particles successfully separate or (b) become attracted again after initial separation. In the figure, also trajectories are plotted in case no excluded volume forces are considered (Note that these simulations are stopped after particles re-collide). It was found that for values of ξ above 600, the relative error in computed particle positions is smaller than 1%. For values of ξ above 10000, overshooting is observed as soon

as particles re-collide and slightly overlap. Based on these results, it was chosen to perform simulations at $\xi = 3000$, which contributes to only a maximum relative error of 0.2% to the computed particle trajectories.

4.B Numerical scheme: error analysis

As a forward Euler method is vulnerable to error propagation, the accuracy of the described numerical method was evaluated by varying the size of the timesteps.

In Figure B.1, the particle separation is plotted for a varying size of the numerical time-step, for the case of two M-270 particles, which are initially aligned at a tilt angle of 10 degrees with respect to the surface. It is found that below a numerical timestep of 10^{-4} s, the solution does not improve significantly anymore.

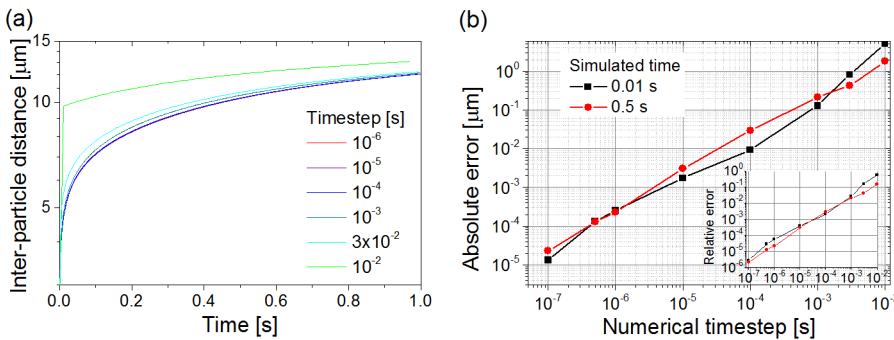


Figure B.1 The influence of the numerical timestep on the computed interparticle distance for the case of a two-particle system, at a starting tilt angle of 10 degrees. (a) Decreasing the numerical timestep, the solution converges. Note that the lines for a timestep of 10^{-5} s and 10^{-6} s coincide with the line for a timestep of 10^{-4} s. (b) Computed absolute error for different numerical timesteps. The inset shows the corresponding relative error.

More clearly, this is shown in Figure B.1 in which both the absolute and relative error are estimated for different simulated times. The absolute error is obtained by computing the same inter-particle distance using a numerical timestep of 10^{-8} s and assuming this as an accurate estimate for the real solution. The validity of this assumption is shown by the result: i.e. a decrease in numerical timestep of a decade, results roughly in a decrease in absolute error by a decade. The estimation at a numerical timestep of 10^{-6} s will therefore be correct to several percent. As shown in the inset of Figure B.1 (right), the relative error made using a numerical timestep of 10^{-6} s is in the order of 10^{-5} . For other computed trajectories we find similar errors, and based on this it is concluded that using a numerical timestep of 10^{-6} s, the relative computational error is clearly below 10^{-3} and thus is negligible.

4.C Breaking two-particle clusters in the absence of a field gradient

Simulations were performed on 2.8 μm magnetic two particle clusters (corresponding to the M270 particles) in the absence of a magnetic field gradient. Since no field gradient is present, no force acts on the particles to keep or bring these particles back into contact with the physical surface, besides Brownian motion (which is a random force).

Simulations were performed with no limitation to the simulated time (after applying the out-of-plane magnetic field), other than that the simulation was stopped as soon as a two-particle cluster was reformed. By repeating such simulations for different initial tilt angles, the average time was determined to reform the cluster. Note that all simulations finally resulted in cluster reformation, which is a consequence of the magnetic dipole-dipole interaction. As shown in Figure C.1, the cluster reformation time increases exponentially as the initial tilt angle decreases. From extrapolation it is found that at an initial tilt angle of 0° , the average cluster reformation time is in the order of 10^5 seconds. Note that no simulations of initial tilt angles below 10° were performed due to the exponential increase in simulation time for lower angles.

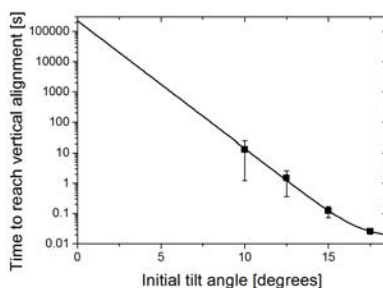


Figure C.1 Time required for cluster reformation in the absence of a field gradient force. Note that all simulations resulted in cluster reformation and not cluster separation. No data is obtained for initial tilt angles below 10 degrees due to the too large amount of simulation time required. The datapoints and errorbars respectively correspond to averages over ~ 50 measurements and the standard deviation therein. The line corresponds to a fit of the data using the fitting function: $y(x) = y(0) + A \cdot \exp(-B \cdot x)$.

5

Quantification of magnetic particle properties by intra-pair magnetophoresis

*The ability to analyze biological material at the single-molecule and single-cell level in a highly parallelized fashion will significantly enhance biomedical research and in vitro diagnostics in the future. Magnetic particles play an important role in this development because such particles can be manipulated by magnetic fields without perturbing the biological matter under study. An important requirement is that the magnetic properties of the particles are accurately known, with single-particle resolution as well as with good statistics. However, a combined accurate and high-throughput method for the characterization of the field-dependent magnetization of magnetic particles does not yet exist. In this chapter we report intra-pair magnetophoresis as a novel method to accurately quantify the field-dependent magnetic moments of magnetic particles and to rapidly generate histograms of the magnetic moments with high statistics. We demonstrate our method with particles of different sizes and from different sources, with a measurement precision of a few percent. We expect that the intra-pair magnetophoresis methodology will be a powerful tool for the characterization and improvement of particles for the upcoming field of particle-based nanobiotechnology.**

*This chapter has been published in: A. van Reenen, Y. Gao, A.H. Bos, A.M. de Jong, M.A. Hulsen, J.M.J. den Toonder and M.W.J. Prins, Accurate Quantification of Magnetic Particle Properties by Intra-Pair Magnetophoresis for Nanobiotechnology. *Appl. Phys. Lett.* **103**, 043704 (2013).

5.1 Introduction

Presently a generation of tools is being developed for the biosciences and *in vitro* diagnostics based on acquiring data at the single molecule and single cell level with good statistics. An example is the flow cytometer, which collects data of single biological cells with high throughput and thereby establishes detailed histograms of cell population characteristics¹⁸². Another example is the field of high-throughput single-molecule DNA sequencing¹⁸³⁻¹⁸⁴, where technologies are able to read the bases of individual nucleic-acid molecules with high throughput. An important advantage of single-cell and single-molecule data compared to ensemble-averaging measurements is that high sensitivities are achieved and that deeper insights are gained into the biological processes, e.g. into the development of population heterogeneities in space and/or in time.¹⁸⁵

Superparamagnetic particles are a potent component in many single molecule analysis technologies^{13, 82, 131-132} because such particles can be manipulated and interrogated by magnetic fields without perturbing the biological matter under study. To be able to use magnetic particles in high-throughput methods with single-particle and single-molecule resolution, it is important that the size as well as the magnetic properties of the particles are accurately known. The size of single magnetic particles can be accurately determined, e.g. by transmission electron microscopy¹⁸⁶, scanning electron microscopy or pore sensing¹⁸⁷. However, the characterization of magnetic properties remains challenging. The magnetic moments of single particles have been measured by Brownian motion analysis¹⁸⁸, field sensing¹⁸⁹⁻¹⁹⁰, and magnetophoresis^{176, 191-192}; but the reported methods all suffer from large measurement uncertainties (above 30%) because of large uncertainties in the fields and field gradients applied within the reference frames of the particles.

In this chapter we describe a way to characterize the magnetic field dependent moments of magnetic particles with a high accuracy. The high accuracy is achieved by recording particle movement in the *high and local field gradients generated by the particles themselves*, see Figure 5.1. We measure the trajectories of pairs of particles, present in a liquid close to a physical surface in an applied magnetic field, and we deduce the magnetic moments from the time dependency of the particle pair separations. The applied magnetic field is generated by two electromagnets with soft-iron poles⁴¹. The field is applied uniformly to the particles and is repeatedly switched between out-of-plane (Figure 5.1b) and in-plane (Figure 5.1c) orientations in order to repetitively induce separation and rejoining of the particle pairs at the surface (Figure 5.1d). In this intra-pair magnetophoresis method (i) the field gradients and therefore the magnetophoretic velocities are high, (ii) the applied field strength is uniform and well-controlled, and (iii) many particles are simultaneously and repetitively measured. In the following we will demonstrate that pair-based distribution functions can be accurately measured and can be translated into single-particle based histograms of the magnetic moments, with a measurement uncertainty of only a few percent. Furthermore, we will show that repeated measurements can be performed on the same particles in order to determine field-dependent magnetization curves and grain size distributions within the magnetic particles.

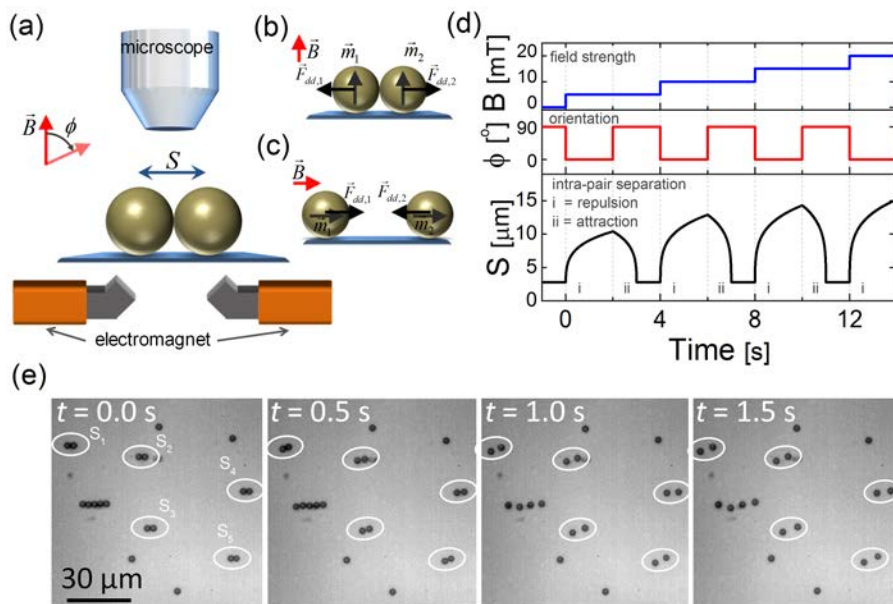


Figure 5.1 Sketch of the intra-pair magnetophoresis methodology. (a) The separation S of magnetic particle pairs due to magnetic dipole-dipole interactions is measured in (b) out-of-plane and (c) in-plane magnetic fields. (d) Repeated separation and rejoining of magnetic particles S (black line) at different field strengths (blue line) with alternating in-plane and out-of-plane orientation (red line). (e) Microscopy images of M-270 superparamagnetic particles at different times, upon application of an out-of-plane magnetic field at $t = 0$. The image is a zoom-in of the total field of view.

5.2 Methods

The magnetic moments have been characterized for different types of superparamagnetic particles. Suspensions were made by dispersing the particles in PBS buffer with 1 mg/ml BSA (to reduce particle-surface interactions) in a small fluidic chamber made of two glass cover slips, separated by a 100 μm thick spacer. The studied particles were \varnothing 2.8 μm , Dynabeads M-270 COOH (Invitrogen); \varnothing 1 μm , Dynabeads MyOne COOH (Invitrogen); and \varnothing 2.6 μm Micromer PEG-COOH (MicroMod) particles. Imaging was performed using a microscope (50x magnification objective; Leica DM4500) and a high speed camera (100 frames per second; IDT MotionPro X3). Typically about 20 particle pairs were simultaneously imaged. Particle pairs were excluded from analysis when other particles were present within a distance of about 15 μm . We applied a magnetic field that alternated between out-of-plane and in-plane orientations at a frequency of 0.5 Hz. Each measurement contained one four-second sequence of the resulting separation and rejoining of particles. In this way, several consecutive recordings were made, as shown in Figure 5.1e. The applied field strength was uniform in the plane of the particles, within a few percent over a 1 mm^2 surface area¹¹⁵. The magnet also creates a field gradient toward the surface, which keeps the particles at the bottom surface of the fluid chamber. Custom image processing software was used to determine the time-

dependent intra-pair separations $r(t)$ (see Figure 5.2). Particle position tracking was based on cross-correlation of the images with a reference image of a particle, which gives positional accuracies well below 100 nm.

5.3 Results

In an out-of-plane oriented magnetic field, the intra-pair separation, S , increases due to the repulsive dipole-dipole forces between the particles with magnetic moments m_1 and m_2 ,

$$F_{dd} = \frac{3\mu_0 m_1 m_2}{4\pi S^4}. \quad (5.1)$$

This force is opposed by the hydrodynamic drag that acts on the particles when they move parallel to the surface¹⁸⁰. The corresponding differential equation can be solved (see Appendix 5.A) resulting in the following time-dependence of the intra-pair separation S :

$$S(t)^5 = \frac{45}{64} \frac{\mu_0 m_1 m_2}{\pi^2 \eta R} t + S(0)^5. \quad (5.2)$$

Here η is the dynamic viscosity (10^{-3} Pa·s for water) and R is the particle radius. Due to the very strong distance dependence of the magnetic dipole-dipole force, the perturbation of the intra-pair separation due to particles at a further distance is very small (a particle at a distance of $10\times$ the particle diameter from the particle pair

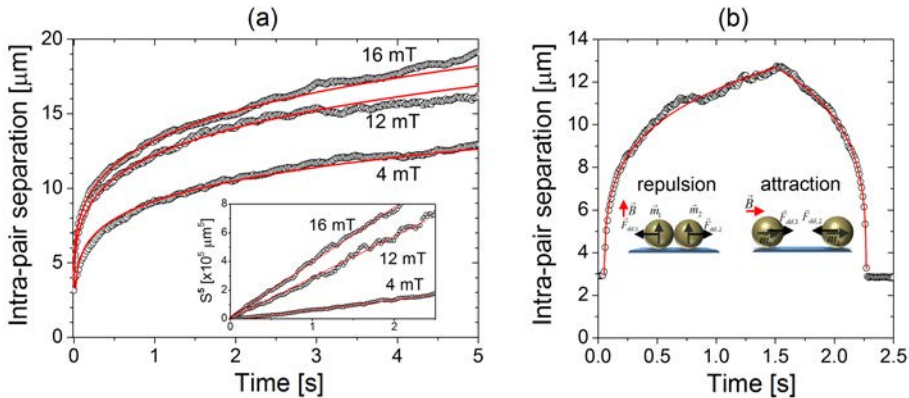


Figure 5.2 (a) Intra-pair separation S as a function of time of a single pair of M-270 particles, determined for different field strengths (open circles). The solid curves correspond to fits based on the solution of the equation of motion [Eq. 5.2]. The inset shows the same data, but now with the fifth power of the intra-pair separation (S^5) on the y-axis. The dynamic range of the intra-pair force in the experiment is on the order of 10^3 (ranging from ~ 10 pN to ~ 0.01 pN at 16 mT, obtained using Eq.5.2 for the smallest and the largest distance). (b) Intra-pair separation measured for repulsive interaction and attractive interaction on the same M-270 particle at a field strength of 13 mT. From the fits (using resp. Eq. 5.2 and A.8), the determined magnetic moment is $(7.18 \pm 0.04) \times 10^{-14} \text{ Am}^2$ from repulsion data and $(7.22 \pm 0.03) \times 10^{-14} \text{ Am}^2$ from attraction data. Comparing the values, we conclude that similar values are obtained using both methods.

exerts a force that is four orders of magnitude smaller than the forces exerted within the particle pair). The observed separation behavior is accurately described by Eq. 5.2, as shown in Figure 5.2. From the fit, the geometric mean of the magnetic moments of the particles is determined. In Eq. 5.2 the hydrodynamic particle-particle interactions have been neglected; this – see Appendix 5.B – gives a slight overestimation of the magnetic moments, by about 0.8% for the 2.8 μm particles and about 0.2% for the 1.0 μm particles. Furthermore, we verified that electrostatic forces do not play a role in our experiments (see Appendix 5.C).

In order to measure complete field-dependent magnetization curves, a magnetic actuation protocol was implemented in which the current through the electromagnets was increased in subsequent repulsion trajectories, as sketched in Figure 5.1d. Measurement results for the M-270 particles are shown in Figure 5.3, for the MyOne particles in Figure 5.4a and for the Micromer particles in Figure 5.4b. The obtained magnetization curves fluctuate around the curve measured by VSM (Vibrating Sample Magnetometry), as is expected for single-particle based measurements compared to an ensemble-averaging method. By fitting the magnetization curves with a log-normal distribution-weighted Langevin equation, the grain size distribution can be obtained (for an explanation see Mihajlovic et al.¹⁹⁰). The inset in Figure 5.3 shows the obtained grain size distributions (colored lines) and the distribution obtained from the VSM measurements (black line).

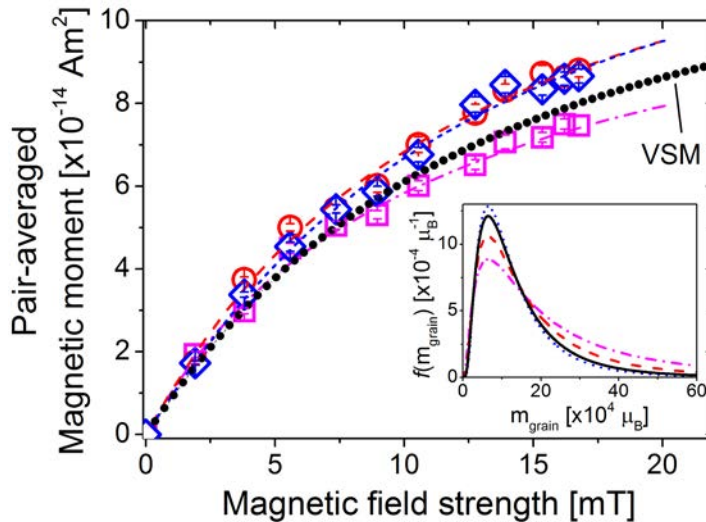


Figure 5.3 Magnetization curves determined for three individual particle pairs (M-270, denoted by open squares, open diamonds and open circles; the error-bars are shown within the symbols). The data for all three pairs were collected within a timespan of 40 seconds. The solid circles correspond to VSM measurements (Vibrating Sample Magnetometry) performed on an ensemble of the same batch of particles. The curves correspond to a log-normal distribution-weighted sum of Langevin curves. The best fitting log-normal distribution functions $f(m_{\text{grain}})$ of the magnetic moments of the particle grains are shown in the inset for the four experimental data-sets. From repeated measurements on the same particles, the error in particle magnetic moment per measurement point is found to be about 4%.

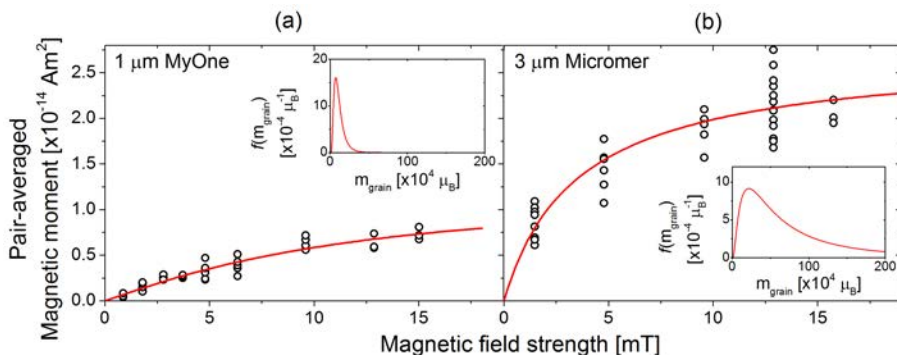


Figure 5.4 Measured and fitted magnetization curves of (a) 1 μm MyOne and (b) 3 μm Micromer superparamagnetic particles. Data-points correspond to different particle pairs, explaining the spread. The data is fitted using a log-normal distribution-weighted sum of Langevin curves.¹⁹⁰ Fit parameters were the distribution center, the distribution width, and the saturation magnetization. The best fitting normal distributions are shown in the insets.

We have recorded the magnetic moments for many particle pairs and different types of particles, yielding the histograms in Figure 5.5a. For each pair-averaged distribution, there exists a unique original single-particle distribution, because pair-averaging causes an over-determination of the original distribution. For example: an original single-particle distribution with two peaks (m_1 , m_2) gives a pair-averaged distribution with three peaks (m_1 , m_2 , and $\sqrt{m_1 m_2}$). For the original distribution, we assumed a parameterized peak function with three underlying parameters, namely the peak position, the peak width and the skewness of the distribution. From the original distribution, we calculate the pair-averaged distribution and we apply an iterative least-squares optimization routine to find the best fit to the data (see Appendix 5.D for the details). Figure 5.5a shows that the fitted histograms describe the measured data well. In Figure 5.5b the corresponding single particle distributions are shown. As expected, the single particle distributions are broader compared to the pair-averaged distributions, roughly by a factor $1/\sqrt{2}$ (also see Appendix 5.E). The data and analysis in Figure 5.5 demonstrate that the intra-pair magnetophoresis method yields accurate distributions of single-particle magnetizations.

Table 5.I summarizes the magnetic particle properties obtained by intra-pair magnetophoresis, including the properties determined by fitting the magnetization curves. Interestingly, the M-270 and the Micromer particles have a similar zero-field magnetic susceptibility but the saturation magnetization differs by about a factor 5. We conclude that the Micromer particles have a lower magnetic content (explaining the lower saturation magnetization) but to achieve the same zero-field susceptibility, the grain size needs to be larger, in agreement with the distribution-weighted Langevin fit of the magnetization curves. We find that the saturation magnetization of MyOne particles is roughly a factor ten lower than that of M-270 particles. Assuming the same iron density within both particles, a decrease of $(2.8/1)^3 \cong 22$ would be expected. Since the average grain size is similar in the two particle types, the iron density within the MyOne particles must be higher compared to the M-270

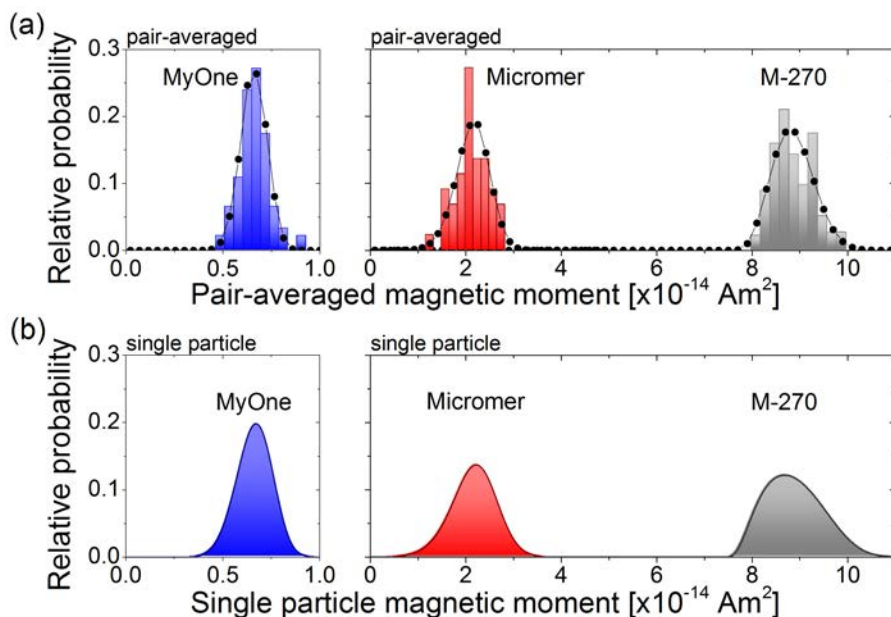


Figure 5.5 Histograms of the pair-averaged and single particle magnetic moments. (a) Measured distributions of pair-averaged magnetic moments for the different types of magnetic particles, i.e. M-270, MyOne and Micromer particles at a field of 13 mT. Each histogram corresponds to about 50 individual measurements on different particle pairs. The curves are obtained by calculating the pair averaged moment distribution from the single particle moment distributions in panel b. (b) Deduced single particle moment distributions. Asymmetric peak functions are shown of single particle moment distributions which lead to the optimal fit of the measured pair-based distributions in panel a.

particles, in agreement with the higher susceptibility found for the MyOne particles. We conclude that intra-pair magnetophoresis yields detailed quantitative information about the magnetic properties of the different types of particles.

We can compare intra-pair magnetophoresis to other magnetophoresis techniques. In existing magnetophoresis techniques the field gradients are generated by magnets and/or magnetic structures that are external to the particles. The applied fields are non-uniform in magnitude and in orientation, which complicates the magnetophoretic analysis, limits the analyzable field of view, and gives large uncertainties in the fields and field gradients experienced within the reference frames of the particles. In intra-pair magnetophoresis, the field gradients are locally very large while the applied field is constant over the surface. The uniformly applied field is well-controlled and the analyzable field of view is large. Furthermore, the field gradients are easily reversed by changing the orientation of the applied field, allowing repeated measurements on the same particles, including measurements at different field strengths so that complete magnetization curves can be established.

TABLE 5.1. Magnetic properties of three different particle types quantified by intra-pair magnetophoresis.

Particle type	Particle diameter [μm]	Zero-field Susceptibility χ	$m_{p,sat}$ ^a [$\times 10^{-14}$ Am ²]	$FWHM/m_{p,max}$ ^b at 13mT [%]	$m_{grain,mean}$ ^c [$\times 10^4$ μB]	$\sigma_{m,grain}$ ^c [$\times 10^4$ μB]
From: supplier		magnetization curve		histogram	magnetization curve	
M-270	2.8±0.1	1.2±0.2	13±1	19±2	5.8±0.8	1.1±0.2
Micromer	2.6±0.1	0.91±0.15	2.7±0.4	49±7	21±3	1.0±0.3
MyOne	0.99±0.04	1.7±0.3	1.2±0.1	34±4	6.6±2.0	0.57±0.3

^a m_{psat} is the average particle saturated magnetic moment.

^b $FWHM/m_{p,max}$ is the full width at half maximum of the single moment distribution, relative to the peak position of the distribution.

^c $m_{grain,mean}$ and $\sigma_{m,grain}$ are the mean and standard deviation of the natural logarithm of the magnetic moment of the grains within the particles.

5.4 Discussion and Conclusions

Here we discuss the outlook for further development of the intra-pair magnetophoresis method. First, it will be interesting to extend the method to the characterization of smaller particles, i.e. sub-micrometer and nanometer sized particles. Magnetic particles can be optically tracked down to very small particle sizes¹⁹³. However, the accuracy of the magnetic moment quantification will decrease if the magnetic forces become smaller because Brownian motion becomes more important in the particle trajectories. For example, the in-plane pair alignment prior to application of the out-of-plane magnetic field is important to reproducibly achieve repulsion between the particles. Comparing the pair alignment energy by magnetic dipole-dipole interaction to the thermal energy, we expect that magnetic particles with a size down to 100 nm should be analyzable by the intra-pair magnetophoresis method (see Appendix 5.G). Another interesting experiment will be to apply intra-pair magnetophoresis to mixed particle types. When a first particle type has been accurately characterized, it can be used to analyze a second particle type in a mixed-particle experiment. It will be particularly useful to analyze broadly distributed particles using particles with a sharp distribution of magnetic properties. Finally, commercially available magnetic particles are known to have broad distributions of magnetic properties, since in industrial settings the magnetic properties are monitored only by ensemble-averaging techniques such as Vibrating Sample Magnetometry. The intra-pair magnetophoresis method is accurate, rapidly yields statistically relevant data, and it is easy to use. We expect that the analysis method will support the development of fabrication processes for next generations of particles with sharply defined magnetic properties. Used in nanobiotechnological research settings, we expect that the intra-pair magnetophoresis method will improve the accuracy of highly parallel single-molecule measurements in magnetic tweezers⁸, magnetic force-induced dissociation experiments¹³⁰, measurements of the mechanical response of cells to actuated particles¹⁹⁴⁻¹⁹⁵, and of particle-based biosensing techniques to measure protein concentrations^{25, 103}.

In summary, the intra-pair magnetophoresis method enables the characterization of magnetic particle properties with an accuracy of a few percent, with good

statistics, yielding histograms and full magnetization curves over a large range of field strengths. The technique makes it possible to characterize particles with different sizes and does not require complicated fabrication techniques. In addition to applications in industry, the intra-pair magnetophoresis method will be easily adopted by academic research groups, as groups working with magnetic particles already have the required infrastructure like microscopes and cameras. We envisage that the intra-pair magnetophoresis methodology will be a very convenient tool to characterize and improve particles in the emerging field of particle-based nanobiotechnology.

5.5 Appendix

5.A Intra-pair separation due to repulsive dipole-dipole interaction between the two particles

In this section, the derivation of Eq. (5.2) is given. This equation describes the center-to-center distance, S , between two particles (with radius R) in the presence of an external magnetic field $\mathbf{B} = B\hat{e}_z$. In Figure S1, the definition of the initial configuration is shown. In particular, the two particles with coordinates $\mathbf{r}_1(t) = (x_1, y_1, z_1)$ and $\mathbf{r}_2(t) = (x_2, y_2, z_2)$ are initially in physical contact with each other, as well as with a physical surface, at $z = 0$, i.e.: $\mathbf{r}_1(0) = (R, 0, R)$ and $\mathbf{r}_2(0) = (-R, 0, R)$. As a consequence, the external magnetic field induces a repulsive dipole-dipole force on the particles, causing the particles to separate.

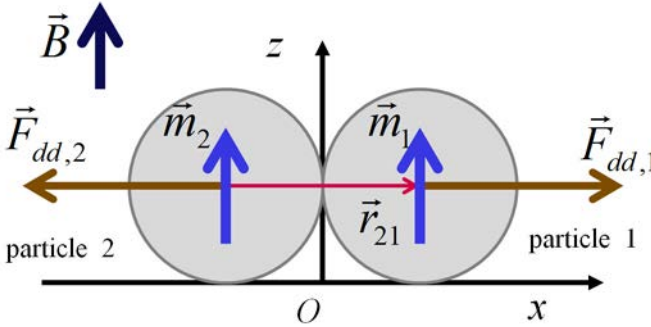


Figure A.1 Sketch of the initial configuration ($t = 0$) of a particle pair on a physical surface upon application of an external magnetic field B . Note that the in-plane component of \vec{r}_{21} is equal to S .

To obtain an equation for the center-to-center distance, we start out from the force balance on particle $i=1,2$, i.e.:

$$\mathbf{F}_{dd,i} + \mathbf{F}_{drag,i} = 0 \quad . \quad (\text{A.1})$$

Here \mathbf{F}_{dd} is the magnetic dipole-dipole interaction, which is opposed by the Stokes drag, \mathbf{F}_{drag} (Reynolds number $< 10^{-4}$, thus inertia may be neglected). For the chosen initial particle configuration both forces are only nonzero in the x -direction. Furthermore, $x = 0$ is located in between the particles, such that $x_1 = -x_2$ (in case of equal radii of the two particles). Using the general definitions for the forces, the force balance becomes, e.g. for particle 1

$$\frac{3\mu_0}{4\pi r^5} \left[(\mathbf{m}_1 \cdot \mathbf{r}_{21})\mathbf{m}_2 + (\mathbf{m}_2 \cdot \mathbf{r}_{21})\mathbf{m}_1 + (\mathbf{m}_1 \cdot \mathbf{m}_2)\mathbf{r}_{21} - \frac{5(\mathbf{m}_1 \cdot \mathbf{r}_{21})(\mathbf{m}_2 \cdot \mathbf{r}_{21})}{r^2}\mathbf{r}_{21} \right] - 6\pi\eta R \frac{dx_1}{dt} \hat{e}_x = 0 \quad . \quad (\text{A.2})$$

Here, \mathbf{r}_{21} is the distance vector, directed from the center of particle 2 to the center of particle 1. The absolute center-to-center distance $r = |\mathbf{r}_{21}| = |\mathbf{r}_{12}|$. In this case, $\mathbf{r}_{21} = (x_1 - x_2)\hat{e}_x$. Furthermore, \mathbf{m}_1 and \mathbf{m}_2 are both oriented along \hat{e}_z , leading to,

$$\frac{3\mu_0 m_1 m_2}{4\pi r^4} \hat{e}_x = 6\pi\eta R \frac{dx_1}{dt} \hat{e}_x . \quad (\text{A.3})$$

We still need to include the additional drag caused by the proximity of the particles to the physical surface at $z = 0$. Leach et al.¹⁹ have reported an equation to determine the effective drag coefficient for a particle moving parallel to a surface:

$$\gamma = 6\pi\eta R \quad \Rightarrow \quad \gamma^{\parallel} = \frac{\gamma}{1 - \frac{9}{16} \frac{R}{z_i} + \frac{1}{8} \left(\frac{R}{z_i}\right)^3} . \quad (\text{A.4})$$

Thus, we obtain for particle 1 (taking $z_l = R$, since the particle touches the surface)

$$\frac{3\mu_0 m_1 m_2}{4\pi r^4} = \frac{32}{3} \pi\eta R \frac{dx_1}{dt} . \quad (\text{A.5})$$

Based on symmetry considerations $x_1 = 1/2r$ (for equally sized particles; see Figure S1; and the magnitude of the dipole-dipole force is equal for both particles), leading to an inhomogeneous first-order nonlinear ordinary differential equation:

$$\frac{3\mu_0 m_1 m_2}{4\pi r^4} = \frac{32}{6} \pi\eta R \frac{dr}{dt} \quad \Rightarrow \quad \frac{dr}{dt} = \frac{9\mu_0 m_1 m_2}{64\pi^2 \eta R r^4} . \quad (\text{A.6})$$

This differential equation can be solved by using a separation of variables:

$$\begin{aligned} \int_{S(0)}^{S(t)} r^4 dr &= \int_0^t \frac{9\mu_0 m_1 m_2}{64\pi^2 \eta R} dt' \\ \frac{1}{5} \left[S(t)^5 - S(0)^5 \right] &= \frac{9\mu_0 m_1 m_2}{64\pi^2 \eta R} t . \\ S(t)^5 &= \frac{45}{64} \frac{\mu_0 m_1 m_2}{\pi^2 \eta R} t - S(0)^5 \end{aligned} \quad (\text{A.7})$$

Resulting in Eq. 5.2.

In a similar way, the intra-pair separation for attractive dipole-dipole interaction can be derived:

$$S(t)^5 = S(0)^5 - \frac{45}{32} \frac{\mu_0 m_1 m_2}{\pi^2 \eta R} t \quad \text{for } S(t) \geq 2R . \quad (\text{A.8})$$

Note this case applies to separated particle pairs $S(0) \geq 2R$ in an in-plane magnetic field. Furthermore, the magnitude of the magnetic dipole-dipole force for rejoining particles is twice that of repelling particles.

5.B Hydrodynamic interactions between particles

In a Stokesian regime, a particle moving in a liquid medium induces a variation in the fluid velocity field. In a multi-particle system, this effect causes the movement

of one particle to induce a hydrodynamic interaction force on another particle. To estimate the effect of these hydrodynamic interactions between separating particle pairs, we numerically simulate the particle separation behavior, using a forward Euler algorithm that was reported by Von Hansen et al.¹⁷⁹ and Sing et al.¹⁹⁶ In particular, the time discretized form of the Langevin equation for the equation of motion is given by

$$\mathbf{r}_i(t + \Delta t) = \mathbf{r}_i(t) + \boldsymbol{\mu}_{\text{self}}(z_i) \cdot \mathbf{F}_i + \boldsymbol{\mu}_{\text{RBP}}(\mathbf{r}_i, \mathbf{r}_j) \cdot \mathbf{F}_j \quad (\text{B.1})$$

in which \mathbf{r}_i is the position of particle i , Δt is the numerical time-step and \mathbf{F}_i is the net force acting on particle i . To determine the net force on the particle, we include magnetic forces and excluded volume forces¹⁹⁶ between the particles and the surface. Furthermore, $\boldsymbol{\mu}_{\text{self}}(z_i)$ is the self-mobility tensor of particle i , which depends on the distance of the particle to the surface ($z = 0$). Note that the entries of the self-mobility tensor is equal to the inverse of the Stokes drag corrected using the correction factors as reported by Leach et al.¹⁸⁰ (which we incorporated in Eq. A.5 for parallel displacement along the surface). To account for the hydrodynamic interactions due to other particles that are moving near a non-slip wall ($z = 0$), we use a Rotne-Prager-Blake tensor, $\boldsymbol{\mu}_{\text{RBP}}(\mathbf{r}_i, \mathbf{r}_j)$ as an approximation^{179, 196}. This tensor does not only account for the hydrodynamic drag on particle i resulting from an external force acting on particle j , but also accounts for the interaction with the image of particle j with respect to the surface as well as for Stokes and source doublets at the position of the image. For the exact equations and further background on the approximation, see von Hansen et al.¹⁷⁹.

Using this approach, we can compare the separation behavior of pairs of particles without hydrodynamic interactions to the separation including hydrodynamic interactions. To allow for an exact comparison, Brownian motion was not included in the model. In Figure B.1 the computed separation of 2.8 μm M270 particles and 1.0 μm MyOne particles is plotted. As expected, hydrodynamic interactions reduce the particle velocity. As in intra-pair magnetophoresis the magnetic moment of the particles is determined, we determine the influence of hydrodynamic interactions on the measured magnetic moment, by applying Eq. 5.2. Compared to the inserted value of the magnetic moment, we find that neglecting hydrodynamic interactions causes an underestimation of the magnetic moment by $\sim 0.8\%$ and $\sim 0.2\%$, for the 2.8 μm and 1.0 μm particles respectively.

We reason that the effect of hydrodynamic interactions on the particle separation in time is minor because only two particles are interacting, and only initially these particles are in close contact. Due to hydrodynamic interactions, both particles move away from each other at a slightly smaller velocity, but in time this is compensated by the repulsive magnetic dipole-dipole interaction force, which is stronger ($F_{\text{dd}} \propto r^{-4}$) compared to the case the particles would have already separated further away.

In conclusion, by comparing numerical simulations of the separation of particle pairs with and without hydrodynamic interactions, we conclude that hydrodynamic interactions have only a minor influence on the particle separation and on the mag-

netic moments determined from the measurements. Neglecting the hydrodynamic interactions in the fits of intra-pair magnetophoresis data causes a slight underestimation of the magnetic moments, by about 0.8% for the 2.8 μm particles and about 0.2% for the 1.0 μm particles.

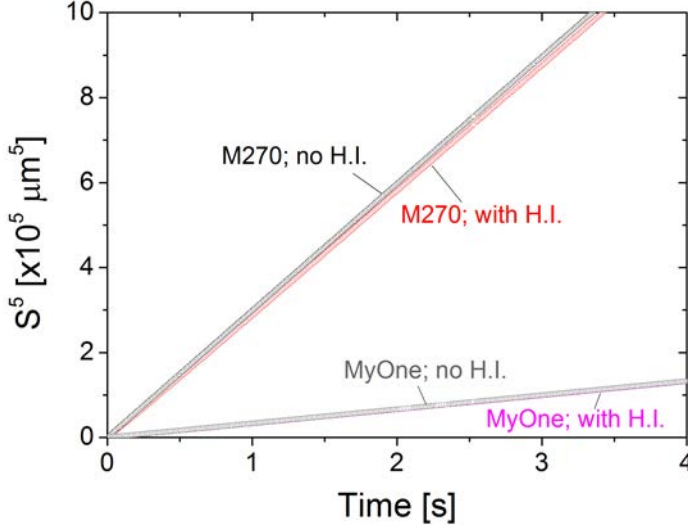


Figure B.1 Computed trajectories of M270 and MyOne particle pairs, with and without hydrodynamic interactions (H.I.) between the particles. The numerical timestep was 10 μs , but the plotted curves contain timesteps of 0.01 s. In case of the MyOne particle pairs, both curves mainly overlap. Using Eq. 5.2, we determine the magnetic moment of the particles.

5.C Electrostatic interactions between particles

As colloidal particles generally carry a surface charge, electrostatic interactions might affect the particle-pair separation behavior. Here we estimate and compare the repulsive electrostatic forces that are mutually exerted by the particles. Between two particles in a liquid medium, the electrostatic (double-layer) interaction energy between two spheres of equal size and at a surface-to-surface separation x , is¹²⁸

$$E_{es} = \frac{R}{2} Z \exp(-\kappa x). \quad (\text{C.1})$$

Here κ is the inverse Debye length, which depends on the ionic strength of the liquid medium, and Z is the interaction potential, which depends on the surface potential ψ_0 of both surfaces and on the dielectric constant of the medium ϵ , i.e.

$$Z = 128\pi\epsilon\epsilon_0 \left(\frac{k_B T}{e} \right)^2 \tanh\left(\frac{ze\psi_0}{4k_B T} \right), \quad (\text{C.2})$$

with z the valency of the electrolyte. As an approximation of the surface potential, we use the Zeta potential of the particles which we measured using a Malvern

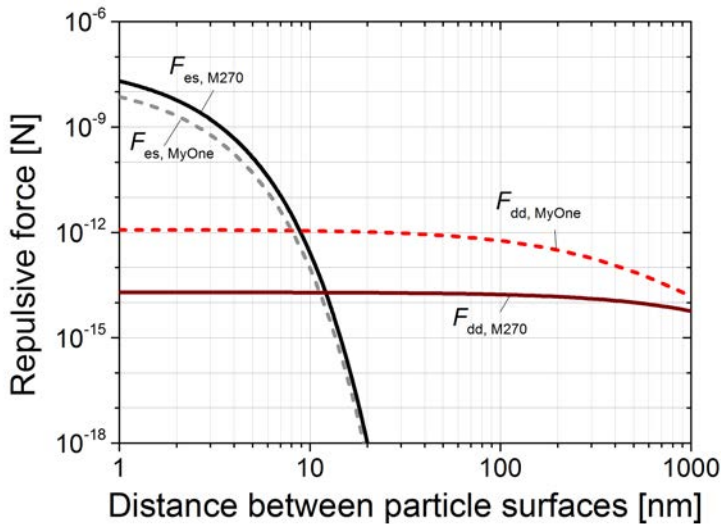


Figure C.1 Comparison between the electrostatic interaction and the magnetic dipole-dipole interaction between the paired particles. Interactions were computed for both the $\varnothing 2.8 \mu\text{m}$ M270 particles (solid lines) and $\varnothing 1.0 \mu\text{m}$ MyOne particles (dashed lines) at an external field strength of 1 mT.

Zetasizer nano ZS. The zeta-potential for all particles (M270, Micromer and MyOne) was found to range between ~ -30 and -50 mV at pH = 7.4 (i.e. in PBS). Note that all surfaces were carboxylated, i.e. containing acidic end-groups.

Using Eq. C.1 and C.2, we can compute the strength of the repulsive electrostatic force on each particle and compare this to the weakest force that was obtained for the magnetic dipole-dipole interaction, i.e. the repulsive force at $B = 1$ mT. As shown in Figure C.1, the electrostatic interaction is only significant at a distance of up to about 10 nanometers. This distance is small compared to the distances measured using intra-pair magnetophoresis: from 100 nm up to 10 to 20 μm (see Figure 5.2). As a result, the separation behavior might only be affected during the first 100 ms after application of the out-of-plane magnetic field. Moreover, in case electrostatic interactions would have been significant, the 5th power of the separation would not depend linearly on time. However, as can be seen in the inset of Figure 5.2, such nonlinearity is not observed, indicating that the electrostatic repulsion does not cause a significant additional separation of the particles during the measurement.

Based on these arguments, it is concluded that electrostatic repulsion does not have a measurable influence on the intra-pair separation behavior of the particle pairs, and thus does not influence the characterization of the magnetic moment.

5.D Translating a pair distribution into a single moment distribution

The method used to determine the single moment distribution from the measured pair-averaged moment distribution is described here. First we describe how a pair-averaged distribution follows from the original distribution and subsequently the applied fitting routine is explained.

To determine the transformation of an original distribution to a pair-averaged distribution, we first inspect the representation of our measurement data. The pair-averaged distribution in Figure 5.5a is a plot of two arrays, i.e. one array containing the values of the magnetic moment, $\mathbf{m}_{\text{pair-averaged}}$, and another array containing the relative probability, $\mathbf{p}_{\text{pair-averaged}}$. As an example, let us assume an original distribution function $\mathbf{p}(\mathbf{m})$ containing peaks at $m = 2$ and $m = 4$, i.e. $\mathbf{m} = [1 \ 2 \ 3 \ 4 \ 5]$ and $\mathbf{p} = [0 \ 1 \ 0 \ 1 \ 0]$. From the original distribution, the pair distribution may be obtained by first multiplying each value of \mathbf{p} with all values of \mathbf{p} , which corresponds to multiplying two magnetic moments, each independently picked from the original distribution:

$$\mathbf{pp}^T = \begin{bmatrix} 0 \\ 1 \\ 0 \\ 1 \\ 0 \end{bmatrix} \begin{bmatrix} 0 & 1 & 0 & 1 & 0 \end{bmatrix} = \begin{bmatrix} 0 & 0 & 0 & 0 & 0 \\ 0 & 1 & 0 & 1 & 0 \\ 0 & 0 & 0 & 0 & 0 \\ 0 & 1 & 0 & 1 & 0 \\ 0 & 0 & 0 & 0 & 0 \end{bmatrix},$$

$$\mathbf{pp}^T = \begin{bmatrix} 0 \\ 1 \\ 0 \\ 1 \\ 0 \end{bmatrix} \begin{bmatrix} 0 & 1 & 0 & 1 & 0 \end{bmatrix} = \begin{bmatrix} 0 & 0 & 0 & 0 & 0 \\ 0 & 1 & 0 & 1 & 0 \\ 0 & 0 & 0 & 0 & 0 \\ 0 & 1 & 0 & 1 & 0 \\ 0 & 0 & 0 & 0 & 0 \end{bmatrix},$$

with corresponding moments,

$$\mathbf{mm}^T = \begin{bmatrix} 1 \\ 2 \\ 3 \\ 4 \\ 5 \end{bmatrix} \begin{bmatrix} 1 & 2 & 3 & 4 & 5 \end{bmatrix} = \begin{bmatrix} 1 & 2 & 3 & 4 & 5 \\ 2 & 4 & 6 & 8 & 10 \\ 3 & 6 & 9 & 12 & 15 \\ 4 & 8 & 12 & 16 & 20 \\ 5 & 10 & 15 & 20 & 25 \end{bmatrix}.$$

In order to obtain a pair distribution with constant bin-sizes (e.g. bins with $\Delta m = 2$), the above matrices are converted into arrays as:

$$\mathbf{m}_{\text{pair}} = [2 \ 4 \ 6 \ 8 \ 10 \ 12 \ 14 \ 16 \ 18]$$

$$\mathbf{p}_{\text{pair}} = [0 \ 1 \ 0 \ 2 \ 0 \ 0 \ 0 \ 1 \ 0]$$

Going from the pair distribution to the pair-averaged distribution, we take the square-root of the moment values and redistribute the measured counts into an equally binned distribution, which leads to

$$\begin{aligned} \mathbf{m}_{\text{pair-averaged}} &= [0.5 \quad 1 \quad 1.5 \quad 2 \quad 2.5 \quad 3 \quad 3.5 \quad 4 \quad 4.5] \\ \mathbf{p}_{\text{pair-averaged}} &= [0 \quad 0 \quad 0 \quad 1 \quad 0 \quad 2 \quad 0 \quad 1 \quad 0] \end{aligned}$$

This example shows that indeed three peaks appear in the pair distribution, namely at $\sqrt{m_1^2}$, $\sqrt{m_1} \cdot \sqrt{m_2}$ and $\sqrt{m_2^2}$, as is expected for an original distribution containing $m_1 = 2$ and $m_2 = 4$.

As shown in the example above, we can compute the pair-averaged moment distribution starting from the original single particle moment distribution. Conversely, we use this technique to propose a single particle moment distribution and then iteratively modify the proposed distribution to achieve a good fit to a measured pair distribution. We apply an iterative least-squares optimization routine and for the original distribution we use a parameterized peak function with three underlying parameters, namely the peak position c , the width w and the asymmetry a . The function was reported before for similar data transformation purposes. We will briefly describe the function here; for more details, see reference¹⁹⁷.

The used function $P(\delta, c, w, a)$ describes a smooth peak function in the range of $0 \leq \delta \leq 1$,

$$P(\delta, c, w, a) = \frac{\sin^2(\pi\delta)\Gamma(w+1)}{\Gamma(wg(\delta, a)+1)\Gamma(w-wg(\delta, a)+1)} c^{wg(\delta, a)} (1-c)^{w-wg(\delta, a)}, \quad (\text{D.1})$$

where δ corresponds to the normalized magnetic moment within a certain range of moments, i.e., $0 \leq m \leq m_{\text{max}}$:

$$\delta = \frac{m}{m_{\text{max}}}. \quad (\text{D.2})$$

In Eq. D.1 Γ is the Euler Gamma function, and the function $g(\delta, a)$ is a transformation of $\delta \rightarrow g(\delta, a)$ which introduces the asymmetry to the peak function

$$g(\delta, a) = (1+a)\delta + x\delta^2 + y\delta^3 + z\delta^4. \quad (\text{D.3})$$

The coefficients x , y and z are chosen such that (i) in case of zero asymmetry, $g(\delta, 0) = \delta$, (ii) the end-points of the function are unchanged, i.e. $g(0, a) = 0$ and $g(1, a) = 1$, and (iii) the peak position $\delta = \delta_{\text{peak}}$ is unchanged, i.e.

$$g(\delta_{\text{peak}}, a) = \delta_{\text{peak}} \quad \text{and} \quad \left. \frac{dg}{d\delta} \right|_{\delta=\delta_{\text{peak}}} = 1.$$

Applying this function in the fitting routine, first a choice has to be made in the range of moments ($0 \leq m \leq m_{\text{max}}$) over which the function is calculated. The range was chosen wider than the range in which pair-averaged values were found. For example, in case of the M-270 particle, m_{max} was chosen to be $13 \times 10^{-14} \text{ Am}^2$, while

measured pair-averaged moments only reached $10 \times 10^{-14} \text{ Am}^2$. Second an initial guess of all parameters was made, i.e. $c = 0.5$ (corresponds to a peak at the center: $\delta_{\text{peak}} = 0.5$), $w = 5$ (corresponds to a broad peak), and $a = 0$ (corresponds to no asymmetry). After the initialization, the three peak parameters were fitted one after another and the process was repeated until convergence was obtained.

We note that several parameterizations can be used to solve the transformation problem. The validity of the used parameterization is determined by comparing the calculated pair distribution with the measured pair distribution, see Figure 5.5a. The accurate description of the data makes us conclude that the used parameterization is suited to retrieve the single particle moment distributions. In case the measured distribution would contain more than one peak or a different shape, one may need to use superpositions of Eq. D.1 or other more suitable functions (e.g. see reference ¹⁹⁸).

5.E Gaussian distributions: change in width by pair-averaging

Here, an equation is derived to determine the change in width of a Gaussian distribution in the magnetic moment per single particle, $\sigma_{m_1} = \sigma_{m_2} = \sigma_m$, as compared to width in the pair-averaged distribution, $\sigma_{m_{av}} = \sigma_{\sqrt{m_1 m_2}}$. In case both m_1 and m_2 are randomly taken from the same population with $\sigma_{m_1} = \sigma_{m_2} = \sigma_m$, and their average value is measured, i.e. $m_{av} = \sqrt{m_1 m_2}$ with $\sigma_{m_{av}} = \sigma_{\sqrt{m_1 m_2}}$. Then the resulting standard deviation in the pair-averaged moment is given by

$$\sigma_{m_{av}} = \sqrt{\left(\frac{\partial m_{av}}{\partial m_1}\right)^2 \sigma_{m_1}^2 + \left(\frac{\partial m_{av}}{\partial m_2}\right)^2 \sigma_{m_2}^2}. \quad (\text{E.1})$$

Filling in the definition for the pair-averaged moment: $m_{av} = \sqrt{m_1 m_2}$, we obtain

$$\sigma_{m_{av}} = \sigma_m \sqrt{\left(\frac{\sqrt{m_2}}{2\sqrt{m_1}}\right)^2 \sigma_{m_1}^2 + \left(\frac{\sqrt{m_1}}{2\sqrt{m_2}}\right)^2 \sigma_{m_2}^2}. \quad (\text{E.2})$$

Finally, we use $m_1 \pm \sigma_{m_1} \approx m_2 \pm \sigma_{m_2} \approx m \pm \sigma_m$ (which is valid in case of many measurements on different two-particle clusters), we obtain:

$$\sigma_{m_{av}} = \frac{1}{\sqrt{2}} \sigma_m. \quad (\text{E.3})$$

From this it follows that the width in the pair-averaged distribution differs from the width in the original (Gaussian) distribution, by a factor of $2^{-0.5}$.

5.F Influence of the magnetic field due to particle magnetization

We analyzed the influence of the particle magnetization on the magnetic field of a neighboring particle at an intra-pair separation distance r . First of all, we consider the magnetic field due to a magnetic dipole:

$$\mathbf{B}_{\text{moment}}(\mathbf{r}) = \frac{\mu_0}{4\pi} \left[\frac{3\mathbf{r}(\mathbf{m} \cdot \mathbf{r})}{r^5} - \frac{\mathbf{m}}{r^3} \right]. \quad (\text{F.1})$$

In case the external magnetic field, and as a result the magnetic moment, is oriented in the $+\hat{\mathbf{e}}_z$ direction, the magnetic field at a position next to the location of this moment (i.e. in the plane $z = 0$) is given by

$$\mathbf{B}_{\text{moment}} = -\frac{\mu_0}{4\pi} \frac{m}{r^3} \hat{\mathbf{e}}_z \quad \text{for } z = 0 \text{ and } r \neq 0. \quad (\text{F.2})$$

Using Eq. F.2, we estimate the magnetic field due to a neighboring dipole moment with size m for any given intra-particle separation distance. Using the measured magnetization curves, as shown in Figures 3 and S5, we computed the ratio between the external field B_{ext} and the field induced by a neighboring magnetic moment B_{moment} , as is shown in Figure F.1. From Figure F.1a, it follows that for the Dynal M-270 particles, the maximum reduction in field strength is in any case less than 4%. Furthermore, the relative reduction in field strength falls off rapidly with increasing intra-particle distance, as also follows from Figure F.1b. Comparing this to the measured data in Figure 5.2, only a minor effect would be expected in the first ~ 0.1 seconds after applying the external field, while measurement data over 5 seconds may be recorded. Furthermore, in case this effect would be significant, non-linearity should be observed for the r^5 -dependence in the inset of Figure 5.2, which we do

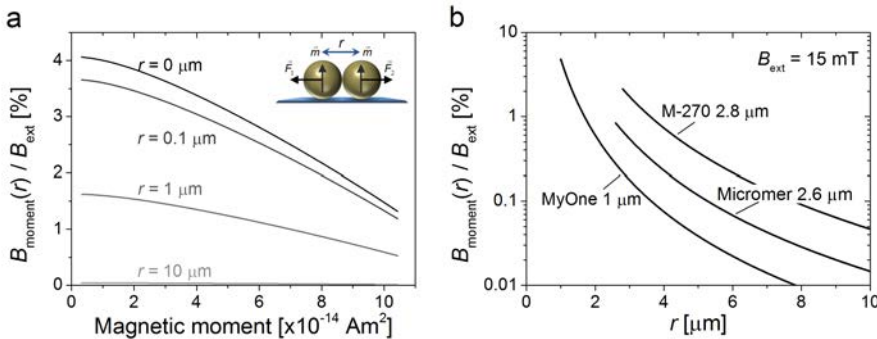


Figure F.1 Effect of the magnetic field due to magnetic particle magnetization B_{moment} compared to the external field B_{ext} . (a) Magnetic induction due to a magnetized particle at distance r , relative to the external magnetic field due to the electromagnets. Data corresponds to Dynal M-270 ($2.8 \mu\text{m}$) particles. Note that B_{ext} is related to the magnetic moment based on the magnetization curve in Figure 3. Data is shown for different particle intra-pair separation distances r . (b) Magnetic induction due to a magnetized particle in an external field of 15 mT, for different particle types.

not observe. Therefore we conclude that magnetization effects on particle-pairs contribute a negligible effect on the magnetic field strength experienced by the particles.

5.G Estimation of the smallest particle size for intra-pair magnetophoresis

The smallest magnetic particle size that may be characterized with intra-pair magnetophoresis is foremost limited by the in-plane alignment of the particle pairs, prior to the application of the out-of-plane magnetic field. Only if the out-of-plane field is orthogonal to the particle pair axis, will a repulsive force be exerted on the particle. For in-plane alignment, an in-plane magnetic field is applied. Brownian motion of the particles, however frustrates in-plane alignment. Estimating the magnetic alignment energy as a function of particle size, and comparing this to thermal energy, allows an estimation of the minimum particle size that is suited for intra-pair magnetophoresis.

The alignment of particle pairs to the physical surface is achieved using in-plane magnetic fields. From the dipole-dipole interaction (see Eq. A.2, the first term), it follows that the energetic minimum of this interaction is at alignment of the magnetic moments. Based on the dipole-dipole interaction, we can estimate the probability that particle pairs (radius R) stay aligned with the external field with an angular deviation less than α , by assuming a Boltzmann distribution for the different states of alignment. More precisely, we define α to be the angle between the moment vector and the center-to-center vector. The resulting probability function is then equal to:

$$P(R) \propto \exp\left(-\frac{F_{dd} \cdot h}{kT}\right) = \exp\left(-\frac{\frac{3\mu_0 m^2}{4\pi R^4} [1 + 2 \cos(\alpha) - 5 \cos^2(\alpha)] \cdot 2 \sin(\alpha)}{kT}\right). \quad (\text{G.1})$$

Assuming that the magnetic content scales proportionally to the particle size, R^3 , and using the magnetic moment found for the Dynal MyOne particles as a reference, we can now estimate the probability that particle-pairs stay aligned in the field with a deviation of less than 5° . From Figure G.1 it follows that particle-pairs with a radius larger than ~ 100 nm stay aligned with the in-plane magnetic field within 5° . For these particle sizes, the out-of-plane magnetic field, which immediately follows the in-plane field, will induce repulsive interactions. Note however that for particles with a smaller radius (e.g. ~ 75 nm), still $\sim 80\%$ of the particle-pairs will be aligned within 5° , and thus also allow intra-pair magnetophoresis, albeit with a decreased efficiency. Taking this into account, we estimate that the minimum particle size for which repulsion should be observable, is about 50 nm in particle radius. It should be noted that besides the magnetic dipole-dipole interactions, also a magnetic field gradient oriented toward the surface will improve the in-plane alignment of the particle pairs.

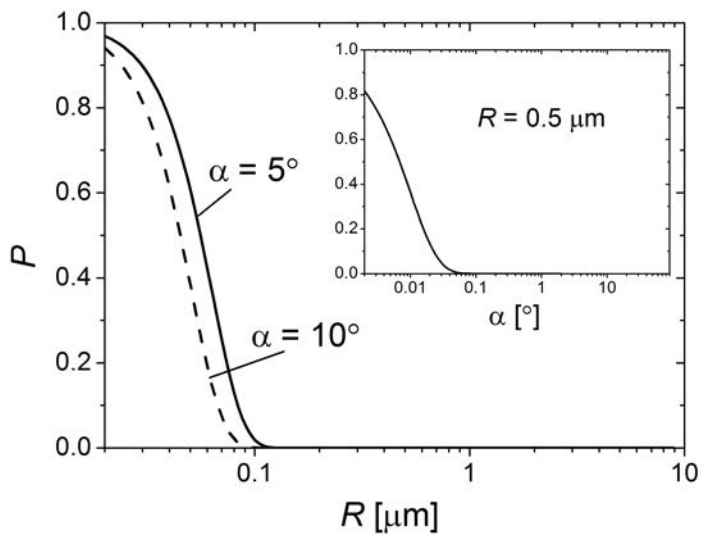


Figure G.1. Probability of particle-pair alignment with an external field with an angular deviation of less than $\alpha = 5, 10$ degrees, as a function of the particle radius. The inset shows the probability of field alignment within less than α for particles with a radius of $0.5 \mu\text{m}$ (i.e. corresponding to Dynal MyOne particles).

6

Magnetic field-induced rotaphoresis for controlled redistribution of magnetic particles over a surface

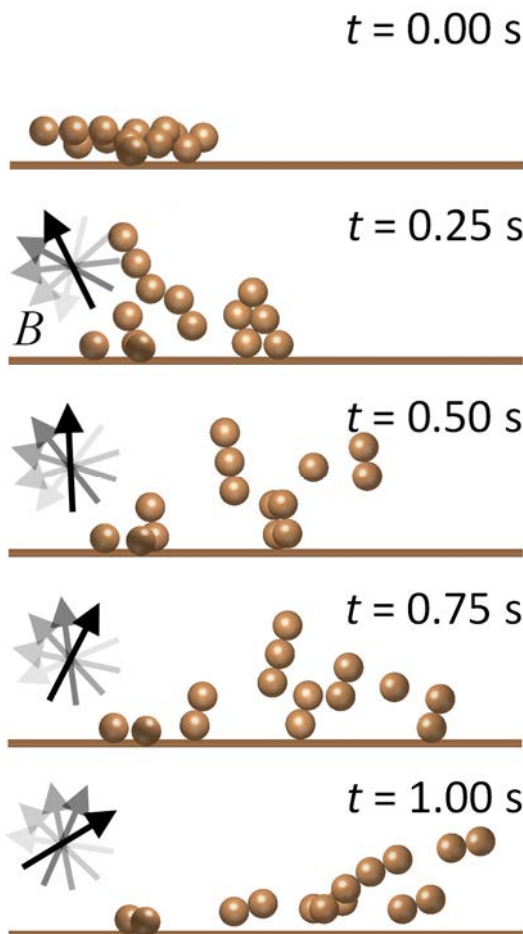
*Optimal performance of magnetic particle-based assays in lab-on-chip devices requires a high level of control over the behavior of magnetic particles. By the application of magnetic fields, both the individual and the collective behavior of the particles can be manipulated. However, this ability is often accompanied by the aggregation of the magnetized particles as well as the drift of particles towards external magnets. Here, we report a method to overcome these effects by magnetic field-induced rotaphoresis: the conversion of rotational motion of particles near a surface into effective translational motion. Using experiments and numerical simulations, we show that particles in the vicinity of a physical surface can be moved along the surface at several mm/s by using an out-of-plane rotating magnetic field. In addition, we show that particle clusters within the ensemble are completely disaggregated within a few seconds by increasing the frequency of the rotating field and by modulating its amplitude. We demonstrate that this method is effective for particles with various sizes and surface properties. As only externally generated magnetic fields are used, magnetic field-induced rotaphoresis is a useful tool in the development of stationary-fluidic assays on a chip.**

*This chapter is in preparation for publication: A. van Reenen, A.M. de Jong, and M.W.J. Prins, Magnetic Rotaphoresis for Controlled Assembly of Colloidal Magnetic Particles at a Solid-Liquid Interface.

6.1 Introduction

Magnetic particles are effectively applied in lab-on-chip systems to perform separation, purification and immunoassays.^{13, 18, 82} In such applications, magnetic particles are used as carriers, substrates or labels because magnetic particles are very versatile: magnetic particles rapidly capture analytes from a liquid due to their high surface-to-volume ratio and have adaptable surface properties;^{25, 28, 82} magnetic particles can be manipulated by using externally generated magnetic fields;^{25, 115, 119} and magnetic particles can be sensitively detected with magnetic and optical fields^{25, 103, 199}. In many microfluidic systems, fluids are actively moved on the chip; however, the application of magnetic fields to magnetic particles removes the necessity to actuate fluids, as the particles themselves can be used as the moving components inside the fluid, with advantages for miniaturization, integration, reliability and cost-effectiveness.

The use of magnetic particles to control assays consisting of multiple process steps, such as washing steps⁹⁻¹¹, buffer exchange⁹⁻¹¹, analyte capture from liquid^{25, 28,}



⁸², sandwich formation^{25, 62, 103} and detection^{25, 62, 200}, requires that the particles maintain their effectiveness over all these steps, and thus that their behavior and distribution within the fluid volume can be controlled. Unfortunately, a high level of control over magnetic particles is frustrated by the effect of particle aggregation in a magnetic field due to magnetic dipole-dipole interactions. Furthermore, external (electro)magnets ultimately act as magnetic point-sources to which particles are at-

Figure 6.1 Schematic overview of rotaphoresis applied to an ensemble of magnetic particles near a surface. The particles are kept near the surface for example by an applied field gradient. In addition, a rotating magnetic field is applied, rotating out-of-plane, i.e. rotating in the plane perpendicular to the surface. The field applies a torque to the aggregated particles and causes them to rotate. The interaction with the surface causes the rotating aggregates (i) to translate over the surface, (ii) to disaggregate into smaller components, and finally (iii) to evenly redistribute over the surface.

tracted, resulting in particles are attracted, resulting in undesired particle drift, which is difficult to overcome with stationary magnets.

To effectively overcome magnetic particle clustering and drift, we report the effect of rotaphoresis: the conversion of rotational motion of particles near a surface into effective translational motion, see Figure 6.1. The rotation of chains of particles has been studied before with the aim to generate fluid flow in solution⁴¹ or fluid flow near a surface¹⁹⁶; here, rotating chains are studied with the purpose to rapidly translate, disaggregate and redistribute ensembles of particles over a surface.

In the experiment, the particles are brought in the vicinity of a physical surface by a field gradient directed toward the surface, and in addition a magnetic field is applied that rotates out-of-plane with respect to the surface. The resulting rotational motion of the particle ensemble can translate the ensemble away from magnet poles, in a direction opposite to the in-plane magnetic field gradient. Furthermore, we show that particle clusters within such an ensemble can be disaggregated by increasing the frequency of the rotating field and by increasing the amplitude of the out-of-plane component of the rotating field. In experiments and numerical simulations, we demonstrate that rotaphoresis can be used to displace and disaggregate magnetic particles with various sizes and surface properties. As only externally generated magnetic fields are used, the approach is suited for application in particle-based microfluidic assays that are entirely controlled by magnetic fields.

6.2 Experimental section

To show the broad applicability of the approach, several types of magnetic particles were used in experiments. Most experiments were performed using 2.8 μm diameter carboxyl M270 particles from Dynal Biotech. Other particles that were used are, from large to small size: 2.8 μm diameter streptavidin-coated M270 particles from Dynal Biotech; 2.6 μm diameter carboxyl micromer particles from Micromod; 1.0 μm diameter carboxyl and streptavidin MyOne particles from Dynal Biotech; and 500 nm diameter carboxyl and streptavidin MasterBeads from Ademtech. Particles were suspended in undiluted phosphate buffered saline containing 0.1% bovine serum albumin (Merck) and 0.02% Tween-20 (Thermo Scientific).

Particle suspensions (of about 0.5 mg/mL) were pipetted in 38 μL fluid chambers, assembled by attaching adhesive Secure-Seal™ Hybridization chambers (\varnothing 9 mm, height = 0.6 mm; Electron Microscopy Sciences) to a glass cover slip (22×22 mm² from VWR) that was cleaned beforehand using isopropanol. On the non-adhesive side, the Hybridization chambers contained a 0.25 mm thick polycarbonate sheet containing two inlets to fill the 38 μL incubation chamber. This sheet was transparent to allow imaging from this side using a microscope (Leica DM6000). Before an experiment, the incubation chamber was filled with assay buffer containing no particles for 30 minutes to block the chamber walls. After blocking, the assay buffer was removed from the fluid chamber and the chamber was filled with the particle suspension. To prevent evaporation losses, the fluid chamber was sealed using adhesive port seals as supplied together with the Hybridization chambers.

To apply magnetic fields to the suspended particles, the fluid chamber was placed in a 5-pole electromagnet setup as shown in Figure 6.2. The setup consists of a quadrupole electromagnet (800 windings with $\varnothing 0.25$ mm copper wires) to generate magnetic fields, oriented in-plane with respect to the bottom surface of the fluid chamber (see Figure 6.2a,c). In addition, a separate electromagnet (1600 windings with $\varnothing 0.25$ mm copper wires) is positioned below the center of the quadrupole electromagnet to generate perpendicular fields. Using the quadrupole electromagnet, magnetic fields can be generated that rotate in-plane, whereas by combining the bottom electromagnet with two opposite electromagnets of the quadrupole, magnetic fields can be generated that rotate out-of-plane. To guide field lines to the incubation chamber, soft iron parts were implemented in the setup.

The electromagnets were powered separately using a controller that was steered by LabView software. Applied actuation protocols varied in time in terms of the amplitude, frequency and shape (i.e. sinusoidal) of the current. The calibration of the magnetic field was performed using a Gauss meter (5100 series F.W. Bell) and can be found in Appendix 3.A in Chapter 3.

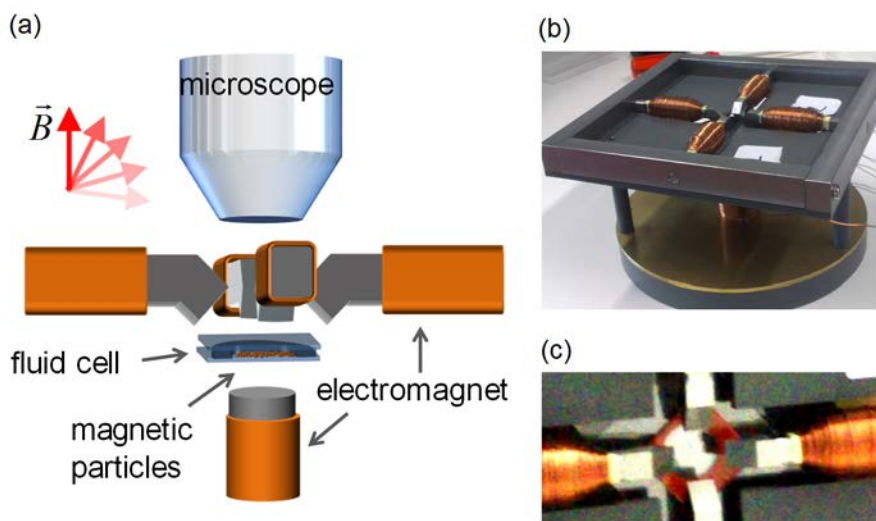


Figure 6.2 A 5-pole electromagnet was used to apply fields in all directions. The setup consists of a quadrupole electromagnet and a separate electromagnet oriented orthogonal with respect to the center of the quadrupole. (a) Schematic drawing of the center of the setup, indicating the position of the magnets and the microscope with respect to the fluid cell. (b) Picture of the 5-pole electromagnet system. The quadrupole electromagnets are connected via a soft-iron yoke, to guide the field lines. (c) Picture of the fluid cell positioned within the center of the 5-pole electromagnet (compare to panel a).

6.3 Numerical methods

A numerical model (Matlab, Mathworks) based on Brownian dynamics was used to simulate the response of ensembles of magnetic particles to applied magnetic fields.

Several methods have been reported to numerically simulate multi-particle behavior away from a surface⁴¹ or near a surface¹⁹⁶. The Brownian dynamics simulation¹⁷⁷ of an N -particle system involves integrating the following Langevin equation:

$$\frac{\partial}{\partial t} \mathbf{r}_i = \sum_j^N \left(\boldsymbol{\mu}_{ij} \cdot \nabla_{\mathbf{r}_j} U(t) + \nabla_{\mathbf{r}_j} \cdot \mathbf{D}_{ij} \right) + \mathbf{v}_i^{\text{ran}}(t), \quad (6.1)$$

where \mathbf{r}_i is the position of particle i and $\boldsymbol{\mu}_{ij}$ is the mobility matrix approximated by the Rotne-Prager-Blake tensor.¹⁹⁶ In particular, this tensor accounts for the hydrodynamic interactions of particles with other particles and the surface; for the explicit entries, see for example von Hansen *et al.*¹⁷⁹. Furthermore, $U(t)$ is the time-dependent interaction potential, that takes into account magnetic dipole-dipole interactions, field gradient forces, gravitational forces, but also excluded volume forces to account for steric repulsion between particles and the surface; see Gao *et al.*⁴¹ for the implementation applied here. To include Brownian motion of the particles, a stochastic random velocity $\mathbf{v}_i^{\text{ran}}(t)$ is introduced, which follows from the fluctuation-dissipation theorem^{154, 196}:

$$\langle \Delta \mathbf{r}_i^{\text{ran}}(t) \Delta \mathbf{r}_j^{\text{ran}}(t) \rangle = 2k_B T \boldsymbol{\mu}_{ij} \delta t, \quad (6.2)$$

in which $\Delta \mathbf{r}^{\text{ran}}$ is the random position vector, which relates to the random velocity. To obtain the random displacement for each particle, we refer to the method as discussed in Chapter 4 in section 4.2. To compensate for the spatial variation in the particle mobility for Brownian motion, the term containing the diffusion tensor $\mathbf{D}_{ij} = k_B T \boldsymbol{\mu}_{ij}$ is used in Eq. 6.1.^{177, 179}

In simulations, Eq. 6.1 is solved with iterative time-steps of $\delta t = 2 \mu\text{s}$ which was found to be sufficiently small to generate constant results.^{41, 196}

6.4 Results and discussion

6.4.1 Rotaphoresis to redistribute particle clusters over a surface

When exposed to magnetic fields, ensembles of magnetic particles reduce their magnetic potential energy by forming clusters, by aligning with the fields, and by moving in the direction of field gradients. To overcome these effects, we make use of a kinetic phenomenon that we call rotaphoresis, as sketched in Figure 6.1. Rotaphoresis refers to the translation and redistribution of ensembles of particles over a surface, generated by a rotational excitation in combination with a surface interaction. The rotational excitation is applied by a rotating magnetic field and the surface interaction is controlled by a field gradient. Rotaphoresis can be achieved in various actuation configurations. A straightforward field configuration is the application of a rotating field with constant field amplitude and the normal vector of the plane of rotation parallel to the surface, as in Figure 6.1. However, the rotating field does not necessarily need to be constant, and the normal vector of the plane of rotation can also have a component along the surface normal. Therefore, we will report the induced behavior of magnetic particles for different rotaphoretic field protocols.

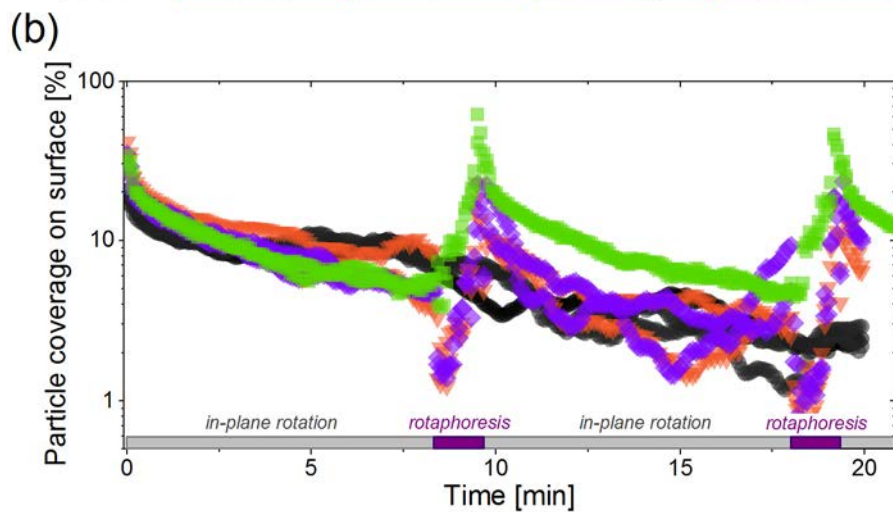
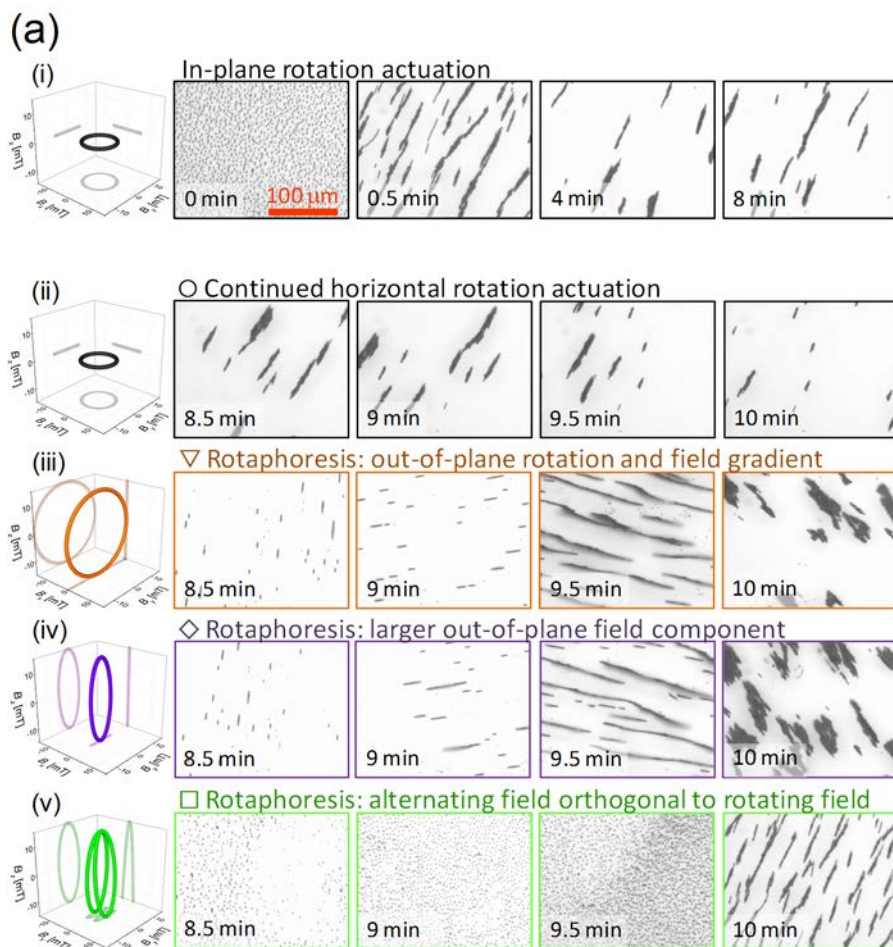


Figure 6.3 Effect of different actuation protocols to overcome aggregation and drift of 2.8 μm Dynal M-270 particles. (a) Top-view microscope images for different times and different rotaphoresis protocols. (b) From the images, the relative coverage of the surface by particles is determined and plotted in the diagram, as a function of time. The applied magnetic actuation is shown in the top-left 3D diagrams and is as follows: (i) First, aggregation and drift of particles is induced by applying for 500 seconds (~ 8.3 minutes) a magnetic field of 6 mT rotating in-plane at 0.1 Hz with respect to the surface on which the particles are initially sedimented. After 500 seconds, different actuation protocols are applied: (ii, \bigcirc) the in-plane rotating field is continued; (iii, ∇) an out-of-plane rotating magnetic field of 15 mT (20 Hz) with a field gradient of 2 T/m towards the surface. Two variations to this rotaphoresis protocol were (iv, \diamond) a modulation of the amplitude, i.e. with a high out-of-plane component of 15 mT and a small in-plane component of 5 mT, or (v, \square) a similar amplitude modulation combined with a small alternating field component orthogonal to the rotaphoretic field (2.5 mT, 10 Hz). To redisperse particles over the whole surface and from all sides, the field actuation was rotated clockwise over 90° (as seen from the top) for three times and applied for 20 seconds in each direction.

The rotaphoresis experiments start with a homogeneous distribution of particles on a surface (see Figure 6.3 at $t = 0$ min, particles are sedimented on a surface) to which particle clustering and drift are applied. The clustering and drift are applied by a magnetic field that rotates in-plane with respect to the surface ($B = 6$ mT; $f = 0.1$ Hz; for 0-8 min). In Figure 6.3, microscope images show that such a field causes the particles to aggregate into rotating chains of that move away from the center of the fluid chamber. As a measure for the amount of particles that are present in the center of the fluid chamber, images were processed to determine the relative surface area that was occupied by magnetic particles within the recorded field of view. As shown in Figure 6.3 (black circles), the particle coverage on the surface decreases roughly exponentially from initially about 25%, down to 2.5% after 20 minutes. After several minutes, the majority of the particles have moved to the edge of the fluid chamber, toward the poles of the external magnets. In essence, external magnets act as magnetic point sources, generating in-plane field gradients directed toward the magnets.

To move the magnetic particles away from magnetic point sources, magnetic rotaphoresis was applied. In order to move particles away from all four electromagnets of the quadrupole (see Figure 6.2c), the rotaphoretic field was applied to move particles successively for 20 seconds in all four directions (i.e., like north, east, south, west). After application of the protocol, the in-plane rotation was applied again for 500 s (8.3 min), followed by the same rotaphoresis protocol, etc..

The simplest rotaphoresis actuation protocol is applying a field that rotates out-of-plane with respect to the surface, combined with a field gradient oriented towards the surface to keep the particles near the surface. As shown in Figure 6.3 (orange triangles), this protocol causes particles to move away from the edges of the fluid chamber (e.g., see the image at $t = 9.5$ min). In particular, the particle coverage on the surface is brought back to $\sim 20\%$. However, particles are not well dispersed, but rather they are aggregated in large multi-particle clusters, as can be seen by comparing the images at $t = 0$ min and $t = 9.5$ min. As soon as the in-plane rotating field is applied again, the particle coverage drops down again to a similar percentage as for the case that no rotaphoresis would have been applied. From these results, we con-

clude that this rotaphoresis protocol allows displacing particles away from external magnetic point sources, but the particles are not redistributed and rather form large multi-particle clusters.

Based on an approach reported by Gao et al.¹¹⁵, a rotaphoresis protocol was tested with an out-of-plane component of the rotating field larger than the in-plane component. The effect is that after the application of the in-plane field (orienting clusters parallel to the surface) the stronger out-of-plane field induces repulsive magnetic dipole-dipole interactions between the particles. While disaggregation of clusters was observed in recorded movies, for high local particle concentrations the particles remain ordered as long chains, as disaggregated particles tend to stay in the plane of the rotating cluster and do not sufficiently separate to prevent aggregation. As a result, no effective particle redistribution is obtained as shown in Figure 6.3 (purple diamonds).

To solve this problem, the rotaphoretic field was made to move its orientation in three dimensions instead of two, by also powering the two magnets that are not used for generating the out-of-plane rotating field. For example, when the out-of-plane rotating field is generated by the north and south electromagnet of the quadrupole and the electromagnet below the fluid chamber, the east and west magnet are also powered using a smaller current and at a lower frequency. This causes the rotating field to change direction over time: the normal vector of the plane of rotation has a component that is parallel to the surface and a time-dependent component along the surface normal, i.e., the field shows rotation combined with a wiggling motion orthogonal to the rotation direction. As shown in Figure 6.3 (green squares) this rotaphoretic field surprisingly causes particle clusters to completely disaggregate, and evenly redistributes particles over the surface. Furthermore, the initial particle configuration and coverage are retrieved, and subsequent in-plane field rotation has a similar effect as it had at $t = 0$. Recorded movies showed in more detail that particles, as they disaggregate, move in layers over the surface. In particular, it is observed that large particle clusters move faster over the surface than small particle clusters, and non-clustered particles show almost no translational motion. On a larger scale, it is observed that dense particle concentrations move faster than dilute particle concentrations. This behavior is characteristic for effective redistribution of particles over the surface: groups of particles near the edge (e.g. the west side) of the fluid chamber rapidly move towards the center (e.g. to the east side) or another direction (e.g. to the north or south side), and leave behind smaller clusters and finally individual particles. The process stops when the particle population is diluted and redistributed.

Based on these results, we conclude that rotaphoresis is able to revert magnetically-induced drift and aggregation of magnetic particles, and to completely redistribute particles over a surface within 80 seconds. Next, we will study the applied rotaphoresis in more detail by quantifying the particle velocities and by modeling the disaggregation behavior.

6.4.2 Particle velocities induced by rotaphoresis

By means of rotaphoresis, magnetic particles can be efficiently moved over a surface. It is observed that particles move faster when the (local) particle concentration is higher, and single particles are almost immobile. We quantified the maximum rotaphoretic velocity that can be achieved, when starting out with a dense pack of particles that is centered within the fluid chamber using a small ferromagnet: see

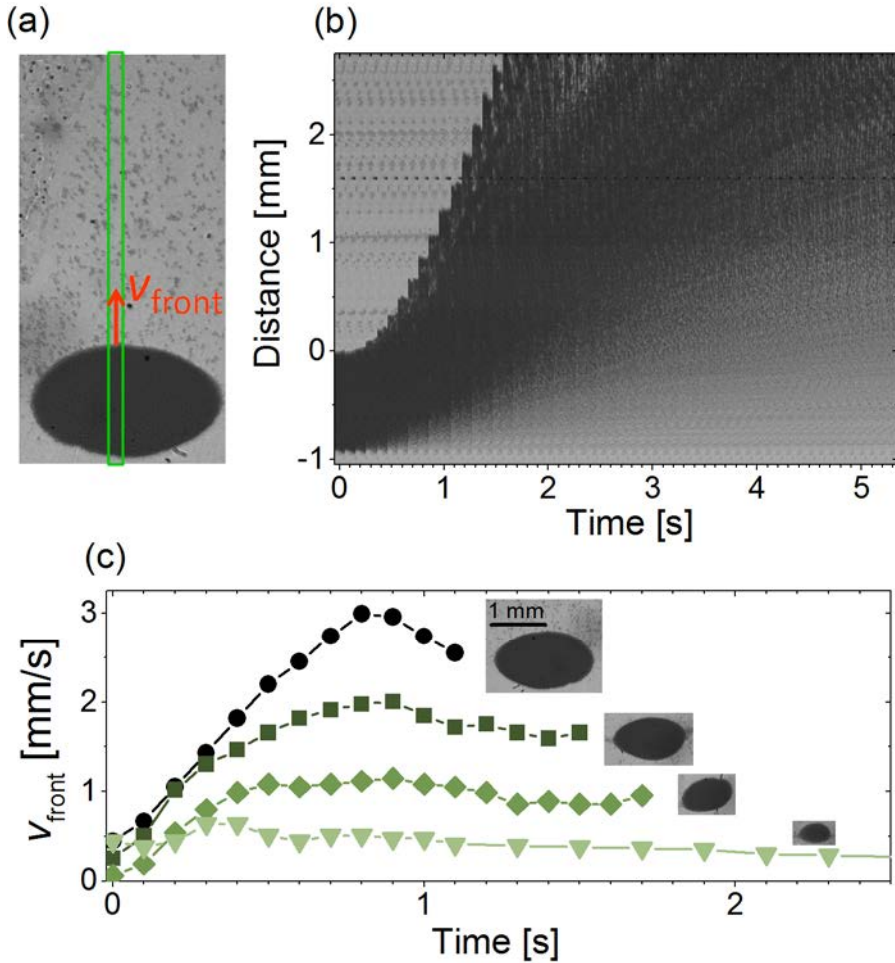


Figure 6.4 Maximum velocity induced to magnetic particles ($2.8 \mu\text{m}$ Dynal M-270 particles) by rotaphoresis. (a) Microscope image of a concentrated pack of particles with a diameter of $\sim 1.5 \text{ mm}$. The red arrow indicates the velocity of the particles at the front. The image is cropped from the sides according to the green rectangle to obtain (b) a kymograph of the response of the particles to a rotaphoretic field. (c) The velocity of the particles at the front of the pack during rotaphoresis, for different amounts of particles, as represented by the inset images with the same relative scales. Different amounts were obtained by corresponding dilutions by 1, 3, 9 and 27 times. The applied rotaphoretic field rotated out-of-plane at 20 Hz with 5 mT in-plane and 15 mT out-of-plane components, combined with an orthogonal field of 2.5 mT, alternating at 10 Hz.

Figure 6.4a. Applying rotaphoresis and recording the response, we obtain a kymograph as shown in Figure 6.4b. In the images, a gradient in image brightness is observed that appears behind the moving cluster. The gradient indicates that the particle density is reduced, in agreement with the fact that clusters break up in increasingly smaller clusters until separate particles are obtained.

From the kymograph, the velocity of the particles moving at the front can be determined; see Figure 6.4c for different amounts of particles. Particle clusters are observed to accelerate initially and for larger clusters, higher front velocities are obtained, i.e., of several mm/s. At a certain point, the front velocity saturates and thereafter decreases. Such a decrease is expected as rotaphoresis gradually lowers the local particle density. The observed maximum in the particle velocities is not determined by the magnet configuration, as for the different sizes of the packs of particles, the maximum is reached at a different position within the fluid chamber. For larger packs, the maximum is obtained over a larger distance, because it takes longer before the particle concentration at the front decreases (e.g., see the gradient in image brightness in Figure 6.4b).

Concerning the physical background of the collective particle movement, it would be interesting to numerically model the observed particle behavior. However, this is challenging, as the smallest particle cluster in Figure 6.4 contains still more than 100 000 particles. To numerically simulate such a system, for each particle Eq. 6.1 needs to be integrated, which for each particle includes calculating the hydrodynamic and magnetic interactions with the other particles. An alternative approach might be to consider the particle collection as a magneto-rheological fluid, but this is outside the scope of this Chapter.

The experimentally determined particle velocities are high, i.e., several mm/s, which is much larger than the velocities achievable by typical magnetic field gradients. For example, typical magnetic field gradients (0.1 to 10 T/m) generate magnetophoretic velocities up to few tens of $\mu\text{m/s}$ for single particles. Thus rotaphoresis is a very effective mechanism to move magnetic particles over a surface.

6.4.3 Disaggregation of particle clusters by rotaphoresis

In experimental data, rotaphoresis was observed to disaggregate large particle aggregates on almost all relevant length scales, i.e. from mm-sized aggregates down to particle clusters consisting of several particles. Here, we are interested in the final disaggregation step, where relatively small particle clusters are turned into isolated particles, as this is the most challenging to achieve. Large clusters can be broken into small clusters by applying a rotating field⁴¹ or fields in alternating directions²⁵, but more sophisticated protocols are needed in order to achieve complete disaggregation. Figure 6.5 shows that rotaphoresis is capable to disaggregate a relatively small particle cluster within two seconds. After 0.08 s, only single particles and two-particle clusters remain, demonstrating that breaking large particle clusters is easier than disaggregating two-particle clusters.

To better understand the physics underlying the rotaphoresis-induced disaggregation, we simulated a collection of N magnetic particles near a surface by num-

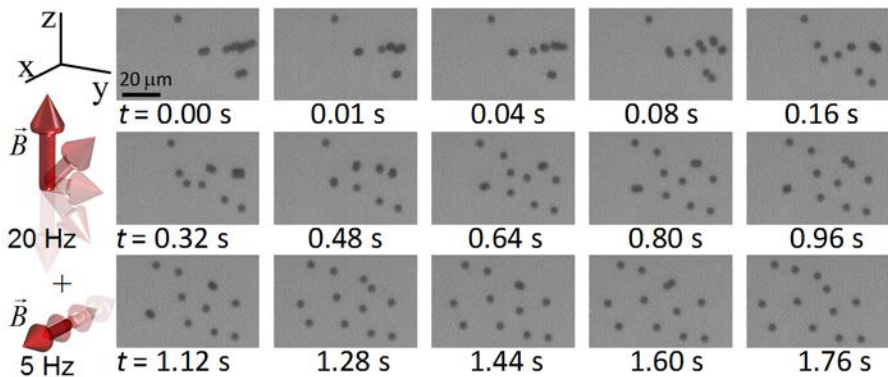


Figure 6.5 Microscope images of the disaggregation of a particle cluster by rotaphoresis. The applied rotaphoretic field rotated out-of-plane at 20 Hz with 5 mT in-plane and 15 mT out-of-plane components, combined with an orthogonal field of 2.5 mT, alternating at 10 Hz.

erically integrating Eq. 6.1. Relatively small particle clusters (e.g., $N = 14$) were simulated, to reduce computational times and efficiently study the influence of the many actuation parameters on the particle behavior.

In simulations, first the different rotaphoresis protocols were applied as in experiments corresponding to Figure 6.3: see Figure 6.6a. In an out-of-plane rotating field with constant amplitude, particles formed into rotating chains that erect themselves from the surface. Additionally applying a field gradient towards the surface, particles still formed chains, but stayed closer to the surface. When also modulating the amplitude of the rotating field such that the out-of-plane component was larger than the in-plane component, it is found that particle clusters disaggregate almost completely. Out of the 14 particles, six particles remained as two-particle clusters after two seconds of simulated time. Finally, adding also magnetic actuation in the direction orthogonal to the rotating field, it is observed that particle clusters completely disaggregate into separated particles within 0.32 seconds.

To study the two latter cases in more detail, we analyzed simulations for different sized of the in-plane and out-of-plane components of the rotating field (Figure 6.6b and c). For both cases, complete disaggregation is obtained for a limited combination of in-plane and out-of-plane fields. In case additional actuation orthogonal to the rotating field is applied, the range of possible field components is slightly broadened, but mostly for small out-of-plane components. In both cases, the possible range of in-plane field components does not increase linearly with the out-of-plane field component. This is mainly caused by the saturation in the particle magnetization within this regime¹⁶⁷, as the magnetic dipole-dipole interaction between particles depends on the particle magnetization and not directly to the external field. Importantly, these results show that complete disaggregation requires that the in-plane fields are smaller than the out-of-plane fields. Mostly likely, this is necessary to prevent the reformation of particle clusters during the actuation.

Interestingly, the simulations indicate that magnetic actuation orthogonal to the rotating field is not required to disaggregate particle clusters, in contrast to experi-

mental data shown in Figure 6.3. We attribute this to the relatively small particle cluster that was simulated. In the recorded movies, particle concentrations are such that long, linearly-shaped clusters are formed with widths of several particle diameters. These clusters are oriented in the plane of the rotating field and in-plane with

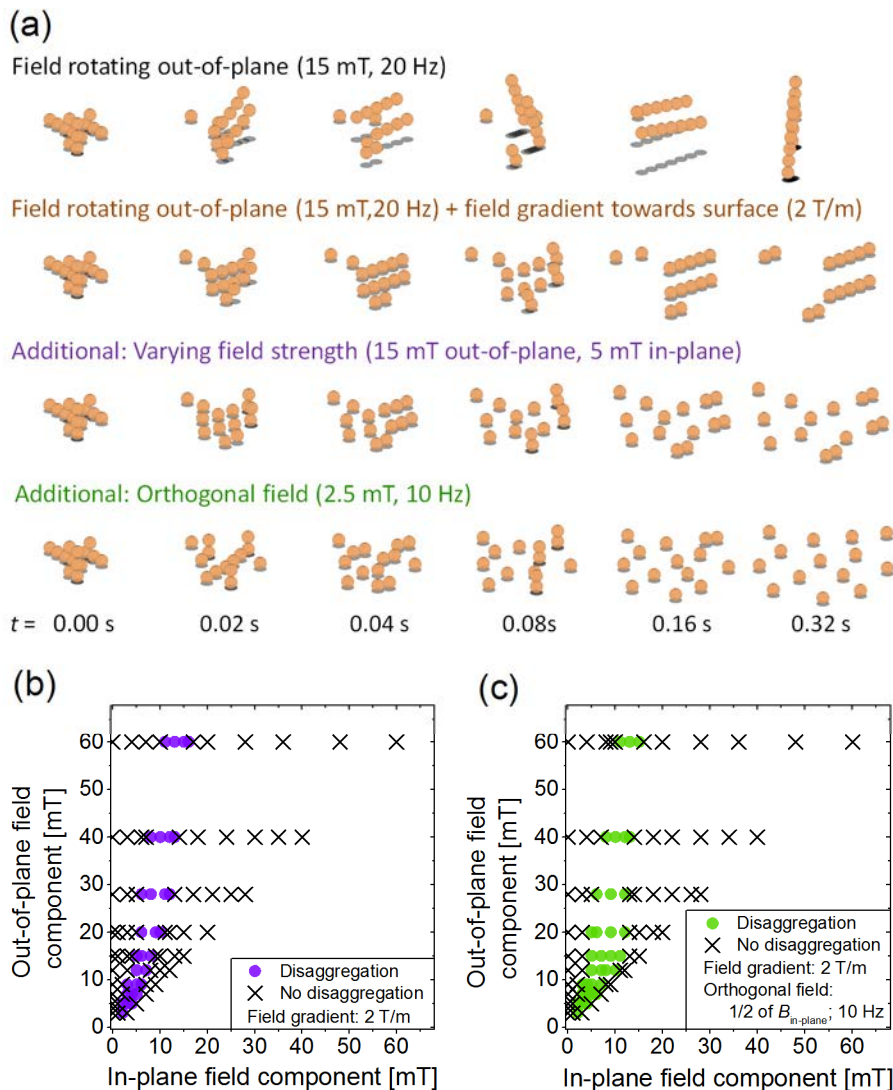


Figure 6.6 Simulation of disaggregation induced by a rotaphoretic field. (a) Snapshots of numerical simulations of a 14-particle cluster for different rotaphoretic field configurations. The shadows indicate the location of the nearby surface. (b) Influence of the relative size of the in-plane and out-of-plane field components of the rotaphoretic field, for the case that only an out-of-plane rotating (20 Hz) magnetic field is applied and a field gradient of 2 T/m. (c) Influence of the relative size of the in-plane and out-of-plane field components of the rotaphoretic field, for the case of additional actuation orthogonal to the rotating field.

respect to the surface; e.g., see the snapshot at 9.5 min in panel iv of Figure 6.3a. Such clusters are observed to only translate over the surface at a relatively low velocity. This weak response is caused by several factors. Firstly, due to the relatively high frequency of the rotating field, the required hydrodynamic drag is too high to erect such large clusters from the surface.⁴¹ Secondly, the induced repulsive forces between the particles are directed mostly towards the long axis of the clusters, and will therefore be largely cancelled. To overcome these inhibiting effects, a field can be applied orthogonal to the rotating field. Such a field will cause large particle clusters to also rotate in-plane and thereby break up in smaller clusters that can respond to the out-of-plane field rotation. The application of magnetic fields in all three dimensions therefore seems essential to control the particle disaggregation.

Obtained movies and simulations were analyzed in more detail by determining the average cluster velocities for different particle chain lengths. As shown in Figure 6.7, both in experiments and in simulations we observe dispersive translational motion, i.e., longer chains moved faster compared to shorter chains. This behavior is similar as found on a macroscopic scale (Figure 6.4). In particular, the chain velocity is found to increase almost linearly with the length of the particle chain. Larger chain lengths, however, were not observed for the applied rotaphoretic field, or only for times much shorter than the period of the rotating field. This is due to the fact that for larger chains the hydrodynamic drag is so large that the chains rapidly break up in smaller chain fragments. Shorter chains encounter less hydrodynamic resistance by their rotation, but the presence of the surface enhances the resistance to also break up these chains, down to the level of separated particles. We think that this behavior, combined with the chain-length-dependent translational motion, is the reason for rotaphoresis to be so effective in dispersing magnetic particles over a surface.

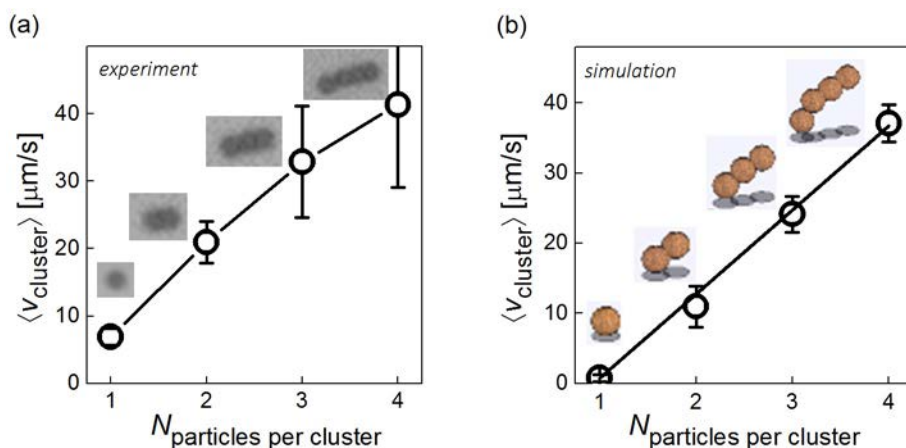


Figure 6.7 Average velocity of particle chains with different sizes, as found (a) in experiments and (b) in simulations. Errors correspond to the standard deviation in the average velocity for different clusters. The lines are drawn to guide the eye. In both cases, the rotaphoretic field rotated out-of-plane at 20 Hz with 5 mT in-plane and 15 mT out-of-plane components, combined with an orthogonal field of 2.5 mT, alternating at 10 Hz.

Table 6.1 Overview of rotaphoresis applied to different types of particles. In all cases, applied weight percentages were 0.3 mg/mL. Information on the particle size and magnetic properties were obtained either from the suppliers or from scientific literature¹⁶⁷.

Particle type	Particle diameter [μm]	Surface functionalization	Saturation magnetization [emu/g]	Maximum induced velocity [mm/s]	Disaggregation observed
Dynal M270	2.8 ± 0.1	Carboxylic acid	7.1 ± 0.5	3.0 ± 0.2	Yes
		Streptavidin		2.6 ± 0.2	Yes
		Protein G		2.7 ± 0.3	Yes
Micromod Micromer	2.6 ± 0.1	Carboxylic acid	2.6 ± 0.4	2.6 ± 0.2	Yes
Dynal MyOne	0.99 ± 0.04	Carboxylic acid	13 ± 0.1	4.0 ± 0.3	Yes
		Streptavidin		3.8 ± 0.3	Yes
Ademtech Masterbead	0.5 ± 0.1	Carboxylic acid	40 ± 5	2.7 ± 0.2	Yes
		Streptavidin		2.6 ± 0.3	Yes

6.4.4 Influence of particle size and surface functionalization

To assess the general applicability of rotaphoresis, we tested rotaphoresis on different types of magnetic particles, as listed in Table 6.1. In particular, we varied both the size and the surface functionalization of the particles. For each type, the maximum induced velocity was measured for the same weight percentage of particles in the solution (see Table 6.1). It was found for all particle types that induced particle velocities are comparable and not strongly related to the particle magnetization. Furthermore, Figure 6.8 shows that the complete disaggregation for different particles. These results show that rotaphoresis is applicable to wide range of particle types.

It is interesting that the applied protocols are still effective in case the particles are functionalized with proteins. Protein-coated particles often suffer from non-specific interactions¹²⁸ which causes adhesion between particles. The effectiveness of rotaphoretic disaggregation for functionalized particles is important, as this makes the method applicable in biological assays based on magnetic particles^{9-11, 25, 62, 200}.

Finally, we compare magnetic rotaphoresis for particle redistribution to other methods that have been reported. To redistribute particles, particle clusters need to break up and disaggregate into separate particles. A commonly applied method is to simply remove the magnetic field (e.g. see¹⁰²⁻¹⁰³) and allow Brownian motion to separate clustered particles. However, more often than not particles remain largely clustered, especially when functionalized with reactive molecules (e.g. proteins) and/or suspended in regular buffer solutions (which efficiently shield any present surface charges) or in complex matrices such as undiluted plasma (clear data on this is shown by Ranzoni et al.¹⁰³). To overcome such adhesive interactions between particles, the particle functionalization can be optimized¹⁰³ and magnetic forces can be applied. In previous work¹¹⁵, we have shown that the alternated application of in-plane and out-of-plane magnetic fields can almost completely disaggregate particle clusters containing up to 100 particles within 50 seconds. Here, we show complete disaggregation within only a few seconds. Moreover, rotaphoresis allows to simulta-

neously control the transport of particles over the surface, even in the opposite direction of magnetic field gradients.

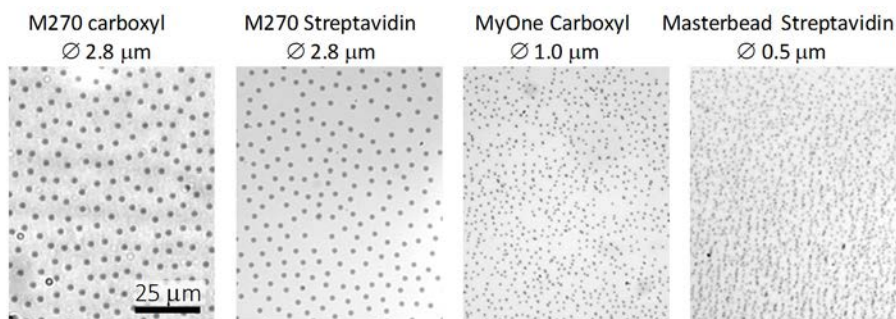


Figure 6.8 Microscope images of magnetic particle distributions after rotaphoresis for different types or functionalizations of particles. The applied rotaphoretic field is: field rotating out-of-plane at 20 Hz with in-plane component of 5 mT and out-of-plane component of 15 mT; orthogonal field of 2.5 mT alternating at 10 Hz.

6.5 Conclusions

We have developed a method to rapidly and effectively transport and redistribute collections of magnetic particles over a surface, by applying magnetic rotaphoresis. Rotaphoresis refers to the translation and redistribution of particles by a rotational excitation in combination with a surface interaction. The rotational excitation is applied by a rotating magnetic field and the surface interaction is controlled by a field gradient. Experimental data shows that magnetic particles can be moved over a surface at velocities of several mm/s. Experiments and numerical simulations demonstrate that particle clusters can be completely disaggregated within several seconds. Rotaphoresis works for particles with various sizes and surface functionalizations.

The behavior of ensembles of magnetic particles in time-dependent magnetic fields in three dimensions is complex due to the interplay between several magnetic, hydrodynamic and steric interactions. This rotaphoresis study shows that very interesting phenomena occur and that such phenomena can be highly controllable and useful. Both numerical and experimental tools have been developed to study this rather complex regime where many particles interact with the fluid, with each other and with interfaces. It will be interesting to further expand the experimental and numerical toolbox, e.g. for studies in different fluids and near fluid-fluid interfaces.

Rotaphoresis is an effective tool to improve control over magnetic particles in lab-on-chip applications where external magnets are used. We expect that rotaphoresis will be suited for application in agglutination assays¹⁰²⁻¹⁰³ and surface-based assays²⁵, where particles are used as a label to sandwich analytes respectively between two particles or between a particle and a sensor surface. Rotaphoresis may help to enhance particle-particle or particle-surface contact, or to redistribute particles for further processing. As rotaphoresis is completely controlled by externally applied magnetic fields and does not require the actuation of fluids, we believe that rotapho-

resis will be a valuable tool in the development of miniaturized, integrated, and cost-effective lab-on-chip assays that are entirely controlled by magnetic fields.

Magnetic field accelerated molecular bond formation in surface-binding assays based on magnetic particles

*Magnetic particles are used in bioanalytical assays as labels to signal specific molecular binding at a sensor surface. Here, we report on the use of magnetic fields to accelerate the target-induced binding process of magnetic particles to the sensor surface. The binding process is largely determined by the dynamic behavior of the magnetic particles, which is driven by random thermal motion supplemented with applied magnetic forces and torques. We quantify and model the remanent properties of superparamagnetic particles, by which torques can be applied. Using assay experiments and numerical Brownian dynamics simulations, we study the influence of magnetic fields to enhance the exposure of the particles to the sensor surface. We find that pulsed magnetic fields with varying orientations and field gradients can increase specific binding rates by a factor of 3 ± 1 , independent of the particle size. However, a fraction of particles with captured targets are observed to bind non-specifically to the surface. This suggests that it will be beneficial to incorporate magnetic stringency steps in the actuation protocol, in order to break weak non-specific bonds while not affecting the specific bonds. The methods presented in this Chapter allow further detailed studies on the physical and biochemical interactions in particle-based immunoassays, which are expected to lead to actuation protocols that enhance the sensitivity and specificity of magnetic particle-based detection assays.**

*Parts of this chapter have been published in: A. van Reenen, F. Gutiérrez-Mejía, L.J. van IJzendoorn and M.W.J. Prins, Torsion Profiling of Proteins using Magnetic Particles. *Biophysical Journal* **104**, 1073-1080 (2013); and other parts are in preparation for publication: A. van Reenen, A.M. de Jong, M.W.J. Prins, Magnetic field accelerated molecular bond formation in surface-binding assays based on magnetic particles.

7.1 Introduction

Micro- and nanoparticles are frequently applied as labels in affinity biosensing for the high detection signals per label, the high stability, and the convenient bio-functionalization of particles²⁰¹. A disadvantage of using such particles as labels is that they diffuse more slowly compared to molecular labels. One way to resolve the kinetics limitations is by using superparamagnetic particles which can be actuated by magnetic fields. The actuation by magnetic fields has the advantage that transport and binding can be accelerated, and that well-controlled stringency forces can be applied to the particles, resulting in rapid and compact biosensing systems^{25, 99, 103}.

An interesting question in the field of particle-based biosensors is how the particle-to-surface binding process can be measured and modeled, including the influence of magnetic fields and the role of the small targets that cause the specific binding between particle and surface. In several magnetic particle-based affinity assays, target analytes are first captured from the fluid by the particles and subsequently a target-induced molecular sandwich is formed at a planar biofunctionalized sensor surface.^{25, 117, 119, 202} In such assays, the magnetic particles have a diameter ranging from 100 nm up to several μm , which is much larger than the size of the target analytes. Due to their size, the magnetic particles can be actuated and detected with ease, but the formation of the molecular sandwich at a sensor surface can be hindered by the particle size. To enhance the interaction of particles with the surface, several methods have been applied, such as the application of fluid flows¹¹⁸⁻¹¹⁹, field

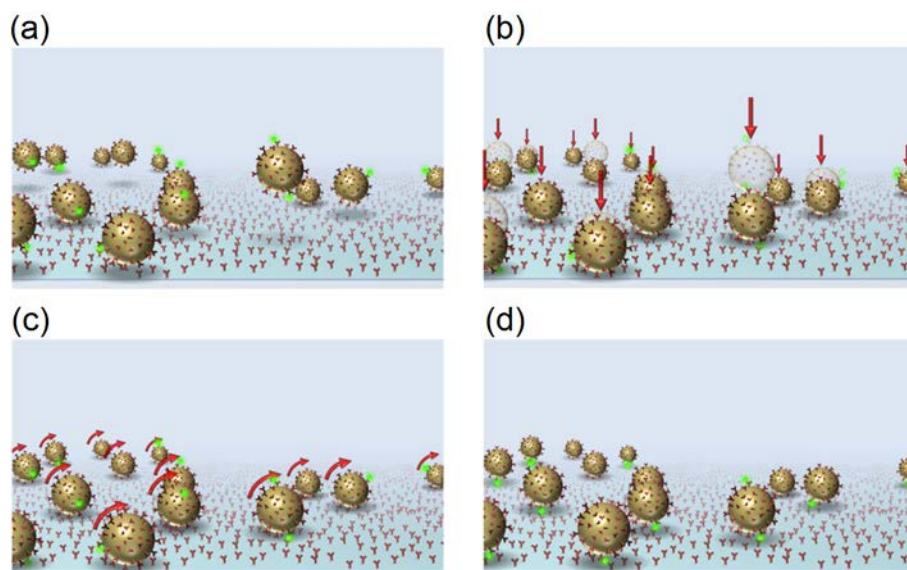


Figure 7.1 Formation of a molecular sandwich in a magnetic particle-based assay, accelerated by magnetic actuation (red arrows) to bring and keep particles (brown) with captured analytes (green) near a bio-functionalized surface. (a) Initially, particles are randomly distributed and oriented due to Brownian motion and Brownian rotation. (b) Magnetic field gradients are used to bring particles in close contact with the surface and (c) rotating magnetic fields are used to bring captured analytes in contact with the surface in order to (d) specifically bind the particles to the surface.

gradients^{111, 118-119} and alternating in-plane and out-of-plane magnetic fields²⁵. Thus far, the influence of the applied methods on the particle dynamics have not been studied and characterized in detail.

Here, we present a comprehensive study of the dynamics of magnetic particles with captured targets near a reactive surface (see Figure 7.1). To separate the underlying physics from the biochemistry that is involved in the binding process, we compare numerical Brownian dynamics simulations with experimental data. We use a model system of magnetic microparticles and fluorescent nanoparticles as targets which bind to a surface via the biotin-neutravidin complex. We use fluorescent nanoparticles to provide direct information about the bond specificity, as well as to simplify the comparison with numerical simulations. Using these tools, we first characterize the remanent magnetic properties of superparamagnetic particles, based on which the particles can be rotated.¹³⁴ Subsequently, we study the influence of magnetic fields to accelerate and optimize the particle exposure to the surface. Finally we quantify the influence of non-specific interactions in these types of assays and discuss how such interactions can be minimized in a magnetic incubation protocol.

7.2 Methods

In this Section, we give details on the used experimental model system (see Figure 7.2a) and explain the experimental protocols used to label particles, characterize the particles and perform incubation experiments. Also the numerical Brownian dynamics simulation method is described for simulating a particle with a captured target near a surface.

7.2.1 Materials

For experiments, superparamagnetic particles (M-270 carboxylated; 2.8 μm diameter; from Dynal Invitrogen, Carlsbad, CA) were coated with recombinant protein G (Merck Whitehouse Station, NJ) using standard EDC-NHS coupling chemistry as described by the manufacturer. Particles were stored in phosphate buffered saline (PBS) buffer containing 0.02% Tween-20 and 10 mg/mL BSA.

As captured targets on the magnetic particles, fluorescent nanoparticles were used (Fluospheres®, biotinylated, yellow/green, 0.2 μm diameter) which were purchased from Invitrogen (Carlsbad, CA).

Fluid chambers (Figure 7.2c) consisted of a polystyrene bottom surface ($22 \times 22 \times 0.18 \text{ mm}^3$ cover slips; Agar Scientific) that was attached to a glass surface ($18 \times 18 \text{ mm}^2$ cover slips; VWR international) by means of an imaging spacer (SecureSeal™ 0.12 mm thickness and a $\varnothing 9 \text{ mm}$ well; Sigma-Aldrich). In surface binding experiments, the polystyrene surfaces were washed and coated with neutravidin (Thermo Scientific) by means of physisorption; a 90 μL droplet containing 0.5 mg/mL neutravidin in PBS was pipetted into an unclosed well. After 20 minutes, the droplet was removed by means of a pipette and the well was washed by adding and removing for five times a droplet of PBS containing 1 mg/mL BSA and 0.01% Tween-20. Subsequently, the surface was blocked against non-specific interactions

by incubating a 90 μL droplet of PBS containing 1 mg/mL BSA and 0.01% Tween-20 for 10 minutes. In case of no surface binding experiments, only the blocking step was performed. Fluid chambers were prepared prior to use.

To actuate the magnetic particles, we used an adapted version of the magnet setup as presented in chapter 3. To enable imaging by the immersion objective, a larger soft-iron yoke was made for the quadrupole electromagnet, effectively resulting in a further separation of the electromagnets to a final tip-to-tip distance of 23 mm (see Figure 7.2b). Calibration data of this setup is shown in Appendix 7.A.

Samples were analyzed using a 63 \times water immersion objective lens on a Leica DM6000M microscope mounted with an EMCCD camera (Luca S from Andor). For excitation of the fluorescent particles, an excitation light source (EL6000; from Leica) was used in combination with a Leica L5 filter cube. To visualize the fluorescent particles and the magnetic particles, images were recorded with combined fluorescence and bright field transmitted light (Figure 7.2d). Images were analyzed using customized software developed in MATLAB (The MathWorks, Natick, MA) and ImageJ.

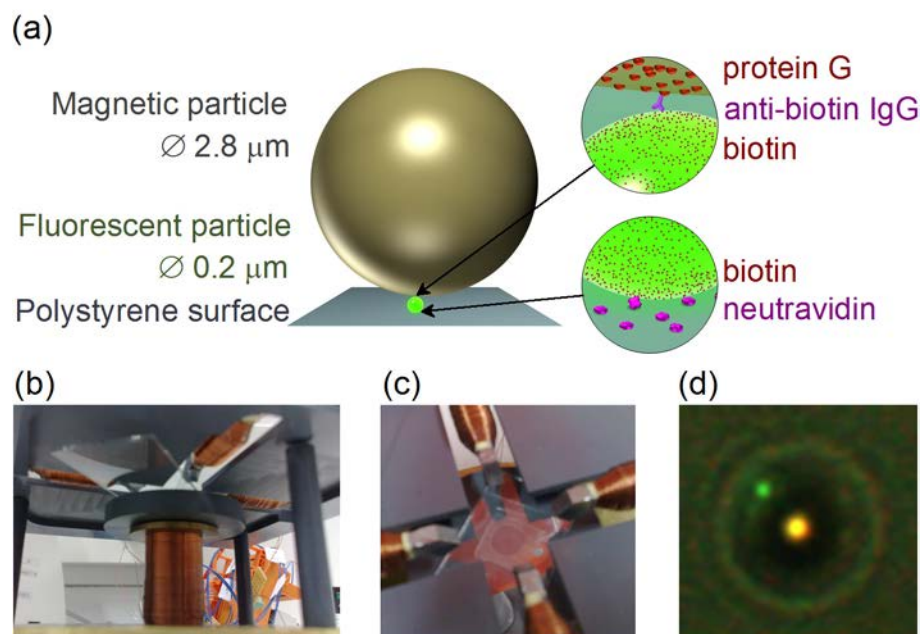


Figure 7.2 Experimental setup to study the binding of a captured target on a magnetic particle to a bio-functionalized surface. (a) Overview of the bound model system consisting of protein G-coated magnetic particles with biotin-coated fluorescent nanoparticle as captured targets which bind to a neutravidin-coated polystyrene surface. The insets show the involved bio-molecules sketched to scale. (b) The 5-pole electromagnet used to actuate (c) the particles in a fluid chamber in the center of the magnet system. (d) Microscope image of a fluorescent particle (green) attached to a magnetic particle (dark circle) as obtained by combining fluorescence and bright-field transmitted light. The bright yellow spot at the center of the particle is an artifact due to the applied bright-field light, and it is exploited to track the particle center. The particle orientation is tracked by determining the relative position of the fluorescent particle with respect to the center of the magnetic particle.

7.2.2 Attaching fluorescent nanoparticles to magnetic microparticles

Fluorescent nanoparticles were attached to magnetic particles in a two-step assay. First magnetic particles (at 2.5×10^7 particles/mL) were incubated with a low concentration (13 pM) of anti-biotin antibodies (Thermo Scientific). The reagents were incubated in a 78 μ L PBS solution containing 1 mg/mL BSA (blocking agent) and 0.01% Tween® 20 (surfactant), for 50 minutes on a vortexer. Subsequently, biotin-labeled fluorescent targets (1×10^9 particles/mL, 160 μ L) were added and incubated for 20 minutes on the vortexer. Fluorescent targets were at an excess compared to anti-biotin antibodies in order to bind all bound antibodies and avoid agglutination. After incubation, the magnetic particles were washed using a magnet and redispersed in 100 μ L PBS with 1 mg/mL BSA and 0.01% Tween® 20. Particles were immediately used after preparation.

7.2.3 Characterization of the remanent magnetic moment

In previous work, it was shown by Janssen et al.¹³⁴ that the remanent magnetic moment of superparamagnetic particles can be extracted from the response to a rotating magnetic field. The method was shown on a batch of particles, (i.e., Dynal M-280 particles) which exhibited a surface roughness such that the orientation of the particles could be tracked from bright-field microscopy data. The particles used in this study (i.e., Dynal M-270), are much smoother and do not allow tracking of their orientation as easily. We therefore used the 200 nm fluorescent particles to also track the particle orientation. Attachment of the fluorescent particles was performed in a slightly different way but with the same result (see Van Reenen et al.¹³³ for the details).

In experiments, a droplet of 9 μ L and $2 \times 10^4 \mu\text{L}^{-1}$ magnetic particles was inserted in a fluid chamber containing a surface blocked with BSA. The fluid chamber was closed and placed under the microscope together with the magnetic setup. The particles were allowed to sediment onto the surface by the force of gravity for 2 minutes. Subsequently a rotating field was applied. Images were recorded (see Figure 7.2d) and analyzed using customized Matlab software. By determining the center of the magnetic particle and the position of the fluorescent particles, the particle orientation could be obtained. The orientation of the magnetic particle can be determined for each frame with an estimated accuracy of 2° ¹³³.

7.2.4 Sandwich formation experiments

The following protocol was used to study the rate at which bonds are formed at a reactive surface by a magnetic particle with captured fluorescent targets. First, biotin-coated fluorescent targets were attached to the particles following Section 7.2.2. Meanwhile, fluid chambers were prepared with a neutravidin-coated polystyrene surface following Section 7.2.1. Subsequently, a 9 μ L droplet of 2×10^7 magnetic particles/mL was pipetted onto the neutravidin surface and the reaction chamber was closed using a glass cover slip. The time was recorded at which the droplet was placed on the surface. The reaction chamber was put in the center of the 5-pole electromagnet and a magnetic actuation protocol was started. For control experiments

the reaction chamber was not placed in the magnetic setup. After a certain incubation time – typically several minutes – the incubation was stopped by turning the incubation chamber upside down to separate bound from unbound particles by means of sedimentation. Finally, the reaction chamber was placed under the microscope to analyze the binding.

To quantify the binding, images were taken of the particles at the neutravidin-coated surface as well as of the unbound particles that had sedimented to the glass surface. Images of both surfaces – i.e. taken at different heights – corresponded to the same lateral position in the reaction chamber. To distinguish specific bonds from non-specific bonds, we combined fluorescence with bright-field transmitted light in a single image. In case a fluorescent particle was observed near the center of the magnetic particle, the particle was considered as being bound specifically. Furthermore, the used exposure time was 5 seconds, which is long enough to let unbound fluorescent particles fade out from the images due to their Brownian motion ($r_{\text{rms}} = \sqrt{4DR_{\text{FP}}} \approx 7 \mu\text{m}$). As bound fluorescent particles are much more restricted in their motion due to the bond, these particles remained visible in the images.

7.2.5 Brownian dynamics simulation of the surface binding reaction

To support experimental data with theory, a numerical model was used based on Brownian dynamics. The dynamic behavior of a magnetic particle with a captured target was simulated within the vicinity of a reactive surface.

The Langevin equation for the displacement of the particle is similar to Eq. 6.1 but then for a single particle:

$$\frac{\partial}{\partial t} \mathbf{r} = \boldsymbol{\mu}_{\text{self}} \cdot \nabla U(t) + k_B T (\nabla \cdot \boldsymbol{\mu}_{\text{self}}) + \mathbf{v}^{\text{ran}}(t), \quad (7.1)$$

with $\boldsymbol{\mu}_{\text{self}}$ the self-mobility of the particle which is approximated by the Stokes drag on a sphere, corrected for the vicinity of the surface (compare Eq. 6.1).¹⁷⁹⁻¹⁸⁰ The second term in Eq. 7.1 is due to the spatial variation of the self-mobility and compensates the flux caused by the position dependent random velocity contribution \mathbf{v}^{ran} , which represents the Brownian motion (also see Eq. 6.2).¹⁷⁹ Furthermore, the energy potential $U(t)$ consists of a gravitation and a magnetic energy term:

$$U(t) = \frac{4}{3} \pi R_{\text{MP}}^3 (\rho_{\text{MP}} - \rho_{\text{fluid}}) gh - \mathbf{m} \cdot \mathbf{B}, \quad (7.2)$$

in which g is the gravitational constant, h the height of the particle with respect to the surface, \mathbf{m} the magnetic moment of the particle and \mathbf{B} the magnetic field. ρ_{MP} and ρ_{fluid} are the volumetric mass density of respectively the particle and the fluid. Following the specifications of the manufacturer, $\rho_{\text{MP}} = 1.4 \times 10^3 \text{ kg/m}^3$; and the fluid density is assumed to be equal to water at $T = 293 \text{ K}$: $\rho_{\text{fluid}} = 1.0 \times 10^3 \text{ kg/m}^3$.

We also consider rotation of the particle about each axis

$$\frac{\partial}{\partial t} \boldsymbol{\psi} = \boldsymbol{\mu}_{\text{self,rot}} \cdot (\mathbf{m}_{\text{rem,net}} \times \mathbf{B}) + \boldsymbol{\omega}^{\text{ran}}(t), \quad (7.3)$$

with $\mathbf{m}_{\text{rem,net}}$ the vector describing the size and orientation of the remanent moment in the superparamagnetic particle. This orientation is assumed to be fixed with respect to the orientation of the particle, and any rotation applied to the particle is also applied to the remanent moment of the particle. The random angular velocity contribution ω^{ran} is implemented similar to Eq. 3.6. Last of all, $\mu_{\text{self,rot}}$ is the rotational self-mobility of the particle which is approximated by the Stokes drag on a sphere in the vicinity of the surface. Specifically, we use the Faxè's correction as reported by Leach et al.¹⁸⁰ for a sphere rotating about an axis parallel to the surface normal:

$$\beta^{\parallel} = \frac{\beta}{1 - (1/8)(R_{MP}/h)^3}; \quad (7.4)$$

and for a sphere rotating about an axis perpendicular to the surface normal:

$$\beta^{\perp} = \frac{\beta}{1 - (5/16)(R_{MP}/h)^3 + (15/256)(R_{MP}/h)^6}. \quad (7.5)$$

In Eq. 7.4 and 7.5, $\beta = 8\pi\eta R_{MP}^3$ corresponds to the rotational drag coefficient on a sphere in a viscous medium.

To simulate the displacement and the rotation of a magnetic particle over time, we integrate Eq. 7.1 and Eq 7.3 using a forward Euler algorithm with time-steps of 0.01 ms. To account for the physical surface, reflective boundary conditions were assumed. The height of the particle at $t = 0$ is randomly chosen following a Boltzmann factor which includes the gravitational energy. The orientation of the particle and the magnetic moment at $t = 0$ is chosen randomly for each simulation. As shown in Appendix 7.C, for a time-step below 0.2 ms a correct root-mean-square rotation of the particle is obtained.

Finally, we model the captured target on the particle as a reactive sphere with radius R_{target} , which represents a bound target particle. In case of a fluorescent particle that is coated with biotin, we apply $R_{\text{target}} = 100$ nm, and assume binding as soon as the target comes into contact with the reactive surface (hit-and-stick behavior). This assumption seems valid as the fluorescent particle is completely coated with an excess of biotin and the surface is coated with an excess of neutravidin (which has four binding sites). Biotin and neutravidin have a high affinity²⁰³, and when the surfaces come into contact, multiple biotin-groups will come into contact with multiple neutravidin molecules.

7.3 The remanent moment of superparamagnetic particles

Here, we present the characterization of the remanent moment of the used superparamagnetic particles. Data and observations from experiments were combined in a numerical model to determine the remanent moment as well as to obtain insight in the magnetization dynamics of superparamagnetic particles. The size and behavior

of the remanent moment will determine the fields necessary to rotate particles near a reactive surface.

7.3.1 Response of magnetic particles in a rotating magnetic field

The remanent moment of Dynal M-270 superparamagnetic particles was characterized by studying the rotational response of the particles to a continuously rotating magnetic field – similar as reported by Janssen et al.¹³⁴. The particle rotation frequency was measured for different field strengths and field rotation frequencies (Figure 7.3a). Magnetic particles are observed to keep up with the magnetic field rotation up to the so-called breakdown frequency. Above the breakdown frequency, the average particle rotation frequency declines and a wiggling behavior is observed as shown in Figure 7.3b. In a repetitive fashion, particles rotate in the same direction as the magnetic field for some time, thereafter slow down, rotate backwards shortly, and then rotate along with the rotating field again. The breakdown occurs when the magnetic torque cannot overcome the viscous drag that comes along with synchronous rotation of the particle with the field.

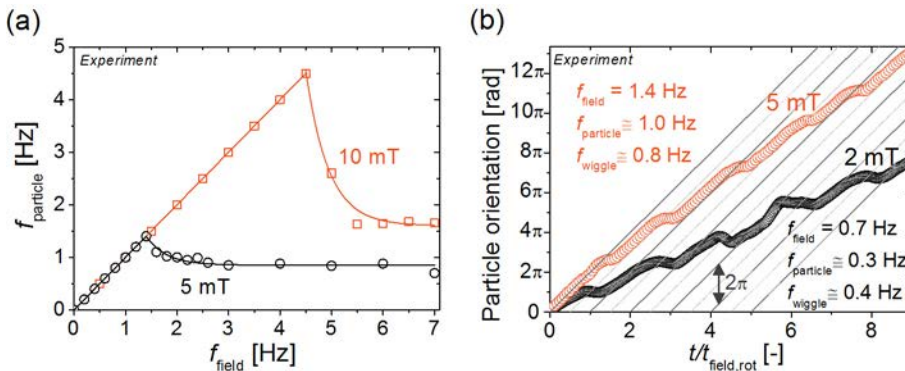


Figure 7.3 Experimentally determined rotational response of unbound Dynal M-270 superparamagnetic particles in a rotating magnetic field. (a) The rotation frequency of an unbound particle as a function of the rotation frequency of the applied magnetic field, for field strengths of 5 mT and 10 mT. The particle continuously follows the magnetic field up to the breakdown frequency. Above the breakdown frequency, the particle rotation frequency decreases due to remagnetization of the particle magnetic moment (characterized by the wiggles). (b) The angular behavior of a particle for a field rotation frequency above the breakdown frequency. The response is plotted for two different field strengths (on the x-axis normalized with the field rotation time), showing a different response for the two cases. Since the difference is related to the relative orientation of the magnetic field, we also show the orientation of the magnetic field as solid grey lines phase-shifted by multiples of 360° . The dotted grey lines correspond to a 180° phase-shift of the magnetic field. For the case of 2 mT, the particle orientation only shows one wiggle for a full cycle of the field relative to the particle orientation. For the case of 5 mT, two wiggles are found per full cycle of the magnetic field with respect to the particle orientation, indicating uniaxial remagnetization of the remanent moment of the particle.

Janssen et al.¹³⁴ also observed a breakdown frequency and wiggling behavior of magnetic particles, but for a slightly different type of superparamagnetic particles, namely Dynal M-280 particles (diameter of $2.8 \mu\text{m}$), and for fields up to 2 mT. The

wiggling frequency appeared to correspond to the difference between the field rotation frequency and the net particle rotation rate, which means that every wiggle period corresponds to one full rotation of the field relative to the magnetic particle. This observation proves that at low fields the magnetic torque is dominantly generated by a magnetic moment that has a fixed orientation inside the particle. In later experiments on M-270 particles at higher fields, Janssen et al.¹⁵³ observed a switching of the magnetization in the particles, but the dynamic properties were not quantified in detail.

We have studied the magnetic properties of the M-270 particles by recording the breakdown frequency and wiggling behavior at different field strengths. For field strengths below 4 mT, we observe the same behavior as reported by Janssen et al.¹³⁴, i.e. every wiggle corresponds to one full rotation of the field relative to the magnetic particle; see the black circles in Figure 7.3b. Accordingly, the frequency at which wiggles occur is found to be approximately equal to the difference between the field rotation frequency and the average particle rotation frequency. However, above 4 mT we observe a different behavior of the particle, as shown by the orange circles in Figure 7.3b. In this case, the wiggling frequency equals *twice* the difference between the field rotation frequency and the average particle rotation frequency. So two wiggling cycles occur during one relative rotation of the field with respect to the particle. In other words, the particle is dragged along with the field twice during one relative field rotation. This proves that the magnetic moment of the particle reorients during one relative field rotation. So at fields above 4 mT the magnetic moment of the particle becomes dynamic and has two preferential magnetization directions, indicating a dominant uniaxial magnetic anisotropy of the magnetic particles.

An important consequence of the dynamic magnetic moment is that the size of the magnetic moment can no longer be directly determined from the breakdown frequency, because the angle difference between the moment and field becomes uncertain.

Furthermore, we find that remagnetization of the magnetic moment does not occur at a phase difference above 90° between the field and the magnetic moment, but well below 90° , i.e. at $35 \pm 10^\circ$. This becomes especially clear when analyzing the rotational response of particles that are bound to a surface and experience a constraint in the orientation as reported elsewhere.¹³³ It is found that the small remagnetization angle is present for all particles with a variation of $\sim 10\%$ and per particle varies less than 4% for repeated remagnetizations.¹³³

Considering the observed uniaxial magnetic anisotropy, a single remanent moment remagnetizes only when the coercive field is overcome, i.e. at an angular difference between the moment and the field above 90° . Nevertheless, smaller angles are observed in experiments. To reconcile this observation with uniaxial anisotropic behavior, we consider an effective particle magnetic moment that is built up from several independent magnetic moments within the particle.

At an angle of $35 \pm 2^\circ$, a fraction of moments within the effective particle magnetic moment already remagnetizes. For this fraction, the angular difference has

to be larger than 90° (or else no remagnetization is possible), and thus their orientation deviates at least $90^\circ - 35^\circ = 55^\circ$ degrees from the effective magnetic moment. Assuming a symmetric angular distribution of the magnetic moments, the angular spread of the magnetic moments has to be at least two times 55° , i.e. 110° .

Fast remagnetization of the effective particle magnetic moment can be understood using the following rationale. When a first fraction of magnetic moments has remagnetized over 180° , the direction of the magnetic torque due to these particular moments reverses. As a consequence, the total magnetic torque on the particle decreases, leading to a decreased angular velocity of the particle and thus in a larger phase lag between the original magnetic moment and the field. Due to this increase in the phase lag, more magnetic moments in the particle remagnetize, causing the particle to rotate backwards even further. This is repeated until the total moment is remagnetized. In this way, partial remagnetization speeds up remagnetization of the total magnetic moment, explaining the relatively fast remagnetization of the total magnetic moment.

The origin of the observed remagnetization of the particle's remanent moment can be attributed to the anisotropy of the ferrimagnetic (magnetite) grains of which the particles consist. Three types of anisotropy are possible: magneto-crystalline, shape and surface anisotropy. It was reported by Klaue et al.²⁰⁴, that the saturation behavior of the remanent moment of Dynal M-280 particles corresponds quantitatively to values for the magneto-crystalline anisotropy. However, this saturation was observed at relatively large field strengths, over 100 mT, whereas for the M-270 particles, remagnetization already occurs at 5 mT. These large differences indicate a large difference between ferromagnetic properties of different types of superparamagnetic particles. Consequently, it is not unlikely that for the M-270 particles other forms of anisotropy such as shape anisotropy govern the ferromagnetic behavior instead of magneto-crystalline anisotropy. Moreover, based on the uniaxial remagnetization behavior observed in our experiments, it is unlikely that magneto-crystalline anisotropy of the grains is the dominant type of anisotropy, because magnetite exhibits 4 dominant easy axes. Therefore we exclude magneto-crystalline anisotropy as a possible cause of the ferromagnetic behavior of these particles.

Since the detailed shape of the magnetite grains is unknown, it is difficult to estimate the significance of surface anisotropy. Shape anisotropy however can easily allow for uniaxial anisotropy of the grains, as the presence of one elongated dimension with respect to the others would already cause this type of anisotropy. By estimating the anisotropy energy density for a magnetite prolate spheroid (see Appendix 7.B), we find that for a deviation larger than 5% in aspect ratio compared to a sphere, shape anisotropy already dominates over magneto-crystalline anisotropy.

Note that one magnetic particle contains a large ensemble of grains with a log-normal size distribution and a random orientation. Only the large grains contribute to the remanent moment of the particle. The net remanent moment can be due to the discrete character of a limited number these grains or to a production process that does not yield a completely random distribution.

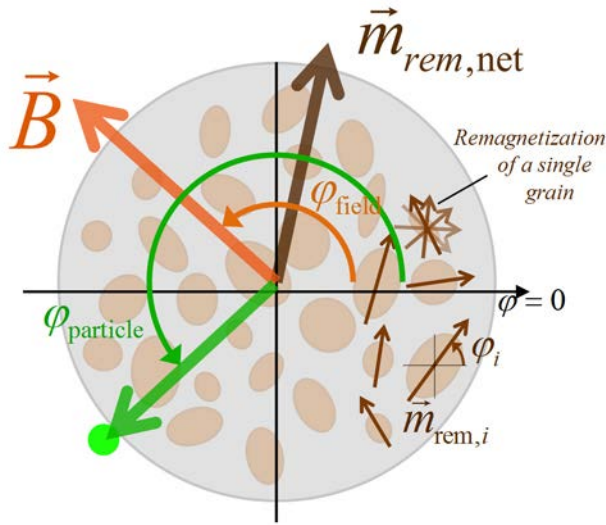


Figure 7.4 Overview of the different parameters used to study the remagnetization dynamics of a superparamagnetic particle. In the background, a sketch is shown of the cross-section of a superparamagnetic particle, showing magnetite grains (brown ovals) with varying shape, size and orientation within a polystyrene matrix (gray). Each grain has its own remanent magnetic moment (brown vectors), which adds up to the total remanent magnetic moment of the magnetic particle. This magnetic moment remagnetizes as the coercive fields of the separate grains are overcome by the magnetic field (orange vector). In experiments, the orientation of the magnetic particle is tracked by determining the position of a fluorescent particle (green vector) which is attached to the surface of the magnetic particle.

7.3.2 Numerical model of the remagnetization dynamics

Based on the observations on the remagnetization behavior of the remanent moment of superparamagnetic particles, a numerical model was developed to verify the proposed rationale.

Essentially, the observed behavior is attributed to a granular distribution of remanent moments with an uniaxial magnetic anisotropy within one grain, which together add up to a net non-zero magnetic moment ($m_{rem,net}$) of the particle (see Figure 7.4). Assuming a discrete distribution consisting of N magnetic grains, the magnetic torque τ_m may thus be expressed as follows:

$$\tau_m = B \sum_{i=1}^N m_{rem,i} \sin(\varphi_i - \varphi_{field}) \quad (7.6)$$

with

$$m_{rem,net} = \sum_{i=1}^N m_{rem,i} \sin(\varphi_i) > 0 \cdot$$

Here, B is the field strength; $m_{rem,i}$ is the size of magnetic moment i ; φ_{field} is the field orientation and φ_i is the orientation of magnetic moment i . For simplicity, we as-

sume a distribution of equally sized magnetic moments over a total angular range which is less than 180° , i.e.

$$\tau_m = m_{\text{rem},i} B \sum_{i=-N}^N \sin(i \cdot \Delta\varphi - \varphi_{\text{field}}) \quad \text{with } N \cdot \Delta\varphi < \frac{\pi}{2}. \quad (7.7)$$

Note that Eq. 7.7 describes the torque exerted on a distribution of static magnetic moments, but remagnetization does not follow from the equation. Remagnetization occurs when the coercive field is overcome, and as a consequence φ_i is history dependent. Numerically, this process can be treated by evaluating at each next time-step the previous orientation of the separate magnetic moments with respect to the field orientation. In case the coercive field is overcome, 180° is added to the orientation of the corresponding magnetic moment i , to reflect the remagnetization.

Using this approach to compute the magnetic torque at time t , the angular displacement after a certain time-step Δt is determined following a forward Euler numerical scheme. Specifically, the magnetic torque is balanced with the hydrodynamic drag and inertia is neglected as Reynolds number for this system is much smaller than 1 ($\text{Re} < 10^{-3}$ at 10 Hz rotation). From the torque balance, the angular velocity at time t can be computed and is used to determine the particle orientation at $t + \Delta t$, i.e.

$$\varphi_{\text{particle}}(t + \Delta t) = \varphi_{\text{particle}}(t) + \Delta t \cdot \frac{\tau_m + \tau_{\text{BR}}}{8\pi\eta C_{\text{drag}} R_{\text{MP}}^3}, \quad (7.8)$$

with η the dynamic viscosity, C_{drag} a correction factor to account for the vicinity of the surface, estimated at 1.14 based on the method of reflections²⁰⁵, as reported by Leach et al.¹⁸⁰; R_{MP} is the particle radius and Δt is the numerical time-step which is set at 0.2 ms. The random torque τ_{BR} is computed in a similar way as presented in Eq. 3.6 (see Appendix 7.C for a validation of the method). The magnetic torque is

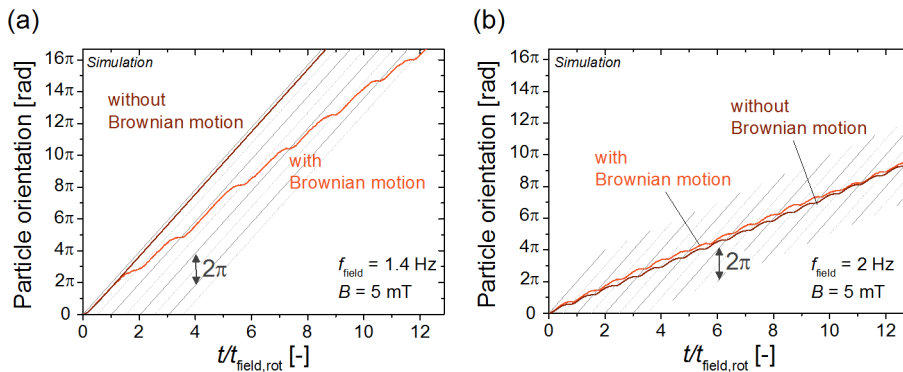


Figure 7.5 Simulated unbound particle rotation with and without Brownian motion included at a field strength of 5 mT and a field frequency of (a) 1.4 Hz and (b) 2 Hz. (Note that $f_{\text{field}} = t_{\text{field,rot}}^{-1}$.) Simulation time steps were 0.2 ms. A moment distribution is assumed consisting of 22 separate magnetic moments of equal size (i.e. $1.5 \times 10^{-18} \text{ Am}^2$), which are equally distributed from -63° to $+63^\circ$, in steps of 6° .

added corresponding to Eq. 7.7 and combined with evaluating whether the coercive fields of the separate magnetic moments are overcome. The angular moment distribution is chosen such to obtain a computed torque that is close to the experimentally determined magnetic torque and the angle difference upon remagnetization. Specifically, 22 magnetic moments ($2N = 22$ in Eq. 7.7) of equal size $\mu = 1.5 \times 10^{-18} \text{ Am}^2$ are spread out over 126° with $\Delta\varphi = 6^\circ$.

In Figure 7.5, the simulated time-dependent behavior is shown for a 5 mT magnetic field rotating at a frequency of 1.4 Hz (a) and 2 Hz (b). Numerical data is shown with and without Brownian rotation included. In particular, for the case of 1.4 Hz with Brownian motion, the computed curve is similar to the experimental curve obtained at this frequency and magnetic field strength, which is shown in Figure 7.3b. Based on this qualitative agreement, and also on the fact that the simulated particles remagnetize at the experimentally observed angular difference – i.e. around 35 degrees – we conclude that the numerical model accurately describes the experimental data. The numerical model can therefore be used to increase the understanding of the rotational particle behavior.

Comparing the average particle rotation frequency in Figure 7.5, it is observed that for a field rotation frequency of 1.4 Hz, there is a large difference in the rotational behavior if Brownian rotation is included. In case of a field rotation frequency of 2 Hz, this difference is much less and Brownian rotation may even lead to a faster average particle rotation frequency.

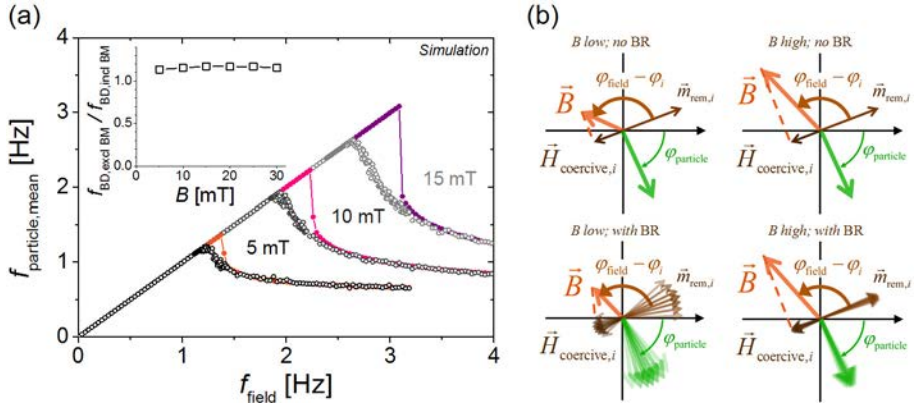


Figure 7.6 (a) Rotation frequency of the particles plotted as a function of the field rotation frequency, for different field strengths. The open circles (black and grey-scale) correspond to simulations including Brownian rotation, whereas the closed circles (red, pink and purple) correspond to simulations without Brownian rotation. The inset shows the comparison between numerically obtained breakdown frequencies for the cases with and without Brownian motion. The data is shown as a function of the field strength. (b) Schematic representation of the remagnetization of the magnetic moment of a single magnetic grain, for the case the magnetic field strength B is low or high, and with and without Brownian rotation of the particle (BR). The Brownian rotation of the particle is represented by the green arrow, but is also made visible in the orientation of the grain magnetic moment (dark brown arrow) as physical orientation of the grain is fixed within the magnetic particle. In particular note the effect of the different cases on the relative orientation of the field with respect to the particle moment ($\varphi_{\text{field}} - \varphi_i$) that is required to overcome the coercive field, $H_{\text{coercive}, i}$.

To study the influence of Brownian rotation on the particle rotation in further detail, the average particle rotation frequency over 20 seconds of simulation was determined for different field frequencies and magnetic field strengths as shown in Figure 7.6a. It is found that Brownian rotation most strongly influences the rotational behavior of the particles near the breakdown frequency. In particular, the breakdown frequency is lowered due to Brownian rotation. This can be explained as follows. Just below the breakdown frequency – in case of no Brownian rotation – the particle and the field are at a maximum angular difference between field and effective magnetic moment such that no remagnetization of single magnetic moments within the particle occurs. In this configuration, a small increase in the angular difference causes a first fraction of magnetic moments within the particle to collapse, which leads via a cascade of other moments which collapse to fully remagnetize the particle. The closer the field frequency is to the breakdown frequency, the smaller this increase needs to be for a collapse of the magnetic moment. Brownian rotation, however, causes the particle orientation to fluctuate around the equilibrium orientation, and can trigger such a collapse even when the field frequency is below the breakdown frequency. As a result, the experimentally observed breakdown frequency is lower as expected on a balance between the magnetic torque and hydrodynamic drag alone.

The breakdown frequency both with and without Brownian rotation was determined for different field strengths. In the inset of Figure 7.6a the relative difference, $f_{\text{BD, excl BM}} / f_{\text{BD, incl BM}}$, is shown as a function of field strength. Remarkably, it is found that the relative difference is almost constant for the simulated field strengths. For increasing field strengths, a smaller relative difference would be expected, because a higher field rotation frequency is required to reach a collapse of a magnetic moment. At higher field rotation frequencies, there is less time to build up Brownian fluctuations. It should be noted however that $f_{\text{BD, excl BM}} / f_{\text{BD, incl BM}}$ does not depend linearly on the relative difference in $(\varphi_{\text{field}} - \varphi_{\text{moment,net}})$ with and without Brownian rotation. For example, at 5 mT, this angular difference between field and particle moment at the breakdown frequency changes from $(51 \pm 1)^\circ$ to $(39 \pm 5)^\circ$ for respectively no Brownian rotation and with Brownian rotation included. At a field strength of 30 mT, these values are found to be $(31 \pm 1)^\circ$ and $(26 \pm 2)^\circ$. Thus, for increasing field strengths – or: for an increasing breakdown frequency – the decrease in critical breakdown angle due to Brownian rotation becomes less (also see Figure 7.6b). In spite of this, the corresponding relative decrease in breakdown frequency due to Brownian rotation is roughly constant over the range of 5 to 30 mT. Since the simulated data correspond closely to experimental results, we will use this relative difference to correct for influences of Brownian rotation on the breakdown frequency. To that end, a correction factor C_{BR} is defined which is found to be $C_{\text{BR}} = 1.16 \pm 0.05$ from averaging the numerically determined relative differences in Figure 7.6a.

7.3.3 Determining the magnitude of the remanent moment

Based on the previous experimental and theoretical analysis, we can determine the remanent moment from the response of superparamagnetic particles in a rotating magnetic field. First, we determine the magnetic torque from the angular velocity of

particles at the breakdown frequency, ω_{BD} , by balancing the magnetic torque with the hydrodynamic drag:

$$\tau_{\text{m}} \equiv Bm_{\text{rem,net}} \sin(\phi_{\mu} - \phi_{\text{field}}) = 8\pi C_{\text{drag}} C_{\text{BR}} \eta R_{\text{MP}}^3 \omega_{\text{BD}}, \quad (7.9)$$

with ϕ_{μ} the orientation of the net magnetic moment and the factors C_{drag} and C_{BR} to respectively correct for additional drag by the presence of a nearby surface and the influence of Brownian rotation on the breakdown frequency, as discussed in the previous paragraphs.

In Figure 7.7a, the experimentally determined breakdown frequency is plotted as a function of the applied magnetic field strength. On the right axis, the corresponding magnetic torque is given.

As follows from Eq. 7.9, the net magnetic moment can be determined if the relative orientation between the moment and the field is known. As shown in Figure 7.7b, the angular difference between moment and field at the breakdown frequency decreases for increasing field strength. This can be explained by the fact that the coercive field of the separate remanent moments in the particle will be overcome at smaller angles for higher field strength.

Finally, using Eq. 7.9 and inserting the magnetic torque (Figure 7.7a) and the corresponding angular difference between moment and field (Figure 7.7b), we obtain a value for the remanent moment of the superparamagnetic particles, as shown

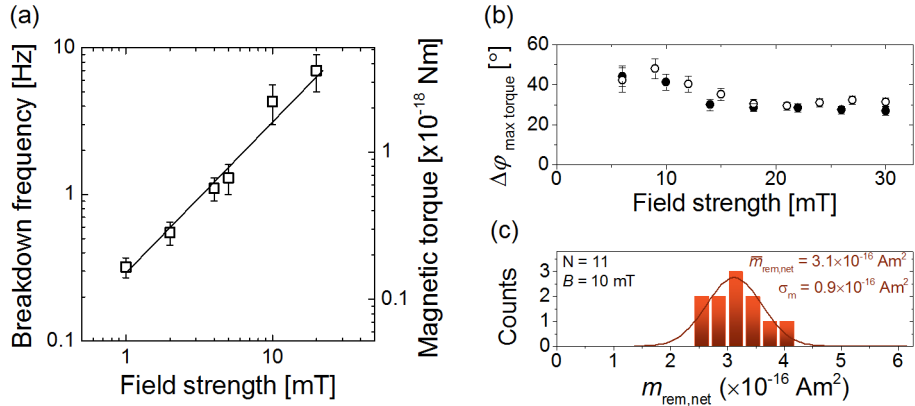


Figure 7.7 Quantification of the remanent moment of Dynal M-270 superparamagnetic particles. (a) Experimentally determined breakdown frequency of magnetic particles for different magnetic field strengths. Using Eq. 7.9, the corresponding magnetic torque exerted on the particles just below the breakdown frequency can be determined. An approximate linear relation is obtained in this range of field strengths. To compute the remanent moment from the magnetic torque, it is necessary to know the relative orientation of the field with respect to the magnetic moment. (b) Experimentally determined relative field orientation with respect to the magnetic moment of the particle at the moment of particle remagnetization. Data originates from another study on the rotation of particles bound to a surface¹³³. The different datasets (open and closed circles) correspond to two different particles. (c) Using the determined magnetic torque and relative field orientation, the size of the remanent moment of the superparamagnetic particles can be computed. The histogram here shows the data obtained for 11 different particles at a field strength of 10 mT. The mean and the standard deviation in the remanent moment are shown in the figure.

in Figure 7.7c. Specifically the average remanent moment is found to be 3.1×10^{-16} Am² with a particle-to-particle variation of 30%.

It is interesting to note that Klaue et al.²⁰⁴ reported a much larger particle-to-particle variation of the maximum magnetic torque (~55%) on similar particles (2.8 μm, Dynal M-280). Janssen et al.¹³⁴ also measured a large particle-to-particle variation (~70%) of the remanent moment of Dynal M-280 particles – using a similar approach as shown here, but without remagnetization. Interestingly, the M-270 particles exhibit much smaller sustainable torques at the same field strengths (~10 fold lower), with a smaller variation (~30%). For the M-280 particles Klaue et al. found saturation in the applicable torque (corresponding to overcoming the coercive field) at field strengths of ~150 mT. In our experiments with the M-270 particles, the coercive field is already overcome at field strengths of 5 mT, which indicates that the internal magnetic structure is very different. Finally, it should be noted that these particles are produced for their superparamagnetic properties (i.e. a high magnetic susceptibility) and that the remanence and coercive field which are studied here are neither specified nor controlled by the supplier.

7.4 Binding of particles with a target to a reactive surface

In this Section, we present results on the rate at which magnetic particles with captured targets bind to a reactive surface and how this rate can be enhanced by magnetic actuation. Results were obtained using numerical Brownian dynamics simulations and experiments on a model system. The numerical simulations were used to determine the important time-scales for the experiments as well as to develop an ansatz for a relevant magnetic actuation protocol to accelerate bond formation in the assay experiments.

7.4.1 Numerical Brownian dynamics simulations

Based on Brownian dynamics (see Section 7.2.5), we simulated the exposure of an isolated particle ($R_{MP} = 1.4$ μm) with one captured target to a reactive surface (see Figure 7.8). In the simulations, target radii were chosen of $R_{target} = 100$ nm or 5.5 nm, respectively corresponding to the fluorescent particles of the experimental model system or the hydrodynamic radius of an antibody in buffer¹⁶⁵. Furthermore, the magnetic particles were subjected to Brownian motion, Brownian rotation, gravity, magnetic forces and hydrodynamic interactions.

First, the particle behavior was simulated in the absence of an external magnetic field. In Figure 7.8a, simulated trajectories of the particle orientation are shown at different times. During the first few seconds, Brownian rotation is efficient at exposing the surface area of the particle to the reactive surface. However, over longer time-scales, the exposure becomes less efficient and several hundreds of seconds are required before almost the complete particle surface has been exposed to the reactive surface. This effect is inherent to the random rotation, of which the first moment vanishes whereas the second moment increases only linear over time. The rotation of the particle is proportional to the square-root of the elapsed time, and thus becomes less efficient at larger time-scales.

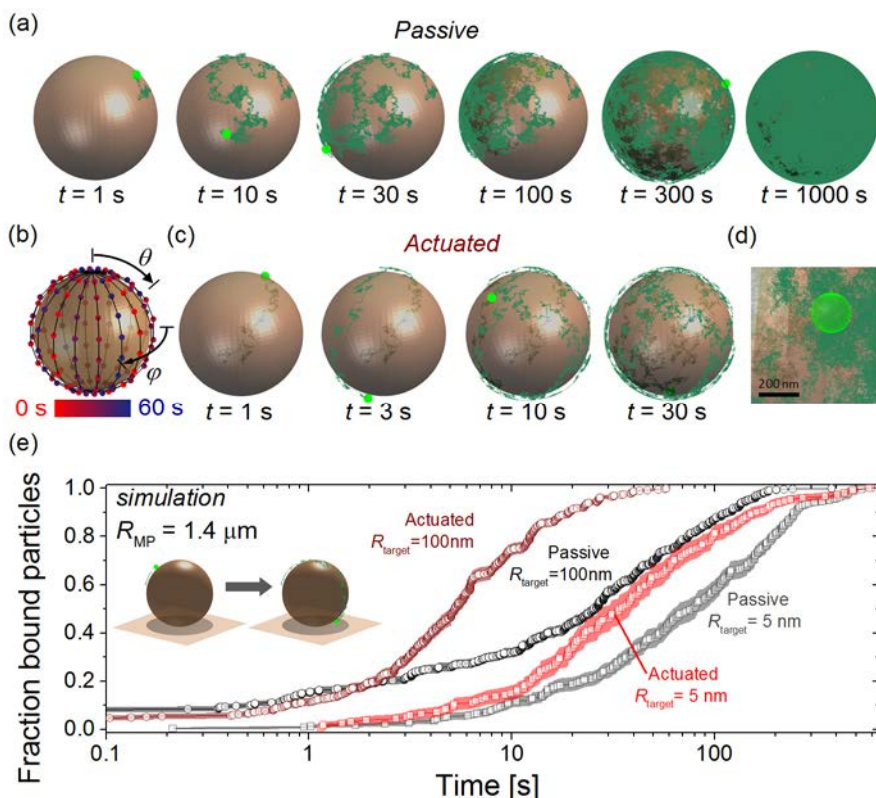


Figure 7.8 Numerical simulation of the exposure of a magnetic microparticle (brown) with a captured target (green), with and without magnetic actuation. (a) Simulated trajectory (dark green) of the orientation of a magnetic particle ($R_{\text{MP}} = 1.4\text{ }\mu\text{m}$) near a surface in case of no magnetic actuation. (b) Schematic representation of the applied magnetic actuation protocol to accelerate the exposure of the particle surface to the reactive surface. In a pulsed sequence, the magnetic field is applied in the orientations indicated by the colored circles. The colors correspond to the time at which a certain orientation is applied. The lines aid in visualizing the direction in which the field was rotated in subsequent steps. In a single pulse the magnetic field is on for 0.2 s and off for 0.2 s . (c) Simulated trajectory of the orientation of a magnetic particle near a surface in case of pulsed magnetic actuation as shown in panel b with a field strength of 5 mT . (d) Enlarged view of the trajectory for the case of no actuation at $t = 300\text{ s}$. (e) Fraction of bound particles as a function of the incubation time with and without actuation and for two target sizes, R_{target} . For each case, data is obtained from ~ 400 repeated simulations of the particle orientation in time and each data-point corresponds to a single simulation. A simulation is stopped as soon as the target comes into contact with the surface, as shown by the inset illustration. The shaded areas correspond to errors based on Poisson statistics.

To overcome the decrease in exposure efficiency, we applied time-dependent magnetic fields in the simulations to make the rotation of the particle proportional to the time. It is however important to consider that the application of a magnetic field reduces the Brownian rotation of the particle. To still exploit the effects of Brownian rotation at short time-scales, magnetic torques should not be too large, but large enough to induce particle rotation. To further exploit Brownian rotation, magnetic

fields can be applied in pulses, such as to rapidly rotate particles into a particular orientation and subsequently enable unrestrained Brownian rotation to maximize the particle exposure at the particular orientation.

Based on these considerations, we studied the effect of the following magnetic actuation protocol. In pulses, magnetic fields of $B = 5$ mT were alternated with no magnetic field in steps of 0.2 s. The applied fields were static, but in subsequent steps, the orientation of the field was rotated over 20° in a way such that the whole surface of the particle was exposed to the surface, as shown in Figure 7.8b. This was done by rotating the field (starting from an out-of-plane orientation, i.e. $\theta = 0$; compare Figure 7.8b) about different axes which are lying in-plane. More specifically $\theta_{\text{axis}} = 90^\circ$ and φ_{axis} was altered after each full rotation in the following way: $\varphi_{\text{axis},1} = 0^\circ$; $\varphi_{\text{axis},2} = 90^\circ$; $\varphi_{\text{axis},3} = 45^\circ$; $\varphi_{\text{axis},4} = 135^\circ$; $\varphi_{\text{axis},5} = 22.5^\circ$; $\varphi_{\text{axis},6} = 112.5^\circ$; $\varphi_{\text{axis},7} = 67.5^\circ$; $\varphi_{\text{axis},8} = 157.5^\circ$. It should be noted that simply orienting the magnetic moment in all possible directions is not enough to expose the complete surface of the particle to the reactive surface because the orientation around the moment axis is not affected by the magnetic field. Using the protocol described above, we circumvent this and allow orienting a particle without Brownian motion in all the directions as illustrated in Figure 7.8b to the surface. To maximize contact with the surface, a magnetic field gradient was applied with a magnitude of 3.6 T/m and an orientation towards the surface.

Figure 7.8c shows an example of the simulated trajectories of the particle orientation in case the described magnetic actuation protocol is applied. It is found that the whole particle surface area is efficiently exposed to the surface by the combination of magnetic fields and Brownian rotation. After several tens of seconds, nearly the whole surface of the particle has been exposed to the surface.

Simulations were repeated and the time was recorded to bind a captured target on the particle surface to the reactive surface. The starting conditions were chosen randomly: random values were generated for the particle height, the orientation of the remanent moment and the position of the binding site on the particle. The particle height was determined based on a balance between thermal energy and the weight and buoyancy of the particle. In Figure 7.8e, the fraction of bound particles as a function of time is shown for four different cases: for particles with targets with a radius of 100 nm or 5.5 nm and for passive or active incubation. For both radii of the targets, it is found that the applied magnetic actuation protocol (Figure 7.8b) results in an increase of the rate at which particles bind to the surface. For targets with a radius of 100 nm and 5.5 nm, the incubation time needed to bind half of the particles is decreased respectively by a factor of 4.9 ± 0.6 and 2.3 ± 0.4 . From this it follows that the magnetic actuation protocol is less efficient for protein-sized targets, but can still half the incubation time.

We explored the effect of magnetic actuation for magnetic particles with a smaller size. As the rotational mobility of a particle scales with R_{MP}^{-3} , the need to enhance the rotational mobility for smaller sized particles seems less relevant. However, to bind to the surface, the particle also needs to be in contact with the surface. For

smaller magnetic particles, the influence of gravity is less and does not keep particles close to the surface anymore. In this regime, magnetic actuation can be used to promote surface contact by using field gradients. Based on this, we studied a similar actuation protocol as for larger particles (Figure 7.8b), but (i) with angular steps of 90° instead of 20° , or (ii) with a fixed and in-plane field orientation in subsequent pulses. Applying such protocols to particles with a radius of $R_{MP} = 0.25 \mu\text{m}$, we also find an increase in the binding rate (see Figure 7.9). Specifically, in case of alternating field orientations, the time to bind 50% of the particles is decreased by a factor of 3.1 ± 0.6 for targets with $R_{\text{target}} = 100 \text{ nm}$, and a factor of 2.8 ± 0.6 for targets with $R_{\text{target}} = 5.5 \text{ nm}$. In case of a fixed field orientations, the decrease with $R_{\text{target}} = 5.5 \text{ nm}$ is only by a factor of 2.1 ± 0.5 . So, for small particle sizes, the binding rate is mostly improved by the application of magnetic field gradients to keep particles close to the surface. Varying the field orientation on the other hand still has a positive effect on the binding rate for small particles.

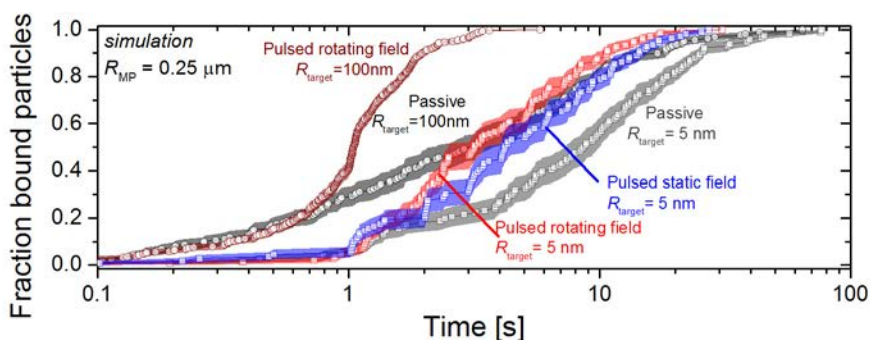


Figure 7.9 Numerical simulations of the incubation of a 500 nm particle with a single captured target at a surface, with and without magnetic actuation. The fraction of bound particles is plotted as a function of the incubation time and for two target sizes, R_{target} . The dark red and red open squares correspond to a magnetic actuation protocol in which the magnetic field (5 mT) is applied for 0.5 s with pauses of 0.5s, and the orientation of the field rotated in subsequent pulses about the x -axis and the y -axes in steps of 90° . The blue open squares corresponds to a magnetic actuation protocol with the same pulsation, but in every pulse the field is oriented in the same direction: in the z -direction. In both cases the field gradient towards the surface is 3.6 T/m. For each case, data is obtained from ~ 150 repeated simulations of the particle orientation in time. The shaded areas correspond to errors based on Poisson statistics.

Based on these numerical Brownian dynamics simulations, we conclude that the application of a – still non-optimized – magnetic actuation protocol can reduce incubation times by 2 to 4 times. The effectiveness of magnetic actuation is found to be only weakly dependent on the size of the magnetic particle. The simulations however do not include all the biological or non-specific interactions between the particles and the surface that are present in an actual assay. We assumed that particles bind upon first contact of the target with the surface, but, in an actual assay, reacting proteins only bind within a specific relative orientation. Nevertheless, it is not certain whether such constraints would limit the binding process. Depending on the manner in which the reacting proteins are attached to the particle and the surface,

they can exhibit many fluctuations in their configuration and orientation on the time-scale of an encounter. While incorporating or studying these effects in the numerical model is an interesting direction, it is more interesting to first compare the obtained theoretical data with experimental results.

7.4.2 Experimental results

The specific binding of magnetic particles with a captured target to a bio-functionalized surface was quantified. A model system was used comprising protein G coated magnetic particles, provided with a few biotin-coated fluorescent nanoparticles that act as captured targets (see section Appendix 7.D for a characterization of the number of nanoparticles per magnetic particle). In experiments the particles were incubated on a neutravidin-coated polystyrene surface for 2 minutes, with and without the application of a magnetic actuation protocol. The applied actuation protocol was exactly the same as described in the previous section and shown in Figure 7.8b. To reduce non-specific binding, the neutravidin-coated surface was blocked with BSA (see section 7.2.4). After incubation, the incubation chamber was turned upside down and both bound and unbound particles were imaged with combined fluorescence and bright-field microscopy, by imaging respectively the top and the bottom substrate at the same lateral position.

Figure 7.10a shows an example image of the bound particles after incubation with magnetic actuation. In the image both the magnetic particles and the captured targets can be distinguished, enabling to determine whether particles were bound by means of a specific bond or not. Bonds were considered specific when the fluorescent particle ($R_{\text{target}} = 0.1 \mu\text{m}$) is located less than approximately $\sqrt{(1.4+0.1)^2 - (1.4-0.1)^2} \approx 0.75 \mu\text{m}$ away from the center of the magnetic particle ($R_{\text{MP}} = 1.4 \mu\text{m}$). For larger distances, the fluorescent particles cannot be in contact with the surface and bonds were considered to be non-specific.

Per image, we quantified the number of specific bonds N_s , non-specific bonds N_{ns} and unbound particles N_{nb} . We also characterized the number of captured targets on the magnetic particles (see Appendix 7.D) and we determined that $\eta_{\text{reactive}} \approx 14\%$ of the incubated particles contained 1 or 2 targets. To compare results in a clear way, we define

$$f_{s,\text{total}} = \frac{N_s}{N_{\text{total}}} = \frac{N_s}{N_{nb} + N_{ns} + N_s},$$

as the fraction of specific bonds with respect to all magnetic particles within the same certain field of view, and

$$f_{s,\text{reactive}} = \frac{N_s}{\eta_{\text{reactive}} \cdot N_{\text{total}}} = \frac{1}{\eta_{\text{reactive}}} f_{s,\text{total}},$$

as the fraction of specific bonds with respect to the amount of particles within the same field of view that contain one or more targets.

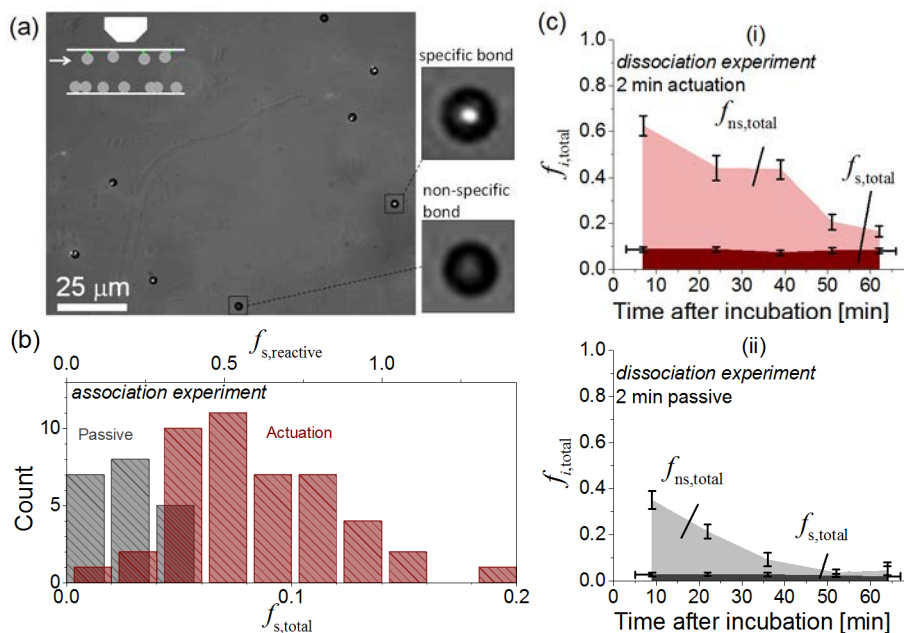


Figure 7.10 Experimental quantification of the binding of magnetic particles with fluorescent and biotinylated targets to a neutravidin-coated surface, with and without the application of time-dependent magnetic fields. After incubation of 2 minutes, the fluid chamber is turned upside down to separate bound from unbound particles. (a) Image of bound particles (dark circles) with combined fluorescence showing the binding sites as smaller white dots. The zoom-in images on the right-hand side show a specific bond and a non-specific bond. (b) Histogram showing the fraction of particles that have bound specifically, as measured per image. Data is shown as a function of $f_{s,total}$ and $f_{s,reactive}$. (c) Dependence of the fractions of specific and non-specifically bound particles on the time after incubation, in case of (i) actuation and (ii) no actuation.

By analyzing many images, we determined histograms of the fraction of particles that had bound specifically with and without magnetic actuation (Figure 7.10b). After two minutes of incubation, the specific fraction $f_{s,total}$ was larger in case magnetic actuation was applied. On average, $f_{s,total}$ was higher by a factor of ~ 3.3 . Considering only the particles with captured targets, we find that $f_{s,reactive} \approx 0.6$ after two minutes in case of actuation and $f_{s,reactive} \approx 0.18$ in case of no actuation. Compared to Figure 7.8e, these fractions are significantly less than found in the simulations, where almost complete binding of all reactive particles is expected for both cases after two minutes. In simulations, however, non-specific interactions between the particles and the surface were not considered, while in experiments non-specific binding of particles did occur; as shown for example in Figure 7.10a.

In Figure 7.10c, the experimentally determined fractions of non-specific bonds are shown. In case of magnetic actuation, we found that about 50% of the incubated particles were bound non-specifically to the surface, 10 minutes after turning the fluid chamber upside down. When no magnetic actuation was applied, only 30% of the particles were bound non-specifically to the surface. These fractions are large compared to the fractions of specific bonds. In contrast, control experiments in

which no neutravidin was incubated on the surface show only about 5% non-specific binding of particles. This indicates that the presence of neutravidin at the surface enhanced adhesive interactions with the protein G coated particles. Neutravidin has a near-neutral isoelectric point of $pI = 6.3$ and thus carries a slightly negative charge (at $pH = 7.4$), but a smaller charge compared to BSA which has a pI of 4.7.²⁰⁶ As protein G-coated magnetic particles are also negatively charged ($pI = 4.6$), the electrostatic repulsion between the particles and the surface is expected to be weaker for neutravidin than for BSA, and thus should lead to less repulsive interactions. The strong effect of electrostatic interactions on non-specific binding was also reported by De Palma et al.¹¹³. Besides this, the application of magnetic fields to bring particles to the surface increases the contact between the surfaces and will further enhance non-specific binding.

Interestingly, by monitoring the number of (non-)specific bonds over time (see Figure 7.10c), we find that the fraction of non-specific bonds decreases within a time-span of one hour, while the fraction of specific bonds remains almost constant. First of all, these apparently different thermal dissociation rates are an indication that both fractions are indeed different types of bonds; in other words, one fraction is (relatively) short-lived and non-specific, whereas the other fraction is specific and long-lived. Based on the different life-times of the bonds, it is possible to discriminate the bonds in force-induced dissociation assays. In such assays, stringency is applied to the magnetic particles by the application of for example magnetic field gradients¹²⁹⁻¹³⁰ or fluid flows¹¹⁸. While stringency can be applied as a washing step after incubation of particles at the surface, magnetic fields can also be used to break non-specific bonds during incubation as was shown by Bruls et al.²⁵. For the magnetic actuation protocols applied here, stringency may be included during a few seconds after a particular number of pulses.

Overall, these experimental results provide evidence that the application of magnetic fields allows accelerating specific bond formation, but also show that magnetic actuation makes the assay more susceptible to non-specific interactions. Non-specific interactions do not only hinder further detection steps, but also hinder the specific bond formation process. Magnetic actuation for the incubation of particles at a surface should therefore not be focused solely on maximizing the particle exposure, but also on overcoming non-specific interactions.

It is interesting to estimate the potential impact of magnetic actuation to form bonds at a sensor surface in case non-specific interactions are overcome. In case of 200 nm targets, no magnetic actuation would result in a binding probability $p_s \approx 0.18$ within two minutes (Figure 7.10c,ii), whereas the magnetic actuation should be able to yield $p_s \approx 1$ (Figure 7.8e). In other words, magnetic actuation would lead to ~6 times more specific bonds. For more realistic targets (like proteins), data in Figure 7.8e shows that specific bond formation is slower by a factor of 3. Combined with non-specific interactions, we estimate a $p_s \approx 0.18 / 3 = 0.06$ after 2 minutes without actuation. In the same time, magnetic actuation without non-specific interactions could result in $p_s \approx 0.84$ (see Figure 7.8e), which would increase the number of specifically bound particles by a factor 14. According to these estimations, it is possible

to significantly gain in detection signal by actuating magnetic particles to bind targets to a sensor surface.

7.5 Discussion and Conclusions

The dynamics of a magnetic particle near a surface were studied in the context of the formation of a target-induced sandwich bond, for the case that a target analyte is first captured from the sample fluid by a magnetic particle and subsequently binds to a reactive sensor surface.

First, we characterized the response of a superparamagnetic particle to a rotating magnetic field. To understand the magnetization behavior of the particles in detail, we developed a numerical model and compared it to experimental data to determine the remanent moment of the particles. Subsequently, numerical Brownian dynamics simulations were used to develop a magnetic actuation protocol to accelerate binding of a target captured by a magnetic particle to a reactive surface. It was found that binding could be achieved within several minutes. To maximize the exposure of particles to the surface, magnetic fields were applied in pulses to rapidly rotate particles over large angles and allow efficient particle rotation over smaller angles by Brownian rotation. Based on the simulations, we find that magnetic actuation can reduce the incubation times by at least a factor two. Experimental data confirmed that magnetic actuation can improve the binding rate, but also emphasize that non-specific interactions can significantly inhibit the formation of specific bonds.

To achieve rapid and specific bond formation in magnetic particle-based assays, we conclude that magnetic actuation should consist of: (i) magnetic field gradients to improve contact between particles and the surface; (ii) magnetic fields that vary in orientation to enhance the exposure of the particle surface, but applied (iii) in pulses to also exploit Brownian rotation; and (iv) magnetic stringency by magnetic forces or torques to break weak non-specific bonds during incubation. Based on the obtained numerical and experimental data, we estimate in case of micron-sized magnetic particles that magnetic actuation can increase specific bond formation with captured proteins by at least one order of magnitude. In case of nanometer-sized magnetic particles, we expect that the effect is less, as magnetic actuation is less important to expose the particle surface to the reactive surface, but magnetic actuation is still important to reduce the effects of non-specific interactions.

The proposed magnetic actuation protocol has a large amount of features. Interestingly, the required fields and field gradients can in principle be generated by a system with only three electromagnets placed in a plane orthogonal to the reactive surface, i.e. a simplified version of the system in Figure 7.2b. Furthermore, the magnetic fields do not need to be strong and only need to be applied for short durations. This limits heating effects caused by the electromagnets.

The insights from this study were obtained using a model assay in which 200 nm fluorescent particles were used as targets that were captured by a magnetic particle. In a diagnostic immunoassay, the target will most often be a protein, and thus smaller than the fluorescent particle. From the numerical simulations we find that magnetic actuation is still effective, but less, for smaller targets. Concerning the flu-

id matrix, in this study we focused on fluids with a viscosity similar to water. In practice, the viscosity may be higher, for example when the whole assay is performed in a biological fluid such as blood or saliva. In such cases, random rotation of the particles will decrease and the impact of magnetic actuation can be even larger, as magnetic fields can be used to overcome the additional viscous drag.

Finally, the combination of numerical simulations with the model assay can be an interesting approach to further study molecular binding interactions, including specific and non-specific interactions with corresponding association and dissociation rates. For example, the influence of the protein binding affinities on the binding rate can be studied; but also the potential energy landscapes corresponding to the specific interactions in terms of relative distance and orientation of the binding sites.

In conclusion, we have presented a comprehensive methodology to study binding interactions in particle-based sandwich immunoassays. We have shown that dynamic magnetic actuation can be used to improve the rate of target-induced binding in surface-binding assays. The obtained results and insights provide a solid basis to further study and develop high-sensitivity magnetic particle based assays for point-of-care diagnostics.

7.7 Appendix

7.A Calibration of the magnetic setup

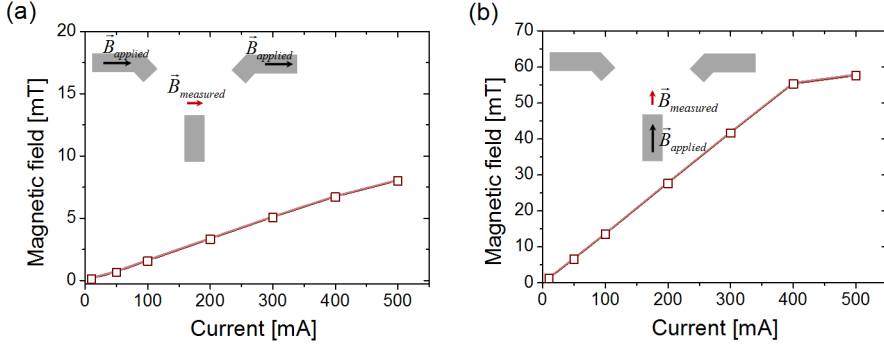


Figure A.1 Calibration data of (a) the in-plane magnetic field and (b) the out-of-plane magnetic field at the position of the fluid cell. The inset images show a side cross-section of the magnet setup in which the magnets are indicated that are used to apply a magnetic field at the position of the fluid cell. Magnetic fields were measured using a Gauss meter (5100 series from F.W. Bell). We acknowledge Stefano Cappelli, who performed the measurements.

7.B Comparing magneto-crystalline anisotropy with shape anisotropy

Here the magneto-crystalline anisotropy and shape anisotropy of the magnetite grains in the superparamagnetic particles are estimated and compared.

Magnetite has a face centered cubic (fcc) inverse spinal crystal structure with a lattice constant of 0.8397 nm.²⁰⁷ Its magneto-crystalline anisotropy energy density u_{ma} may be described as

$$u_{ma} = K_1 \left(\cos^2 \theta_1 \cos^2 \theta_2 + \cos^2 \theta_2 \cos^2 \theta_3 + \cos^2 \theta_3 \cos^2 \theta_1 \right) + K_2 \left(\cos \theta_1 \cos \theta_2 \cos \theta_3 \right) \quad (\text{B.1})$$

with K_1 and K_2 the first and second order anisotropy constants, i.e. $-1.35 \cdot 10^4 \text{ J/m}^3$ and $-0.44 \cdot 10^4 \text{ J/m}^3$ at 300 K respectively.²⁰⁸ θ_1 , θ_2 and θ_3 are the angles between the magnetization and the three crystal axes, i.e. along the x , y and z axis. Minimizing this equation, the first order solution yields four easy axes: along the $\langle 111 \rangle$, $\langle 11-1 \rangle$, $\langle 1-11 \rangle$ and $\langle 1-1-1 \rangle$ direction; and three hard axes along the three crystal axes x , y and z : resp. $\langle 100 \rangle$, $\langle 010 \rangle$ and $\langle 001 \rangle$.

If an external magnetic field is applied in any arbitrary direction with respect to a magnetite grain, the magnetization of the grain will orient itself in such a way that the anisotropy energy is balanced to the magnetic energy. Due to the anisotropy, the final orientation will depend on the history of the grain's magnetization. To change the magnetization from one easy axis to another, an energy barrier has to be overcome, which is $0.55 \cdot 10^4 \text{ J/m}^3$ at maximum and $0.2 \cdot 10^4 \text{ J/m}^3$ at minimum, as follows from Eq. B.1.

Besides the crystal structure of the magnetite grains, the shape of the grains may also cause preferential directions for the magnetization, i.e. shape anisotropy. The strength of shape anisotropy on a magnetized object can be determined by estimating the demagnetizing field for a particular magnetization direction. For a sphere, the demagnetizing field is the same in any direction and no shape anisotropy is present. However, it is unlikely that the shape of the magnetite grains is perfectly spherical, but rather a spheroid with different axis lengths. For simplicity, we estimate the strength of the shape anisotropy for two simplified cases: a prolate and an oblate spheroid.

The demagnetizing field, H_d , along the different principal axes of the spheroid, is

$$H_{d,i} = -N_{dm,i} M_i, \quad i = x, y, z, \quad (\text{B.2})$$

with N_{dm} the demagnetizing factor, which depends on the shape of the spheroid. M is the magnetization and it is equal to the saturation magnetization of the grain, since each grain acts as a single domain (grain diameters are typically smaller than 15 nm).²⁰⁹ The saturation magnetization may be calculated by using the mass density of Fe_3O_4 ($\rho = 5.17 \text{ gr/cm}^3$)²¹⁰, the molar mass ($M_r = 232 \text{ g/mol}$), Avogadro's number N_A and the magnetic moment of a Fe^{2+} atom ($\mu_{\text{Fe}_3\text{O}_4} = 4.6 \cdot 10^{-23} \text{ J/T}$)²¹⁰, i.e.

$$M = M_{sat} = \frac{\rho N_A}{M_r} \mu_{\text{Fe}_3\text{O}_4} = 6.2 \times 10^5 \text{ Jm}^{-3} \text{T}^{-1}. \quad (\text{B.3})$$

In order to obtain convenient equations for the demagnetizing factors for a spheroid with semi-axes a , b and c resp. in the z , x and y direction, it is assumed that

$$a > b = c,$$

in case of a prolate spheroid and

$$b = c > a,$$

in case of an oblate spheroid. The corresponding demagnetizing factors in these directions will be labeled N_z , N_x and N_y . For a prolate spheroid, the demagnetizing factors have been reported²¹¹⁻²¹² to be

$$N_z = \frac{1}{(m^2 - 1)} \left[\frac{m}{2\sqrt{m^2 - 1}} \cdot \ln \left(\frac{m + \sqrt{m^2 - 1}}{m - \sqrt{m^2 - 1}} \right) - 1 \right], \quad (\text{B.4})$$

$$N_x = N_y = \frac{m}{2(m^2 - 1)} \left[m - \frac{1}{2\sqrt{m^2 - 1}} \cdot \ln \left(\frac{m + \sqrt{m^2 - 1}}{m - \sqrt{m^2 - 1}} \right) \right]$$

with the aspect ratio defined as $m = a/b > 1$. For an oblate spheroid these equations are

$$N_z = \frac{n^2}{(n^2 - 1)} \left[1 - \frac{1}{\sqrt{n^2 - 1}} \cdot \arcsin \left(\frac{\sqrt{n^2 - 1}}{n} \right) \right], \quad (\text{B.5})$$

$$N_x = N_y = \frac{1}{2(n^2 - 1)} \left[\frac{n^2}{\sqrt{n^2 - 1}} \cdot \arcsin \left(\frac{\sqrt{n^2 - 1}}{n} \right) - 1 \right]$$

where $n = b/a = m^{-1} > 1$.

The anisotropy energy density equals the inner product of the demagnetizing field with the magnetization:

$$u_{shape} = -\mathbf{M} \cdot \mathbf{B} = -\frac{\mu_0}{2} \mathbf{M}_{sat} \cdot \mathbf{H}_d = \quad (\text{B.6})$$

$$+ \frac{\mu_0}{2} (N_x M_{sat,x}^2 + N_y M_{sat,y}^2 + N_z M_{sat,z}^2)$$

where the factor 2 is inserted since it concerns the self-energy of the system. Combining Eq. B.6 with Eq.'s B.4 and B.5, the energy density is calculated for the case that the magnetization orients along the easy axis or along the hard axis for different aspect ratios of a/b (see Figure B1).

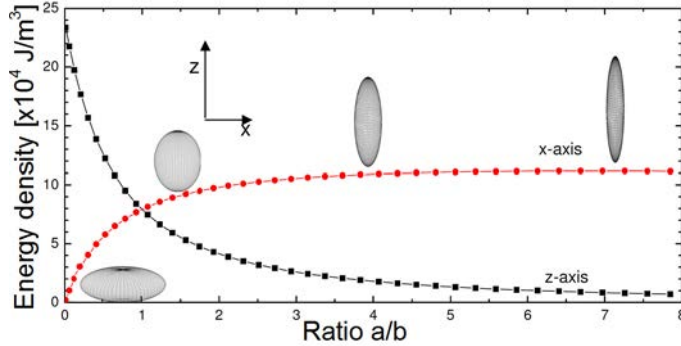


Figure B.1 The energy density along the z and x -axis for different types of rotating spheroids. For $a/b < 1$ the spheroid is oblate, while for $a/b > 1$ it is prolate. As is shown by the drawn spheroids, the volume of the grains kept constant for different aspect ratios. Note that for a sphere the energy density is the same in both directions, so it does not exhibit shape anisotropy.

In Figure B.1, the hard axis can be identified as the direction in which the energy density is at a (local) maximum while for the easy axis the energy density is at a (local) minimum. To compare the strength of shape anisotropy with the magneto-crystalline anisotropy for a single grain, the aspect ratio is determined at which the energy difference between the easy and hard axis is the same for both types of anisotropy. For a prolate spheroid, this is at an aspect ratio of 1.06, while for an oblate spheroid this is at an aspect ratio of 0.95. These aspect ratios are close to almost spherical magnetite grains. Thus, unless all the grains are spherical, it can be concluded that the shape anisotropy dominates the magneto-crystalline anisotropy.

7.C Validation of numerical Brownian rotation

The numerical scheme for Brownian rotation was validated by setting the magnetic torque to zero, i.e. via $B = 0$. As a typical timestep, 0.2 ms was taken and the numerical scheme was executed. As shown in Figure C.1, the angular displacement due to Brownian rotation is accurately simulated using Eq. 7.8 with $\Delta t = 0.2$ ms. The displacement after a single time-step as well as after many time-steps agree with the root-mean-squared values $(2D_{\text{rot}}t)^{0.5}$ as expected based on a rotational diffusion constant according to the Stokes-Einstein relation.

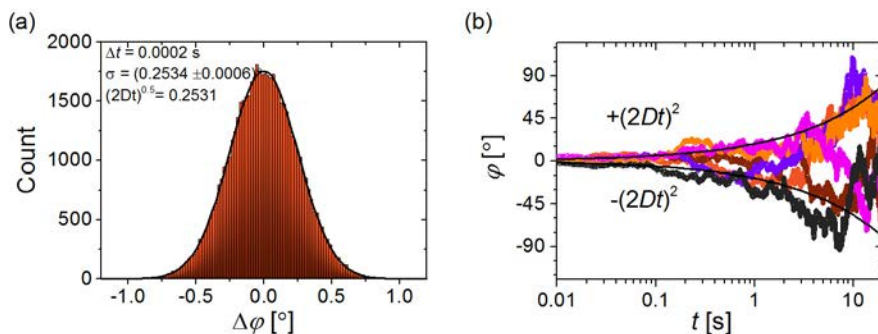


Figure C.1. (a) Histogram of computed angular displacement due to Brownian motion over 0.2 ms. In total 50,000 computations were made to obtain the distribution. The black curve represents a Gaussian distribution with the width which corresponds to the root-mean-squared angular displacement as analytically expected for Brownian rotation. (b) Simulated angular displacement over time in the absence of a magnetic torque. The simulated time-step is 0.2 ms. The black curves represent the analytically expected rms angular displacement due to Brownian rotation.

7.D Statistics of fluorescent target capture by magnetic particles

For a comprehensive study of the sandwich formation of particles containing one or more targets, it is important to control the sensitivity and selectivity of the assay, as it is difficult to discriminate (non-)specific bonds between proteins. Use of a target that is clearly visible under a microscope and within a large field of view can significantly simplify bond discrimination. We therefore investigated the use of biotin-coated fluorescent particles with a diameter of 200 nm as targets on the magnetic particles. These spherical targets were attached in a two-step assay to the magnetic particles as explained in section 7.2.2. In short, we first incubated protein G-coated magnetic particles with relatively low concentrations of anti-biotin antibodies, followed by the addition of an excess of biotin-coated fluorescent particles; and finally a magnetic washing step was carried out to remove unbound reagents. Here, the results of this procedure will be presented and discussed.

To quantify the number of fluorescent targets per particle, suspensions of particles were inserted in a 9 μL fluid chamber and concentrated at the bottom surface by holding a small ferromagnet for a few seconds below the fluid chamber. In this way, several hundreds of particles could be imaged within one field of view. To relate the

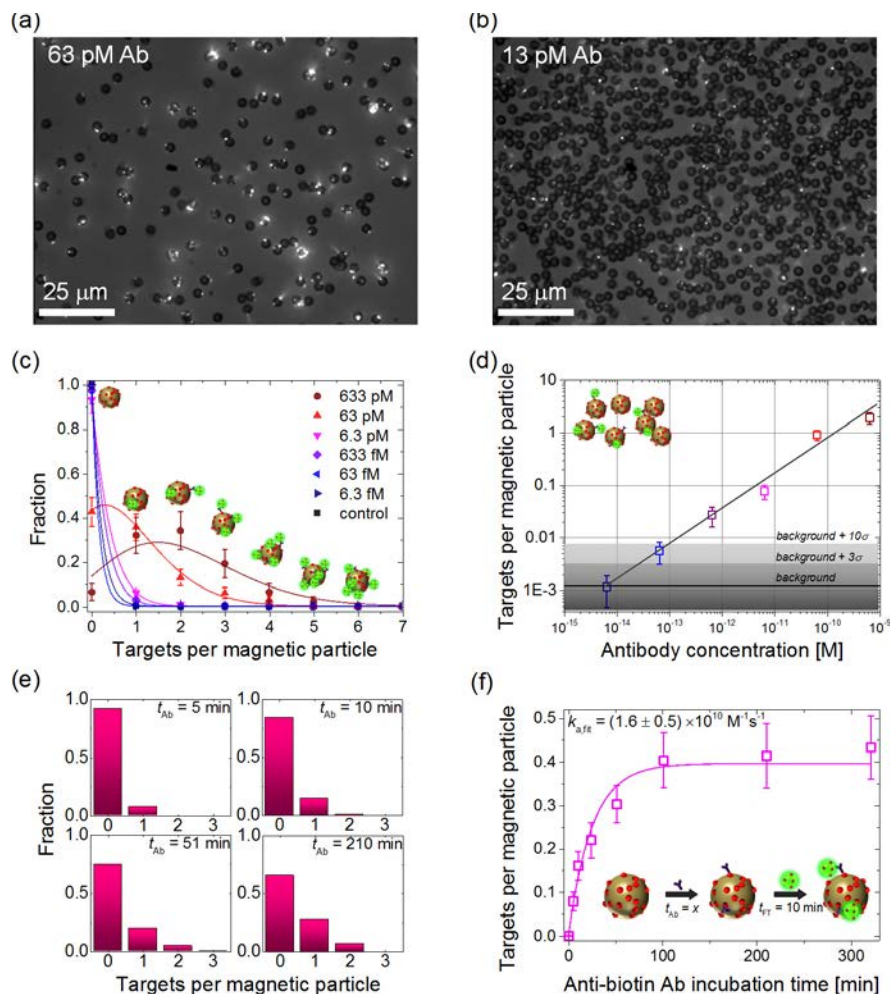


Figure D.1 Binding fluorescent targets to magnetic particles. The procedure consists first of the incubation of magnetic particles with a varying concentration of anti-biotin antibodies for a varying time t_{Ab} , followed by the addition and incubation for $t_{FT} = 10$ min of an excess of biotin-coated fluorescent particles to bind to captured antibodies and finally a magnetic washing step to remove unbound antibodies and fluorescent particles. To quantify the attachment of fluorescent targets, a 9 μL fluidic chamber was filled with a particle suspension and particles were concentrated at the bottom surface using a small ferromagnet. In (a) and (b) images are shown with combined fluorescence and bright-field transmitted imaging of the particles with bound fluorescent targets, for respective antibody concentrations of 63 pM and 13 pM. (c) Using the images, the binding of fluorescent targets was quantified for different antibody concentrations. The error bars correspond to counting errors according to Poisson statistics. The solid lines represent fits to the data of Poisson distributions. In (d) a corresponding dose-response curve is shown with the average number of targets per magnetic particle. We determine a LoD of ~26 fM and a LoQ of ~100 fM, according to the background signal with respectively three and ten times the standard deviation. In (e) the binding of fluorescent targets is quantified for an antibody concentration of 13 pM for different antibody incubation times. In (f) the corresponding average number of targets per magnetic particles is plotted as a function of the incubation time. The data is fitted using Eq. 2.8 to determine the association rate constant.

fluorescent targets to the magnetic particles, images were recorded with combined fluorescence and bright-field transmitted imaging of the sample. As shown in Figure D.1a,b particles were obtained with apparent random distribution of targets. Furthermore, almost no aggregation of particles is observed other than little aggregation which is due to the application of a strong magnetic field to concentrate particles at the surface. This indicates that particles containing a target almost do not cross-react anymore via the bound targets, as intended by the incubation of an excess of fluorescent targets compared to the antibody concentration.

From the images such as shown in Figure D.1a,b, we quantified the number of targets per particle and obtain distributions as shown in Figure D.1c. Note that only the targets were counted which were present on the upper half of the particles that is exposed to the camera. As shown, the data can be reasonably fitted by Poisson distributions, indicating that the target capture process is governed by Poisson statistics, confirming that the capture events occur randomly and independently. From the data the average number of bound particles is determined for different concentrations, leading to the dose-response curve shown in Figure D.1d. The dose-response curve is found to be slightly sub-linear with a limit-of-detection (LoD) of ~ 26 fM and a limit-of-quantification of ~ 0.1 pM as determined by respectively three and ten times the standard deviation of the control signal.⁷⁷

From the data we determine the optimal antibody incubation concentration for sandwich formation experiments to be in-between 6 pM and 60 pM, because particles having a single target are preferred. Within this concentration range, the number of particles with a single target is relatively high while the number of particles having two or more targets is still relatively low. Particles with two or more targets will complicate the analysis and comparison to numerical simulations, while particles without a target complicate the generation of statistically relevant data. This is because these particles will not be considered, but are still present in the experiments.

Using an antibody concentration of 13 pM, we quantified target binding as a function of the incubation time of the antibodies, as shown in Figure D.1e,f. It is found that after several hours the number of targets per particle becomes saturated, indicating that the binding reaction has reached an equilibrium. As the magnetic particles can bind many antibodies, we applied an equation similar to Eq. 2.8 as derived in section 2.2 for a similar system. Using this equation, we determine an association rate constant of $(1.6 \pm 0.5) \times 10^{10} \text{ M}^{-1}\text{s}^{-1}$ for protein G-coated particles binding to anti-biotin IgG. This value is slightly less compared to what we found in the previous chapter for protein G-coated particles binding to goat anti-mouse IgG labeled with Alexa fluor dye 488. Such variations in affinity of protein G to different types of antibodies are however not uncommon. Concerning further experiments, an antibody incubation time was chosen of 50 minutes.

8

Conclusions and Outlook

Magnetic particles are being applied in integrated lab-on-a-chip diagnostic assays to perform microfluidic processing steps. In this thesis, we have investigated a number of individual process steps, with two aims: first, to obtain a fundamental understanding of the processes, and second, to optimize the processes using novel magnetic actuation protocols. We have developed model descriptions of the binding processes and of the behavior of ensembles of magnetic particles, and we have compared these to experimental data. Based on the obtained insights, we have developed and characterized dynamic actuation methods (i) to rapidly and efficiently capture molecular analytes from sample fluid, (ii) to control and redistribute particle distributions and (iii) to bind captured analytes to a sensor surface using magnetic particles. In this Chapter, we summarize the scientific and technological advancements described in this thesis and put the achievements into the perspective of future integrated point-of-care biosensing systems.

8.1 Introduction

In this thesis, we have on the one hand studied a number of fundamental biophysical aspects involved in the microfluidic application of magnetic particles, and on the other hand developed novel actuation functionalities of magnetic particles for lab-on-a-chip diagnostic assays. In this Chapter, we discuss both topics and the future prospects.

8.2 Fundamental biophysical tools

In order to enable research on the application of magnetic particles in microfluidic diagnostic assays, it is essential to understand the particle properties, the particle behavior and the different binding processes on a fundamental level. Therefore, we have developed accurate characterization methods, insightful experimental model systems and detailed theoretical model descriptions. In the following paragraphs, we will discuss these different biophysical research tools.

8.2.1 Characterization of magnetic particles

In the research presented in this thesis, superparamagnetic particles play a vital role as they are the key actors in the different microfluidic processes. Their usefulness in these processes is strongly determined by their specific properties. The paramagnetic behavior allows particles to translate and interact with other particles only when exposed to external magnetic fields. A weak remanent magnetization allows inducing rotation to single particles. Besides magnetic properties, the shape and the size of the particles play an important role, as these govern the surface-to-volume ratio of the particles, but also the translational and rotational mobility of the particles in a fluid. Last of all, the surface chemistry determines the applicability and effectiveness in a (bio-)chemical context.

To control all of these different properties in a fabrication process, the availability of accurate and rapid characterization techniques is important. To characterize geometrical properties, several microscopic tools are available that give details on all relevant scales, such as scanning electron microscopy. For the (bio-)chemical surface properties, many (bio-)chemical methods exist to quantify the overall performance of the assay. For the characterization of the magnetic properties of magnetic particles, the standard technology is vibrating sample magnetometry (VSM), but this technique can only be applied to large ensembles of particles. As a result, only ensemble-averaged magnetic properties can be characterized such as the average susceptibility and saturation magnetization.

To characterize magnetic properties at the level of a single particle, no standard technology exists that is accurate and can rapidly yield results. In Chapter 5, we have shown that field-induced disaggregation of particle clusters, i.e., intra-pair magnetophoresis, can be used to characterize the magnetic properties of magnetic particle distributions with a high level of detail. The method is easy to use and allows determining magnetization curves, grain size distributions and histograms of magnetic particle properties. In Chapter 7, we developed experimental and numeri-

cal methods to study and characterize the remanent magnetization properties of particles. The response of particles to a rotating field can be used to determine the remanent magnetic moment, but also to obtain more details on the magnetic anisotropy and grain distributions within the particles.

We expect that the methods presented in this thesis to characterize magnetic particle properties can significantly aid the further development of particles for nanobiotechnological applications such as high-sensitivity biosensing systems. To optimize particle properties, fabrication processes are required in which several parameters can be scaled in a controlled way to study their effect on the various particle properties. Industrial companies have already developed fabrication processes to generate magnetic particles with well-defined geometrical, biofunctional, and ensemble-averaged magnetic properties. We expect that industrial companies will be leading in the further development of magnetic particles, and that the speed of development of particles with more sharply defined magnetic properties will depend on the commercial value that the companies foresee in the corresponding applications.

While accurate characterization methods as developed in this thesis can provide data on the overall magnetization properties of magnetic particles, they provide too little data to also understand the exact magnetic behavior of superparamagnetic particles. For a more detailed understanding, we believe that it is necessary to determine the detailed configuration and shape of the grains inside the particles. Based on such data, it should be possible to model and understand the complex magnetic behavior from a bottom-up approach. In the end, such models should be predictive and as such they can be very useful in the production of magnetic particles with properties attuned to their particular purpose.

8.2.2 Experimental model systems to study magnetic particle-based binding processes

To study the different binding processes relevant in lab-on-a-chip diagnostic assays, several model systems have been used in this thesis, each with their own possibilities and limitations. As the target analyte plays a central role in diagnostic assays, model systems were chosen with two types of targets: (i) bio-functionalized fluorescent nanoparticles (e.g., $\text{\AA} 200$ nm) and (ii) antibodies labeled with fluorescent dye molecules. By using fluorescent targets, it is possible to measure in real time the presence of the targets using microscopy techniques, without requiring any fluid handling steps. The direct measurements make it possible to perform experiments at a high rate, which allows studying the binding process with a high efficiency.

Due to their relatively large size, single fluorescent nanoparticles can be easily located in real-time during experiments, i.e., not only in the fluid, but also on the surface of the magnetic particles after capture. In this way, the capture (Chapter 2) and surface-binding (Chapter 7) process could be quantified with single-target resolution. Furthermore, the spherical shape and almost uniformly reactive surface of the nanoparticle targets are a good starting point for a closer comparison with theoretical model descriptions as compared to proteins such as antibodies, which have a dynamic structure and a more complex binding behavior. On the other hand, the large size

of the nanoparticles compared to proteins implies that the results obtained with fluorescent nanoparticles have a limited applicability.

Therefore, we also used antibodies labeled with fluorescent dye molecules to study the capture process (Chapter 3). As single-target detection is not easily performed on magnetic particles, we used elevated target concentrations and measured average fluorescence intensities generated by multiple captured antibodies on the particle surface. As a result, the process could not be studied anymore with single-target resolution, but combined with data on fluorescent nanoparticles it allowed us to obtain a fundamental insight in the capture processes. In the future, we expect that microscopy techniques will improve to enable the position tracking of single (fluorescently labeled) biomarkers or other proteins in particle-based binding processes. With such data, the different binding processes can be studied in even more detail and will allow one to study the effect of for example different molecular architectures to improve the probability that binding sites encounter, align and react.

The magnetic particles used in the experiments had a size between 500 nm and 3 μm . The largest particles are advantageous for experimental research, because applied magnetic forces are high and their position can be accurately tracked using video microscopy. Furthermore, the geometry and magnetic properties of the micrometer-sized magnetic particles were more sharply defined compared to the submicrometer-sized magnetic particles. However, the large particle size reduces Brownian motion and Brownian rotation, and promotes sedimentation. These factors make the potential impact of magnetic particle actuation on the different binding processes larger for the micrometer-sized magnetic particles. Still, also submicrometer-sized particles suffer from local target depletion in capture processes at elevated particle concentrations. Furthermore, in surface-binding assays, the large Brownian motion of submicrometer-sized particles needs to be countered by field gradients, in order to keep the particles in contact with the surface. Therefore, we expect that magnetic actuation will also be effective – be it less – in assays comprising submicrometer-sized magnetic particles.

In applied research, experimentation is crucial to identify all the relevant interactions in a technical design. In case of microfluidic diagnostic assays, non-specific interactions between the various constituents can significantly compromise the effectiveness of the assays. To develop a robust and reliable assay based on magnetic particles, it will be important to also study the influence of non-specific interactions in the different processing steps, i.e., not only in the surface-binding step, but also during target capture. Ultimately, the assay should be specific and sensitive in a complex matrix, in which, besides the few targets, many other proteins and other biomaterials are present.

8.2.3 Simulation models to study microfluidic process steps based on magnetic particles

As a last biophysical tool, we used numerical Brownian dynamics simulations to model the complex interplay between hydrodynamic and physicochemical interactions in magnetic particle-based microfluidic processes. Brownian dynamics (BD) is a simulation technique that has been mostly used to study the large-scale dynamics of polymers, nanoparticles or proteins in a dilute solution^{178, 213}. In Chapters 4 and 6, we have applied BD to simulate the dynamics of (magnetic) microparticles in the presence of solid-liquid interfaces and time-dependent magnetic fields. BD is suitable to simulate such systems, as hydrodynamic interactions and Brownian motion forces are well-defined and computationally cheap for spherical objects. This enabled us to simulate the dynamics of several tens of particles over relatively long time-scales (several tens of minutes) with small timesteps (1 – 100 ns). Compared to experiments, BD can be used to study in much more detail the complex response of magnetic particles to magnetic fields that vary at high frequencies. We anticipate that, if the applied methods are made more efficient, and performed on dedicated simulation computers, it should be possible to simulate the behavior of up to 10^3 particles or even more. Such systems are increasingly more realistic to the particle systems as studied in experiments and will give an even better insight in the complex particle dynamics on a global scale as well as on the scale of single particles. For a microfluidic biosensor, controlling the particle behavior on both scales is essential to enable a strong performance of the assay. Ideally, a simulation method should be developed that can simulate the behavior of all particles and corresponding interactions in the microfluidic chamber.

As described in Chapters 3 and 7 of this thesis, BD simulations were also used to study molecular binding processes. To model the molecular binding, however, it was necessary to impose several crude assumptions concerning the relative binding configuration (distance and orientation) and reaction probability (e.g., hit-and-stick). In spite of the assumptions, the simulations were found to confirm experimental data and provide interesting insights in the binding processes. Using current computational methods, we expect that these processes can be studied in further detail. For example the influence of the relative binding orientation or the chemical reaction can be studied by comparing simulation data to experiments with varying targets and capture molecules, on the particle and on the sensor surface. Ultimately, to study the binding processes on the molecular scale, molecular dynamics (MD) simulations should be developed, in which the molecular structure and specific interactions of the reacting (bio)molecules should be included. MD simulations would be useful to study novel molecular architectures to improve the exposure of binding sites into the fluid and to reduce non-specific interactions as much as possible.

In the scientific development process of technological applications, from the start, experimentation and observation are vital to identify and study all the practical interactions within a system. As the research progresses, experiments may become less efficient, while theoretical descriptions become more and more powerful when

they are able to describe the experimental observations. Ultimately, such theoretical descriptions should become comprehensive and predictive for the studied phenomena. In case of lab-on-chip biosensing systems based on magnetic particles, we foresee the development of comprehensive theoretical models for the microfluidic assays. These models should combine BD simulations of large particle systems and MD simulations of the detailed binding processes. As such, these models will contain both the macroscopic and microscopic effects, and thereby cover the whole microfluidic assay. Finally, the models will provide engineers with a powerful tool to design a final and optimal device architecture.

8.3 Function-oriented research

Based on the obtained fundamental understanding of the behavior of magnetic particles and the different binding processes, novel magnetic actuation techniques were developed to improve the functioning of magnetic particles in lab-on-a-chip applications. In the following paragraphs, the different techniques will be put into perspective.

8.3.1 Specific capture of analytes using magnetic particles

We have studied the application of magnetic particles to capture targets from a fluid by specific binding to affinity molecules on the surface of the particles. The particle-based capture process was elucidated and we distinguished three stages. First, volume transport creates encounters between the particles and the targets. This transport is influenced by the relative translational motion of the reagents, e.g. by diffusion. Second, during an encounter, near-surface transport can create alignment between binding sites and depends on both the relative translational and rotational mobility of the reagents. And third, aligned binding sites can bind by means of a chemical reaction. Using various experimental model systems, we obtained evidence that the two stages concerning physical transport of reagents are mostly limiting the association process of proteins to a magnetic particle.

The particle-based association process is particularly effective because magnetic particles have a high surface-to-volume ratio and because their surface is completely covered with binding sites. As a result, during the incubation, depletion zones in the target concentration form near the particle surface and these zones increase when particles are present at higher concentrations. Depletion zones cause the capture rate to drop and make the use of capture particles less effective.

To reduce depletion zones, we applied magnetic actuation protocols to enhance particle-fluid interactions. We have found that protocols with a combination of field gradients and rotating magnetic fields are the most effective. Specifically, field gradients induce movement of particles through the fluid, while rotating magnetic fields cause dynamic rotational behavior of magnetic particle chains that induce local fluid mixing within the range of the particle chain. On a model system comprising 2.8 μm -sized particles and fluorescently labeled antibodies, we quantified association rate constants and studied their dependence on various actuation parameters. Without magnetic actuation, association rate constants equal to $k_a = 0.16 \pm 0.02 \times 10^{10} \text{ M}^{-1} \text{ s}^{-1}$

$^1\text{s}^{-1}$ were measured, and with magnetic actuation, values were obtained as high as $k_a = 6.0 \pm 0.6 \times 10^{10} \text{ M}^{-1}\text{s}^{-1}$. We quantified the dependence of the association rate on actuation parameters such as the field strength and rotation frequency, and also on assay parameters such as the particle size, particle functionalization, particle concentration, the medium properties, and the target size and target properties. By comparing association rate constants, we estimate that magnetic actuation can improve capture rates by a factor of 10^1 to 10^2 , at the concentrations at which magnetic particles are often used in assays. Compared to the method of vortex mixing, which is commonly used to speed up reactions in large fluid volumes, we find that magnetic actuation can achieve similar or even higher effective association rate constants. When applied in more complex sample fluids, we anticipate that an even larger impact can be obtained because such fluids are typically more viscous and thereby make diffusive processes even less efficient.

As capture of biological targets from sample fluids is a general aspect of almost all lab-on-chip biosensing assays, we foresee a broad applicability of the developed methods.

8.3.2 Redistribution of magnetic particles

To obtain a better control over the collective behavior of magnetic particles, we studied the response of magnetic particles in experiments and using numerical Brownian dynamics simulations.

In a magnetic field, magnetic particles tend to aggregate and form clusters due to induced magnetic dipole-dipole interactions between the particles. Such clustering may be enhanced by attractive non-specific binding between the particles, whereafter the clustering cannot simply be undone by removing the magnetic field. Furthermore, magnets that are used to actuate magnetic particles typically cause particles to drift towards the magnet poles, resulting in heterogeneous particle distributions. To overcome aggregation and drift of magnetic particles, we have developed magnetic actuation protocols which take advantage of repulsive dipole-dipole interactions and particle-surface interactions to disaggregate and displace particles over a surface. The first method to disaggregate multi-particle clusters consists of bringing clusters to a physical boundary using a field gradient and subsequently breaking the cluster by applying an out-of-plane magnetic field, as described in Chapter 4. Alternatively, particle spreading can be achieved by rotating multi-particle clusters orthogonal to the surface, by so-called rotaphoresis, as described in Chapter 6. Rotaphoresis causes clusters to move over the surface at several mm/s while simultaneously being disaggregated. For both methods, we reproduced the experimentally observed behavior using numerical Brownian dynamics simulations. Furthermore, simulations were used to study and further optimize actuation protocols as a function of various parameters, such as different particle properties, field properties, fluid properties and interactions between particles mutually and with the fluid or the surface.

The developed protocols open up new possibilities to use magnetic particles in a microfluidic context. We envisage that the field-induced redistribution of particles can be of use in all types of detection assays discussed in Table 1.1. In magnetic

carrier assays, redistribution can improve accessibility of the particle surface within different assay steps and after transfer steps. In agglutination assays, particle redistribution may improve signal-to-noise ratios by reducing non-specific particle clustering. It also allows one to integrate particle concentration and particle transfer steps in these assays, as after these steps the aggregates could be redistributed. Applied fields should however be tuned to only break non-specific clustering, and keep most specific bonds intact. Lastly, in surface-binding assays, particle redistribution may be useful to facilitate efficient binding of target analytes to the sensor surface, as steric hindrance effects due to aggregate formation can be overcome. As particle disaggregation and/or redistribution can be achieved by using magnetic fields alone, the developed methods can relatively easily be integrated in magnetic actuation-based systems.

8.3.3 Sandwich formation in surface-binding assays with magnetic particles

In Chapter 7 we studied methods to efficiently bind captured target analytes to a sensor surface in surface-binding assays based on magnetic particles. While it can be advantageous to use magnetic particles to capture target analytes from sample fluid, the subsequent assay steps involving the captured target will suffer from the reduced mobility of the target due to its immobilization on a relatively large colloidal particle. We therefore studied methods to magnetically actuate the magnetic particles in order to direct and accelerate the subsequent surface-binding reaction. Using field gradients, contact of magnetic particles with a reactive surface can be enhanced, and by applying magnetic fields, the orientation of magnetic particles can be altered to expose the complete particle surface to the reactive surface. These considerations were investigated using a numerical model based on Brownian dynamics of a magnetic particle with a captured target. To optimize the exposure of the particle surface, we applied magnetic fields in pulses to combine field-induced reorientation with Brownian rotation of the particle at relatively small angles. We find from simulations that nearly all particles with captured targets can be bound within 2 minutes, at a rate that is 2 to 4 times faster compared to no actuation. Experimental data showed a similar increase for magnetic actuation, but also underscored the negative influence on the binding rate of non-specific interactions between the bio-functionalized surfaces.

In further investigations, incubation protocols should be integrated with stringency steps at certain intervals to break non-specific bond-formation. We estimate that such a protocol has the potential to improve the efficiency to bind targets to the surface in surface-binding assays by more than a factor 10. Even larger improvements are expected when the binding process is performed in a complex fluid with a higher viscosity. From a scientific point of view, as simulation and experimental data can be closely compared, it will be interesting to expand the numerical model to further study the molecular binding process on a realistic biomarker system.

8.4 Integration: towards particle-based assays controlled and optimized by magnetic fields

Current quantitative lab-on-chip biosensing systems consist of a disposable cartridge and a reusable analyzer instrument. Cartridges are single-use objects for reasons of biochemical irreversibility and bio-safety. Therefore, it is important that a system architecture is chosen which limits the complexity of the cartridge. The development of a biosensing cartridge presents challenges in the domains of device technology (e.g. fluidics and detection) and biochemistry (e.g. reagents and bio-functionalization), and the challenges depend on the architectural choices. Broadly speaking, in the magnetic carrier-only concepts, the reagents can be close to the ones developed for pipetting-based assays; however, multiple fluids need to be controlled in the cartridge, which complicates the device technology. The agglutination assays are simpler in terms of device technology, but are demanding on the reagents because the assays are performed in one step without separation or stringency. The surface-binding assays allow sensitive particle detection and stringency, yet require careful control of the surface bio-functionalization.

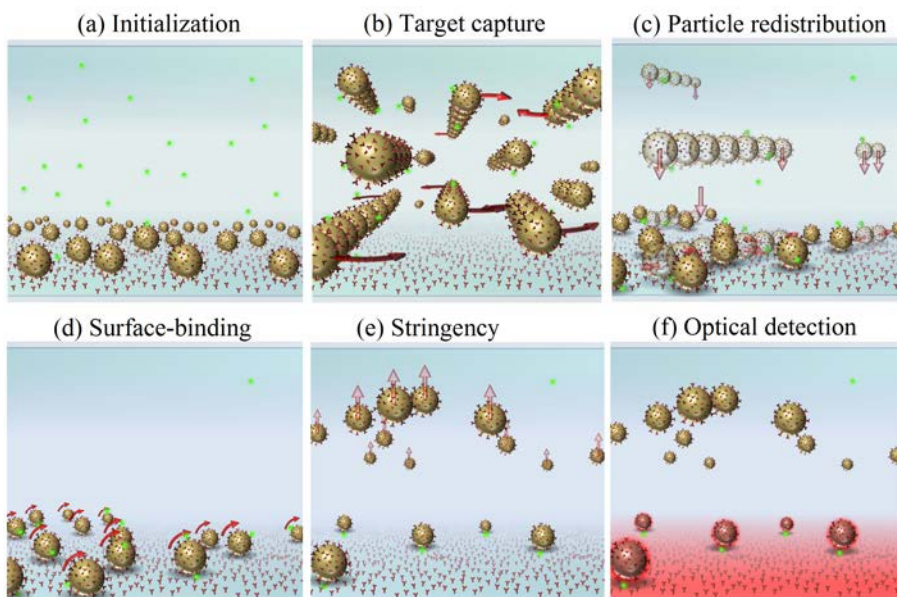


Figure 8.1 Envisaged actuation process steps in a magnetic particle-based biosensing assay using dynamic magnetic field actuation. (a) First the sample fluid containing the target proteins (small green spheres) enters the microfluidic reaction chamber with the magnetic particles. (b) Magnetic particles are actuated dynamically (rotation and translation) using magnetic fields to rapidly capture targets. (c) Magnetic particles are brought back to the sensor surface using field gradients. Subsequently particle clusters are disaggregated and redistributed over the surface using magnetic fields. (d) Magnetic particles are actuated to rapidly bind captured targets to a sensor surface. (e) Stringency is applied to remove unbound and non-specifically bound particles from the sensor surface. (f) Specifically bound particles remain at the surface to be detected, e.g., optically using frustrated total internal reflection.

We anticipate that the different actuation principles presented in this thesis can be integrated to realize rapid and efficient capture and subsequent labeling in a lab-on-chip surface-binding assay, as for example sketched in Figure 8.1. Integration can be significantly facilitated by using the developed principles of field-induced disaggregation or rotaphoresis, which actively reset the particle distributions. Based on the generated experimental and numerical data, it may be possible to magnetically modulate the total kinetics of a surface-binding assay by at least by one order of magnitude, and possibly even more than two orders of magnitude. Such an improvement would significantly improve the possibilities of a magnetic particle-based biosensor. Magnetic actuation could be applied in order to reduce the measurement time, but it could also be used to improve the signal-to-noise ratio and thereby lower the limit-of-quantification.

Magnetic actuation is an enabler for lab-on-chip integration because it allows a large diversity of sophisticated fluidic and molecular process steps to be controlled by means of externally generated fields, which can strongly simplify the cartridge design. In terms of microfluidics, the stationary-fluidic concepts as developed in this thesis are very attractive because they do not require continuous fluid actuation to be integrated in the system. Technologies based on continuous fluid actuation generally require large fluid volumes and/or complex cartridge architectures. Stationary assay concepts also require some kind of fluid actuation, namely to guide the to-be-tested fluid sample into the cartridge. From the perspective of fluid handling, the simplest solution for a magnetically-controlled assay is a cartridge in which the initial transport of sample into the cartridge is effectuated by passive capillary forces. In the future, we expect that stationary-fluidic concepts will continue to gain attention, as these concepts maximally exploit the functional properties of magnetic particles to facilitate lab-on-chip integration.

In the field of integrated magnetically actuated assays, individual process steps are being studied as well as the integration of different process steps. The use of magnetic actuation processes for integration purposes is proceeding steadily. We foresee that the actuation principles presented in this thesis can be applied to further enhance system integration and overall analytical performance. As this thesis shows, dynamic field generation opens up a new range of possibilities to manipulate magnetic particles in ways that are not possible with static field generation. Scientifically speaking, in this thesis we have provided detailed characterizations and models of several magnetic actuation processes, which will facilitate further development and optimization of the processes. Magnetic actuation principles will be carefully attuned to specific biomaterials and reagents, and vice versa, biomaterials will be designed specifically for use in actuated assays. Concerning the magnetic particles, particle-based assays will benefit from the ongoing optimization of particles regarding their surface bio-functionalization, surface smoothness, and their size and magnetization uniformity.

Importantly, the performance of novel lab-on-chip analytical systems should be demonstrated by reporting dose-response curves on real-life samples. Blood is the most important matrix for *in vitro* diagnostic testing, yet it is a challenging fluid to work with due to the high concentrations of cells and proteins, which may cause

clogging, steric hindrance, molecular interferences, non-specific adhesion, etc. Novel technologies are always first studied with spiked buffers or diluted plasma or serum, yet the step to whole plasma, whole blood and other realistic bodily fluids should also be made. Furthermore, dose-response curves should be reported with sufficient statistics, so that reliable LoDs and LoQs can be determined including confidence intervals.

Overall we see many avenues for further innovation of microfluidic Point-of-Care Testing based on magnetic particles. Magnetic particles are fundamentally suited for developing miniaturized biosensing systems and enable a range of unique stationary-fluidic system concepts. We expect that integrated magnetic actuation-based biosensing systems will have a large impact on society in the future. Such systems will allow quantitative decentralized *in vitro* diagnostic testing in a rapid manner with a user-friendly “sample-in result-out” type of performance, in hand-held and desktop-sized instruments. By virtue of these properties, magnetic actuation-based biosensing systems can help to improve patient treatment, patient monitoring and disease management, with impact on the quality, accessibility and cost-effectiveness of future healthcare.

Bibliography

1. Christensen, C.M., Grossman, J.H. & Hwang, J. The Innovator's Prescription: A Disruptive Solution for Health Care. (McGraw-Hill, 2009).
2. Forsman, R.W. Why is the laboratory an afterthought for managed care organizations? *Clin Chem* **42**, 813-816 (1996).
3. The Lewin Group, The value of Diagnostics, Innovation, Adoption, and Diffusion into Health Care, from <http://www.lewin.com> (2005).
4. von Lode, P. Point-of-care immunotesting: Approaching the analytical performance of central laboratory methods. *Clin Biochem* **38**, 591-606 (2005).
5. Kovarik, M.L. et al. Micro Total Analysis Systems for Cell Biology and Biochemical Assays. *Analytical Chemistry* **84**, 516-540 (2012).
6. Whitesides, G.M. The origins and the future of microfluidics. *Nature* **442**, 368-373 (2006).
7. Wild, D. The Immunoassay Handbook. (Elsevier, Amsterdam; 2005).
8. Rapley, R. (ed.) The Nucleic Acid Protocols Handbook. (Humana Press, Totowa, New Jersey; 2000).
9. Nam, J.M., Thaxton, C.S. & Mirkin, C.A. Nanoparticle-based bio-bar codes for the ultrasensitive detection of proteins. *Science* **301**, 1884-1886 (2003).
10. Chen, Z. et al. Protein microarrays with carbon nanotubes as multicolor Raman labels. *Nat Biotechnol* **26**, 1285-1292 (2008).
11. Osterfeld, S.J. et al. Multiplex protein assays based on real-time magnetic nanotag sensing. *Proc Natl Acad Sci U S A* **105**, 20637-20640 (2008).
12. Zheng, G.F., Patolsky, F., Cui, Y., Wang, W.U. & Lieber, C.M. Multiplexed electrical detection of cancer markers with nanowire sensor arrays. *Nat Biotechnol* **23**, 1294-1301 (2005).
13. Todd, J. et al. Ultrasensitive flow-based immunoassays using single-molecule counting. *Clin Chem* **53**, 1990-1995 (2007).
14. Fan, R. et al. Integrated barcode chips for rapid, multiplexed analysis of proteins in microliter quantities of blood. *Nat Biotechnol* **26**, 1373-1378 (2008).
15. Fredriksson, S. et al. Protein detection using proximity-dependent DNA ligation assays. *Nature Biotechnology* **20**, 473-477 (2002).
16. Chin, C.D., Linder, V. & Sia, S.K. Commercialization of microfluidic point-of-care diagnostic devices. *Lab Chip* **12**, 2118-2134 (2012).

17. Bock, J.L. The new era of automated immunoassay. *Am J Clin Pathol* **113**, 628-646 (2000).
18. Gijs, M.A.M., Lacharme, F. & Lehmann, U. Microfluidic applications of magnetic particles for biological analysis and catalysis. *Chem Rev* **110**, 1518-1563 (2010).
19. Horak, D., Babic, M., Mackova, H. & Benes, M.J. Preparation and properties of magnetic nano- and microsized particles for biological and environmental separations. *J Sep Sci* **30**, 1751-1772 (2007).
20. Bean, C.P. & Livingston, J.D. Superparamagnetism. *J Appl Phys* **30**, S120 (1959).
21. Kang, T.G., Hulsen, M.A., Anderson, P.D., den Toonder, J.M. & Meijer, H.E. Chaotic mixing induced by a magnetic chain in a rotating magnetic field. *Phys Rev E Stat Nonlin Soft Matter Phys* **76**, 066303 (2007).
22. Pamme, N. Magnetism and microfluidics. *Lab Chip* **6**, 24-38 (2006).
23. Pipper, J., Zhang, Y., Neuzil, P. & Hsieh, T.M. Clockwork PCR including sample preparation. *Angewandte Chemie-International Edition* **47**, 3900-3904 (2008).
24. Lehmann, U., Vandevyver, C., Parashar, V.K. & Gijs, M.A. Droplet-based DNA purification in a magnetic lab-on-a-chip. *Angew Chem Int Ed Engl* **45**, 3062-3067 (2006).
25. Bruls, D.M. et al. Rapid integrated biosensor for multiplexed immunoassays based on actuated magnetic nanoparticles. *Lab Chip* **9**, 3504-3510 (2009).
26. Hayes, M.A., Polson, N.A. & Garcia, A.A. Active control of dynamic supraparticle structures in microchannels. *Langmuir* **17**, 2866-2871 (2001).
27. Rida, A. & Gijs, M.A. Manipulation of self-assembled structures of magnetic beads for microfluidic mixing and assaying. *Anal Chem* **76**, 6239-6246 (2004).
28. Lacharme, F., Vandevyver, C. & Gijs, M.A. Full on-chip nanoliter immunoassay by geometrical magnetic trapping of nanoparticle chains. *Anal Chem* **80**, 2905-2910 (2008).
29. Rida, A. & Gijs, M.A.M. Dynamics of magnetically retained supraparticle structures in a liquid flow. *Appl Phys Lett* **85**, 4986-4988 (2004).
30. Wang, Y., Zhe, J., Chung, B.T.F. & Dutta, P. A rapid magnetic particle driven micromixer. *Microfluid Nanofluid* **4**, 375-389 (2008).
31. Lee, S.H., van Noort, D., Lee, J.Y., Zhang, B.T. & Park, T.H. Effective mixing in a microfluidic chip using magnetic particles. *Lab Chip* **9**, 479-482 (2009).
32. Suzuki, H., Ho, C.-M. & Kasagi, N. A chaotic mixer for magnetic bead-based micro cell sorter. *J. MEMS* **13**, 779-790 (2004).
33. Lund-Olesen, T., Buus, B.B., Howalt, J.G. & Hansen, M.F. Magnetic bead micromixer: Influence of magnetic element geometry and field amplitude. *J Appl Phys* **103**, 07E902 (2008).
34. Wittbracht, F., Weddemann, A., Eickenberg, B., Zahn, M. & Hutten, A. Enhanced fluid mixing and separation of magnetic bead agglomerates based on dipolar interaction in rotating magnetic fields. *Appl Phys Lett* **100**, 123507 (2012).
35. Moser, Y., Lehnert, T. & Gijs, M.A.M. Quadrupolar magnetic actuation of superparamagnetic particles for enhanced microfluidic perfusion. *Appl Phys Lett* **94**, 022505 (2009).

36. Vuppu, A.K., Garcia, A.A. & Hayes, M.A. Video microscopy of dynamically aggregated paramagnetic particle chains in an applied rotating magnetic field. *Langmuir* **19**, 8646-8653 (2003).
37. Vuppu, A.K. et al. Phase sensitive amplification for biochemical detection using paramagnetic particle chains in an applied rotating magnetic field. *J Appl Phys* **96**, 6831-6838 (2004).
38. Vuppu, A.K. et al. Modeling microflow and stirring around a microrotor in creeping flow using a quasi-steady-state analysis. *Lab Chip* **4**, 201-208 (2004).
39. Calhoun, R. et al. Paramagnetic particles and mixing in micro-scale flows. *Lab Chip* **6**, 247-257 (2006).
40. Krishnamurthy, S. et al. Dynamics of rotating paramagnetic particle chains simulated by particle dynamics, Stokesian dynamics and lattice Boltzmann methods. *Microfluid Nanofluid* **5**, 33-41 (2008).
41. Gao, Y., Hulsen, M.A., Kang, T.G. & den Toonder, J.M.J. Numerical and experimental study of a rotating magnetic particle chain in a viscous fluid. *Phys Rev E* **86**, 041503 (2012).
42. Martin, J.E., Shea-Rohwer, L. & Solis, K.J. Strong intrinsic mixing in vortex magnetic fields. *Phys Rev E* **80**, 016312 (2009).
43. Roy, T., Sinha, A., Chakraborty, S., Ganguly, R. & Puri, I.K. Magnetic microsphere-based mixers for microdroplets. *Phys Fluids* **21**, 7 (2009).
44. Biswal, S.L. & Gast, A.P. Micromixing with linked chains of paramagnetic particles. *Analytical Chemistry* **76**, 6448-6455 (2004).
45. Ottino, J.M. *The Kinematics of Mixing: Stretching, Chaos, and Transport*. (Cambridge University Press, Cambridge, England; 1989).
46. Holzinger, D., Lengemann, D., Gollner, F., Engel, D. & Ehresmann, A. Controlled movement of superparamagnetic bead rows for microfluid mixing. *Appl Phys Lett* **100**, 153507 (2012).
47. Gao, Y. et al. Chaotic Fluid Mixing by Alternating Micro-Particle Topologies to enhance Biochemical Reactions. *Microfluid Nanofluid* **16**, 265-274 (2014).
48. Lee, J.T., Abid, A., Cheung, K.H., Sudheendra, L. & Kennedy, I.M. Superparamagnetic particle dynamics and mixing in a rotating capillary tube with a stationary magnetic field. *Microfluid Nanofluid* **13**, 461-468 (2012).
49. Smith, C.E. & York, C.K. Methods of Isolating Biological Target Materials using Silica Magnetic Particles. *US patent* **6 027 945** (2000).
50. den Dulk, R.C., Schmidt, K.A., Sabatte, G., Liebana, S. & Prins, M.W. Magneto-capillary valve for integrated purification and enrichment of nucleic acids and proteins. *Lab Chip* **13**, 106-118 (2013).
51. Chiou, C.H., Shin, D.J., Zhang, Y. & Wang, T.H. Topography-assisted electromagnetic platform for blood-to-PCR in a droplet. *Biosens Bioelectron* **50**, 91-99 (2013).
52. Berensmeier, S. Magnetic particles for the separation and purification of nucleic acids. *Appl Microbiol Biotechnol* **73**, 495-504 (2006).
53. Schreiber, G., Haran, G. & Zhou, H.X. Fundamental aspects of protein-protein association kinetics. *Chem Rev* **109**, 839-860 (2009).
54. Zhou, H.X. Rate theories for biologists. *Q Rev Biophys* **43**, 219-293 (2010).

55. Gabdoulline, R.R. & Wade, R.C. Biomolecular diffusional association. *Curr Opin Struct Biol* **12**, 204-213 (2002).
56. Singhal, A., Haynes, C.A. & Hansen, C.L. Microfluidic measurement of antibody-antigen binding kinetics from low-abundance samples and single cells. *Anal Chem* **82**, 8671-8679 (2010).
57. van Reenen, A., de Jong, A.M. & Prins, M.W.J. Accelerated particle-based target capture - the roles of volume transport and near-surface alignment. *J Phys Chem B* **117**, 1210-1218 (2013).
58. Schmitz, K.S. & Schurr, J.M. Role of Orientation Constraints and Rotational Diffusion in Bimolecular Solution Kinetics. *J Phys Chem-Us* **76**, 534-& (1972).
59. Stenberg, M. & Nygren, H. Kinetics of antigen-antibody reactions at solid-liquid interfaces. *J Immunol Methods* **113**, 3-15 (1988).
60. Squires, T.M., Messinger, R.J. & Manalis, S.R. Making it stick: convection, reaction and diffusion in surface-based biosensors. *Nature Biotechnology* **26**, 417-426 (2008).
61. van Reenen, A. et al. Accelerated target capture by dynamic magnetic particle actuation. *16th International Conference on Miniaturized Systems for Chemistry and Life Sciences, Okinawa, Japan*, 926-928 (2012).
62. Moser, Y., Lehnert, T. & Gijs, M.A.M. On-chip immuno-agglutination assay with analyte capture by dynamic manipulation of superparamagnetic beads. *Lab Chip* **9**, 3261-3267 (2009).
63. Sjolander, S. & Urbaniczky, C. Integrated Fluid Handling-System for Biomolecular Interaction Analysis. *Analytical Chemistry* **63**, 2338-2345 (1991).
64. Hayes, M.A., Polson, T.N., Phayre, A.N. & Garcia, A.A. Flow-based microimmunoassay. *Anal Chem* **73**, 5896-5902 (2001).
65. Choi, J.W. et al. An integrated microfluidic biochemical detection system for protein analysis with magnetic bead-based sampling capabilities. *Lab Chip* **2**, 27-30 (2002).
66. Slovakova, M. et al. Use of self assembled magnetic beads for on-chip protein digestion. *Lab Chip* **5**, 935-942 (2005).
67. Teste, B. et al. Microchip integrating magnetic nanoparticles for allergy diagnosis. *Lab Chip*, **11**, 833-840 (2011).
68. Peyman, S.A., Iles, A. & Pamme, N. Mobile magnetic particles as solid-supports for rapid surface-based bioanalysis in continuous flow. *Lab Chip* **9**, 3110-3117 (2009).
69. Bronzeau, S. & Pamme, N. Simultaneous bioassays in a microfluidic channel on plugs of different magnetic particles. *Anal Chim Acta* **609**, 105-112 (2008).
70. Kim, K.S. & Park, J.K. Magnetic force-based multiplexed immunoassay using superparamagnetic nanoparticles in microfluidic channel. *Lab Chip* **5**, 657-664 (2005).
71. Lee, H., Jung, J., Han, S.I. & Han, K.H. High-speed RNA microextraction technology using magnetic oligo-dT beads and lateral magnetophoresis. *Lab Chip* **10**, 2764-2770 (2010).
72. Ganguly, R., Hahn, T. & Hardt, S. Magnetophoretic mixing for in situ immunochemical binding on magnetic beads in a microfluidic channel. *Microfluid Nanofluid* **8**, 739-753 (2010).

73. Tanaka, K. & Imagawa, H. Rapid and reagent-saving immunoassay using innovative stirring actions of magnetic beads in microreactors in the sequential injection mode. *Talanta* **68**, 437-441 (2005).
74. Lee, J.T., Sudheendra, L. & Kennedy, I.M. Accelerated Immunoassays Based on Magnetic Particle Dynamics in a Rotating Capillary Tube with Stationary Magnetic Field. *Analytical Chemistry* **84**, 8317-8322 (2012).
75. Tekin, H.C. & Gijs, M.A.M. Ultrasensitive protein detection: a case for microfluidic magnetic bead-based assays. *Lab Chip* **13**, 4711-39 (2013).
76. Armbruster, D.A. & Pry, T. Limit of blank, limit of detection and limit of quantitation. *Clin Biochem Rev* **29 Suppl 1**, S49-52 (2008).
77. Chandran, S. & Singh, R.S. Comparison of various international guidelines for analytical method validation. *Pharmazie* **62**, 4-14 (2007).
78. Wellman, A.D. & Sepaniak, M.J. Multiplexed, waveguide approach to magnetically assisted transport evanescent field fluoroassays. *Anal Chem* **79**, 6622-6628 (2007).
79. Herrmann, M., Veres, T. & Tabrizian, M. Quantification of low-picogram concentrations of TNF-alpha in serum using the dual-network microfluidic ELISA platform. *Anal Chem* **80**, 5160-5167 (2008).
80. Sista, R.S. et al. Heterogeneous immunoassays using magnetic beads on a digital microfluidic platform. *Lab Chip* **8**, 2188-2196 (2008).
81. Ng, A.H., Choi, K., Luoma, R.P., Robinson, J.M. & Wheeler, A.R. Digital microfluidic magnetic separation for particle-based immunoassays. *Anal Chem* **84**, 8805-8812 (2012).
82. Rissin, D.M. et al. Single-molecule enzyme-linked immunosorbent assay detects serum proteins at subfemtomolar concentrations. *Nat Biotechnol* **28**, 595-599 (2010).
83. Kan, C.W. et al. Isolation and detection of single molecules on paramagnetic beads using sequential fluid flows in microfabricated polymer array assemblies. *Lab Chip* **12**, 977-985 (2012).
84. Fu, Z. et al. Microfabricated renewable beads-trapping/releasing flow cell for rapid antigen-antibody reaction in chemiluminescent immunoassay. *Anal Chem* **83**, 2685-2690 (2011).
85. Tang, D., Yuan, R. & Chai, Y. Magnetic control of an electrochemical microfluidic device with an arrayed immunosensor for simultaneous multiple immunoassays. *Clin Chem* **53**, 1323-1329 (2007).
86. Do, J. & Ahn, C.H. A polymer lab-on-a-chip for magnetic immunoassay with on-chip sampling and detection capabilities. *Lab Chip* **8**, 542-549 (2008).
87. Witters, D., Knez, K., Ceysens, F., Puers, R. & Lammertyn, J. Digital microfluidics-enabled single-molecule detection by printing and sealing single magnetic beads in femtoliter droplets. *Lab Chip* **13**, 2047-2054 (2013).
88. Rissin, D.M. et al. Multiplexed single molecule immunoassays. *Lab Chip* **13**, 2902-2911 (2013).
89. Hahn, Y.K. & Park, J.K. Versatile immunoassays based on isomagnetophoresis. *Lab Chip* **11**, 2045-2048 (2011).

90. Berry, S.M., Alarid, E.T. & Beebe, D.J. One-step purification of nucleic acid for gene expression analysis via Immiscible Filtration Assisted by Surface Tension (IFAST). *Lab Chip* **11**, 1747-1753 (2011).
91. Sur, K. et al. Immiscible phase nucleic acid purification eliminates PCR inhibitors with a single pass of paramagnetic particles through a hydrophobic liquid. *J Mol Diagn* **12**, 620-628 (2010).
92. Zhang, Y. et al. A surface topography assisted droplet manipulation platform for biomarker detection and pathogen identification. *Lab Chip* **11**, 398-406 (2011).
93. Strohmeier, O. et al. Centrifugal gas-phase transition magnetophoresis (GTM)--a generic method for automation of magnetic bead based assays on the centrifugal microfluidic platform and application to DNA purification. *Lab Chip* **13**, 146-155 (2013).
94. Sista, R. et al. Development of a digital microfluidic platform for point of care testing. *Lab Chip* **8**, 2091-2104 (2008).
95. Shikida, M., Takayanagi, K., Honda, H., Ito, H. & Sato, K. Development of an enzymatic reaction device using magnetic bead-cluster handling. *J. Micromech. Microeng.* **16**, 1875-1883 (2006).
96. Bordelon, H. et al. Development of a low-resource RNA extraction cassette based on surface tension valves. *ACS Appl Mater Interfaces* **3**, 2161-2168 (2011).
97. Casavant, B.P. et al. The VerIFAST: an integrated method for cell isolation and extracellular/intracellular staining. *Lab Chip* **13**, 391-396 (2013).
98. den Dulk, R.C., Schmidt, K.A., Gill, R., Jongen, J.C.B. & Prins, M.W.J. Magneto-capillary valve for lab-on-a-chip sample preparation. *Proc. MicroTAS 2010 Int. Conf.*, 665-667 (2010).
99. Gottheil, R. et al. Moving the solid phase: a platform technology for cartridge based sandwich immunoassays. *Biomed Microdevices* **16**, 163-172 (2013).
100. Shin, D.J., Chen, L. & Wang, T.H. A Simple Integrated Diagnostic Platform for DNA Testing of Chlamydia Trachomatis Infection. *Proc. MicroTAS 2013 Int. Conf.*, 1350-1352 (2013).
101. Tsuchiya, H., Okochi, M., Nagao, N., Shikida, M. & Honda, H. On-chip polymerase chain reaction microdevice employing a magnetic droplet-manipulation system. *Sensor Actuat B-Chem* **130**, 583-588 (2008).
102. Degre, G., Brunet, E., Dodge, A. & Tabeling, P. Improving agglutination tests by working in microfluidic channels. *Lab Chip* **5**, 691-694 (2005).
103. Ranzoni, A., Sabatte, G., van IJzendoorn, L.J. & Prins, M.W.J. One-step homogeneous magnetic nanoparticle immunoassay for biomarker detection directly in blood plasma. *Acs Nano* **6**, 3134-3141 (2012).
104. Baudry, J. et al. Acceleration of the recognition rate between grafted ligands and receptors with magnetic forces. *Proc Natl Acad Sci U S A* **103**, 16076-16078 (2006).
105. Park, S.Y., Handa, H. & Sandhu, A. High speed magneto-optical valve: Rapid control of the optical transmittance of aqueous solutions by magnetically induced self-assembly of superparamagnetic particle chains. *J Appl Phys* **105** 07B526 (2009).

106. Park, S.Y., Handa, H. & Sandhu, A. Magneto-optical biosensing platform based on light scattering from self-assembled chains of functionalized rotating magnetic beads. *Nano Lett* **10**, 446-451 (2010).
107. Park, S.Y., Ko, P.J., Handa, H. & Sandhu, A. Exploring magneto-optical properties of biofunctionalized magnetic chains for developing label-free immunoassays. *J Appl Phys* **107**, 09B324 (2010).
108. Issadore, D. et al. Miniature magnetic resonance system for point-of-care diagnostics. *Lab Chip* **11**, 2282-2287 (2011).
109. Koh, I., Hong, R., Weissleder, R. & Josephson, L. Sensitive NMR sensors detect antibodies to influenza. *Angew Chem Int Ed Engl* **47**, 4119-4121 (2008).
110. Ranzoni, A., Schleipen, J.J.H.B., van IJzendoorn, L.J. & Prins, M.W.J. Frequency-selective rotation of two-particle nanoactuators for rapid and sensitive detection of biomolecules. *Nano Lett* **11**, 2017-2022 (2011).
111. Dittmer, W.U. et al. Sensitive and rapid immunoassay for parathyroid hormone using magnetic particle labels and magnetic actuation. *J Immunol Methods* **338**, 40-46 (2008).
112. Morozov, V.N. & Morozova, T.Y. Active bead-linked immunoassay on protein microarrays. *Anal Chim Acta* **564**, 40-52 (2006).
113. De Palma, R. et al. Magnetic Particles as Labels in Bioassays: Interactions between a Biotinylated Gold Substrate and Streptavidin Magnetic Particles. *Journal of Physical Chemistry C* **111**, 12227-12235 (2007).
114. De Palma, R., Reekmans, G., Laureyn, W., Borghs, G. & Maes, G. The optimization of magnetosandwich assays for the sensitive and specific detection of proteins in serum. *Anal Chem* **79**, 7540-7548 (2007).
115. Gao, Y. et al. Disaggregation of microparticle clusters by induced magnetic dipole-dipole repulsion near a physical surface. *Lab Chip* **13**, 1394-1401 (2013).
116. Morozov, V.N., Groves, S., Turell, M.J. & Bailey, C. Three Minutes-Long Electrophoretically Assisted Zeptomolar Microfluidic Immunoassay with Magnetic-Beads Detection. *J Am Chem Soc* **129**, 12628-12629 (2007).
117. Shlyapnikov, Y.M. et al. Rapid simultaneous ultrasensitive immunodetection of five bacterial toxins. *Anal Chem* **84**, 5596-5603 (2012).
118. Morozova, T.Y. & Morozov, V.N. Force differentiation in recognition of cross-reactive antigens by magnetic beads. *Anal Biochem* **374**, 263-271 (2008).
119. Tekin, H.C., Cornaglia, M. & Gijs, M.A.M. Attomolar protein detection using a magnetic bead surface coverage assay. *Lab Chip* **13**, 1053-1059 (2013).
120. Kriz, C.B., Radevik, K. & Kriz, D. Magnetic permeability measurements in bioanalysis and biosensors. *Anal Chem* **68**, 1966-1970 (1996).
121. Chemla, Y.R. et al. Ultrasensitive magnetic biosensor for homogeneous immunoassay. *Proc Natl Acad Sci U S A* **97**, 14268-14272 (2000).
122. Baselt, D.R. et al. A biosensor based on magnetoresistance technology. *Biosens Bioelectron* **13**, 731-739 (1998).
123. Koets, M., van der Wijk, T., van Eemeren, J.T.W.M., van Amerongen, A. & Prins, M.W.J. Rapid DNA multi-analyte immunoassay on a magneto-resistance biosensor. *Biosens Bioelectron* **24**, 1893-1898 (2009).

124. Gaster, R.S., Hall, D.A. & Wang, S.X. nanoLAB: an ultraportable, handheld diagnostic laboratory for global health. *Lab Chip* **11**, 950-956 (2011).
125. Aytur, T. et al. A novel magnetic bead bioassay platform using a microchip-based sensor for infectious disease diagnosis. *J Immunol Methods* **314**, 21-29 (2006).
126. Colle, F. et al. Lens-free imaging of magnetic particles in DNA assays. *Lab Chip* **13**, 4257-4262 (2013).
127. Wang, Y., Dostalek, J. & Knoll, W. Magnetic Nanoparticle-Enhanced Biosensor Based on Grating-Coupled Surface Plasmon Resonance. *Analytical Chemistry* **83**, 6202-6207 (2011).
128. Leckband, D. & Israelachvili, J. Intermolecular forces in biology. *Q Rev Biophys* **34**, 105-267 (2001).
129. Danilowicz, C., Greenfield, D. & Prentiss, M. Dissociation of ligand-receptor complexes using magnetic tweezers. *Anal Chem* **77**, 3023-3028 (2005).
130. Jacob, A., van IJzendoorn, L.J., de Jong, A.M. & Prins, M.W.J. Quantification of Protein-Ligand Dissociation Kinetics in Heterogeneous Affinity Assays. *Anal Chem* **84**, 9287-9294 (2012).
131. Vilfan, I.D., Lipfert, J., Koster, D.A., Lemay, S.G. & Dekker, N.H. Magnetic Tweezers for Single-Molecule Experiments: Springer Handbook of Single-Molecule Biophysics. (Springer, New York; 2009).
132. De Vlaminck, I. & Dekker, C. Recent advances in magnetic tweezers. *Annu Rev Biophys* **41**, 453-472 (2012).
133. van Reenen, A., Gutierrez-Mejia, F., van IJzendoorn, L.J. & Prins, M.W.J. Torsion profiling of proteins using magnetic particles. *Biophys J* **104**, 1073-1080 (2013).
134. Janssen, X.J.A., Schellekens, A.J., van Ommering, K., van IJzendoorn, L.J. & Prins, M.W.J. Controlled torque on superparamagnetic beads for functional biosensors. *Biosens Bioelectron* **24**, 1937-1941 (2009).
135. Boas, D.A., Pitris, C. & Ramanujam, N. Handbook of Biomedical Optics. (CRC Press, Boca Raton, FL, 2011).
136. Lee, G.U., Metzger, S., Natesan, M., Yanavich, C. & Dufrene, Y.F. Implementation of force differentiation in the immunoassay. *Anal Biochem* **287**, 261-271 (2000).
137. Ebersole, R.C., US Patent number 4 219 335 (1978).
138. Sieben, S., Bergemann, C., Lubbe, A., Brockmann, B. & Rescheleit, D. Comparison of different particles and methods for magnetic isolation of circulating tumor cells. *J Magn Magn Mater* **225**, 175-179 (2001).
139. Kielhorn, E., Schofield, K. & Rimm, D.L. Use of magnetic enrichment for detection of carcinoma cells in fluid specimens. *Cancer* **94**, 205-211 (2002).
140. Sabatte, G., Feitsma, H., Evers, T.H. & Prins, M.W.J. Protein biomarker enrichment by biomarker antibody complex elution for immunoassay biosensing. *Biosens Bioelectron* **29**, 18-22 (2011).
141. Yeung, S.W. & Hsing, I.M. Manipulation and extraction of genomic DNA from cell lysate by functionalized magnetic particles for lab on a chip applications. *Biosens Bioelectron* **21**, 989-997 (2006).
142. Boom, R. et al. Rapid and simple method for purification of nucleic acids. *J Clin Microbiol* **28**, 495-503 (1990).

143. Schurr, J.M. The role of diffusion in bimolecular solution kinetics. *Biophys J* **10**, 700-716 (1970).
144. Arlett, J.L., Myers, E.B. & Roukes, M.L. Comparative advantages of mechanical biosensors. *Nat Nanotechnol* **6**, 203-215 (2011).
145. Smoluchowski, v.M. Versuch einer mathematischen Theorie der Koagulationskinetik kolloider Loeschungen. *Z Phys Chem* **92**, 129-168 (1917).
146. Collins, F.C. & Kimball, G.E. Diffusion-controlled reaction rates. *J. Colloid Sci.* **4**, 425-437 (1949).
147. Janssen, X.J.A., van Reenen, A., van IJzendoorn, L.J. & Prins, M.W.J. The rotating particles probe: A new technique to measure interactions between particles and a substrate. *Colloids surf A: Physicochem. Eng. Aspects* **373**, 88-93 (2011).
148. Waite, T.R. Theoretical treatment of the kinetics of diffusion-limited reactions. *Physical Review* **107**, 463-470 (1957).
149. Lee, N.K. et al. Ligand-receptor interactions in chains of colloids: when reactions are limited by rotational diffusion. *Langmuir* **24**, 1296-1307 (2008).
150. Srisa-Art, M., Dyson, E.C., deMello, A.J. & Edel, J.B. Monitoring of real-time streptavidin-biotin binding kinetics using droplet microfluidics. *Anal Chem* **80**, 7063-7067 (2008).
151. Fosdick, R.L. & Kao, B.G. Steady flow of a simple fluid around a rotating sphere. *Rheologica Acta* **19**, 675-679 (1980).
152. Shoup, D. & Szabo, A. Role of diffusion in ligand binding to macromolecules and cell-bound receptors. *Biophys J* **40**, 33-39 (1982).
153. Janssen, X.J.A. et al. Torsion stiffness of a protein pair determined by magnetic particles. *Biophys J* **100**, 2261-2267 (2011).
154. Grassia, P.S., Hinch, E.J. & Nitsche, L.C. Computer-Simulations of Brownian-Motion of Complex-Systems. *J Fluid Mech* **282**, 373-403 (1995).
155. Pliny Naturalis Historia, book XXXIII, chapter 32.
156. de Lacerda, L.D. & Salomons, W. Mercury from Gold and Silver Mining: A Chemical Time Bomb? (Springer-Verlag, Berlin; 1998).
157. Dabrowski, A. Adsorption--from theory to practice. *Adv Colloid Interface Sci* **93**, 135-224 (2001).
158. Tien, C. & Ramarao, B.V. Granular Filtration of Aerosols and Hydrosols. (Elsevier Science & Technology Books, 2007).
159. Çeçen, F. & Aktas, Ö. Activated Carbon for Water and Wastewater Treatment, Integration of Adsorption and Biological Treatment. (Wiley-VCH, 2012).
160. Agricola, G. De re metallica. (Basel, 1556).
161. Brown, P.R. High Pressure Liquid Chromatography: Biochemical and Biomedical Applications. (Academic Press, London; 1973).
162. Vogelstein, B. & Gillespie, D. Preparative and analytical purification of DNA from agarose. *Proc Natl Acad Sci U S A* **76**, 615-619 (1979).
163. Franke, T., Schmid, L., Weitz, D.A. & Wixforth, A. Magneto-mechanical mixing and manipulation of picoliter volumes in vesicles. *Lab Chip* **9**, 2831-2835 (2009).

164. Read, T., Olkhov, R.V. & Shaw, A.M. Measurement of the localised plasmon penetration depth for gold nanoparticles using a non-invasive bio-stacking method. *Phys Chem Chem Phys* **15**, 6122-6127 (2013).
165. Weiss, M., Elsner, M., Kartberg, F. & Nilsson, T. Anomalous subdiffusion is a measure for cytoplasmic crowding in living cells. *Biophys J* **87**, 3518-3524 (2004).
166. Kundu, P.K., Cohen, I.M. & Dowling, D.R. Fluid Mechanics - 5th ed. (Elsevier, Amsterdam; 2012).
167. van Reenen, A. et al. Accurate Quantification of Magnetic Particle Properties by Intra-pair Magnetophoresis for Nanobiotechnology. *Appl Phys Lett* **103**, 043704 (2013).
168. Akerstrom, B. & Bjorck, L. A physicochemical study of protein G, a molecule with unique immunoglobulin G-binding properties. *J Biol Chem* **261**, 10240-10247 (1986).
169. Allauzen, S., Mani, J.C., Granier, C., Pau, B. & Bouanani, M. Epitope mapping and binding analysis of insulin-specific monoclonal antibodies using a biosensor approach. *J Immunol Methods* **183**, 27-32 (1995).
170. Homola, J., Yee, S.S. & Gauglitz, G. Surface plasmon resonance sensors: review. *Sensor Actuat B-Chem* **54**, 3-15 (1999).
171. Lipfert, J., Kerssemakers, J.W., Jager, T. & Dekker, N.H. Magnetic torque tweezers: measuring torsional stiffness in DNA and RecA-DNA filaments. *Nat Methods* **7**, 977-980 (2010).
172. Melle, S., Calderon, O.G., Rubio, M.A. & Fuller, G.G. Microstructure evolution in magnetorheological suspensions governed by Mason number. *Phys Rev E* **68** 041503 (2003).
173. Zylka, W. & Ottinger, H.C. A Comparison between Simulations and Various Approximations for Hookean Dumbbells with Hydrodynamic Interaction. *J Chem Phys* **90**, 474-480 (1989).
174. van Ommering, K., Lamers, C.C.H., Nieuwenhuis, J.H., van IJendoorn, L.J. & Prins, M.W.J. Analysis of individual magnetic particle motion near a chip surface. *J Appl Phys* **105**, 104905 (2009).
175. Derks, R.J.S., Frijns, A.J.H., Prins, M.W.J. & Dietzel, A. Multibody interactions of actuated magnetic particles used as fluid drivers in microchannels. *Microfluid Nanofluid* **9**, 357-364 (2010).
176. Shevkoplyas, S.S., Siegel, A.C., Westervelt, R.M., Prentiss, M.G. & Whitesides, G.M. The force acting on a superparamagnetic bead due to an applied magnetic field. *Lab Chip* **7**, 1294-1302 (2007).
177. Ermak, D.L. & McCammon, J.A. Brownian dynamics with hydrodynamic interactions. *J. Chem. Phys.* **69**, 1352-1360 (1978).
178. Schmidt, R.R., Cifre, J.G. & de la Torre, J.G. Comparison of Brownian dynamics algorithms with hydrodynamic interaction. *J Chem Phys* **135**, 084116 (2011).
179. von Hansen, Y., Hinczewski, M. & Netz, R.R. Hydrodynamic screening near planar boundaries: effects on semiflexible polymer dynamics. *J Chem Phys* **134**, 235102 (2011).
180. Leach, J. et al. Comparison of Faxen's correction for a microsphere translating or rotating near a surface. *Phys Rev E Stat Nonlin Soft Matter Phys* **79**, 026301 (2009).

181. Upadhyayula, S. et al. Coatings of polyethylene glycol for suppressing adhesion between solid microspheres and flat surfaces. *Langmuir* **28**, 5059-5069 (2012).
182. Shapiro, H.M. Practical Flow Cytometry, Edn. 3rd. (John Wiley & Sons, Hoboken, NJ; 2005).
183. Eid, J. et al. Real-Time DNA Sequencing from Single Polymerase Molecules. *Science* **323**, 133-138 (2009).
184. Bentley, D.R. et al. Accurate whole human genome sequencing using reversible terminator chemistry. *Nature* **456**, 53-59 (2008).
185. Leake, M.C. The physics of life: one molecule at a time. *Philos Trans R Soc Lond B Biol Sci* **368**, 20120248 (2013).
186. Pyrz, W.D. & Buttrey, D.J. Particle size determination using TEM: a discussion of image acquisition and analysis for the novice microscopist. *Langmuir* **24**, 11350-11360 (2008).
187. Vogel, R. et al. Quantitative sizing of nano/microparticles with a tunable elastomeric pore sensor. *Anal Chem* **83**, 3499-3506 (2011).
188. van Ommering, K., Nieuwenhuis, J.H., van IJzendoorn, L.J., Koopmans, B. & Prins, M.W.J. Confined Brownian motion of individual magnetic nanoparticles on a chip: Characterization of magnetic susceptibility. *Appl Phys Lett* **89**, 142511 (2006).
189. Li, G.X. et al. Detection of single micron-sized magnetic bead and magnetic nanoparticles using spin valve sensors for biological applications. *J Appl Phys* **93**, 7557-7559 (2003).
190. Mihajlovic, G. et al. Magnetic characterization of a single superparamagnetic bead by phase-sensitive micro-Hall magnetometry. *Appl Phys Lett* **91**, 172518 (2007).
191. Lim, J. et al. Magnetophoresis of Nanoparticles. *Acs Nano* **5**, 217-226 (2011).
192. Janssen, X.J.A., van IJzendoorn, L.J. & Prins, M.W.J. On-chip manipulation and detection of magnetic particles for functional biosensors. *Biosens Bioelectron* **23**, 833-838 (2008).
193. Kusumi, A., Sako, Y. & Yamamoto, M. Confined Lateral Diffusion of Membrane-Receptors as Studied by Single-Particle Tracking (Nanovid Microscopy) - Effects of Calcium-Induced Differentiation in Cultured Epithelial-Cells. *Biophys J* **65**, 2021-2040 (1993).
194. Bausch, A.R., Ziemann, F., Boulbitch, A.A., Jacobson, K. & Sackmann, E. Local measurements of viscoelastic parameters of adherent cell surfaces by magnetic bead microrheometry. *Biophys J* **75**, 2038-2049 (1998).
195. Irmischer, M., de Jong, A.M., Kress, H. & Prins, M.W.J. A method for time-resolved measurements of the mechanics of phagocytic cups. *J R Soc Interface* **10**, 20121048 (2013).
196. Sing, C.E., Schmid, L., Schneider, M.F., Franke, T. & Alexander-Katz, A. Controlled surface-induced flows from the motion of self-assembled colloidal walkers. *Proc Natl Acad Sci U S A* **107**, 535-540 (2010).
197. Van Mensfoort, S.L.M. et al. Measuring the light emission profile in organic light-emitting diodes with nanometre spatial resolution. *Nature Photonics* **4**, 329-335 (2010).

198. Carvelli, M., van Reenen, A., Janssen, R.A.J., Loebl, H.P. & Coehoorn, R. Exciton formation and light emission near the organic-organic interface in small-molecule based double-layer OLEDs. *Org Electron* **13**, 2605-2614 (2012).
199. Gaster, R.S. et al. Quantification of protein interactions and solution transport using high-density GMR sensor arrays. *Nat Nanotechnol* **6**, 314-320 (2011).
200. Gaster, R.S. et al. Matrix-insensitive protein assays push the limits of biosensors in medicine. *Nat Med* **15**, 1327-1332 (2009).
201. Kawaguchi, H. Functional polymer microspheres. *Prog. Polym. Sci.* **25**, 1171-1210 (2000).
202. De Palma, R. et al. Magnetic bead sensing platform for the detection of proteins. *Anal Chem* **79**, 8669-8677 (2007).
203. Helm, C.A., Knoll, W. & Israelachvili, J.N. Measurement of Ligand Receptor Interactions. *P Natl Acad Sci USA* **88**, 8169-8173 (1991).
204. Klaue, D. & Seidel, R. Torsional stiffness of single superparamagnetic microspheres in an external magnetic field. *Phys Rev Lett* **102**, 028302 (2009).
205. Happel, J. & Brenner, H. Low Reynolds Number Hydrodynamics. (Kluwer Academic Publishers, Dordrecht; 1983).
206. Ge, S., Kojio, K., Takahara, A. & Kajiyama, T. Bovine serum albumin adsorption onto immobilized organotrichlorosilane surface: influence of the phase separation on protein adsorption patterns. *J Biomater Sci Polym Ed* **9**, 131-150 (1998).
207. Wyckoff, R.W.G. Crystal Structures - 2nd edition. (Krieger, Malabar, FL, 1982).
208. Frankel, R.B. & Blakemore, R.P. Magnetite and magnetotaxis in microorganisms. *Bioelectromagnetics* **10**, 223-237 (1989).
209. Fonnum, G., Johansson, C., Molteberg, A., Morup, S. & Aksnes, E. Characterization of Dynabeads by magnetization measurements and Mossbauer spectroscopy. *J Magn Mater* **293**, 41-47 (2005).
210. Housecroft, C.E. & Sharpe, A.G. Inorganic Chemistry - Second Edition. (Pearson, 2005).
211. Osborn, J.A. Demagnetizing Factors of the general ellipsoid. *Phys Rev* **67**, 351-358 (1945).
212. Beleggia, M., De Graef, M. & Millev, Y. Demagnetization factors of the general ellipsoid: An alternative to the Maxwell approach. *Philosophical Magazine* **86**, 2451-2466 (2006).
213. Gabdouliline, R.R. & Wade, R.C. Brownian dynamics simulation of protein-protein diffusional encounter. *Methods* **14**, 329-341 (1998).

Samenvatting

De toenemende gemiddelde levensduur en de toename van chronische ziekten resulteren in een grote druk op de gezondheidszorg. Hierdoor neemt de behoefte toe aan gebruiksvriendelijke en kosteneffectieve medische technologieën. *In vitro* diagnostiek (IVD) speelt een grote rol binnen de gezondheidszorg, en binnen de IVD markt is gedecentraliseerd diagnostisch testen een groeiend segment, ook wel point-of-care testing (POCT) genoemd. Apparaten voor POCT moeten compact en volledig geïntegreerd zijn voor maximaal gebruiksgemak. Een nieuwe klasse van POCT technologieën is in opkomst, gebaseerd op het manipuleren en detecteren van magnetische deeltjes met groottes van tientallen tot duizenden nanometers. Het gebruik van magnetische deeltjes heeft belangrijke voordelen. Ze hebben een relatief groot reactieoppervlak dat kan worden gefunctionaliseerd met (bio)chemische moleculen. Daarnaast zijn ze optisch goed detecteerbaar, en kunnen ze worden gemanipuleerd met behulp van magnetische velden voor volledige controle in een geïntegreerde test. Op basis van deze eigenschappen worden magnetische deeltjes toegepast om belangrijke processtappen in geïntegreerde microfluidische tests uit te voeren, zoals mengen, vangen van bepaalde (bio)chemische bestanddelen, wassen, en labelen voor de uiteindelijke detectie.

Dit proefschrift beschrijft onderzoek aan de magnetische manipulatie van magnetische deeltjes in het kader van de toepassing in biosensoren. We hebben het begrip hierover vergroot door middel van experimentele studies in combinatie met theoretische modelbeschrijvingen van magnetisch aangestuurde processen. We hebben verschillende (bio)chemische bindingsprocessen gekarakteriseerd, beperkende factoren daarin geïdentificeerd en nieuwe protocollen voor magnetische aansturing ontwikkeld om de bindingsstappen te versnellen en om toekomstige integratie mogelijk te maken. Meer specifiek zijn methodes onderzocht (i) om snel en efficiënt bestanddelen te vangen vanuit een monstervloeistof, (ii) om verdelingen van magnetische deeltjes te beheersen, en (iii) om gevangen bestanddelen op een snelle wijze te binden aan een sensoroppervlak. Ten slotte hebben we de integratie van de verschillende processen in een biosensor beschouwd.

Magnetische deeltjes zijn uitermate geschikt om specifieke bestanddelen (zogenoemde targets) zoals eiwitten te vangen vanuit biologische monsters vanwege het grote reactieoppervlak dat op velerlei wijzen gefunctionaliseerd kan worden. In het eerste deel van dit proefschrift hebben we dit vangproces ontrafeld door experimenten met verschillende modelsystemen te vergelijken met numerieke simulaties. Ten

eerste zorgt fysisch transport (bv door diffusie) ervoor dat de magnetische deeltjes in aanraking komen met de targets. Vervolgens zorgt een combinatie van relatieve translatie en rotatie van beide deeltjes voor een wederzijdse uitlijning van de specifieke bindingsplaatsen die aanwezig zijn op beide deeltjes. Ten slotte vindt er een chemische reactie plaats om het target te binden aan het magnetische deeltje. In experimenten waarin eiwitten als targets werden gebruikt, hebben we gevonden dat het vangproces voornamelijk wordt gelimiteerd door de eerste twee transportprocessen. We hebben aangetoond dat dit het gevolg is van uitgeputte eiwitconcentraties nabij het reactieve magnetische deeltjesoppervlakte, met name bij hoge concentraties van magnetische deeltjes. Door de magnetische deeltjes met behulp van magnetische velden in beweging te brengen, kunnen deze uitgedunde zones worden verkleind. In het bijzonder hebben we gradiënten in het magnetische veld en roterende magnetische velden gebruikt om te zorgen voor translatie en rotatie van ketens van magnetische deeltjes door het vloeistofvolume. Gebruikmakend van fluorescent gelabelde eiwitten als targets hebben we associatiesnelheidsconstanten bepaald voor verschillende aansturingprotocollen en verschillende concentraties van de magnetische deeltjes. We hebben gevonden dat magnetische actuaties de vangsnelheden kan verhogen met 1 tot 2 ordes van grootte. In een microfluidische diagnostische test kan dit worden gebruikt om incubatietijden te verkorten of om de vangefficiëntie (en daarmee mogelijk ook de detectielimiet) te verbeteren.

Als magnetische deeltjes worden blootgesteld aan magnetische velden, dan hebben ze de neiging om samen te klonteren en af te drijven naar de externe stuurmagneten. Dit effect is meestal ongewild en vermindert de toepasbaarheid van magnetische manipulatie van magnetische deeltjes. Het is niet voordehandliggend hoe het omgekeerde proces bereikt kan worden, d.w.z. het uitspreiden en verplaatsen van deeltjes van de stuurmagneten af. In het tweede deel van dit proefschrift presenteren we twee nieuwe manieren om met behulp van magnetische velden samengeklonterde deeltjes te verdelen over een oppervlakte. In de ene benadering stabiliseren we afstotende magnetische krachten tussen deeltjes door ze vast te houden nabij een oppervlakte door middel van gradiënten in het magnetische veld. Om dit proces en experimentele data te analyseren, hebben we een numeriek model voor de geïnduceerde deeltjesdynamica ontwikkeld op basis van Brownse dynamica. Daarnaast bleek de ontwikkelde methode geschikt om de magnetische eigenschappen van magnetische deeltjes nauwkeurig te karakteriseren; deze methode noemen we intrapair magnetophoresis. In de andere benadering om magnetische deeltjes te verspreiden over een oppervlak, passen we zogenaamde rotaphoresis toe, waarin een magnetisch geïnduceerde draaiing van samengeklonterde deeltjes wordt omgezet in een lineaire verplaatsing door middel van een nabij oppervlak en een neerwaartse kracht. Door het afstemmen van de tijdsafhankelijke eigenschappen van het magnetisch veld, kunnen grote clusters van deeltjes worden voortbewogen over een oppervlakte met snelheden van enkele millimeters per seconde, terwijl ze zich binnen enkele seconden volledig uitspreiden. Op basis van dit onderzoek concluderen we dat interessant en functioneel deeltjesgedrag kan worden verkregen door de toepassing van tijdsafhankelijke magnetische velden in drie dimensies. De ontwikkelde methoden

vergroten de beheersbaarheid van ensembles van magnetische deeltjes en kunnen toegepast worden in een biosensor systeem.

In het derde deel van dit proefschrift hebben we onderzocht of magnetische velden kunnen worden ingezet om targets, gevangen door magnetische deeltjes, versneld aan een sensoroppervlak te binden. Om het bindingsproces in detail te analyseren, hebben we gebruik gemaakt van een modelsysteem met relatief grote targets, namelijk fluorescerende deeltjes met een diameter van 200 nanometers. Dit stelde ons in staat om specifieke bindingen van magnetische deeltjes met het oppervlak (via een target) te onderscheiden van niet-specifieke bindingen (zonder target). Door middel van numerieke simulaties van de bindingsreactie werd eerst een magnetisch actuatieprotocol ontwikkeld om het oppervlak van de magnetische deeltjes (met mogelijke targets) optimaal in contact te brengen met het sensoroppervlak. Uit de simulaties bleek dat het mogelijk zou moeten zijn om incubatietijden te verminderen met ongeveer een factor 3. Experimentele gegevens lieten echter zien dat niet-specifieke interacties de blootstelling van het volledige deeltjesoppervlak aan het sensoroppervlak in grote mate belemmerde. Op basis van onze resultaten en de huidige literatuur verwachten wij dat het breken van niet-specifieke bindingen door middel van magnetische veldgradiënten binnen het ontwikkelde incubatieprotocol, de specifieke bindingsvorming verder kan versnellen met ten minste een orde van grootte.

De methoden beschreven in dit proefschrift ondersteunen de ontwikkeling van geïntegreerde diagnostische tests waarin alle microfluidische processtappen snel en efficiënt worden uitgevoerd met behulp van magnetische velden. We voorzien dat de integratie van methoden om bindingsprocessen te versnellen kan worden vergemakkelijkt met behulp van de methoden om magnetische deeltjes uit te spreiden over een oppervlak. Onze vindingen laten zien dat belangrijke processtappen in een diagnostische test beduidend sneller kunnen worden uitgevoerd door magnetische deeltjes te manipuleren. Met een versnelling van mogelijk 1 tot 2 ordes van grootte in deze processtappen zou de prestatie van een biosensor behoorlijk verbeterd kunnen worden.

We verwachten dat geïntegreerde biosensor-systemen gebaseerd op magnetische manipulatie van magnetische deeltjes een grote impact op de samenleving kunnen hebben. Dergelijke systemen zullen het mogelijk maken om nabij de patiënt in een klein apparaat kwantitatieve *in vitro* diagnostische testen uit te voeren op een snelle en gebruiksvriendelijke manier ("sample-in result-out"). Op basis van deze eigenschappen kunnen de POCT systemen helpen om in de toekomst de kwaliteit, de beschikbaarheid en de kosteneffectiviteit van gezondheidszorg te verbeteren.

Publications

Journal papers:

- [A. van Reenen](#), S. Paquay, S.R. Kuijpers, A. M. de Jong, P.P.A.M. van der Schoot, M.W.J. Prins, “Magnetic field-enhanced molecular bond formation in surface-bound assays based on magnetic particles”, *in preparation*.
- [A. van Reenen](#), A. M. de Jong, M.W.J. Prins, “Dynamic actuation of magnetic particle chains for accelerated target analyte capture from liquid”, *in preparation*.
- [A. van Reenen](#), A. M. de Jong, M.W.J. Prins, “Magnetic Rotaphoresis for Controlled Assembly of Colloidal Magnetic Particles at a Solid-Liquid Interface”, *in preparation*.
- Y. Gao, J. Beerens, [A. van Reenen](#), M.A. Hulsen, A.M. de Jong, M.W.J. Prins, J.M.J. den Toonder, “Strong vortical flows generated by a swarm of rotating particle chains”, *submitted*.
- [A. van Reenen](#), A.M. de Jong, J.M.J. den Toonder, M.W.J. Prins, “Integrated Lab-on-Chip Biosensing Systems based on Magnetic Particle Actuation – a Comprehensive Review”, *Lab Chip*, DOI: 10.1039/C3LC51454D, 2014.
- [A. van Reenen](#), Y. Gao, A.M. de Jong, M.A. Hulsen, J.M.J. den Toonder, M.W.J. Prins, “Dynamics of Magnetic Particles near a Surface: Model and Experiments of Field-Induced Disaggregation”, *Phys Rev E*, *accepted*.
- [A. van Reenen](#), Y. Gao, A.H. Bos, A.M. de Jong, M.A. Hulsen, J.M.J. den Toonder, M.W.J. Prins, “Accurate Quantification of Magnetic Particle Properties by Intra-pair Magnetophoresis for Nanobiotechnology”, *Appl. Phys. Lett.*, vol 103, pp 043704, 2013.
- Y. Gao, [A. van Reenen](#), M.A. Hulsen, A.M. de Jong, M.W.J. Prins, J.M.J. den Toonder, “Chaotic Fluid Mixing by Alternating Microparticle Topologies to Enhance Biochemical Reactions”, *Microfluidics Nanofluidics*, vol 14, 2013.
- Y. Gao[†] & [A. van Reenen](#)[†], M.A. Hulsen, A.M. de Jong, M.W.J. Prins, J.M.J. den Toonder, “Disaggregation of microparticle clusters by induced magnetic dipole-dipole repulsion near a surface”, *Lab Chip*, vol 13, pp 1394-1401, 2013.
- [A. van Reenen](#), A. M. de Jong, M.W.J. Prins, “Accelerated Particle-Based Target Capture – The Roles of Volume Transport and Near-Surface Alignment”, *J. Phys. Chem. B*, vol 117, pp 1210-1218, 2013.

[†] Equal contributions

- [A. van Reenen](#), F. A. Gutiérrez-Mejía, L. J. van IJzendoorn, M.W.J. Prins, “Torsion Profiling of Proteins Using Magnetic Particles”, *Biophysical Journal*, vol 104, pp 1073-1080, 2013.

Non-related to this work:

- W.K. Wijting, [A. van Reenen](#), J. Laven, R.A.T.M. van Benthem, G. de With, “Competitive Adsorption of (Phosphorylated) Ethoxylated Styrene Oxide Polymer and Polyacrylic Acid on Silica Coated Iron Oxide Pigment”, *Colloids and Surfaces A: Physicochem. Eng. Aspects*, vol 449, pp 19-30, 2014.
- M. Carvelli, [A. van Reenen](#), R.A.J. Janssen, H.P. Loebel, R. Coehoorn, “Exciton formation and light emission near the organic–organic interface in small-molecule based double-layer OLEDs”, *Organic Electronics*, vol 13, pp 2605-2614, 2012.
- X.J.A. Janssen, [A. van Reenen](#), L.J. van IJzendoorn, A.M. de Jong, M.W.J. Prins, “The rotating particles probe: A new technique to measure interactions between particles and a substrate”, *Colloids and Surfaces A: Physicochem. Eng. Aspects*, vol 373, pp 88-93, 2011.

Patent:

- [A. van Reenen](#), Y. Gao, A.M. de Jong, M.A. Hulsen, J.M.J. den Toonder, M.W.J. Prins. Accelerated capture of biomarkers using magnetic particles. *Invention disclosure-Philips Research*. Submitted, 2012.

Book chapter:

- [A. van Reenen](#), A.M. de Jong, J.M.J. den Toonder, M.W.J. Prins, “Magnetic Particle Actuation in Stationary Microfluidics for Integrated Lab-on-Chip Biosensors”, *submitted for publication as a book chapter in Microfluidics for Medical Applications by A. van den Berg and L.I. Segerink, RSC publishing*.

Conference proceedings:

- F.A. Gutiérrez-Mejía, [A. van Reenen](#), L.J. van IJzendoorn, M.W.J. Prins. “Altering the Torsional Rigidity of Proteins with Surfactants.” *9th EBSA European Biophysics Congress*, Lisbon, Portugal, July 13 – 17, *European Biophysics Journal*, Vol 42, pp 170, 2013.
- [A. van Reenen](#), Y. Gao, A.M. de Jong, M.A. Hulsen, J.M.J. den Toonder, M.W.J. Prins. “Dynamic magnetic particle actuation for rapid biosensing”, *proceedings of the 17th International Conference on Miniaturized Systems for Chemistry and Life Sciences, MicroTAS 2013*, Freiburg, Germany, October 27 – 31, pp. 209-211, 2013.
- Y. Gao, [A. van Reenen](#), M.A. Hulsen, A.M. de Jong, M.W.J. Prins, J.M.J. den Toonder. “Manipulation of magnetic particles in microfluidic volumes”, *proceedings of the 17th International Conference on Miniaturized Systems for Chemistry and Life Sciences, MicroTAS 2013*, Freiburg, Germany, October 27 – 31, pp. 98-100, 2013.
- [A. van Reenen](#), Y. Gao, A.M. de Jong, M.A. Hulsen, J.M.J. den Toonder, M.W.J. Prins. “Accelerated target capture by dynamic magnetic particle actuation”, *proceedings of the 16th International Conference on Miniaturized Systems for Chemistry and Life Sciences, MicroTAS*, Okinawa, Japan, October 28 – November 1, pp. 926-928, 2012.

- Y. Gao, [A. van Reenen](#), M.A. Hulsen, A.M. de Jong, M.W.J. Prins, J.M.J. den Toonder. “Chaotic fluid mixing by alternating micro-particle topologies to enhance biochemical reactions”, *proceedings of the 16th International Conference on Miniaturized Systems for Chemistry and Life Sciences, MicroTAS*, Okinawa, Japan, October 28 – November 1, pp. 320-322, 2012.
- [A. van Reenen](#), A.M. de Jong, M.W.J. Prins. “Quantification of the mix and catch efficiency by microparticles for biosensing with single-molecule resolution”, *proceedings of the 15th International Conference on Miniaturized Systems for Chemistry and Life Sciences, MicroTAS*, Seattle, USA, November 2 – 6, pp. 1627-1629, 2011.

Conference presentations (oral):

- A. van Reenen, A.M. de Jong, M.W.J. Prins. “How Magnetic Actuation overcomes Diffusion Limitations in Particle-based Target Capture for Microfluidic Biosensing”, *1st International conference on Micro & Nanofluidics, Flow 14*, Enschede, The Netherlands, 18-21st May 2014.
- [A. van Reenen](#), A.M. de Jong, M.W.J. Prins. “Physics of Magnetic Particle Actuation for Rapid Biosensing”, *Dutch FOM Physics conference*, Veldhoven, The Netherlands, 21st Jan 2014.
- [A. van Reenen](#), Y. Gao, A.M. de Jong, M.A. Hulsen, J.M.J. den Toonder, M.W.J. Prins. “Dynamic magnetic particle actuation for rapid biosensing”, *International Gordon Research Seminar on the physics & chemistry of microfluidics*, Lucca, Italy, 8th Jun 2013.
- [A. van Reenen](#), A.M. de Jong, M.W.J. Prins. “Accelerated Target Capture by Dynamic Magnetic Particle Actuation”, *MicroNanoConference*, Ede, The Netherlands, 10th Dec 2012.
- [A. van Reenen](#), A.M. de Jong, M.W.J. Prins. “Accelerated Target Capture by Dynamic Magnetic Particle Actuation”, *European Microfluidics conference*, Heidelberg, Germany, 3th Dec 2012.
- [A. van Reenen](#), L.J. van IJzendoorn, M.W.J. Prins. Protein Twisting by Magnetic Particle Actuation, *Dutch FOM Biophysics conference*, Veldhoven, The Netherlands, 5th Oct 2010.

Other presentations (oral):

- [A. van Reenen](#), “Biophysics for Biosensing”, *Paradoksymposium*, University of Twente, The Netherlands, 9 May 2012.
- [A. van Reenen](#), “Protein Twisting by Magnetic Particle Actuation”, *cNM Research Day*, Eindhoven University of Technology, The Netherlands, 30th Jun 2010.

Conference poster presentations (only international):

- [A. van Reenen](#), Y. Gao, A.M. de Jong, M.A. Hulsen, J.M.J. den Toonder, M.W.J. Prins. “Dynamic magnetic particle actuation for rapid biosensing”, *proceedings of the 17th International Conference on Miniaturized Systems for Chemistry and Life Sciences, MicroTAS*, Freiburg, Germany, 2013.

- A. van Reenen, Y. Gao, A.M. de Jong, M.A. Hulsen, J.M.J. den Toonder, M.W.J. Prins. “Dynamic magnetic particle actuation for rapid biosensing”, *Gordon Research Conference on the physics & chemistry of microfluidics*, Lucca, Italy, 2013.
- A. van Reenen, Y. Gao, A.M. de Jong, M.A. Hulsen, J.M.J. den Toonder, M.W.J. Prins. “Accelerated target capture by dynamic magnetic particle actuation”, *proceedings of the 16th International Conference on Miniaturized Systems for Chemistry and Life Sciences, MicroTAS*, Okinawa, Japan, 2012.
- A. van Reenen, A.M. de Jong, M.W.J. Prins. “Quantification of the mix and catch efficiency by microparticles for biosensing with single-molecule resolution”, *proceedings of the 15th International Conference on Miniaturized Systems for Chemistry and Life Sciences, MicroTAS*, Seattle, USA, 2011.

Curriculum vitae

Alexander van Reenen was born on the 6th of March 1987 in Eindhoven, The Netherlands. After finishing secondary school (Christiaan Huygens College, Eindhoven) in 2005, he went on to study Applied Physics at the Eindhoven University of Technology and received his MSc degree with the highest honours ('cum laude') in Applied Physics in 2010. During his studies, he did a minor in Chemical Engineering, did an internship on the modeling of organic light-emitting diodes at Philips Research (Eindhoven, The Netherlands) and graduated in the Molecular Biosensors for Medical Diagnostics (MBx) group of Prof. Menno Prins on a novel method to profile the torsion of protein complexes using magnetic particle actuation.

In September 2010, Alexander started working as a PhD student in the MBx group under the supervision of Prof. Menno Prins and Dr. Arthur de Jong. He studied the dynamic actuation of magnetic particles for future lab-on-chip biosensors. This thesis summarizes the main results of his work.

Dankwoord

En zo komt aan vier jaar promotieonderzoek een eind. Werk door mij uitgevoerd, maar wat zeker niet tot dit resultaat had kunnen leiden zonder de uiteenlopende hulp en steun van vele anderen, die ik hier bij name wil noemen en bedanken.

Menno, mijn promotor, jij hebt mij geïnspireerd en geleerd om nog kritischer onderzoek te doen, praktisch te denken en het grotere geheel in gedachten te houden. Ik vond het een privilege om in jouw groep fundamenteel onderzoek te kunnen doen met een concrete en realistische toepassing in het vizier. Je onophoudelijke enthousiasme over het onderzoek werkte erg aanstekelijk en inspireerde mij om het beste uit mezelf te halen. Je hebt menig uur besteed aan mijn vele pennevruchten, en telkens wist je ze nog scherper en nog beter te maken. Ik heb erg veel van je geleerd. Mijn dank daarvoor!

Arthur, als mijn co-promotor en dagelijkse begeleider wist je met een nuchtere en realistische blik uit mijn wilde ideeën de haalbare opties te destilleren of nieuwe te bedenken. Daar heb ik veel van geleerd. Je gaf me de vrijheid om een eigen draai aan het project te geven, wat me de ruimte gaf om me het project eigen te maken en zelfstandig uit te voeren. Desondanks hield je de grenzen in de gaten en gaf je sturing waar nodig. Dankjewel voor je begeleiding!

Zoals al te zien is in de publicatielijst, heb ik veel te danken aan Yang Gao. Als ik later aan mijn promotieonderzoek terugdenk, zal ik me zeker de vele uren herinneren die wij in het lab hebben doorgemaakt om ons onderzoek lopend te krijgen, ... en onze wereldbeelden uit te wisselen. In hetzelfde project, met eigen doelen, verschillende expertises, maar vele raakvlakken, zijn we op het juiste moment geconvergeerd, en uiteindelijk op tijd weer gedivergeerd, wat een explosie aan onderzoeksresultaten heeft opgeleverd. Niet te vergeten zijn ook de conferenties in Okinawa, Lucca, Heidelberg en Freiburg! Bedankt voor de extra dimensie die je hebt gegeven aan mijn promotieonderzoek!

Mijn tweede promotor, Jaap den Toonder, wil ik bedanken voor zijn betrokkenheid en ideeën voor mijn onderzoek. Je stond wat verder weg van mijn onderzoek, maar onder andere dankzij de intensieve samenwerking met Yang heb je op verschillende manieren bijgedragen.

Mijn dank gaat ook uit naar andere mensen binnen (of gerelateerd aan) het STW project waar mijn onderzoek onder viel: Hans van Zon, Martien Hulsen, en Neehar Moharana. Ook bedank ik de leden van mijn promotiecommissie voor het lezen en beoordelen van mijn proefschrift.

Zoals eerder genoemd heb ik mijn werkleven doorgebracht binnen de vakgroep MBx. Leo, via jou ben ik de vakgroep binnengekomen en het was een onvergetelijke ervaring om er in te werken: bedankt! De werksfeer wordt bepaald door de aanwezige mensen en dat waren er velen, die ik allemaal wil bedanken: Matthias, Loes, Marijn, Asha, Claudia, Andrea, Konrad, Denis, Roland, Stefano, Fabiola, Emiel, Peter en Michael. Hoewel ik erg werk-gefocused kan zijn, zorgden eerst Konrad en later Emiel voor gezonde afleiding en humor in de werkkamer. Het is goed om een ontspannen kamersfeer te hebben waar je kunt werken, en daar hebben jullie aan bijgedragen! Ook wil ik de stagairs bedanken die ik heb mogen begeleiden: Koen, Benice, Arjen, Lukas en Maarten.

Stephan, mijn tweelingbroer, onze carrièrepaden zijn langzaam maar zeker aan het scheiden. En toch lijken we nog steeds enorm op elkaar. Het was leuk om onze promotieonderzoeken te vergelijken en elkaar zodoende verschillende inzichten te geven. Het is waardevol om iemand in de familie te hebben die je werk precies begrijpt, en waarmee je ook nog eens heel veel andere zaken deelt. Tweeling zijn is speciaal, en dat besef ik steeds meer!

Mijn ouders wil ik bedanken voor hun rotsvaste vertrouwen en steun. Dat ik tot hier gekomen ben is voor een groot deel dankzij jullie. Daarnaast wil ik ook Vincent, mijn andere broer, en verdere (schoon)familie bedanken, onder andere voor de pogingen om mijn werk te begrijpen.

Janine, jou noem ik in het bijzonder. Met geen woorden is het te beschrijven hoe belangrijk jij voor mij bent en hoe dankbaar ik je ben! Jij kent en begrijpt mij en geeft mij rust en energie. Het effect dat je daarmee hebt op mij persoonlijk en op mijn werk zijn enorm. Tijdens het eerste jaar van mijn promotieonderzoek hebben we elkaar trouw beloofd. In de afgelopen jaren zijn we nog dichter naar elkaar toegroeid, en ik kijk ernaar uit om mijn verdere leven met jou te delen, waar we ook terecht komen en wat er ook gebeurt!

Tot slot, een promotieonderzoek is bij uitstek geschikt om over meer zaken na te denken dan alleen een specifiek wetenschappelijk-technisch vraagstuk. De afgelopen vier jaar is mijn geloof in God en Jezus Christus alsmaar gegroeid en dit bepaalt in grote mate hoe ik naar mezelf kijk als mens en naar de wereld om mij heen. Kijken naar de wereld om ons heen, of observeren, is een van de belangrijkste peilers van de wetenschap, die we niet uit het oog moeten verliezen, met name in een wereld van doelgerichtheid en zelfontplooiing; Prediker zei het al (Pred 2:14a): “*De wijze heeft ogen in zijn hoofd, maar de dwaas wandelt in de duisternis*”. Steeds meer leer ik in stille verwondering te kijken naar de schoonheid van de wereld om ons heen. Hiervoor dank ik God, alsook voor de ruimte en al de mensen om mij heen waardoor ik dit werk heb mogen doen.

